

Roadmap for focused ion beam technologies

Katja Höflich,^{1, a)} Gerhard Hobler,^{2, b)} Frances I. Allen,^{3, c)} Tom Wirtz,^{4, d)} Gemma Rius,^{5, e)} Arkady V. Krasheninnikov,⁶ Matthias Schmidt,⁷ Ivo Utke,⁸ Nico Klingner,⁶ Markus Osenberg,⁹ Lisa McElwee-White,¹⁰ Rosa Córdoba,¹¹ Flyura Djurabekova,¹² Ingo Manke,⁹ Philip Moll,¹³ Mariachiara Manoccio,¹⁴ José María De Teresa,¹⁵ Lothar Bischoff,⁶ Johann Michler,⁸ Olivier De Castro,⁴ Anne Delobbe,¹⁶ Peter Dunne,¹⁷ Oleksandr V. Dobrovolskiy,¹⁸ Natalie Freese,¹⁹ Armin Götzhäuser,¹⁹ Paul Mazarov,²⁰ Wolfhard Möller,⁶ Francesc Pérez-Murano,⁵ Patrick Philipp,⁴ Florian Vollnhals,²¹ and Gregor Hlawacek^{6, f)}

¹⁾ *Ferdinand-Braun-Institut gGmbH, Leibniz-Institut für Höchstfrequenztechnik, 12489 Berlin, Germany*

²⁾ *Institute of Solid-State Electronics, TU Wien, Gußhausstraße 25–25a, 1040 Vienna, Austria.*

³⁾ *Department of Materials Science and Engineering, University of California, Berkeley, CA 94720, USA*

⁴⁾ *Advanced Instrumentation for Nano-Analytics (AINA), MRT Department, Luxembourg Institute of Science and Technology (LIST), 4422 Belvaux, Luxembourg*

⁵⁾ *Institute of Microelectronics of Barcelona, IMB-CNM-CSIC, Carrer dels Til·lers s/n, E-08193, Cerdanyola, Spain*

⁶⁾ *Institute of Ion Beam Physics and Materials Research, Helmholtz-Zentrum Dresden-Rossendorf, Bautzner Landstr. 400, 01328 Dresden, Germany*

⁷⁾ *Helmholtz-Centre for Environmental Research GmbH—UFZ, Department of Isotope Biogeochemistry, Permoserstraße 15, 04318 Leipzig, Germany*

⁸⁾ *Laboratory for Mechanics of Materials and Nanostructures, EMPA Swiss Federal Laboratories for Material Science and Technology, Feuerwerkerstrasse 39, CH 3602 Thun, Switzerland*

⁹⁾ *Institute of Applied Materials, Helmholtz-Zentrum Berlin für Materialien und Energie, Hahn Meitner Platz 1, 14109 Berlin, Germany*

¹⁰⁾ *Department of Chemistry, University of Florida, Gainesville, Florida 32611–7200, USA*

¹¹⁾ *Institute of Molecular Science, University of Valencia, Catedrático José Beltrán 2, Paterna 46980, Spain*

¹²⁾ *Helsinki Institute of Physics and Department of Physics, University of Helsinki, P.O. Box 43, Helsinki FIB-00014, Finland*

¹³⁾ *Max Planck Institute for the Structure and Dynamics of Matter, Hamburg, Germany*

¹⁴⁾ *CNR-NANOTEC Institute of Nanotechnology, Via Monteroni, 73100 Lecce, Italy*

¹⁵⁾ *Instituto de Nanociencia y Materiales de Aragon (INMA), Universidad de Zaragoza-CSIC, 50009 Zaragoza, Spain*

¹⁶⁾ *Orsay Physics S. A., 13710 Fuveau, France*

¹⁷⁾ *Université de Strasbourg, CNRS, IPCMS UMR 7504, 23 rue du Loess, F-67034 Strasbourg, France*

¹⁸⁾ *University of Vienna, Faculty of Physics, Boltzmanngasse 5, 1090 Vienna, Austria*

¹⁹⁾ *Faculty of Physics, Physics of Supramolecular Systems, University of Bielefeld, 33615 Bielefeld, Germany*

²⁰⁾ *Raith GmbH, Konrad-Adenauer-Allee 8, 44263 Dortmund, Germany*

²¹⁾ *Institute for Nanotechnology and Correlative Microscopy gGmbH, Forchheim, Germany*

The focused ion beam (FIB) is a powerful tool for the fabrication, modification and characterization of materials down to the nanoscale. Starting with the gallium FIB, which was originally intended for photomask repair in the semiconductor industry, there are now many different types of FIB that are commercially available. These instruments use a range of ion species and are applied broadly in materials science, physics, chemistry, biology, medicine, and even archaeology. The goal of this roadmap is to provide an overview of FIB instrumentation, theory, techniques and applications. By viewing FIB developments through the lens of the various research communities, we aim to identify future pathways for ion source and instrumentation development as well as emerging applications, and the scope for improved understanding of the complex interplay of ion-solid interactions. We intend to provide a guide for all scientists in the field that identifies common research interests and will support future fruitful interactions connecting tool development, experiment and theory. While a comprehensive overview of the field is sought, it is not possible to cover all research related to FIB technologies in detail. We give examples of specific projects within the broader context, referencing original works and previous review articles throughout.

CONTENTS

Important overview tables	3	2. Electronic applications	35
Acronyms	3	3. Modification of magnetic materials	35
I. Introduction	3	4. Optical applications	36
II. Instrumentation	4	5. Property engineering of low-dimensional materials	37
A. Ion sources	5	6. Study of irradiation damage mechanisms	37
B. Beam transport	6	7. Outlook	38
C. Analytical tools and detectors	8	C. FIB-based imaging and tomography	38
D. Other FIB accessories	10	1. A brief history of FIB-based imaging and analysis	38
E. FIB of radioactive samples	11	2. HIM—A tool for imaging of the tiniest living objects	39
F. Software and correlative approaches	11	3. FIB-based tomography in the life sciences	40
III. Simulation approaches for FIB processing	13	4. FIB-based tomography of energy materials	42
A. Simulation techniques based on the binary collision approximation	14	5. Data processing of FIB-based tomographies	44
1. Principle and limitations	14	6. Outlook	44
2. Specific BCA codes	15	D. Elemental Analysis using SIMS	45
3. BCA-based simulations of FIB processing	15	1. Overview	45
B. Molecular dynamics and molecular statics	16	2. Applications in materials science	45
1. Principles and simulation codes	17	3. Applications in life sciences	46
2. Models for the potential energy function	17	4. Outlook	46
3. Applications of molecular dynamics to FIB irradiation	19	E. Applications of gas-assisted FIB processing	48
4. Limitations and extensions	21	1. Basics of ion-induced chemistry	48
C. Kinetic Monte Carlo (kMC)	21	2. Nanostructures for electronics	50
D. Continuum modeling	22	3. Nanostructures for mechanics	51
1. Ion implantation and milling	22	4. Nanostructures for photonics and plasmonics	52
2. Gas-assisted deposition and etching	23	5. Outlook	52
3. Applications to FIB processing	25	F. Novel and unconventional approaches in FIB processing	52
IV. Applications of focused ion beams	26	1. Resist patterning by FIB	52
A. Applications of subtractive FIB processing	27	2. Cryo-FIBID	54
1. FIB for materials science	29	3. FIB irradiation of metalorganic spin-coated layers	55
2. FIB for mechanical testing	29	4. FIB-induced mass transport	55
3. Applications in photonics and plasmonics	30	5. Hybrid fabrication and heterogeneous integration	55
4. Fabrication of custom probes	31	6. Outlook	56
5. FIB processing for quantum materials	31	V. Roadmap	56
6. FIB processing in the semiconductor industry	32	A. Drivers for future applications	56
7. Summary and outlook	32	B. The generic needs of the community	58
B. Engineering materials properties through defects	33	C. Important future developments	59
1. Basics of irradiation-induced defect creation	33	1. Ion beam generation and transport	59
		2. Accessories and complementary instrumentation	61
		3. Automation and data management	64
		4. Process modeling	65
		VI. Executive summary and perspective	67
		Acknowledgements	68
		Author contributions	69
		References	69

^{a)}Electronic mail: katja.hoefflich@fbh-berlin.de

^{b)}Electronic mail: gerhard.hobler@tuwien.ac.at

^{c)}Electronic mail: francesallen@berkeley.edu

^{d)}Electronic mail: tom.wirtz@list.lu

^{e)}Electronic mail: gemma.rius@csic.es

^{f)}Electronic mail: g.hlawacek@hzdr.de

IMPORTANT OVERVIEW TABLES

I	Common FIB sources	6
II	FIB based analytic methods	9
III	BCA simulation codes	16
IV	Useful interatomic potentials	18
V	Subtractive FIB processing	27
VI	FIB based materials property engineering .	34
VII	FIB based imaging of biological structures .	43
VIII	Applications of FIBID	49
IX	Common FIBID precursors	50

ACRONYMS

AES	Auger electron spectroscopy
AFM	atomic force microscope
API	application programming interface
APT	atom probe tomography
BCA	binary collision approximation
BI	backscattered ion
CAD	computer-aided design
CMOS	complementary metal-oxide-semiconductor
CNT	carbon nanotube
DAC	digital-to-analog converter
DC	direct current
DFT	density functional theory
EBIT	electron beam ion trap
EBL	electron beam lithography
EBSD	electron backscatter diffraction
ECR	electron cyclotron resonance
EDS	energy-dispersive X-ray spectroscopy
ESI	electrospray ionization source
EELS	electron energy loss spectroscopy
ETD	Everhardt-Thornley detector
EUV	extreme ultraviolet
ESA	excited surface atom
FEB	focused electron beam
FEBID	focused electron beam-induced deposition
FEBIE	focused electron beam-induced etching
FET	field-effect transistor
FIB	focused ion beam
FIBID	focused ion beam-induced deposition
FIBIE	focused ion beam-induced etching
FIM	field ion microscopy
FinFET	fin field-effect transistor
FMR	ferromagnetic resonance
FOV	field of view
GAP	Gaussian approximation potential
FWHM	full width at half maximum
GFIS	gas field-ionization source
GIS	gas injection system
hBN	hexagonal boron nitride
HIBL	helium ion beam lithography
HIM	helium ion microscope
HSQ	hydrogen silsesquioxane
IBIC	ion beam-induced charge
IC	integrated circuit

ICD	image charge detector
ICP	inductively coupled plasma
IIAES	ion-induced Auger electron spectroscopy
IL	ionoluminescence
ILIS	ionic liquid ion source
kMC	kinetic Monte Carlo
LMAIS	liquid metal alloy ion source
LMIS	liquid metal ion source
LOTIS	low temperature ion source
MC	Monte Carlo
MCP	micro channel plate
MD	molecular dynamics
ML	machine learning
MS	molecular statics
MOTIS	magneto-optical trap ion source
MRAM	magnetic random access memory
NAIS	nano-aperture ion source
NIL	nanoimprint lithography
NSOM	near-field optical microscopy
NV	nitrogen vacancy
OL	optical lithography
PEMFC	proton exchange membrane fuel cell
PFIB	plasma focused ion beam
PI	primary ion
PIXE	particle-induced X-ray emission
QMS	quadrupole mass spectrometer
RBS	Rutherford backscattering spectrometry
RIE	reactive ion etching
SE	secondary electron
SEM	scanning electron microscope
SI	secondary ion
SII	single ion implantation
SIMS	secondary ion mass spectrometry
SNMS	secondary neutral mass spectrometry
SSPD	superconducting single-photon detector
STIM	scanning transmission ion microscopy
TDDFT	time-dependent density functional theory
TEM	transmission electron microscope
TIC	total ion counter
TOF	time-of-flight
TRL	technology readiness level
UHV	ultra-high vacuum
YBCO	yttrium barium copper oxide
YIG	yttrium iron garnet
YSZ	yttrium stabilized zirconia
ZBL	Ziegler-Biersack-Littmark

I. INTRODUCTION

The technological origin of the focused ion beam (FIB) instruments we use today lies in outer space, or more precisely, in the application of ion beams for spacecraft propulsion. In space, thrust can only be generated by ejecting matter, the so-called reaction mass, which must be carried along with the spacecraft. In addition to chemical thrusters based on combustion, ion thrusters have emerged as an important tool for high-precision move-

ment. The positively charged ions that are generated by field ionization or by electrospraying, are accelerated by electric or magnetic fields, and then neutralized before being ejected in the opposite direction to that of the intended motion¹. Different types of thrusters based on liquid metal ion sources are currently being tested in space for ultra-precise position control of satellites, e.g. for the LISA gravitational wave interferometer¹. One of these thruster technologies, the electric field emission propulsion system (part of the LISA Pathfinder mission² and the more recent CubeSat launches³), is in fact very similar to the heart of many of our ground-based FIB instruments.

Whereas the ion thrusters used for astrophysics applications enable the exertion of forces in the micronewton range for the navigation of space objects, our ground-based FIB instruments enable the fabrication, modification and characterization of micrometer- to nanometer-sized objects.

The leading examples of FIB processing are still the site-selective preparation of samples for high-resolution imaging techniques, in particular for the transmission electron microscope (TEM) and for atom probe tomography (APT), and the targeted preparation of cross-sections for imaging using the scanning electron microscope (SEM). Several reviews have already been devoted to these important, well-established applications⁴⁻⁶. Our focus is therefore on novel and advanced applications of the FIB. Since focused ion beams can be used to modify any material down to the nanoscale in a variety of ways, from targeted doping to structural modification and geometric shaping, the FIB is a powerful tool in all areas from basic research to technology.

This document presents the state of the art of FIB research and development today and discusses future perspectives. It is organized as follows: Section II gives an overview of FIB instrumentation, starting with the generation and control of the focused ion beam, leading on to detectors and other complementary tools and accessories. Section III summarizes the theoretical approaches that can be used to describe various aspects of ion-matter interactions, including the binary collision approximation, molecular dynamics, kinetic Monte Carlo techniques, density functional theory, and continuum modeling. The last of these enables modeling over the longest length- and timescales, including treatment of ion- and electron-induced surface chemistry. The wide range of applications of the FIB is discussed in Section IV, which is organized according to the various experimental techniques (subtractive processing; defect engineering; imaging and tomography; elemental analysis; gas-assisted processing; and several other emerging directions). For each field of application, a selection of examples is discussed. As a

service to the community, summary tables with citations have been compiled in order to provide a more comprehensive (albeit non-exhaustive) literature review of each application field. These tables can be used as a starting point to help the reader identify new opportunities using the FIB for their own research.

Central to this document is the roadmap in Section V, which highlights future perspectives for FIB research and development based on the state of the art in the instrumentation, theory, and applications that were described previously. Here we have identified the key drivers for the FIB in different areas of science and technology, and linked these to FIB-specific challenges and the steps needed for future developments. We hope that this roadmap can serve as an incubator for future developments and will provide inspiration for scientific and technological breakthroughs, as well as serve as a unique resource for funding agencies and industry.

II. INSTRUMENTATION

The creation of a finely focused ion beam presents several engineering challenges and the beam requirements can vary widely depending on the application, sometimes with conflicting specifications. For example, for many applications, a high-current beam is desired to enable efficient milling (i.e. material removal by sputtering). However, high-current sources tend to deliver ions with a large energy spread, resulting in strong chromatic aberrations. Because of this (and also due to other reasons, such as spherical aberrations, as discussed later) it is challenging to build a high-current high-resolution source. Similar conflicting scenarios present themselves in many other areas of FIB instrumentation.

In the following, the various components of the FIB instrument are discussed. We start by describing the different ion sources that are used (Section II A). The source defines many properties of the final instrument, including the achievable spot size. Then we address beam transport via the ion optical column (Section II B), and subsequently detectors and analytics (Section II C); these elements, which are used to steer, shape and detect the ions, must be designed in such a way as to ensure the best possible end performance of the particular source being used. In the sample chamber, there are several other components that can be incorporated, including specialized sample stages for in-situ or in-operando experiments, micro-/nanomanipulators, and gas injectors; these are discussed in Section II D. Next, we address considerations concerning experiments with radioactive samples (Section II E). Finally, we outline software needs and correlative approaches for beam control, automation, and multi-modal analysis (Section II F).

¹ Neutralization is important here because otherwise the spacecraft would accumulate negative charge and thus attract the ejected positive ions.

A. Ion sources

In order to achieve high spatial resolution in a FIB instrument, an ion source with high brightness is required⁷. Analog to the definition in electron microscopy, the brightness B of an ion source is a measure of the compactness and directionality of the ion beam, according to:

$$B = \lim_{\Delta A \rightarrow 0} \lim_{\Delta \Omega \rightarrow 0} \frac{\Delta I}{\Delta A \cdot \Delta \Omega}, \quad (1)$$

where the emission current ΔI from a source area ΔA is emitted into a solid angle $\Delta \Omega$ ⁸. In practice, this means that ions are suitable for microscopy and nanofabrication if they are emitted from a highly localized area into a well-defined direction. The reduced brightness is derived from the above definition by taking into account the acceleration voltages of the FIB instrument; representative values for the different ion sources are given in Table I. In general, a smaller (virtual) source size means a higher brightness and consequently a higher achievable lateral resolution. However, for the final resolution of the instrument additional parameters such as the extractable ion current, energy spread, and of course the performance of the ion optics, are of also of importance. In the field of ion sources, the real breakthrough came in the 1970s, with the liquid metal ion source (LMIS), which was originally developed for space thruster applications^{31–33} and the gas field-ionization source (GFIS), which evolved from field ion microscopy (FIM) (dating back to the 1950s³⁴) and was first employed for scanning transmission ion microscopy (STIM) of biological specimens^{35,36}.

The LMIS consists of a capillary or a sharp needle tip, wetted with a molten metal. Through a combination of surface tension and applied electric field, the so-called Taylor cone³⁷ is formed, resulting in the extraction of ions from the source apex by field evaporation. The most common form of LMIS is based on gallium, due to its low melting temperature and low vapor pressure. In fact, the gallium LMIS is still the most used source for FIB instruments, not only because of its high brightness, but also because of its high source stability.

Directly related to the LMIS is the liquid metal alloy ion source (LMAIS), which through the use of a variety of alloys enables access to a much wider range of ion species^{10,13,38–46}. Based on the same principle, the ionic liquid ion source (ILIS) is wetted with a compound that dissociates into molecular anions and cations, such as the ionic liquids $C_6N_2H_{11}-BF_4$, $C_6N_2H_{11}-GaCl_4$ or $C_8N_2H_{15}-I$ ^{14,47–52}. The ILIS is thus capable of producing beams of molecular ions, both positively and negatively charged.

The source of the GFIS operates at low temperature, producing ions from the field ionization of adsorbed gas atoms, and is characterized by the highest brightness and hence the highest deliverable spatial resolution of all sources developed to date^{19,23,53}. This is a consequence

of the atomically sharp emitter, which consists of only three atoms at its tip, the so-called trimer, whereby each atom emits a beamlet and thus forms a virtual source size in the Angstrom range. The trimer must be formed by the user and has a typical lifetime between a few days and a few weeks. The source gases that are widely used for high-resolution imaging and high-resolution (metal-free) milling are He and Ne. Operation of the GFIS with H_2 ⁵⁴, N_2 ^{55,56}, Xe⁵⁷, and Kr⁵⁸ has also been demonstrated.

Another option offering non-metallic ions is the plasma ion source of the so-called plasma focused ion beam (PFIB) instrument. Plasma ion sources achieve high currents of up to 2 μA and have a long lifetime, but lower brightness than LMIS sources. The plasma can be generated by electron impacts, as in a duoplasmatron^{16,59}, by inductive coupling of alternating currents in a radiofrequency antenna (an inductively coupled plasma (ICP))⁶⁰, or by microwaves in an electron cyclotron resonance (ECR) ion source⁶¹.

A further class of ion source is the so-called cold atom ion source. There are two types: the magneto-optical trap ion source (MOTIS) and the low temperature ion source (LOTIS). These use magneto-optical trapping (in combination with laser-cooling in the case of the LOTIS) to generate a trapped cloud of atoms or an intense atomic beam with a (transverse) temperature in the microkelvin regime^{62–66}. The atoms in the trap or beam are then field- or photoionized to produce an isotopically pure, singly-charged ion beam of high brightness and low energy spread.^{27,28,67,68} MOTIS/LOTIS achieve good resolution at low energies, but are only suitable for a few selected ions and require a high degree of sophistication in their design and handling.

Less common source types are Paul traps⁶⁹, the electron beam ion trap (EBIT)⁷⁰, the nano-aperture ion source (NAIS)⁷¹, the multicusp plasma ion sources⁷², the solid electrolyte ion source (SEIS)⁷³ and the electrospray ionization source (ESI)⁷⁴. The NAIS uses an electron-impact gas ion source^{71,75} and can be installed on standard SEM instruments to deliver ions from all noble gases, including protons. A systematic overview of all the ion species that are currently available for FIB instruments is displayed in the form of the periodic table of elements in Figure 1. The most common types of ion sources that are used for FIBs and their key parameters are compared in Table I.

Crucial factors to be optimized for the routine use of new ion sources are source lifetime and stability. Lifetime issues are usually related to contamination and can often be handled by working in cleaner conditions. However, in other cases, lifetime and stability issues can be traced to the source itself. For example, the formation of stable beams from certain elements, such as aluminum and phosphorous extracted from a LMAIS, remains challenging. Source stability is also of particular importance for large volume sputtering applications, as well as for focused ion beam-induced deposition (FIBID) and resist-based FIB lithography. For maximum shape fidelity,

Table I. Most important FIB sources compared according to key parameters. Only common ion species are listed. All published or commercially available ion species can be found in Fig. 1. Superscript q marks different charge states (from 1 to 3) obtained from LMIS/ LMAIS; for plasma sources even higher charge states are obtained. Subscript n for LMIS/LMAIS indicates the possible emission of polyatomic clusters comprising up to 10 ions (or even more). Parameters for ILIS indicated by * are estimated values from reference⁹. For better comparison, the lateral spatial resolutions have been converted to FWHM values assuming a Gaussian beam profile resulting in an error-function-like edge profile.

Source	Common ion species	Reduced brightness ($\text{A m}^{-2} \text{sr}^{-1} \text{V}^{-1}$)	Min. energy spread (eV)	Max. current (nA)	Lateral resolution FWHM (nm)	Key applications
LMIS/ LMAIS	(Li, Si, Ga, Ge, In, Sn, Sb, Au, Pb, Bi, ...) _{1...n} ^{q+}	1×10^{610}	2-40 ^{10,11}	100	2-2.8 ^{12,13}	surface patterning and cross-sectioning, volume imaging, local doping and implantation, SIMS, mask edit, ion thruster
ILIS	EMI ⁺ , BMI ⁺ , BF ₄ ⁻ , I ⁻ , ..., cluster ions	$5 \times 10^{6*9}$	7-10 ^{14,15}	0.75* ⁹	50*-30 000 ⁹	ion thruster, reactive ion etching, SIMS
PFIB	(Xe, Ar, Kr, N, O ...) ^{q+}	1-10 $\times 10^{316}$	7-10 ¹⁶	2500 ¹⁷	20-100 ^{16,18}	high rate sputtering, volume imaging, implantation of gaseous elements
GFIS	(He, Ne) ⁺	1-4 $\times 10^{919-21}$	0.25-1 ^{19,22}	0.15 ²¹	0.5/4.0 ²³⁻²⁵	high resolution imaging and nanostructuring, mask repair, implantation of gaseous elements
LOTIS/ MOTIS	(Li, Cs, Cr, Rb) ⁺	1-240 $\times 10^{526}$	0.2-2 ^{27,28}	0.02 ²⁶	4.9 ²⁶	SIMS, implantation
NAIS	H ^{q+} , Ar ^{q+}	4 · 1 $\times 10^{529}$	0.9-2.3 ³⁰	0.2-20 ²⁹	≈2000 ²⁹	SEM as ion source, proton beam writing

these applications require FIBs that are stable in both the current and in the spatial domain. Examples of poor stability are the short term current fluctuations and long time current drift of the Ne-GFIS, and occasional side emission in LMIS and LMAIS.

B. Beam transport

The main components responsible for transporting the beam in a FIB column from the source to the sample are shown in Fig. 2; the labels on the left correspond to components found in more standard instruments and the labels on the right correspond to additional components found in more specialized instruments. To summarize: After extraction from the source, the ions are formed into a beam by the condenser lens (often after passing through an entrance aperture) and then guided towards the probe current selecting aperture (often via a quadrupole lens). The current selecting aperture defines the probe current by selecting a small portion of the beam and thereby also reducing its angular dispersion. To monitor the beam, a capacitor is used to deflect the beam into a Faraday cup. This allows the beam current to be measured and the beam to be blanked while

not in use to prevent unwanted sample exposure. The lower part of the column often houses a stigmator for final beam shaping, plus an octupole for beam scanning and a second electrostatic lens (objective) for beam focusing. In more specialized instruments, a Wien filter is used to select ions of a specific mass-to-charge ratio.

The two lenses that typically steer and focus the ion beam (the condenser and objective) are convergent electrostatic lenses with a cylindrical geometry. These lenses are composed of several electrodes (typically three, i.e. an Einzel lens), which are electrically biased to generate electric fields that change the trajectories of the transiting ions through the force $\vec{F} = q\vec{E}$ (see Fig. 3). Electrostatic lenses can be operated in retarding mode (the ion energy is reduced inside the lens) or in accelerating mode (the ion energy is increased inside the lens). Figure 3 shows an example of a lens operated in retarding mode. Given the curved shape of the field lines inside the lens, the electric forces imposed on the ions have a radial component, in addition to the deceleration and acceleration axial components of these forces. The radial force components result in the overall focusing effect of the lens⁷⁶. The focal length of the lens depends on the ion energy, the charge state of the ions, the voltage applied to the lens, and the lens geometry (no dependence

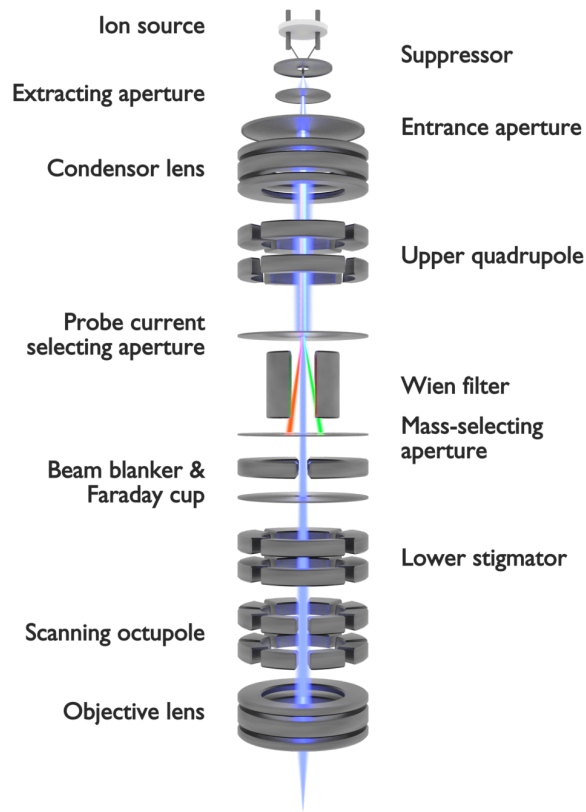


Figure 2. Principal components for beam transport found in a FIB column (not to scale). Components labeled on the left are found in standard Ga-FIB columns, whereas labels on the right indicate components usually only found in special-purpose columns.

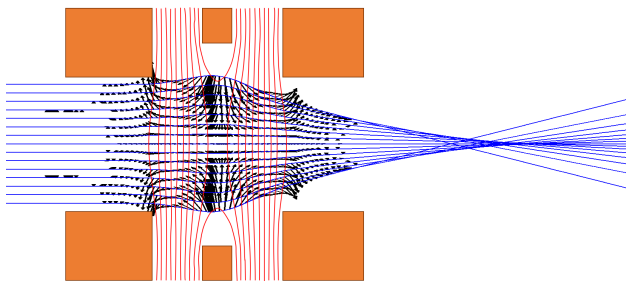


Figure 3. Example of an electrostatic (Einzel) lens, showing three cylindrical electrodes (in orange) where the central one is biased to focus the ions at a given position. Equipotential lines are drawn in red, ion trajectories in blue, and the black arrows indicate the direction and magnitude of the electrostatic force.

poor performance, this will inevitably be propagated to the sample. Consequently, adjusting the design of the beam transport elements on a state-of-the-art FIB column will typically only result in small improvements in the overall FIB performance^{77–79}.

The main gap between the desired performance of a

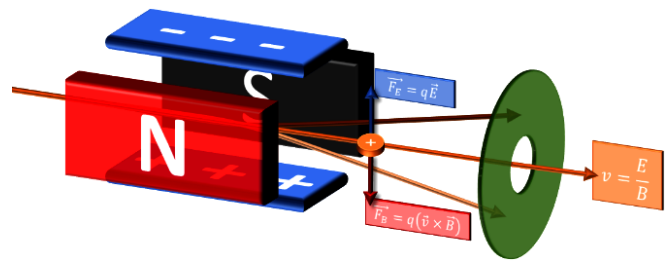


Figure 4. Principle of a Wien filter, with orthogonal electric and magnetic fields and an aperture to select the desired ion velocity.

FIB instrument and the actual performance is currently in the area of low energy beams (<2 keV). With the ongoing trend to reduce the dimensions and increase the complexity of (3D) device and sample architectures, the interactions between the ion beam and the sample become ever more critical. Thus, the penetration depth and straggling of the ions inside the material must be minimized. The key way to reduce these effects is to decrease the energy of the beam, however, the consequence is that the size of the beam spot is increased. This increase in beam spot size is due to chromatic aberrations from the energy spread of the ions in the beam; the relative energy spread and hence aberrations become more pronounced when the beam is retarded.

C. Analytical tools and detectors

Irradiating a sample with an ion beam to trigger and measure a response is a very common analytical technique, and FIB instruments that perform imaging, local irradiation, milling, etc., are typically equipped with various accessories to confer a range of analytical capabilities. For imaging purposes, the secondary electrons (SEs) emitted from the sample surface are routinely detected using an Everhardt-Thornley detector (ETD)⁸⁰. The ETD is scintillator-based, converting SE strikes to photons inside the sample chamber, that then travel via a light guide to a photomultiplier outside the chamber. As a complementary imaging channel, secondary ions (SIs) can be detected using a total ion counter (TIC) (typically in positive SI detection mode implemented as a Faraday cup or a channeltron). In addition to these imaging modes, various other analytical techniques are implemented on FIB platforms; a general overview is given in Table II.

Secondary ion mass spectrometry (SIMS) enables the mapping of elemental/chemical compositions in the form of 2D/3D images or depth profiles with a high sensitivity (down to the ppm level) in combination with a high dynamic range (i.e. a given element can be measured over a concentration range of several orders of magnitude). In principle, all elements, including their isotopes, can be measured. However, for a truly quantitative analy-

Table II. Overview of implemented ion beam based analytical methods using FIB.

Technique	Primary ion (from literature)	Detected Signal	Spatial resolution lateral	depth	References
Quadrupole mass spectrometer (QMS)-secondary ion mass spectrometry (SIMS)	He ⁺ , Ne ⁺ , Ga ⁺ , Cs ⁺ , Xe ⁺ , O ⁺	Secondary ions	100 nm	<20 nm	81–99
Magnetic sector SIMS	Bi ⁺ , Bi ⁿ⁺ , Au ⁺ , Au ⁿ⁺		<15 nm	<2 nm	
Time-of-flight (TOF)/orthogonal TOF-SIMS	O ⁻		<50 nm (<30 nm)	<10 nm	
Secondary neutral mass spectrometry (SNMS)	Ga ⁺	Post-ionized neutrals	20 nm		100–102
Scanning transmission ion microscopy (STIM)	He ⁺	Transmitted ions/neutrals, back-side secondary electrons	<5 nm		103–110
Backscattering spectroscopy	He ⁺	Backscattered ions/neutrals	≈50 nm		99,111–120
Backscattering yield	He ⁺	Backscattered ions/neutrals	5 nm		121,122
Ion-induced spectroscopy	SE He ⁺ , Ar ⁺	Secondary electrons	several nm		123–131
Ion-induced Auger electron spectroscopy (IIAES)	Si ⁺ , Ne ⁺ , Ar ⁺ , Au ⁺ , Kr ⁺ , Ga ⁺	Electrons	10 nm		132–137
Particle-induced emission (PIXE)	X-ray He ⁺ , Ne ⁺ , Ga ⁺	X-rays	100 nm		138,139
Ionoluminescence (IL)	He ⁺	Photons	20 nm		140–145

sis, reference samples are required since the ionization yields strongly depend on the local environment in the sample (known as the matrix effect). Several implementations of FIB-SIMS systems have been explored, with three main system types described in the literature for units installed on both FIB and FIB-SEM instruments: (1) Historically, quadrupole mass spectrometer (QMS) systems have been used on FIB platforms due to their simple design, low weight, and reduced costs^{146,147}. However, QMSs have the disadvantage of not allowing parallel detection (i. e. only one mass can be detected; the detection of several masses requiring sequential analyses and hence a duty cycle), and lower performance in terms of sensitivity. (2) More recently, various orthogonal and linear time-of-flight (TOF)-based mass spectrometers have also been introduced^{83,97}. The TOF systems offer the advantage of parallel detection, but since pulsing of the primary ion or secondary ion beam (or both) is required, a duty cycle results. (3) Magnetic sector SIMS systems (also a more recent introduction) can offer parallel detection if using so-called continuous focal plane detectors, and the highest sensitivity, enabling high-resolution imaging applications. Moreover, magnetic sector systems are operated in direct current (DC) mode (100% duty cycle). In terms of disadvantages, the latter typically have a

larger footprint and are heavier because of the integrated electromagnet.

By combining a gas injection system (GIS) with FIB-SIMS, further improvements in analytical output have been demonstrated. For example, in work combining FIB-TOF-SIMS with a GIS, ionization probability and hence SI signals were found to significantly increase (by 2–3 orders of magnitude), thereby improving the quality of 2D and 3D chemical maps¹⁴⁸. Furthermore, it was observed that co-injection of XeF₂ during the ion bombardment can reduce mass interference^{149,150} and invert the polarity of the negatively-charged SIs to positive¹⁵¹, thus allowing the collection of more complete chemical information. Enhancements in SI yields have also been obtained on magnetic sector SIMS instruments using Cs and O flooding to boost the yield of negative and positive secondary ions, respectively^{152,153}.

Related to SIMS, secondary neutral mass spectrometry (SNMS)^{154,155} can obtain similar information but has the advantage of matrix-independent ionization yields. However, non-resonant ionization yields are low and the method requires significant experimental effort and is therefore associated with high costs.

Scanning transmission ion microscopy (STIM) is performed using the ions of light elements. It can provide

mass-thickness contrast for any type of sample and crystal structure information due to channeling¹⁰⁹. It is a quasi-non-destructive imaging technique, and for biological specimens has been shown to deliver structural contrast comparable to (S)TEM¹⁵⁶. Similarly to TEM, STIM also demands thin samples (<100 nm). Furthermore, in combination with SIMS, STIM can be used to create high-resolution images to correlate with the SIMS-determined elemental/chemical maps¹⁵⁷.

Backscattering spectroscopy in a FIB instrument is similar to Rutherford backscattering spectrometry (RBS), but is performed at much lower energies. As a consequence, time-consuming simulations of the ion spectra are necessary in order to obtain quantitative results from the raw spectra. However, it has been shown that when coupled with a TOF setup, backscattering spectroscopy can deliver damage-free depth-resolved elemental compositions⁹⁹. Signal levels are good as the method also is sensitive to the large number of neutral SIs generated during the primary ion (PI) impact.

One can also simply analyze the yield of the backscattered primary particles, in which case larger solid angles and higher signals can be achieved. This is done using an annular micro channel plate (MCP) located below the objective lens of the microscope. While the backscatter yield approach is feasible regardless of FIB instrument type, it is most useful in a helium ion microscope (HIM). In this case, the backscatter yield of the primary He ions is high enough (in particular for heavier elements), that damage from the primary beam can be neglected⁹⁹. Backscatter yields depend strongly on the atomic number of the target¹¹¹, such that elemental contrast can be obtained from buried layers¹²¹. By the same token, heavier elements are distinguishable from biological cell tissue. To a certain extent, elemental analysis is also possible, but only with prior knowledge of the elements in question¹¹⁷. Since the SE yield depends on the crystal orientation and provides the corresponding simpler and stronger signal can be used to obtain information on bulk crystal structure¹¹⁹, and surface reconstructions in thin-film alloys¹⁵⁸. In addition, it is also useful for various biological applications^{159,160}. In particular the ability to infer crystallographic information from the SE yield has been extended to other ions and automated latter by other groups¹⁶¹.

Ion-induced SE spectroscopy (using He ions) draws on variations in SE energy to map chemical variations on a sample surface^{125,162–164}. The approach allows the user maximize imaging contrast, thus permitting short beam exposure times, which is beneficial for beam-sensitive samples. However, a quantitative application of the SE spectroscopy method is currently limited by the complicated nature of the data obtained and the lack of a definitive reference database.

Ion-induced Auger electron spectroscopy (IIAES) allows the chemical identification of surface layers, including bond structure, via the energy-resolved detection of Auger electrons emitted following an ion-induced inner-

shell electronic transition^{136,165}. For elements in the third row of the periodic table, IIAES has a superior signal-to-noise ratio compared to electron beam based Auger electron spectroscopy (AES).

Ion/particle-induced X-ray emission (PIXE) in a FIB instrument is essentially the equivalent of energy-dispersive X-ray spectroscopy (EDS) in the SEM, whereby characteristic X-rays (used for elemental mapping) are generated as a result of particle bombardment. However, in the FIB case, PIXE suffers from extremely low X-ray yields and hence has not proved practical thus far.

The final entry in Table II, ionoluminescence (IL), has been tested on various materials¹⁴⁰. However, the authors of these works concluded that the merits of this technique only really emerge in the case of in-situ characterization of beam induced defects¹⁴¹, and for the localization of rare earth atoms¹⁴³.

Specialized ion detection methods for single ion implantation (SII) also deserve mention, see Section IV B for more detail. These methods can be categorized into pre- and post-detection techniques. In the pre-detection category, one example is the use of an image charge detector (ICD) incorporated into the FIB column that registers the passage of a single ion (or ion bunch) and is coupled with fast blanking electronics^{166,167}. Post-detection can involve standard SE detection¹⁶⁸, or more complex sample integrated detection schemes such as ion beam-induced charge (IBIC) or source-drain current measurements^{169–172}.

D. Other FIB accessories

In addition to the above-described key components, a number of other accessories have been developed that extend the capabilities of FIB instruments even further. A summary of these is given below.

The most common addition to a FIB instrument is an electron column (SEM). Vice-versa, FIB columns are often added to SEMs. The electron column enables correlative imaging, in-situ monitoring of milling processes, and FIB-SEM volumetric reconstructions. The SEM addition also facilitates sample navigation, since by imaging with electrons rather than ions, beam-damage to the sample can be rendered negligible. Certain FIB-SEM implementations also allow automated metrology and analysis^{173,174}.

For high-resolution, large-area direct patterning applications, laser interferometer stages are a critical addition, since the positioning accuracy and stability of standard mechanical stages are not sufficient for these high-end applications. In conjunction with specialized sample holders, laser interferometer stages enable a sample positioning accuracy in the nanometer range over a lateral distance of several 100 mm¹⁷⁵.

A further (rather common) addition is a gas injection system (GIS), which enables focused ion beam-induced

deposition (FIBID), and in combination with an electron column, also focused electron beam-induced deposition (FEBID)¹⁷⁶.

FIB columns are also sometimes operated in conjunction with an electron flood gun, since by illuminating an insulating specimen under the FIB with low energy electrons, in-situ charge neutralization is achieved. This enables high resolution imaging (in the case of the HIM) of insulating samples without the need for conductive coatings¹⁷⁷ (see Section IV C 2), and FIB milling of insulating samples¹⁷⁸. A low resolution alternative is to use an optical camera for top-down macroscopic sample navigation. The latter has been extended to enable in-situ fluorescence and Raman microscopy¹⁷⁹.

Various types of micro/nanomanipulator have been developed for intuitive control and mechanical manipulation of micro- to nanoscale objects, including in-situ lift-out of lamella specimens for TEM¹⁸⁰, and to allow local electrical connection for various in-situ experiments as demonstrated for SEM^{181–183}.

Through the addition of a femtosecond laser ablation system, large amounts of material can be removed very efficiently above the final target area for subsequent finer milling with the FIB. This enables higher throughput for applications such as advanced package failure analysis and process optimization in the semiconductor industry¹⁸⁴.

Numerous add-ons for a wide range of in-situ characterization experiments have also been developed, both by manufacturers and by researchers. These solutions include electrical probing stations, systems using Peltier elements for heating or cooling samples (not to be confused with more complex cryo-FIB add-ons), in-situ mechanical testing, plasma-based sample cleaners, and automatic laser-based height sensing. Other often sought-after add-ons are inert-gas transfer boxes to allow oxygen-free loading (and unloading) of air sensitive samples¹⁸⁵. Another possible add-on is to incorporate an atomic force microscope (AFM) into the FIB-SEM instrument¹⁸⁶, which can also be implemented in combination with FIB-SIMS to allow an assessment of surface roughness and thus improve the accuracy of the 3D reconstructions⁹⁶. A recent review article summarizing state-of-the-art solutions for in-situ characterization and micro/nanomanipulation has been published by Shi *et al.*¹⁸².

E. FIB of radioactive samples

The use of the FIB to investigate radioactive samples presents a number of critical issues (legal and technical) that need to be addressed. The reason the FIB is such a useful instrument in the analysis of such samples is that it allows the preparation of small-scale specimens (by FIB milling) that by default have significantly reduced radioactivity levels. These small-scale samples can then be handled much more easily for a wide range of characterization experiments, both in-situ and ex-situ, includ-

ing specimens for small-scale mechanical testing, TEM lamellae, and needle-shaped specimens for APT.

The exact protocols to follow may vary widely depending on the individual facility and the local safety regulations. For example, in some facilities a small-scale specimen prepared from a radioactive sample is still considered radioactive even if activities are below any measurable level. In contrast, in other facilities specimens are only considered radioactive if measured activities are above an administrative threshold. Of course, the type of material, form of radioactivity, and isotopes involved, are all key factors to take into account.

FIB instruments that are used for radioactive samples can be categorized as follows:

1. Instruments classed for “low–medium” radioactivity samples, and that also allow experiments with non-radioactive samples
2. “Hot cell” instruments that are highly shielded and may even allow spent fuel samples.

Irrespective of the particular regulations, the main concerns when working with radioactive samples in FIB instruments are:

- Dose limits for the operator when loading and unloading the sample
- Contamination of the instrument to the extent that system maintenance becomes difficult
- Cross contamination between samples in the case of work with radioactive and non-radioactive samples
- Lifetime of detectors and other add-ons installed on the instrument (EDS, EBSD, etc.).

Regarding contamination of the instrument itself, it has been determined that most of the milled material that does not redeposit on the sample is deposited on the pole piece and surrounding areas. In the case of materials that generate dust, the sample stage can also easily become contaminated. One approach to address contamination of the pole piece is to use a dedicated pole piece insert for experiments with radioactive samples. The **ESEM!** (**ESEM!**) can also be helpful here, as it provides another aperture for low-pressure mode and the water vapor that is typically injected helps to volatilize the radioactive sputtered material. Frequent cleaning of areas prone to contamination is another effective strategy to increase the lifetime of the instrument. The inside of the chamber can also be covered to protect from contamination. Some approaches use sample shields to reduce the spread of the sputtered material by capturing most of it inside the shield. However, sooner or later, the entire FIB chamber will need to be treated as radioactively contaminated equipment and be handled appropriately.

F. Software and correlative approaches

The software infrastructure of a FIB instrument needs to control various elementary subsystems, e.g. the vacuum system and sample stage, as well as the ion source and column functions (beam extraction param-

eters, aperture selection, column alignments, etc.). This is implemented by the manufacturer using a graphical user interface that allows control of all FIB system components and integrated add-ons. Customized FIB setups employing e.g. specialized, non-commercial FIB columns or non-standard add-ons, usually use separate control software developed for these specific use cases, which are often difficult to set up and maintain due to closed hardware interfaces and patent issues. Regardless of the particular configuration, software control for the following applications is required:

- Imaging (including 3D volume imaging) and elemental analysis using various detectors, see Sections II C, IV C, and IV D
- Milling, ion irradiation and implantation, see Sections IV A and IV B
- Deposition and resist-based lithography, see Sections IV E and IV F

All of the above demand a scan generator that controls the path of the ion beam on the sample with high precision and repeatability.

Beam scanning is realized using a digital-to-analog converter (DAC) patterning board that determines the number of addressable pixels in each direction (e.g. 65,000 for 16 bits) and sets the voltages of the beam deflection system accordingly. The beam path is then a sequence of pixels with a certain dwell time and spacing depending on the field of view. Simple line-by-line scanning routines are used for imaging and elemental analysis, and the respective detector output is synchronized to assign a signal (e.g. a gray value or a mass spectrum) to each pixel position.

For subtractive processing, deposition, resist lithography, etc., special beam paths are needed. Here, manufacturers typically offer software tools that enable the creation of geometric shapes that are rasterized according to a chosen set of parameters. Grayscale patterning offers an even easier way to realize complex shapes and the milling of 3D profiles, by loading an image in which the grayscale values of the individual pixels correspond to the local relative ion doses to be applied. The latter is an appealing plug-and-play solution for markers, text, and other non-quantitative designs, yet it is difficult to optimize systematically and is therefore not commonly used for actual structures. In the case of more advanced patterning needs, design files can be imported from lithographic software, assigned with parameters, and rasterized, thus enabling complex and large-scale structuring tasks¹⁸⁷. Standalone lithography systems from third-party manufacturers can also be directly integrated as accessories via the use of an external scan control unit for the FIB column. Such systems typically also have access to stage control, allowing multi-step processing with marker-based registration or stitching, the latter requiring a laser interferometer stage for the highest level of positioning accuracy.

The capabilities of these various patterning systems are sufficient for many applications, but reach their limits

when complex geometric shapes and the highest spatial resolution are required, and/or when the position of the beam must be known with certainty at all times. The reason for this is that the user has limited control over the actual raster process and possible auxiliary routines hidden in the proprietary software (e.g. for stabilization of the beam position). The most robust solution is to address pixels directly on the patterning board using a point cloud, which can be encoded in so-called stream files or deflection lists. This allows arbitrarily rasterized beam paths to be executed by the integrated patterning software. Various groups have developed codes to generate such beam paths and the corresponding point clouds for specific tasks^{188,189}. For arbitrary geometric shapes, an open-source Python-based solution is available, which allows the generation of patterns and geometry-adapted beam paths that can be both variably rasterized and optimized¹⁹⁰. For the creation of 3D profiles, approaches based on computer-aided design (CAD) have also been developed^{191–195}. These solutions implement material removal via thin slices plane-parallel to the sample surface, which allows systematic optimization since the amount of material removed per slice remains constant (a significant advantage over the grayscale patterning mentioned above). Modeling of the milling process can also be used to take into account angle-dependent sputtering¹⁹² and redeposition¹⁹⁶, or more generally, non-isotropic surface erosion¹⁹³; for more detail see Sections III A and III D.

In addition to beam control, another software need focuses on enhancing the analytical capabilities of the instrument. Commercial FIBs are often coupled to a SEM column and/or equipped with analytical instrumentation such as SIMS. Most FIB instruments are thus equipped with electron detectors for the collection of SEs, allowing for SEM-like imaging albeit the physics of signal formation is different. Additional detectors offer a variety of other imaging possibilities via the detection of transmitted ions¹⁰⁹, backscattered ions⁹⁹, secondary ions¹⁵⁶, photons^{197,198}, Auger electrons^{136,137}, etc.; see Table II. These FIB instruments thus need to be equipped with the necessary interfaces to allow for either direct control of the beam position, or synchronization between the detector signal and internal scan generation. Such interfaces are standard for commercial FIB platforms that offer these analytical modalities.

For common repetitive FIB tasks, instrument users can employ various forms of software automation. Examples of automated tasks include column alignments and focusing, trench milling (including for TEM lamella preparation), large-scale sequential lithography projects, serial sectioning and complex analytical tasks such as 3D tomography using multiple detectors. In the past, the technical challenges of many of these processes were handled largely without automation by expert FIB operators following intensive training. However, over the last decade this situation has been significantly relieved by the introduction of various semi and fully automated processes by the major FIB manufacturers. It must be stressed that

there is still room for improvement and further automation is highly desired. Here, automation routines that are more customizable or user-programmable with well documented application programming interfaces (APIs) or scripting environments within the FIB software stack would be of great benefit. This would allow standard automation routines to be set up and executed by lab technicians after just a short training period.

Finally, the correlative microscopy and spectroscopy functionalities of modern FIB instruments (both for 2D¹⁵⁷ and 3D^{199–201} analysis; see Sections IV C and IV D) require a combination of the aforementioned software controls as well as advanced software tools for correlation, analysis, and visualization^{202,203}. In the simplest case, a correlative data set is acquired using multiple detectors and a single scan of a surface (or in the case of 3D analysis, a stack thereof) such that multichannel data is available for every beam location (“pixel”). If this is not possible, data sets from separate experiments have to be combined post acquisition under the condition that some form of alignment is possible, e.g., via fiducial markers. For the correlation of 2D images, open-source software is available, e.g. in the form of the Fiji/ImageJ image processing package²⁰⁴ and its plug-ins such as Correlia^{205,206}. Additional resources can be found on the webpages of the COMULIS project²⁰⁷ and the BioImage Informatics Index²⁰⁸. For the most complex cases (e.g. the correlation of X-ray and FIB tomography data), dedicated analytical software²⁰⁹ and novel approaches for data storage and management are required; see Section V C 3.

III. SIMULATION APPROACHES FOR FIB PROCESSING

Simulations carried out at various levels of sophistication have the potential to provide insights into the interaction of the FIB with the target. These calculations can help rationalize the experimental results, optimize the beam parameters (ion energy, incidence angle, etc.), and guide the experimental work. Various theoretical methods have been developed to describe the interaction of the impinging ions with the target and to assess the amount and type of sample modification produced by a given ion irradiation.^{210–212} Among them, atomistic computer simulations, which describe the system as a collection of interacting atoms, have provided lots of insight into the behavior of the materials under the impacts of energetic ions. These approaches can give precise information on ion ranges and energy losses and the types of the irradiation-induced defects formed under the impacts of energetic ions. The defect stability and long-term evolution under ambient conditions or at elevated temperatures during annealing can also be simulated. Continuum medium models, on the other hand, can be computationally more efficient and eliminate the statistical noise inherent in many atomistic methods. They describe the system under investigation by continuum quantities such as concentrations or surface contours, which conceptually

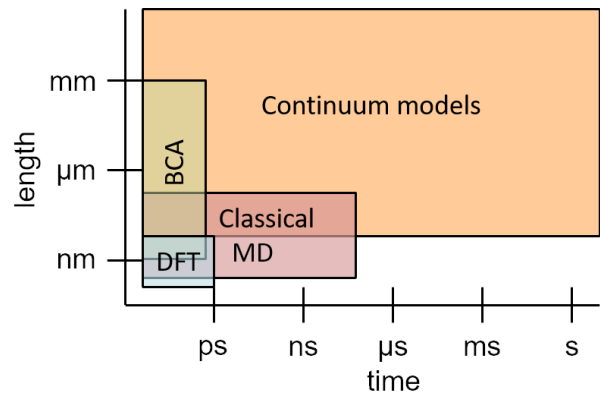


Figure 5. Time and space scales accessible by simulation methods. The smallest time scales are accessible only by certain types of continuum models. kMC can cover the whole length-time space displayed depending on details of the system studied and the sub-method used, and is therefore not included in the graph. Modified after Ref. 213.

require averaging over finite volumes. In practice, these quantities are often discretized on a mesh of elements with size larger than atomic dimensions. In addition, these models require parameters that are to be provided by experiments or more microscopic approaches.

The choice of the simulation method is dictated not only by the main goal of the simulation (e.g., to assess the electronic stopping power or to calculate ion ranges, amount and type of damage, atomic mixing, surface evolution, . . .), but also by the system size, the required level of sophistication, and the computational costs. A typical approach is to find a suitable compromise between the necessary computational resources and accuracy. Multi-scale simulations are frequently used, where more accurate but computationally demanding approaches are employed as tests or to provide parameters for less accurate techniques.

An overview of the time and length scales accessible by the various methods is given in Fig. 5. The binary collision approximation (BCA) method, to be discussed in Section III A, describes the ballistic phase of the slowing down of the ions and of the development of collision cascades. Since the ballistic phase dies out in less than a ps, application of the BCA makes sense only on a sub-ps time scale. Ab-initio methods, in practice mostly density functional theory (DFT), are the most accurate technique, but are restricted to the ps and nm ranges because of their computational expense. Classical molecular dynamics (MD) may be used for systems roughly up to 100 ns and 100 nm. These methods are described in Section III B. Longer time scales are accessible by the kMC method (Section III C), which describes the evolution of a system given the probabilities of events. The actual limits of kMC are determined by the event frequencies and the density of objects in the system to be studied. Finally, continuum models (Section III D) usually study systems beyond the single-digit nm range as they do not

resolve materials on the atomic level.

In the following subsections, a concise review of the available computational techniques with examples of their use is presented. It is hoped that this overview conveys a good idea of the opportunities simulation provides in the field of FIB processing.

A. Simulation techniques based on the binary collision approximation

The BCA is the most widely used method to assess the scattering and slowing of energetic ions in matter and the effects of the associated collision cascades, i.e., sputtering, atomic mixing, and the formation of point defect damage. The motion of each energetic atom is described as a sequence of asymptotic trajectories between binary collisions with target atoms being at rest before the collision. Detailed information on the associated algorithms is provided in the book by Eckstein²¹⁴.

1. Principle and limitations

The binary collisions are normally treated as elastic with repulsive-only screened Coulomb interaction potentials, as, e.g., in the “universal”²¹⁵ or “Kr-C”²¹⁶ parametrization. Energy transfer to the target electrons is included either non-locally along the free paths between the collisions, (e.g., using a universal analytical description²¹⁷ or specific semi-empirical data²¹⁸), or locally dependent on the collisional impact parameter²¹⁹, or as a combination of both.

Simulations based on the BCA are often denoted as Monte Carlo (MC) simulations due to the random choice of collisional parameters such as the impact parameter and the azimuthal position of the target atoms relative to the trajectory of the moving atom. In random and amorphous media, this applies to all binary collisions during the simulation. In contrast, in crystalline media only the initial position of the incident projectile relative to the lattice atoms is treated randomly, while the subsequent slowing down including the generation and termination of a collision cascade is largely deterministic due to the positions of the lattice atoms being fixed apart from thermal vibrations.

A prominent advantage of BCA simulations is their low computational cost and very fast performance, which allows modeling even large systems up to the macroscale, and treating incident ion energies up to the MeV regime. However, in contrast to MD simulations (see Sect. III B), the BCA model fails if a significant fraction of the collisions occurs between moving atoms. Such so-called “collisional spikes” or “elastic thermal spikes”²²⁰ form in dense cascades generated under heavy-ion bombardment in the energy regime around the maximum of the nuclear stopping force²²¹ (typically around 100 keV). However, any collision cascade also dissipates into a collisional spike be-

fore its final thermalization, which sets a low-energy limit to the validity of the BCA. Depending on the material, estimates²¹⁴ and comparisons with molecular dynamics simulations^{222,223} indicate a failure at energies below several tens of eV. Experience, however, demonstrates that sputtering, which is dominated by cascade atom energies slightly above the surface binding energies of 2 eV to 8 eV²²¹, is rather well described^{224,225}. This suggests a practical lower energy limit of validity. Undoubtedly, BCA breaks down below the bulk binding energy of typically a few eV, where the purely repulsive interaction potential is no longer appropriate and many-body interaction has to be taken into account. This excludes, e.g., derivation of local atomic configurations after thermalization.

It must also be noted that BCA simulations require the predefinition of a number of options and parameters, such as the choice of the interaction potential, the addition of ‘soft’ collisions with more distant target atoms, the type of electronic interaction, and the surface binding and atomic relocation threshold energies, which are often difficult to identify and unavailable in the literature, particularly for compounds. (Note that except for the electronic interaction, these predefinitions are unnecessary in MD simulations as, ideally, a proper choice of the interaction potential covers all bulk and surface interactions down to thermal energies.) Whereas ion ranges derived from BCA simulations are mostly reliable within 5% to 10%, sputtering and defect results are significantly influenced by these settings. As a result of parameter variations within reasonable limits, calculated sputtering yields may easily change by more than 50%²²⁶. For the different BCA codes, parameters are often not chosen from sound theoretical or experimental information, but justified from experience in comparing the simulation results to experimental data.

Originally, BCA codes were designed for “static” simulations during which the system is assumed not to be altered by the irradiation. This allows the prediction of range and damage distributions as well as sputtering yields with high statistical precision when a sufficiently large number of incident projectiles is employed. In the simulation of ion implantation into single-crystalline targets, “dynamic” consideration of damage buildup is required if the fluence exceeds a certain threshold,^{227,228} as crystal damage reduces or suppresses channeling. This is done by choosing collision partners randomly instead of from the crystal lattice with a probability proportional to the damage. More often, the term “dynamic BCA simulation” refers to the modification of the chemical composition and geometry of the target, which occurs experimentally at a sufficiently large number of incident ions. Specific BCA codes track implanted ions as well as relocated and sputtered recoil atoms in order to continuously update the local composition in multicomponent systems and the surface position or the surface contour in 1D or 2D/3D systems, respectively. Simultaneously, the composition-dependent local atomic density must be up-

dated by volume relaxation and/or material transport².

2. Specific BCA codes

Among the large variety of BCA based simulation codes which have been described in the literature, we will address in the following only a few selected ones, in particular those which are presently in broader use and/or offer new features with respect to nanosystems, specifically FIB applications. For a rough classification, see Table III; access information for most of the codes can be found in Ref. 256.

TRIM^{229,230} has been the most widely used BCA code over several decades. It offers a very convenient graphical user interface²¹⁸ for fast generation of range and damage statistics, and rough estimates of sputtering yields in amorphous semi-infinite or thin film systems with a flat surface. The restriction to amorphous media is often not a severe limitation as many materials become highly damaged or even amorphized under irradiation and, depending on conditions, most ion or recoil atom trajectories are of random nature, even in crystalline materials. TRIM partly fails in details, such as for sputtered atom angular/energy distributions²⁵⁷.

Sometimes the crystal structure of the irradiated material matters. Typical cases include low-fluence or single-ion implantation aligned with a low-index crystallographic direction²⁵⁸ and the sputtering of elemental metals²²⁵. Codes that consider the crystal structure are Crystal-TRIM^{227,235}, which is restricted to certain materials, and IMSIL^{228,236-238}, which allows more general crystal systems and sputtering simulations.

Based on the early TRIM sputtering version TRIM.SP²²⁶, 1D dynamic relaxation has been implemented in TRIDYN^{231,232} and SDTrimSP²³³. In connection with the recent broad interest in nanostructures, BCA codes have been extended to treat 2D and 3D systems using pixel and voxel grids, respectively. For static operation only, the surface may be defined analytically for simple bodies such as in TRI3DST²⁴² and IM3D²⁴⁴, or triangularized as in a second option of IM3D. With a pure voxel approach, the stepped surface contour resulting from pixel or voxel grids may cause artifacts by, e.g., capturing atoms at glancing incidence which would be reflected in reality. This may be overcome by a local adjustment of the near-surface nodes²³⁸ (IMSIL), or by local planarization of the surface²⁴⁸ (TRI3DYN). In IMSIL for 2D dynamic simulation²³⁷, pixels which are affected by collisional transport become distorted based on an algorithm which optimizes their volumes, and are subsequently projected onto the original pixel

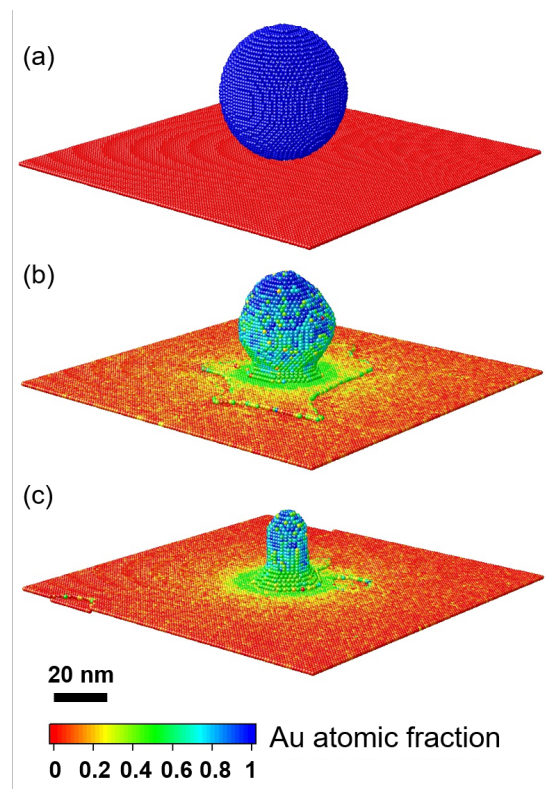


Figure 6. Sputter shaping of a Au nanosphere of 50 nm diameter on Si, (a) initially and (b) after irradiation with 30 keV Ga ions at normal incidence and fluences of $4 \times 10^{15} \text{ cm}^{-2}$ and (c) $1 \times 10^{16} \text{ cm}^{-2}$. The TRI3DYN simulation (with periodic lateral boundary conditions) demonstrates the size reduction and shaping by sputtering, the substrate surface erosion, and the contamination of the original sphere with sputtered substrate material and vice versa. The incorporation of Ga is small and not shown here. For more information, see Ref. 247

grid. In contrast, SDTrimSP-2D²³⁹ relaxes the pixel volumes along one dimension only towards a specified surface. 3D dynamic simulations have been demonstrated using TRI3DYN²⁴⁶⁻²⁴⁸ and EnvizION²⁴⁹⁻²⁵⁵. For overall volume and surface relaxation, TRI3DYN makes use of material exchange with nearby voxels or the surface, whereas the relaxation is limited to near-surface regimes in EnvizION. TRI3DYN even works for macroscopic systems, whereas EnvizION is limited to the nanoscale as each voxel contains only one atom. A characteristic result of a TRI3DYN simulation is presented in Fig. 6, demonstrating surface erosion and contamination during irradiation of a Au nanosphere on a Si surface.

3. BCA-based simulations of FIB processing

1D static BCA simulations have often been employed in understanding experimental findings in connection with the use of FIBs, such as in recent studies of FIBID²⁵⁹⁻²⁶². They have also been used to generate,

² Again, this dynamic modification is straightforward in MD simulations, but in systems exceeding the nanoscale and at larger ion energies it is often impeded by excessive computational cost.

Table III. Classification of selected BCA simulation codes. Note that the individual codes contain specific algorithms, use different parameters, and/or are designed for specific application areas which are not detailed here.

Code	Geometry	Atomic structure	Surface	Dynamic relaxation
TRIM ^{218,229,230}	1D	amorphous	planar	—
TRIDYN ^{231,232}	1D	amorphous	planar	1D
SDTrimSP ²³³	1D	amorphous	planar	1D
IMINTDYN ²³⁴	1D	amorphous	planar	1D
Crystal-TRIM ^{227,235}	1D	crystalline	planar	—
IMSIL ^{228,236–238}	1D/2D	amorph./cryst.	polygons/pixeled (adjusted)	–/1D/2D
SDTrimSP-2D ²³⁹	2D	amorphous	pixeled	2D
CORTEO ^{240,241}	3D	amorphous	voxeled	—
TRI3DST ²⁴²	3D	amorphous	analytical	—
IRADINA ²⁴³	3D	amorphous	voxeled	—
IM3D ²⁴⁴	3D	amorphous	analytical/triangularized	—
SDTrimSP-3D ²⁴⁵	3D	amorphous	voxeled	2D
TRI3DYN ^{246–248}	3D	amorphous	voxeled (planarized)	3D
EnvizION ^{249–255}	3D	amorphous	voxeled	3D, near surface

e.g., angle-dependent sputtering yields and angle-energy distributions of sputtered atoms to describe erosion and re-deposition, respectively, in 2D and 3D “level set”²⁶³ or “segment based”^{264–266} simulation models of the surface contour development during FIB induced erosion, see Section III D.

A direct 2D dynamic BCA simulation of FIB induced erosion is described in Ref. 237, where the milling of trenches is exemplified. The results shown in Fig. 7 demonstrate the slowing of the milling process by atoms sputtered from the bottom and redeposited to the sidewalls. In addition, a high concentration of implanted atoms at the bottom of the trench emerges, which pushes material upwards along the trench sidewalls via volume relaxation. The simulation of the milling of a slit in a membrane is described in Ref. 238.

With a particular focus on FIB processing, Rack and coworkers have published a series of 3D dynamic results obtained with EnvizION^{249–255}. In addition to the collisional BCA simulation and relaxation algorithms, simplified models have been implemented for reactive-gas assisted erosion and deposition, including secondary-electron mechanisms¹³⁰. Selected results have recently been reviewed in Ref. 267. For an introduction to gas-assisted processes see also Section III D 2.

Dynamic BCA simulations may also be employed to characterize specific FIB-based nanoanalytical methods. An example is a 1D TRIDYN simulation of damage buildup during FIB cutting of nanomembranes for TEM analysis²⁶⁸. Another example is a 3D TRI3DYN simulation of STIM in a HIM device (Fig. 8). Simulations such as shown in Fig. 8(a) help to identify the detector geometry for optimum image contrast and resolution. Fig. 8(b) indicates that there is only a minor degradation of the sample by surface sputtering and recoil atom transport between the core and the shell and between the sphere and the substrate.

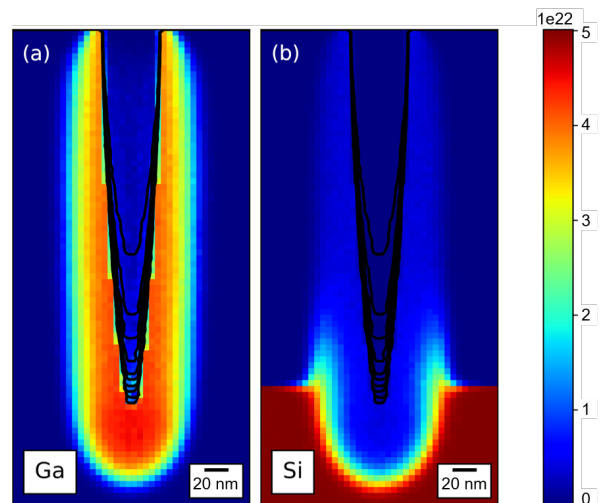


Figure 7. Bombardment of a Si target with a sharp 50 nm wide, 50 keV Ga beam to a fluence of $5 \times 10^{18} \text{ cm}^{-2}$: Final target composition ((a): Ga atoms, (b): Si atoms that originate from a depth larger than 300 nm in the virgin sample) and surface contours after fluence increments of $5 \times 10^{17} \text{ cm}^{-2}$. The scan area of the beam is in the center of the top boundary. The simulations have been performed with IMSIL (see Ref. 237).

B. Molecular dynamics and molecular statics

Although BCA methods are able to provide insights into processes developing during the ballistic (sub-ps) phase of ion irradiation, they cannot predict details of the permanent modification of the target’s atomic structure, such as defect clusters or dislocations including their strain fields. Particularly with heavy ions, heat spikes may develop even in keV energy cascades, and the local melting of the target affects the amount of damage for-

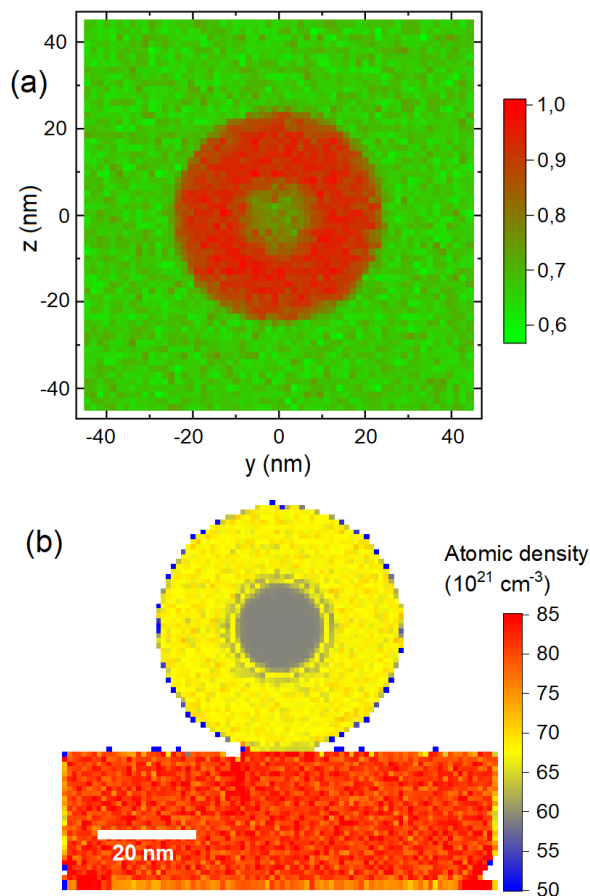


Figure 8. TRI3DYN simulation of STIM in a HIM. (a) Ion transmission relative intensity image from a Au (20 nm diam.) / SiO₂ (50 nm diam.) core/shell nanosphere on a Si₃N₄ membrane of 20 nm thickness. A 20 keV He⁺ beam with a Gaussian beam profile of 0.5 nm FWHM is scanned across an area of 90 nm × 90 nm up to a fluence of $2 \times 10^{16} \text{ cm}^{-2}$, with the transmitted ions being registered in an annular dark-field detector of 0.6 cm and 5 cm inner and outer radius, respectively, mounted 2.5 cm behind the sample. Special evaluation software correlates the detection of the transmitted ions with the actual y - z scan position of the beam. (b) Cross-sectional image of the total atomic density after the irradiation, averaged over a central slice of 2 nm thickness.

mation and atomic mixing²⁶⁹. The accuracy of the BCA diminishes^{222,223} at energies roughly below 100 eV and it completely fails in the low single-digit eV energy range. Hence, MD is often the method of choice for the simulation of phenomena associated with atomic motion at eV and sub-eV kinetic energies.

1. Principles and simulation codes

Most approaches in practical use are based on the Born-Oppenheimer approximation, which assumes that the electronic subsystem relaxes instantaneously to its ground state at any time as the atomic nuclei change their

positions. Consequently, the effect of the electrons can be embodied in a potential energy function that depends only on the nuclear positions²⁷⁰. Analysis of this energy function allows to determine many material properties as well as the time evolution of the system, e.g., in an irradiation experiment. This is even true when deposition of energy into electronic degrees of freedom dominates such as for 30 keV He ions impinging gold clusters²⁷¹, where defect production is still governed by ballistic energy transfer as excitations are quickly delocalized.

In the MD method, Newton’s equations of motion are solved for all atoms in the system, using forces calculated from the potential energy function^{270,272,273}. This is done iteratively with time steps on the order of 1 fs, with the time step being dependent on the ion/atom velocities and their masses. At the end of the simulation, when the energy is equilibrated everywhere in the system, the final structure can be analyzed. Due to the short time step required, total simulation times are limited to the ns or at most μs range for classical MD and ps for ab-initio MD. Longer-time effects are sometimes mimicked by increasing the temperature in the system, which then allows to observe annealing (recombination) of defects and the relaxation of strain²⁷⁴. Detailed descriptions of the principles of the MD methods can also be found in Refs. 212,275.

Molecular statics (MS) methods are concerned with finding minima and saddle points of the potential energy function. The former identify (meta-)stable atomic configurations, while the latter allow the determination of energy barriers for diffusion and chemical reactions. Finding global minima, corresponding to stable as opposed to metastable configurations, can be tricky. Various methods have been developed, see Ref. 270 for details.

Simulation codes can be classified into classical and ab-initio codes. In the first group, the potential energy and forces are calculated by evaluating mathematical expressions with empirical parameters, while in the second group, they are determined by solving approximations to the Schrödinger equation. The most widely used classical MD code is LAMMPS^{276,277}. Another general purpose MD code is DL_POLY²⁷⁸. Codes specifically designed for the simulation of radiation effects include PARCAS²⁷⁹, DYMOCA²⁸⁰, and MOLDY-CASC²⁸¹. GROMACS²⁸² and NAMD²⁸³ are mainly targeted at biomolecular systems. Popular ab-initio codes capable of doing MD simulations are VASP²⁸⁴ and QUANTUM ESPRESSO²⁸⁵.

2. Models for the potential energy function

Among the ab-initio methods, DFT²⁸⁶ with local and semilocal exchange-correlation (XC) functionals provides a good compromise between accuracy and computational expense for the calculation of the potential energy function. While some phenomena such as van der Waals in-

teractions, magnetism (especially when spin-orbit coupling is taken into account), or accurate evaluation of the gap in semiconductors require going beyond “vanilla” DFT by either using more sophisticated XC functionals²⁸⁷ or post-DFT methods (like GW/RPA²⁸⁸), DFT simulations normally provide reliable results with respect to the atomic coordinates and energetics on the scale relevant to the modeling of irradiation effects. DFT is capable of predicting charge states of defects and static charge transfer²⁸⁹, while time-dependent density functional theory (TDDFT) can describe charge transfer dynamics in ion collisions. The advantage of ab-initio simulations is that they do not use any material-dependent parameters that the user must provide. Their disadvantage is their high computational cost, which scales as $n^{2\cdots 3}$, where n denotes the number of valence electrons or atoms in the simulation. This imposes a practical limit to the system size that can be handled by DFT, which currently is on the order of 1000 atoms on supercomputers.

If larger systems need to be handled, empirical interatomic potentials (sometimes also called *force fields*) must be used to describe the potential energy function. The computational expense of these simulations is nearly linear in the number of atoms. On the downside, the mathematical expressions describing the interatomic potentials are only approximations to the true potential energy function, and the parameters in these models must be fitted for each combination of chemical elements as to reproduce physical properties of the material (e.g., lattice parameters, elastic properties, bond energies, energetics of defects, stability of sputtered fragments, etc.). Caution must be exercised when using a parameter set outside the range of atomic arrangements used to fit it. Moreover, the availability of force field parameters can be a limiting factor when looking for new applications, since the development of new parameter sets is a tedious task²⁹⁰. To overcome this bottleneck, various methods have been developed in recent years^{291–298}.

Collections of 1000+ interatomic potentials together with their parameters for individual systems are available at the NIST Interatomic Potentials Repository³¹¹ and the Knowledgebase of Interatomic Models (OpenKIM)³¹². Educated choice of an appropriate interatomic potential is essential for the success of a simulation. In Table IV, the most popular options are listed together with the types of atomic interactions they may describe, and their computational expense. All but the CHARMM force field, which is mainly used to describe biochemical molecules such as proteins, lipids and nucleic acids, allow for bond breaking, a prerequisite for the simulation of almost all radiation effects. For an introductory text on interatomic potentials see Ref. 270.

Overall fitting of a single functional form with a limited number of parameters to reproduce a vast range of material properties has frequently proven to be an unmanageable task. To overcome this limitation, machine learning (ML) potentials have been developed in the recent past^{313,314}. Common to all flavors of ML poten-

Table IV. Some popular interatomic potentials with the type of interaction they are able to describe and execution times per atom relative to the Lennard-Jones potential. Execution times are from Refs. 299 and 300 using LAMMPS. Mean values are given where both references list values. Execution times for ML potentials vary widely, depending on which formalism they are implemented in (see main text), but still scale linearly with the number of atoms n . DFT times are usually orders of magnitude larger than those for empirical interatomic potentials. Ratios strongly depend on the system size as DFT times scale as $n^{2\cdots 3}$, and hence it is not reasonable to give a scaling factor for DFT.

Interatomic potential	Type of interaction	Execution time
Lennard-Jones ³⁰¹	van der Waals	1
EAM ³⁰²	metallic	1.8
Stillinger-Weber ³⁰³	covalent	3.4
Tersoff ³⁰⁴	covalent	4.4
Coulomb-Buckingham ³⁰⁵	ionic	4.7
CHARMM ³⁰⁶	biomolecules	14.1
MEAM ³⁰⁷	metallic/covalent	16.5
COMB ³⁰⁸	chem. reactions	188
ReaxFF ³⁰⁹	chem. reactions	197
Kieffer ³¹⁰	chem. reactions	—
machine-learning	all	$\approx 10\text{--}10000$
DFT	all	\gg

tials is their description of the potential energy function by multi-parameter functions of the local environment around each atom. To determine the parameters, a large data set of potential energies and corresponding interatomic forces for a specific set of chemical elements in different configurations is generated by DFT calculations. Hence, the flexibility of these potentials is much greater than that obtained with empirical interatomic potentials, and if carefully developed, they are able to provide results with accuracy comparable to DFT. There have also been attempts to train ML potentials on-the-fly to handle situations that have not originally been anticipated such as large surface reconstruction or rare chemical events^{315,316}.

As an example, Fig. 9(a) demonstrates the ability of the Gaussian approximation potential (GAP)³¹⁷ (lines) to reproduce the DFT results (symbols) for the cohesive energy of pure W as a function of atomic volume in different phases³¹⁸. Similar agreement between predictions of the tabGAP potential (a more efficient version of GAP³¹⁹) and the DFT calculations of mixing energies and bulk moduli is shown in Fig. 9(b) for multiple combinations of binary, ternary and quaternary alloys.

The interatomic potentials discussed so far describe the potential energy function near equilibrium or a few eV above equilibrium. During irradiation simulations, much higher potential energies occur in close collisions. In this regime, purely repulsive potentials such as also used in BCA simulations, e.g. the universal Ziegler-Biersack-Littmark (ZBL) potential³²⁰ or the potential

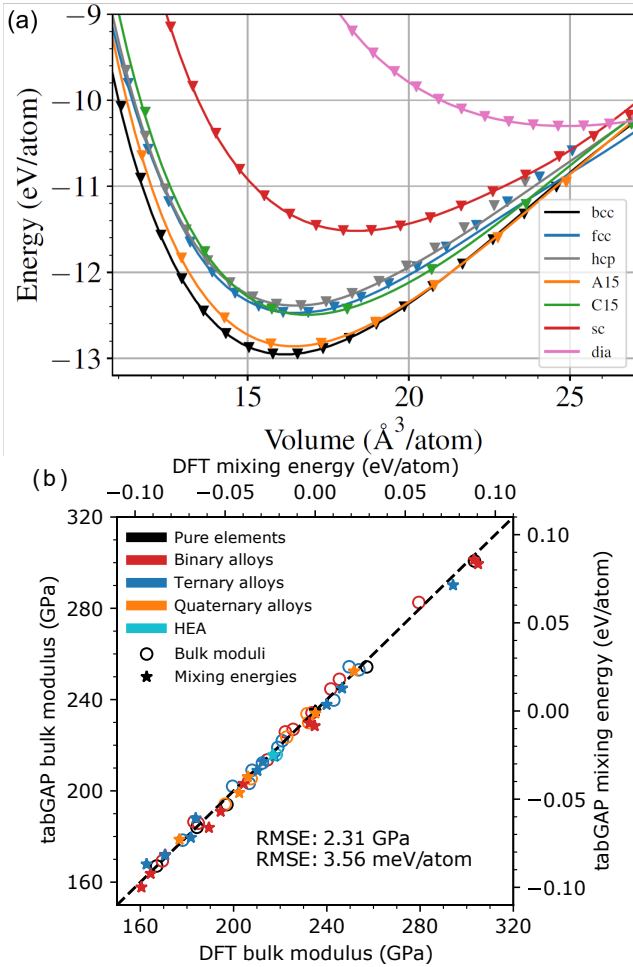


Figure 9. Example of the agreement between the DFT training data set and machine-learned interatomic potentials for both (a) pure GAP and (b) tabGAP. The markers are the DFT data points showing the cohesive energy in various configurations of (a) pure W and (b) high entropy alloy, while the lines are the results of the GAP and tabGAP, respectively.

obtained with the all-electron DFT code DMol³²¹, provide accurate results. They need to be smoothly joined with the material-specific empirical potential at small distances³²². For ML potentials, it is advantageous to already include the repulsive potential in the training phase³¹⁸.

3. Applications of molecular dynamics to FIB irradiation

Large-scale MD simulations have been employed to gain insight into nanostructure formation and modification of nanostructures. Das, Freund, and Johnson³²⁵ investigated the formation of nanopores in Si membranes, which are of interest for biological applications, by a Ga FIB. They identified a local boiling mechanism that could be explosive at high enough ion

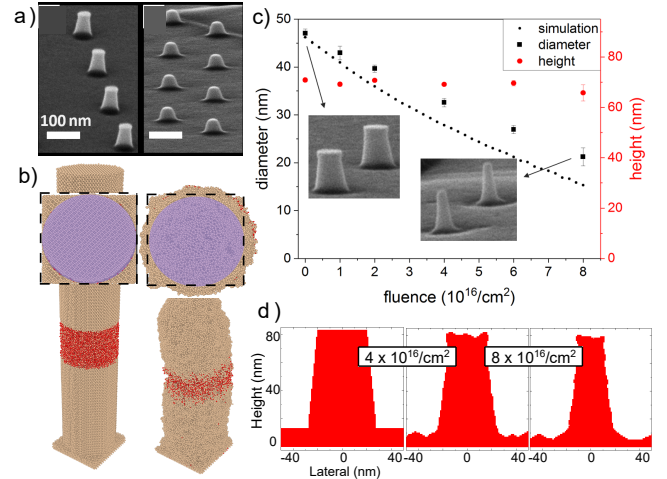


Figure 10. Comparison of deformation of Si nanopillars under high fluence 25 keV ion irradiation. (a) Experimental SEM images³²³ before (left) and after (right) a Ne fluence of $2 \times 10^{16} \text{ cm}^{-2}$ at room temperature. Note the short, but still wide shape of the pillars after irradiation. (b) Results of MD simulations for the Si/SiO₂/Si pillar ($r = 5 \text{ nm}$, $h = 50 \text{ nm}$) before and after a Si fluence of $7.6 \times 10^{15} \text{ cm}^{-2}$. In the top views next to the corresponding side images, the dashed squares outline the bottom pedestal and the blue circles the size of the ion beam throughout the simulation. The irradiated pillar is shorter (side views) and broader (top views). (c) Experimental images of the evolution of a Si nanopillar under prolonged Ne ion irradiation at 400 °C³²⁴. Since Si does not amorphize, the shape is modified only due to erosion from the top and the sides of the pillar, which is well captured by BCA simulations. (d) Corresponding nanopillar images of a BCA simulation³²⁴.

fluxes³²⁵. Moreover, they found recirculating material flow which they explained as driven by temperature-gradient induced surface tension gradients³²⁶. Another interesting phenomenon occurs during ion irradiation of Si nanopillars. At room temperature, the pillars shorten (Fig. 10a), while at elevated temperature, they become thinner (Fig. 10c). In the MD simulation performed at room temperature (Fig. 10b) the Si amorphizes, which initiates viscous flow due to the ion hammering effect³²³, resulting in a shortening of the nanopillar as seen in the experiment (Fig. 10a). In the BCA simulations shown in Fig. 10d, the nanopillar mainly shrinks in diameter, in agreement with the experiment at elevated temperature (Fig. 10c). This is explained by the neglect of viscous flow in the BCA simulations, while viscous flow indeed does not occur when the target remains crystalline at the higher temperature. As a third example, MD simulations have examined how a balance of beam spreading, erosion and defect-induced strain limits the thinning of FIB lamellae³²⁷.

Chemical effects in sputtering cannot be described by BCA simulations, but can be by MD simulations employing reactive force fields. For instance, the sputtering of silicon by low-energy oxygen and silicon ions using the

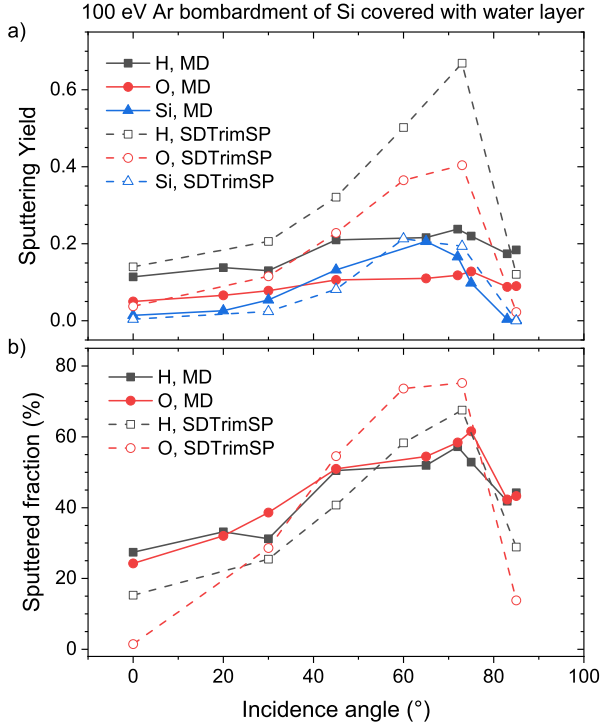


Figure 11. Results obtained by MD and BCA (SDTrimSP) simulations after 100 eV Ar irradiation of Si covered with a monolayer of water molecules to a fluence of 5×10^{15} ions/cm². For MD Si(100) was used, and the SDTrimSP sample was amorphous. The evolution of (a) the sputtering yields and (b) the fraction of deposited H and O atoms that is sputtered, are shown as a function of incidence angles.

Kieffer force field³¹⁰ showed that two mechanisms are mainly responsible for sputtering: (i) emission of atoms forming clusters a few angstroms above the surface and (ii) ejection of clusters that are loosely bound to the sample surface³²⁸. As another example, the impact of residual water molecules on sputter yields of Si bombarded with Ar has been studied (cf. Fig. 11). Here, MD simulations using the ReaxFF potential optimised for the Si-C-O-H system³²⁹ are compared to SDTrimSP BCA simulations. For the MD simulations, a much weaker dependence of the O and H partial sputter yields on the incidence angle is found. The difference might be explained by the random positions of the H and O atoms in the SDTrimSP simulations presenting more efficient scattering centers than the more regular atomic configurations in the MD simulations at incidence angles between about 50° and 80°. At angles closer to perpendicular and grazing incidence, the MD results show higher sputter yields than BCA. This may be explained by the desorption of water molecules which is not included in the BCA model. Note that the maximum Si sputtering yield is found around 65°, while the maxima for H and O are found between 70° and 80°. As a practical conclusion, when the mixing of contaminations into the sample should be minimized, angles closer to grazing incidence

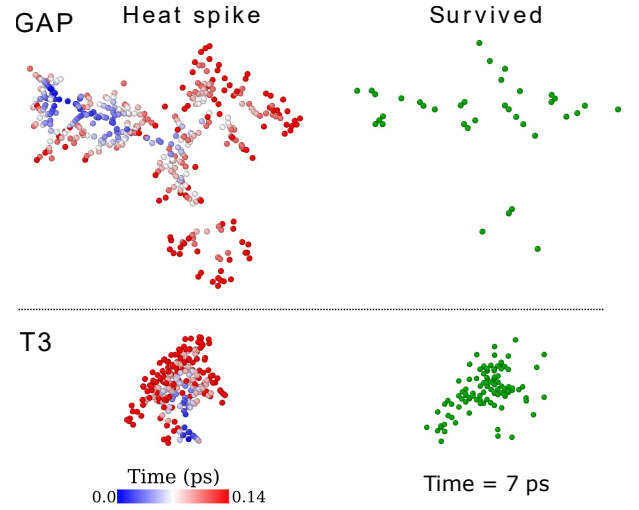


Figure 12. Typical snapshots of 2 keV collision cascades at the heat spike phase and resultant defects in silicon. Heat spike snapshots (left panel) present the atoms with kinetic energy above 1 eV. Atoms have been color-coded based on the time of generation after firing the primary knock-on atom. Surviving defects (right panel) are acquired from Wigner–Seitz analysis of the cell after cooling to 300 K ambient temperature. The comparison visualizes the overestimated defect formation in Si predicted by the classical potential Tersoff (T3)³⁰⁴ compared to GAP³³⁰.

should be favored.

Defect formation in all kinds of materials has been a traditional field of MD simulations²¹². Although much insight has been gained, quantitative and sometimes also qualitative results are in doubt due to the inaccuracies of empirical interatomic potentials. For instance, the threshold displacement energy, the essential parameter for damage calculations in the BCA, turned out to be substantially different for Si when calculated by DFT-MD compared to using the Tersoff or Stillinger-Weber interatomic potentials³³¹. On the other hand, when using a ML potential, essentially the same values were obtained as with DFT³³⁰. Likewise, sputter yields for low-energy Ar irradiation of Si obtained with the ML potential were found to be close to experimental values, while the empirical interatomic potentials largely underestimate the yields³³⁰. Moreover, it was shown that damage buildup in keV energy cascades is strongly overestimated by the empirical potentials, see Fig. 12.

MD simulations have also provided good understanding of ion-impact generated defect formation in free-standing^{332–334} and supported^{335–337} 2D materials, which is of interest for developing ultrathin membranes for ion-beam analysis of gases and other volatile systems³³⁸. As with bulk materials, new insight is gained for 2D materials using DFT-MD^{339–341}. As an example, in the study by Kretschmer *et al.*³⁴¹ the importance of accounting for the chemical interactions when evaluating the threshold displacement energy in graphene and hexagonal boron

nitride (hBN) has been demonstrated.

4. Limitations and extensions

While in the BCA, trajectories are only followed for atoms with energies exceeding a few eV, MD simulates all atoms in a region covering the collision cascade. Therefore, MD simulations are much more computationally demanding than BCA simulations. Taking into account that actual FIB processes often use rather high fluences, it is clear that their computational cost may be a challenge. Moreover, due to the limitation of the MD time step to values resolving lattice vibrations, the time between collision cascades cannot fully be simulated. If relevant, thermally activated events occurring during these time spans may be covered by kMC simulations (see Section III C). Often, such thermally activated events are neglected, and in addition the system is artificially quenched to the ambient temperature at the end of each cascade in order to shorten the time required to dissipate the energy deposited by the collision cascade³²⁸. This comes at the expense of possibly missing some relevant defect annealing.

The limitations of empirical interatomic potentials have already been discussed above. Another drawback of Born-Oppenheimer MD is the absence of an inherent description of electrons in the system. Electronic stopping can be included in MD as a frictional force²⁷², and the same stopping powers may be used as in BCA simulations. Modeling of electronic stopping of channeled ions, however, is much more difficult than in the BCA approach^{342,343}. In addition, there is uncertainty about the low-energy limit to electronic stopping, which has been shown to be relevant to predicting sputter yields³⁴⁴ and damage formation³⁴⁵. A related problem is electron-phonon coupling, which describes the exchange of energy between the electronic and ionic subsystems. Electron-phonon coupling may be included in MD simulations by the so-called two-temperature model³⁴⁶. However, so far no general consensus about the model of electron-phonon coupling nor its significance at FIB-relevant energies has been reached³⁴⁷. Recent insights from TDDFT³⁴⁸ show promise for enabling a physically motivated parametrization of how electronic stopping and electron-phonon coupling relate to each other^{349–351}. However, other possible effects include the modification of atomic interactions due to electron excitations in the system³⁵².

Born-Oppenheimer MD fails to describe, e.g., the transitions between electronic states or the neutralization of ions in the vicinity of a 2D target. These situations may be treated by TDDFT-MD (Ehrenfest dynamics). In irradiation simulations using Ehrenfest dynamics, the nuclei are usually approximated as classical particles moving in the time-dependent average potential of the electrons, while the electron subsystem evolves according to TDDFT. Due to their complexity and high computational cost, Ehrenfest dynamics simulations are cur-

rently feasible using massively parallel computers for systems comprising only tens of atoms and times up to picoseconds. The method has been successfully applied to electronic stopping power calculation in various targets^{353–356}, excitation mediated diffusion modeling³⁵⁷, and simulations of the behavior of inorganic 2D materials under electron beam irradiation³⁵⁸, but its applicability is limited by the mean-field approximation and the resulting propagation of mixed states. For example, the sputtered atoms may have fractional charges. It is also worth noting that this approach has been demonstrated to work for describing the formation of HIM images by assessing spatial distributions of excited electrons just after the impact³⁵⁹.

C. Kinetic Monte Carlo (kMC)

The time scale accessible by MD simulations is in the nanosecond range, which is sufficient for the system to reach thermal equilibrium after an ion impact. After this time, diffusion and interaction of defects take place by thermally activated events. Examples of such events are diffusion hops, attachment of an atom to a cluster, or recombination of two defects. The rate constant of each event may be determined by transition state theory using the potential energy function of the system, e.g., using DFT and the nudged elastic band (NEB) method³⁶⁰. Sometimes, this parametrization can be done directly from experimental data, e.g., by fitting to a known temperature-dependent diffusion coefficient. kMC is a method that evolves systems described by such events stochastically. For a basic introduction to the method see Ref. 361. Another review is found in Ref. 362, and more recent ones with special emphasis on radiation effects and semiconductor processing are in Refs. 363 and 364, respectively. Some alternatives for extending the time scale of MD are discussed in Ref. 365.

Several variants of the kMC method have been developed. On-the-fly kMC determines energy barriers of possible events in the course of a simulation. This technique has been used to simulate defect diffusion in iron³⁶⁶, defect evolution in graphite³⁶⁷ as well as deposition and sputtering³⁶⁸. On-the-fly kMC can easily be combined with MD, since both methods can use the same potential energy function, and neither needs prior knowledge of possible events. The search for possible events makes it the computationally most expensive variant of kMC, though.

Setting up a catalogue of events *a priori* can be approached in two ways. In lattice (or atomistic) kMC, a lattice is defined where each site can be empty or occupied by an atom. Events are hops from one lattice site to another with rates modeled based on the local environment of each site. Examples of use include vacancy diffusion³⁶⁹, solid-phase epitaxial regrowth^{370,371}, sponge structure formation in Ge³⁷², self-organized surface pattern formation³⁷³, damage in hBN³⁷⁴, and phase decom-

position of substoichiometric SiO₂ into Si nanoclusters in an amorphous SiO₂ matrix³⁷⁵.

In object kMC, in addition to vacancies and impurity atoms, also other defects including clusters are treated as individual objects that are followed as they move and/or react with each other. The atoms of the “background” material are not explicitly represented. Therefore, the system size accessible by object kMC is determined by the number of objects in the simulation rather than some fixed volume. The object kMC approach has mainly been used in simulations of radiation effects in nuclear materials³⁷⁶ and semiconductor processing^{364,377}.

Lattice and object kMC can be combined not only with MD^{367,368,373,376}, but also with BCA^{369,375–377}. In addition, kMC schemes are occasionally also used to describe system evolution due to non-thermally activated events. For instance, in Ref. 338 the accumulation of defects in a graphene sheet is modeled based on defect production probabilities obtained by MD simulations of ion impacts.

D. Continuum modeling

Unlike the methods described in the previous subsections, continuum models do not use individual atoms as the objects of simulation, but instead use quantities that are continuous functions of space and time. For example, in a continuum approach the ion beam is described by its (spatially dependent) flux (= number of ions per area and time increment), adsorbed precursor molecules by their concentration (= number of molecules per surface area), and boundaries of solids by mathematical surfaces.

1. Ion implantation and milling

In the absence of ion beam mixing and other secondary effects, the distribution of implanted ions may be obtained by the convolution of the beam flux $F_{\text{beam}}(x, y)$ and a “point response” $f(x, y, z)$. The point response is the probability density function for the stop position of an ion entering a target of the same material at the origin of the coordinate system. For the purpose of this discussion, we assume the ions to be incident along the negative z axis; x and y denote the other two Cartesian coordinates. If the surface is described by a height function $z = h(x, y)$, the increase in the concentration of implanted atoms $C(x, y, z)$ with time t is given by³⁷⁸

$$\frac{\partial C}{\partial t} = \iint F_{\text{beam}}(\xi, \eta, t) f(x - \xi, y - \eta, z - h(\xi, \eta)) d\xi d\eta. \quad (2)$$

For practical reasons, $f(x, y, z)$ is often approximated by a Gaussian function whose parameters can be determined by a BCA simulation. For an unscanned beam, the beam flux $F_{\text{beam}}(x, y, t)$ is constant in time, for a digitally scanned beam it is piecewise constant, and for an analog scanned beam it is a continuous function of time.

Displaced atom and deposited energy distributions can be calculated in a similar way. They may be of interest for estimating the damage to the target, and as input to solving the heat transport equation, respectively.

Sputtering causes the surface to recede. The resulting surface velocity in the direction of the surface normal is given by

$$v_{\perp} = \Omega F, \quad (3)$$

where Ω denotes the atomic volume of the target atoms, and F the flux of atoms through the surface element around the point under consideration. In the absence of secondary effects, F is given by the flux of sputtered atoms, $F = F_{\text{beam}} Y(\theta) \cos \theta$, with θ the local incidence angle of the ions and $Y(\theta)$ the sputter yield. The sputter yield may be determined by BCA simulations or experiment.

As long as an initially flat surface, $h(x, y, t = 0) = 0$, develops only small slopes, the surface contour reflects the beam profile:

$$h(x, y, t) = - \int_0^t v_{\perp} dt = - \Omega Y(0) \int_0^t F_{\text{beam}}(x, y, t) dt. \quad (4)$$

Once larger slopes occur, further prediction of the target topography usually requires iteration³⁷⁹ or more refined numerical techniques. One option is to move surface marker points along the surface normals³⁸⁰. The drawback of this method is that as the nodes move, they tend to form loops which have to be removed. A simple technique to avoid loops, which works for surfaces that remain height functions $h(x, y)$ throughout the simulation, is to interpolate the surface back to an (x, y) grid after each time step³⁸¹. More general solutions are cell-based and level-set methods. The former represent the target by filled or partially filled voxels, while the latter describe the surface as the zero level-set of a distance function and solve a differential equation for this quantity³⁸⁰. Implementations of the marker and level set method for FIB milling have been presented in Refs. 382–387 and Refs. 263,388–391, respectively.

When the surface develops larger slopes, two additional effects come into play (cf. Fig. 13): First, sputtered atoms may be redeposited at other parts of the surface (blue arrow in Fig. 13). Second, ions may be backscattered from their primary incidence point and hit the target somewhere else (red arrow in Fig. 13), where they cause sputtering. These secondary sputtered atoms may be redeposited (cyan arrow in Fig. 13). These processes add significantly to the complexity of the simulation: The angular (and possibly energy) distributions of the sputtered and backscattered atoms (blue and red elliptical lines, respectively, in Fig. 13) have to be described in some way, and the computation of the fluxes at each marker point (D_1 and D_2) requires the summation over the contributions of all other marker points (S_1 and S_2)^{196,386,387}. The summation may be substituted by randomly starting individual rays at the source points, which adds a MC

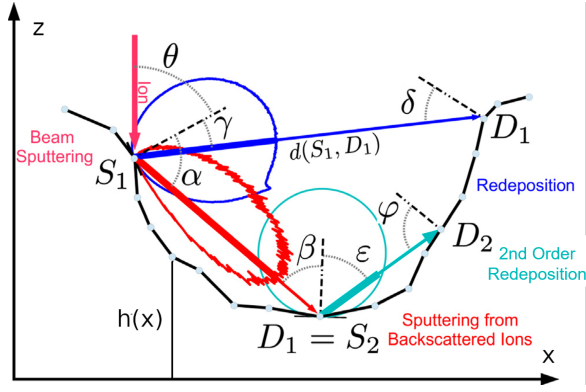


Figure 13. Illustration of ion backscattering (red lines) and redeposition of sputtered atoms (blue and cyan lines) during FIB milling of a trench. The ellipse-like curves represent angular distributions. In this case, the surface may be described by a height function $z = h(x)$. For clarity, no variation in y direction has been assumed.

aspect to the simulation^{388,392}. In contrast to a BCA simulation, however, the atom trajectories are not followed within the target, but their exit characteristics are chosen according to pre-calculated angular (and energy) distributions. In either way, redeposition and backscattering add contributions to the flux F of Eq. (3). The same applies to contributions from etching and deposition in case of gas-assisted processes, see Section III D 2.

In principle, many physical and chemical effects may be considered in a continuum approach. However, each model requires input from more fundamental simulation or experiment when a new ion-material combination is considered. This may be straightforward for the parameters of the most basic models, such as the mean values and standard deviations of implanted ions or the sputter yields. As the model complexity increases, parameter determination becomes more cumbersome.

Our discussion so far has neglected dynamic changes to the target composition. As the irradiation proceeds and ions are implanted, however, the stopping power for the ions changes, and so does the point response $f(x, y, z)$ in Eq. 2. The same applies to sputter yields and angular distributions. Consideration of dynamic effects would also require modeling of atomic mixing. This has not been attempted so far in a multi-dimensional continuum approach. Moreover, sputtering is a non-local effect, i. e., the sputtered atoms are not emitted exactly at the impact point of the ion, which may be important in nanofabrication. In addition, ion implantation and atom relocation may cause topography changes through volume relaxation (cf. Section III A). These effects are building blocks of the theory of spontaneous pattern formation³⁹³, but have not been considered in continuum simulations of FIB processes so far.

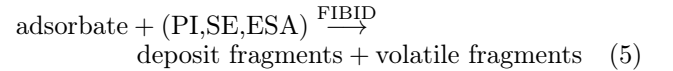
Another effect that can be treated within a continuum approach is beam heating. Temperature distributions can be calculated by solving the heat transport equa-

tion with heat sources given by the energy deposition of the collision cascades, using finite element or finite difference methods^{394,395}. The estimates are important because elevated temperatures may reduce deposition rates in FIBID (see Section III D 2) and may lead to heat damage in biological samples (see Section III D 3).

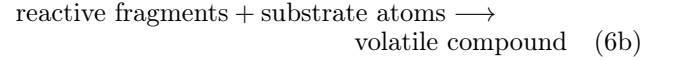
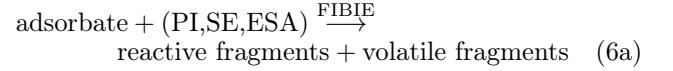
2. Gas-assisted deposition and etching

Gas assistance enables selective 3D nanoprinting and enhanced etch rates in FIB processing. Continuum models attempt to quantify the local deposition or etch rate caused by the chemical surface reaction between the volatile adsorbates and the PIs, their locally generated SEs, and excited surface atoms (ESAs):

Deposition reaction:



Etch reactions:



Metalorganic compounds mostly do the job for FIBID³⁹⁶. For focused ion beam-induced etching (FIBIE), the adsorbed precursor compound needs to dissociate upon irradiation into a reactive species that forms a volatile compound with the underlying substrate without leaving traces of other dissociated precursor elements.

Present FIBID and FIBIE models treat the desorption of volatile fragments in reactions (5) and (6) as instantaneous and assume that etch reaction (6b) is fast compared to reaction (6a), see Ref. 397 for a review. Both processes share the same formalism to calculate the surface coverage Θ (normalized concentration) of adsorbates, which is defined by the rate equation (in units of inverse time):

$$\frac{\partial \Theta}{\partial t} = \nu_{\text{gas}}(1 - \Theta) - \nu_{\text{des}}\Theta - \nu_{\text{dis}}\Theta + D \nabla^2 \Theta. \quad (7)$$

The terms $\nu_{\text{gas}}(1 - \Theta)$ and $\nu_{\text{dif}} = D \nabla^2 \Theta$ are adsorbate source terms by gas and surface-diffusion transport, respectively, while the other two terms are adsorbate sink terms related to the rates of desorption and dissociation, ν_{des} and ν_{dis} , respectively, see Fig. 14. This approach could be extended to multiple chemical pathways as in models developed for FEBID and focused electron beam-induced etching (FEBIE)³⁹⁸.

PIs, SEs, and ESAs are the co-reactants. The concentration of impinging PIs is given by the ion beam spatial profile $F_{\text{beam}}(x, y)$ and the FIB exposure time. Energy and spatial distributions $f(E, \vec{x})$ of SEs and ESAs result

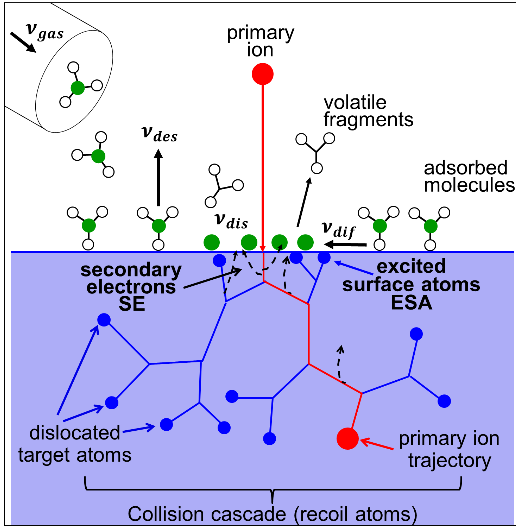


Figure 14. Concept of selective (local) gas assisted FIBID. Volatile physisorbed molecules are dissociated by irradiation into volatile and non-volatile fragments, the latter forming the deposit (green spheres). Primary ions typically arrive at keV energy while ESAs and SEs have an eV energy spectrum. ESAs are generated by the collision cascade (recoil atoms) and have energies below the surface binding energy (not sputtered). Rates (ν) are explained in text. Note that ion sputtering, ligand co-deposition, and incomplete adsorbate dissociation were omitted for clarity.

from the interaction of the PIs and the recoils with the etched substrate or growing deposit. $f(E, \vec{x})$ must be determined from more fundamental simulations. For SEs, BCA simulations of PIs and recoils combined with MC simulations of electron transport³⁹⁹ have been performed using a simple model of SE generation. More refined theories of SE generation also exist^{400–402}. For ESAs, BCA simulations reach their low-energy limit of applicability, since atom energies of around 1 eV can already dissociate the precursors. An alternative for simulations of ESAs would be MD.

Finally, the chemical fluxes of deposition F_{dep} or etching F_{etch} (in units of atoms per area per time) are proportional to the dissociation rate ν_{dis} and the coverage of adsorbates Θ

$$F_{\text{dep,etch}} = m \nu_{\text{dis}} \Theta n_s, \quad (8)$$

where m denotes the number of atoms deposited or etched per dissociated precursor molecule and n_s the number of adsorbate sites per surface area. Note that the product $\nu_{\text{dis}} \Theta$ defines the rate of deposition or etching for a single site in units of inverse time. The flux according to Eq. (8) must be added to the flux of sputtered and redeposited atoms discussed in Section III D 1.

Modeling of the four terms on the right-hand side of Eq. (7) is key to the successful simulation of FIBID and FIBIE. The first term $\nu_{\text{gas}}(1 - \Theta)$ represents a widely used pragmatic simulation approach. It

assumes non-dissociative Langmuir adsorption, which treats adsorption as physisorption with a maximum coverage of one monolayer of adsorbates. Other adsorption schemes include dissociation⁴⁰³, multilayers⁴⁰⁴, and chemisorption⁴⁰⁵. Open source MC codes are available for the calculation of the gas impingement rate ν_{gas} at the irradiated area for given geometrical arrangement of nozzle and substrate^{398,406,407}. Typical values are in the range $0.1 \lesssim \nu_{\text{gas}} \lesssim 10^3 \text{ s}^{-1}$.

The desorption rate ν_{des} , contained in the second term on the right-hand side of Eq. (7), is the inverse of the surface residence time. It depends exponentially on the temperature as well as on the type of adsorption on the growing/etched surface being irradiated. The desorption rate can cover several orders of magnitude depending on the molecule-surface interaction.

The third term, the adsorbate dissociation by irradiation, is key for selective FIBID and FIBIE as it captures the crucial non-thermal irradiation driven chemistry of the process. Different contributions involving PIs, SEs, and ESAs are involved in adsorbate dissociation, see Fig. 14. In principle, the dissociation rate can be calculated from the energy dependent dissociation cross section $\sigma(E)$ and the energy distribution $f(E, \vec{x})$ of the SEs or ESAs via

$$\nu_{\text{dis}}(\vec{x}) = \int_0^\infty \sigma(E) f(E, \vec{x}) dE. \quad (9)$$

$\sigma(E)$ describes the efficiency of reactions (5) and (6) as functions of the energy of PIs, SEs, and ESAs. Such energy dependent calculation is hampered by the fact that so far reliable $\sigma(E)$ only exist for electron induced dissociation reactions of molecules in the gas phase, see for example Ref. 408. A pragmatic approach assumes that such gas phase $\sigma(E)$ can be linearly scaled to the net deposition (etch) cross section, see below. This approach omits the quenching of certain dissociation channels (fragment production) due to the adsorbate state situation^{397,409–411}. Simulations will thus not be accurate with respect to deposit composition but the deposit (etch hole) shape can probably be adequately modeled. The only established energy dependent cross section under deposition conditions exists for the molecule $(\text{CH}_3)_3\text{Pt-CpMe}$ by electrons⁴¹² describing the observed dissociation of one volatile CH_3 ligand from the adsorbed molecule leading to a deposit of Pt:C=1:8 atomic composition.

The ESA induced adsorbate dissociation reactions have not been studied so far, probably due to experimental issues in deconvolution of the naturally involved (secondary) electron contributions. Recent condensed phase studies with Ar-ion irradiation⁴¹³ point to the importance of the additional mechanical sputtering effect of PIs, which can help in removing more ligand fragments than SEs alone and in achieving higher metal content material. Generally, the nature, charge, and energy of ions open up a wide field of fragmentation chemistry with metalorganic or “etch” adsorbates, which is still unex-

plored as such, particularly with respect to missing $\sigma(E)$. Moreover, the energy distributions $f(E, \vec{x})$ in Eq. (9) are not easily obtained in a continuum approach. Therefore, while using Eq. (9) with a MC approach for SE generation and transport is a promising approach, for the ESA mechanism one has to resort to simpler approaches, as is also often done to describe the SE mechanism.

In a simpler approach, dissociation is generically modeled via the dissociation rate $\nu_{\text{dis}}(\vec{x}) = \sigma f(\vec{x})$, where $f(\vec{x})$ is the local flux of the PIs, and σ is the so-called net deposition or etching cross section, that is deduced from fitting the shape of the deposit or etch hole. Such cross sections do not distinguish between the different contributions of PIs, SEs, and ESAs, nor do they distinguish between the fragmentation reactions. The modeled shape or rate can sometimes retroactively be attributed to a certain mechanism, when the yield and/or spatial distribution of either PIs, SEs, or ESAs matches the deposit or etch hole dimensions. In this way, the ESA dissociation mechanism was identified to be dominant for FIBID with noble gas ions heavier than He^{414,415} and the SE dissociation mechanism was identified as important for He-FIBID nanopillar growth.⁴¹⁶ In those cases, $f(\vec{x})$ may be interpreted as the flux of ESAs or SEs. Experimental net cross sections (yields) obtained from ion and electron induced deposition are available for few precursor molecules³⁹⁶, and deposit compositions upon electron irradiation were recently reviewed in Refs. 403,417.

The fourth term, the diffusion rate, is proportional to the surface diffusion coefficient D and the second spatial derivative $\nabla^2\Theta$ of the adsorbate coverage Θ . Thus, it becomes largest for intense and finely focused ion beams and can result in delivery of considerable amounts of adsorbates to non-irradiated surface areas. Increasing temperature increases the surface mobility of the adsorbates exponentially.

The generation of local heat during ion irradiation can be an important factor influencing the outcome of a deposition process. Thermal contributions can alter the non-thermal irradiative dissociation pathways and exponentially change the diffusion constant (mobility) and residence on the surface of the adsorbates. As an example, thermal effects are thought to be responsible for the bending of lateral nanowires as they grow⁴¹⁸. As mentioned in Section IIID1, the temperature distribution needed as input to temperature dependent models of mobility and residence time can be obtained by numerically solving the heat transport equation.^{394,395}

3. Applications to FIB processing

Simulations of FIB milling may be used to investigate the influence of beam shape and scan strategy on the final topography of the target³⁸², and to better understand the milling process. For instance, Lindsey et al.²⁶⁶ investigated microtrench formation in trench milling and clarified the roles of redeposition and backscattering. In

practice, often the inverse problem of determining beam and scan parameters for a desired geometry must be solved. In the simplest case, for low-aspect ratio structures, this can be achieved approximately by choosing the pixel dwell times proportional to the desired depth at the respective pixel positions¹⁹². For higher accuracy, a system of linear equations for the pixel dwell times has to be solved in order to consider the effect of beam overlap^{379,419}. For higher-aspect-ratio structures, when redeposition and/or backscattering need to be considered, repeated numerical simulations of the milling process must be performed until convergence to the desired structure is achieved. In practice, such structures are fabricated by applying variable dwell times across the scan area in multiple passes. Here one can either choose to apply the same pattern in each pass¹⁹⁶, or to define layers to be milled in each pass and to determine individual dwell time profiles¹⁹³.

Finite element and finite difference simulations of heat transport have been performed by Wolff et al.³⁹⁵, who used them to verify a simple model for the estimation of target heating. Schmied et al.⁴²⁰ employed a similar numerical approach to find beam scanning strategies that minimize local thermal stress in soft matter.

Gas-assisted FIB processes have been treated in a continuum approach mostly to help identify in which regime the surface reactions (5) and (6a) take place, i.e., whether they are mass-transport-limited (adsorbate-limited), or reaction-rate limited (PI, ESA, and/or SE limited), or driven by desorption or surface diffusion. These regimes strongly influence shape fidelity, homogeneity, and resolution all of which are of utmost importance for these 3D nanoprinting/nanoetching approaches. A review of both time dependent and steady-state analytical solutions of Eqs. 7 and 8, using simplifying assumptions, is found in Ref. 397. This theoretical framework closely resembles the one used for gas-assisted focused electron beam processing (FEBID/FEBIE) with the exception of physical sputtering and redeposition. Hence, analytical solutions established for the analogue electron-based FIBID/FIBIE variants straightforwardly apply. They include those for surface diffusion steady state and flat-top focused beam profiles^{421,422}, for long freestanding rods⁴²³, 1D time dependent solutions⁴²⁴, and expressions for lateral resolution⁴²⁵ and etch/deposition gas mixtures^{426,427}. Analytical solutions without surface diffusion can be used in the PI, ESA, SE limited processing regimes (no concentration gradient of adsorbates due to high supply from the gas phase), or approximately when adsorbates cannot diffuse into the center of the FIB spot profile due their deposition at the rims. These conditions translate into very small FIB current and exposure (dwell) time⁴²⁸. Without the surface diffusion term, analytical solutions are more easily derived and thus cover a broader range of adsorbate related dissociation mechanisms. These include the resulting deposit composition upon injection of two precursor species⁴²⁹, multistep reactions involved in gas enhanced etching^{398,430}, and ex-

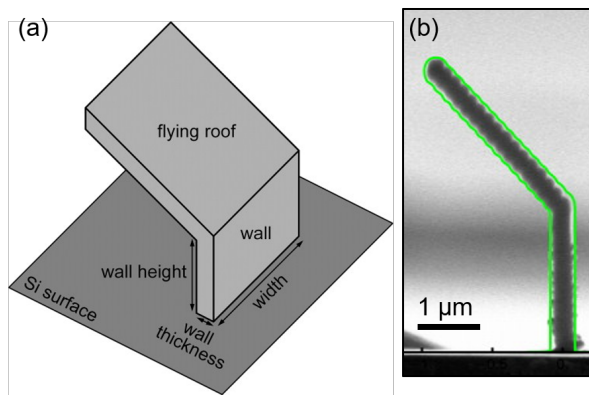


Figure 15. Flying roof fabricated by FIBID. (a) Schematic illustration of the structure. (b) Side view SEM image and simulation (green line) of the structure obtained with a 30 keV Ga beam with a FWHM of 60 nm and pentamethylcyclopentasiloxane as precursor. After wall formation, the beam was moved to the left in 16 steps of 60 nm²⁶⁵.

perimental parameter maps⁴⁰⁴.

Full numerical continuum simulations of a FIBID process using Eqs. (7) and (8) have been performed by Ebm et al.,²⁶⁵ see Fig. 15. In their simulations, they used an ESA-based model assuming the concentration of ESAs to be proportional to the flux of sputtered atoms. They considered the nonlocal nature of sputtering, a prerequisite for obtaining parallel sidewalls in the lower part of the structure and the flying roof in the upper part. Simulations of pillar growth using voxel grids was reported in Ref. 431.

Presently, simulations of FIBID/FIBIE are more advanced in the BCA-based approaches, cf. Section III A 3. One reason might be that pure continuum approaches require the modeling of the SE/ESA intensities $f(\vec{x})$ as an additional step. Also, BCA-based approaches include several collision-cascade related effects which cannot easily be modeled in a continuum approach, see Section III D 1. On the other hand, uncertainties by some of the assumptions of both approaches might be more relevant in practice. These include the way energy and spatial distributions of ESAs and SEs are determined, and assumptions about the fragmentation paths. Further development of either approach holds promise for model-assisted 3D nanoprinting, which has already been demonstrated for FEBID^{432,433} and has been started for FIBID^{251,255,418}.

IV. APPLICATIONS OF FOCUSED ION BEAMS

The various processes that are triggered when a beam of ions interacts with a sample form the basis of the multitude of FIB applications that are routinely used today. Accordingly, this Section is intended to provide a comprehensive overview on the variety of experimental applications structured along the different FIB processing

techniques.

In the following paragraphs, the breadth of FIB techniques is briefly outlined to be highlighted in more detail in the subsequent subsections. Further reviews of these topics can be found in a number of recent articles^{40,267,434,435}.

Subtractive processing: Local material removal by a focused ion beam is based on physical sputtering. The incident projectiles knock out substrate atoms by momentum transfer, but also penetrate the material in a collision cascade. While knocking out atoms is desired, all other interactions with the substrate can cause unwanted side effects such as amorphization, mixing, doping, dealloying and others. Conventional Ga⁺ ion beam tools provide spatial resolution and sputtering yields high enough for multiple prototyping purposes, but other ion species may offer advantages in terms of increased spatial resolution or sputter yield, and reduced damage or chemical reactivity. Section IV A provides an overview on the rich variety of subtractive FIB milling applications.

Defect engineering: FIB irradiation of materials at doses significantly lower than those used for milling has been implemented in a range of applications to locally tune material properties through the introduction of defects (vacancies and implanted ions). For example, by varying the dose, different concentrations of vacancy defects can be introduced into a crystalline material, thus modulating properties such as electrical, magnetic and thermal behavior in the patterned regions. In the case of ion implantation, this can be directed at SII, or can be used to modify the chemical and structural properties of surfaces for resistless patterning. An overview of defect engineering applications is given in Section IV B.

Imaging and tomography: Just as is the case with the SEM, scanning the ion beam over a surface generates secondary electrons that can be detected to form an image. In this respect, there is no difference between imaging using a focused ion or a focused electron beam. Even the same secondary electron detectors can be used. What strongly differs, is the mass of the probe. The mass of the ions is more than three orders of magnitude larger than that of the electrons, which significantly influences the contrast mechanisms and interaction volumes, and can also inflict significant damage on the sample. In this respect, the light ions of He-FIB bring great benefit—Section IV C is dedicated to the application of the helium FIB specifically for the imaging of biological specimens. The focused ion beam can further be used in a subtractive manner as described above to slice the sample and image the resulting cross-sections by SEM. The images are then used for reconstruction of the full 3D information in a so-called FIB-SEM tomography, cf. subsections IV C 3 and IV C 4.

Elemental analysis: Upon ion beam induced physical sputtering atoms and ions originating from the sample are ejected and can be used to study its chemical composition. In SIMS the generated secondary ions are collected and separated by their mass in a spectrometer,

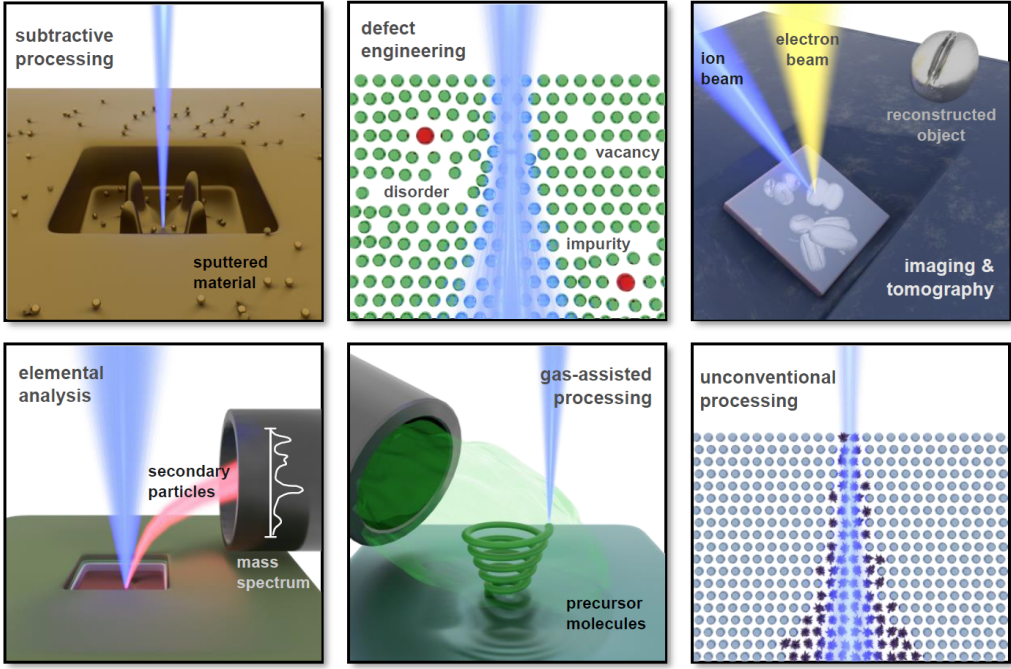


Figure 16. Schematic overview on the different FIB techniques

cf. Section IV D. Other analytical techniques, like EDS or electron backscatter diffraction (EBSD) are of minor importance for conventional FIB system as the generation rate of X-ray quanta is negligible and the typical penetration depth of the conventional Ga ions is too low to receive sufficient information on the lattice orientation.

Gas-assisted FIB-processing: Bottom-up prototyping of nanostructures using the FIB is known as FIBID. In this technique, the FIB is scanned over the sample surface generating SEs that induce the partial decomposition of precursor molecules, dissociating them into volatile and non-volatile components. The volatile products are pumped away, while the non-volatile products are deposited on the surface, thus creating a nanostructure in a single-step process. The flexibility of FIBID in terms of shape and resolution (20 nm to 30 nm for Ga-FIBID, and 10 nm for He-FIBID) make it highly desirable for applications that require unique and precise planar or 3D designs. FIBID applications are discussed further in Section IV E.

Unconventional FIB-processing Similar to gas-assisted processing, focused ion beams can be used for the

local chemical modification of lithographic resists as well as of condensed or spin-coated metalorganic precursors. Such ‘unconventional’ FIB processing can increase processing speed and provide new chemical reaction pathways for ion-induced deposition of high-purity metals. Focused ions can also be used to form self-assembled structures or combined with the wealth of other nanofabrication techniques to obtain the best of different worlds. Recent advances in the area of FIB-based resist lithography and further non-standard FIB approaches are described in Section IV F.

A. Applications of subtractive FIB processing

As the material removal using a focused ion is local and direct, it offers an extraordinary flexibility of both the target geometry to be realized and the substrate materials and geometries. Often the process can be even monitored in-operando by scanning electron microscopy for direct alignment and quality control.

Table V: Overview of applications of subtractive FIB-processing, in which material is locally removed by ion-beam based physical sputtering.

Research area	Application	Ion	Material/Device
Materials science	TEM sample preparation	Ga	wide range of materials ⁴
		Xe	Al and Si ⁴³⁶ , Al alloy ⁴³⁷
		Ne	Al alloy and Si ⁴³⁸
	APT sample preparation	Ga	wide range of materials ⁴³⁹

continued on the next page.

Table V: continued

Research area	Application	Ion	Material/Device
		Xe	Al alloy ⁴⁴⁰ , Ti alloy ⁴⁴¹
		Ne	Al alloy and AlO _x thin-film structure ⁴⁴²
	3D analysis	Ga, Xe	slice and image ⁴⁴³
	mechanical testing	Ga	micro/nanopillars, notches, ‘dogbone’ tensile bar specimens ^{4,444–469} , SiO ₂ suspended membrane beams ⁴⁷⁰
Optics	photonic components	O	optical bridge in diamond ⁴⁷¹
		Ga	aspherical microlens in silicon ⁴⁷² , solid immersion lenses in silicon ⁴⁷³ and around pre-localized quantum emitters in diamond ^{188,474,475} , triangular nanobeam cavities in diamond ⁴⁷⁶ and in YVO ₄ ^{477–479}
			Fresnel zone plates for X-ray microscopy ⁴⁸⁰
			photonic crystal cavity around quantum emitters in diamond ⁴⁸¹
			tapered nanoantenna for single photon emission of CdSe quantum dots ⁴⁸²
	fiber-based optical components	Ga	lab-on-a-fiber ⁴⁸³ , Bragg gratings and microlenses in silica nanofibers ⁴⁸⁴ , superconducting single-photon detector (SSPD) on optical fiber ^{485,486}
	plasmonic antennae	Ga	Au bowties for extreme ultraviolet (EUV) light generation ⁴⁸⁷ , inverse Ag bowties ⁴⁸⁸ , ring-shaped beam patterning of Au antenna arrays ⁴⁸⁹ , Yagi-Uda-type antennae ^{490,491} , $\lambda/2$ antennae ⁴⁹² , asymmetric Ag oligomers ⁴⁹³
		He	Al bowtie structures ⁴⁹⁴ , gaps in Au bowtie antennas ^{495,496} , Au coaxial nanoresonators ⁴⁹⁷ , Au oligomers ¹⁹⁰ , inverse Au oligomers ^{498,499}
	plasmonic waveguides	Ga	Au groove waveguides ⁴⁹¹ forming logic gates ⁵⁰⁰ , two-wire waveguides in Au ^{501,502} forming spin optical nanodevice ⁵⁰³
Electronics	superconductive circuitry	Ne	nanoSQUIDs in Nb ⁵⁰⁴
		Ga	nanoSQUIDs in Nb ^{505–508}
		Xe	nanoSQUIDs in Nb ⁵⁰⁹
	semiconductor technology	Ga	photo mask repair ^{510,511} including deposition ⁵¹² and etching ⁵¹³ , circuit edit ⁵¹⁴
	Au	X-ray mask repair ⁵¹⁵	
		He, H, N	photo mask repair ^{54,516–519} , circuit edit ^{519,520}
Magnetism	spintronics and magnonics	Ne	permalloy microstrip trimming ⁵²¹ , environment depend FMR ⁵²²
		Ga	magnetic reversal ⁵²³ , spin wave phase inverter ⁵²⁴
Quantum Materials	unconventional superconductivity	Ga	Sr ₂ RuO ₄ ^{525,526}
	Josephson-vortices	Ga	strongly layered high-Tc superconductors ^{527,528}
	time-reversal symmetry breaking	Ga	Delafossite ⁵²⁹
	topological protected surface states	Ga	topological semi-metals ^{530–533}
	critical charge and bandstructure	Ga	μ -crystals ^{534–536}
	strain engineering	Ga	Sr ₂ RuO ₄ ⁵³⁷ , CeIrIn ₅ ^{538,539}
	control of superconducting currents	Ga	vortex pinning ⁵⁴⁰ , directional vortex motion ^{541–543}
Custom-probes and sensors	near-field microscopy	Ga	circular ⁵⁴⁴ and bowtie ⁵⁴⁵ nanoaperture, tip-on-aperture geometry ^{546,547} , Au bowtie ⁵⁴⁸ and nanocone antenna ⁵⁴⁹ , nanoslit grating in Au conical taper ⁵⁵⁰

continued on the next page.

Table V: continued

Research area	Application	Ion	Material/Device
		He	square nanopores in pyramidal Au nanocavities ⁵⁵¹ , Au nanopyramid antenna ⁵⁵²
		Xe	probe shaping for nearfield scanning microwave microscope ⁵⁵³
	atomic force microscopy	Ga	nanoscale apertures for liquid and ion transport ⁵⁵⁴⁻⁵⁵⁶ , tip sharpening ⁵⁵⁷ , modified mechanical response ⁵⁵⁸
	magnetic force microscopy	Ga	V-shaped magnetic nanostructure at probe tip ⁵⁵⁹
	mechanical high Q resonators	He	phononic crystal ⁵⁶⁰
		Ga	graphene trampoline ⁵⁶¹

1. FIB for materials science

Arguably the most widespread application of the FIB has been the site-selective fabrication of cross-section samples for high-resolution imaging using a TEM^{4,5,562-564}. Due to the prevalence of Ga-FIB instruments, Ga ions are most typically employed and various strategies have been developed to mill and extract cross-sections from bulk materials and to thin samples to electron transparency. This includes low-energy FIB milling under glancing incidence to minimize surface amorphization, and the use of material specific capping layers and rocking stages to avoid *curtaining* artifacts. More recently, the use of other FIB species for TEM lamella preparation has been demonstrated, such as the Ne-FIB⁴³⁸ and the Xe-FIB⁴³⁶. The advantage of a noble gas ion species is that it does not chemically react with the sample or accumulate along grain boundaries, as can be the case with Ga⁵⁶⁵.

In the same manner FIB milling has emerged as an important tool for the creation of needle-shaped specimens for APT^{6,439}. Similar consideration to the case of TEM sample preparation apply. Also here, minimal damage layer, and the possible indiffusion of in particular Ga atoms⁵⁶⁶ has to be taken into account. The required needle geometry is achieved via annular milling with different currents and subsequently smaller milling areas.

Another important application is the site-specific preparation of cross-section cuts that enable in-situ and ex-situ imaging⁵⁶⁷ and/or other analysis such as EDS or EBSD (e.g. Kalácska *et al.*⁴⁶⁷). By automating this process, full (destructive) tomographies can be performed by slicing the sample, extracting the desired information from each slice, and reconstructing the data in three dimensions (see for example Kubis *et al.*⁸² and Section IV C 3).

All of these techniques are part of the standard materials science repertoire used to study the microstructure, composition, and properties of materials and devices at specific target locations. In depth overviews on these can be found for example in Giannuzzi and Stevie⁵⁶⁸.

2. FIB for mechanical testing

As technology miniaturizes, the external dimensions of components in devices approach characteristic internal length scales such as dislocation interspacing. The mechanical properties of such small volumes of material are still not fully understood. In 2004, Uchic *et al.*⁴⁴⁶ suggested use of FIB milling to machine micropillars to study size dependent mechanical properties of metals exploiting conventional nanoindentation equipment for microcompression experiments. In contrast to conventional cleanroom based lithography and etching, FIB machining allows for virtually any material to be shaped into a micropillar at a specific target location. To achieve uniform pillar circumferences with minimal taper lathe milling in combination with annular milling is often applied⁵⁶⁹. While the former can introduce sever levels of stress⁵⁷⁰ which might result in cracking or destruction of the sample during APT, it is better suited for insulating, or very inhomogeneous samples comprising layers with very different sputter yields.

Today, most mechanical testing experiments are performed in SEM or TEM to capture changes from almost atomic to micron scale (e.g., formation of dislocations, stacking faults, twins, grain orientations, contraction and expansion of volume). Complex workflows include some or all of the following steps: (a) micropillar machining, (b) tilting of the sample towards a mechanical testing device for in-situ SEM testing, (c) deposition of a regular pattern of points of FIB or focused electron beam (FEB) deposits on the sample side-walls to follow deformations via digital image correlation algorithms, (d) in-situ mechanical testing under SEM observation, and (e) finally back-tilting for subsequent post-mortem FIB slicing for 3D tomographic or 3D EBSD analysis of the deformed microstructure or the fracture pattern inside the loaded sample⁴⁶⁷.

FIB machining of sharp notches with a specified orientation to the loading axis enabled a number of fracture mechanics studies⁴⁶⁵. For in-situ tensile testing in TEM, milling protocols were developed to prepare electron transparent nanospecimens⁴⁵⁸.

To reduce ion beam-induced surface damage defects, a multistep milling strategy is typically employed. In this approach, beam voltage and current are sequentially

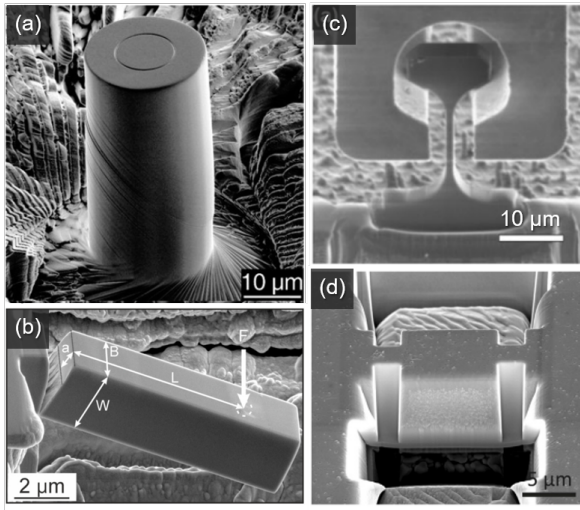


Figure 17. Popular FIB-machined sample geometries for micromechanical testing: (a) micropillars⁴⁴⁶, (b) notched micro-cantilevers⁴⁶⁵, (c) micro-tensile bars⁴⁶⁶ and (d) micro-shear tests⁴⁶⁰.

stepped down to the last polishing step⁴. Among the still open questions are how much damage (amorphization, implantation) is induced by FIB milling into the structures and how the damaged zones affect the mechanical behaviour of the milled structure⁴⁵⁴. This depends on the penetration (implantation) depth of ions as well as the collision cascade (amorphization) they trigger (see sections III A 3, III B 3, and III D 1).

Once other ion sources, in particular He, Ne, Xe, became available the hope was to avoid the Ga damage issues. Best *et al.*⁴⁶³ found, however, that using either He, Xe or Ga for machining of notches would affect the measured fracture toughness value. While He ions were demonstrated to yield suitable sharp notches with radii below 10 nm, Xe ion beams were resolution limited. In addition, it was unclear how the penetration depth of the different ions would affect the fracture toughness⁴⁶³. Currently combinations of FIB with other technologies are getting more and more popular. Laser machining of large volumes and FIB fine sculpturing have recently become available from several manufacturers in a single setup.

3. Applications in photonics and plasmonics

Miniaturized on-chip photonic components are designed to guide or focus light while having a footprint as small as possible. The fabrication relies mostly on conventional large-scale lithographic techniques but there are applications where a maskless direct-write strategy has significant advantages. The prime examples are localized light sources, with the extreme case of single photon sources, where often the optical component has to be built around a pre-localized (quantum) emitter.

Such quantum emitters may be defects in wide-bandgap materials (cf. Section IV B 4) where out-coupling of the generated quantum light is typically hindered by the large refractive index of the host material, e.g. diamond. Here, FIB milling either using Ga ions^{188,474,475} or, to reduce Ga-induced damage, oxygen ions⁴⁷¹, was successfully used to engrave solid immersion lenses that enhance the photon collection efficiencies. In the same manner, photonic crystal cavities with small mode volumes have been cut into a suspended diamond layer around pre-localized quantum emitters and proven to enhance spontaneous emission⁴⁸¹. An even further reduction of optical mode volume can be achieved using metallic nanostructures since these have the ability to concentrate light below the diffraction limit by collective excitations of the free electron gas⁵⁷¹. Since such plasmon-polariton modes are strongly dependent on geometry, FIB-processing is a powerful tool for rapid prototyping of nanoscale resonators, sub-wavelength apertures⁵⁷² and optical antennas⁵⁷³.

Due to the extreme plasmonic field confinement, molecular species can be detected down to the single molecule level by surface enhanced Raman scattering⁵⁷⁴ as the prime example, by enhanced fluorescence⁵⁷⁵ or by enhanced Förster resonant energy transfer⁵⁷⁶. The latter two examples employ Ga ion beam milling to fabricate an antenna-in-a-box geometry, where the gap region of a dimer antenna provides for local electric field enhancement and correspondingly enhanced local density of optical states. The remaining metallic film around the antenna blocks fluorescence contributing to the background. In general, Ga-FIB top down patterning, especially of single-crystalline Au or Ag nanoflakes, is often employed for high-fidelity rapid prototyping of plasmonic components^{502,577–580}. When comparing the performance and material properties of plasmonic antennas, electron beam lithography (EBL) may lead to better results than FIB milling, depending on the actual geometry and processing conditions, and especially in case of Ga⁵⁸¹. However, EBL fails in fabricating truly 3D profiles, as used e.g., in the case of 3D Janus plasmonic helical nanoapertures for polarization-encrypted data storage⁵⁸². A particularly beautiful example of the 3D capabilities combines the local material removal by Ga ion beam milling in a suspended gold film with a low dose irradiation at selected edges. The latter induces a stress distribution that lead to up- or downwards bending of the predefined structures⁵⁸³. This nano-kirigami has been demonstrated for various designs realizing optical chirality, polarization and phase engineering and showing potential for opto-mechanical applications⁵⁸⁴. In addition, resolution and shape fidelity of FIB milling using light ions stand out compared to any other lithographic techniques^{190,434}, but they come at the cost of the slow speed of an inherently serial process. To resolve this issue, lithographic large area processing by EBL can be combined with the ultimate resolution of focused ion beam processing using He. Extremely narrow gaps between

large areas of lithographically defined plasmonic gold⁵⁸⁵ or aluminium⁴⁹⁴ antennas were realized using this approach. The achievable spatial resolution can be significantly improved while keeping a reasonable processing speed by combining Ga ion beam patterning with He patterning⁴⁹⁵. Another approach to increase speed of top-down FIB processing relies on milling only the outlines of desired plasmonic features which are then obtained by peeling off the surrounding material^{586–588}. This “sketch and peel technique” combining Ga ion beam patterning for the outlines with He FIB for the definition of ultra-narrow gaps was used to reproducibly demonstrate strong coupling in plasmonic dimer antennas⁵⁸⁹.

4. Fabrication of custom probes

Since FIB milling is not restricted to planar sample geometry, a vast body of research exists on the modification of optical fibers⁴⁸³, nanofibers⁴⁸⁴ and nano-probes. The comprehensive review by Sloyan *et al.*⁴⁸³ presents examples for optical near-field imaging, plasmonics, beam shaping, fiber-based photonic cavities, fiber-chip coupling and many more. He ion based manufacturing was reviewed in detail by Allen⁴³⁴. The direct control over precise nanostructure geometries by FIB milling is especially interesting in near-field optical microscopy (NSOM), where a metal coated glass fiber tip localizes the excitation and/or collection of light by making use of a nanoaperture or antenna for plasmonic field concentration. In applications concerned with NSOM, FIB milling has been employed to fabricate high-definition plasmonic circular nanoapertures⁵⁴⁴ at the tip of a metal coated fiber glass tip. Further signal enhancement and fluorescent background reduction can be achieved by adding a tip at the aperture rim combining the concepts of scattering and aperture NSOM^{590,591}. While in these works the tip was grown by FEBID and metallized afterwards, later work engraved the tip-on-aperture geometry from the metallic (Al) fiber coating by Ga FIB milling and tuned the tip resonance to act as a monopole antenna, thus achieving single molecule imaging⁵⁴⁶ and imaging of proteins on cell membranes⁵⁴⁷. Additional geometries realized in this way are bowtie⁵⁴⁵ nanoapertures on the end of metal-coated fiber tips and square plasmonic nanoapertures in pyramidal cavity structures⁵⁵¹, with the latter example employing He FIB milling. Further specific geometries of metallic tips and metal-coated fiber tips have been fabricated to control the plasmonic response for other purposes. These include nanocones for resonance and radiation pattern tuning⁵⁴⁹ by Ga FIB milling, nanopyramids for optimizing local electric near-fields⁵⁵² by He FIB milling, and nanoslit gratings into the conical taper of metallic tips for nanofocusing upon far-field illumination⁵⁵⁰, again by Ga-FIB milling.

FIB milling has also been employed to modify AFM probes for specialized applications. For example, nanoscale apertures have been milled into hollow pyra-

midal AFM tips so that that when the tips are loaded with liquid they can be used to dispense attoliter volumes to create droplet arrays⁵⁵⁴. Such tips can also be used for the manipulation and analysis of single cells via so-called fluidic AFM⁵⁵⁵. Tips can be sharpened using FIB milling and can also be detached from their initial substrate and mounted onto a cantilever of choice with the help of a micro-manipulator. This technique has, for example, been used to produce customized tips with high aspect ratios⁵⁵⁷. In other work, the AFM cantilevers themselves have been fashioned with FIB-milled apertures to enable ion implantation through those apertures aided by scanning probe alignment⁵⁵⁶. FIB milling of larger patterns into piezoresistive cantilevers has been used to increase deflection sensitivity to optimize cantilever performance⁵⁵⁸.

5. FIB processing for quantum materials

“Quantum Materials” are materials in which quantum phenomena manifest in non-trivial ways, leading to response functions that are qualitatively distinct from those of standard electronic materials such as silicon or copper. They generally arise from the non-locality of quantum systems, with topology, frustration, and correlation playing a central role in the field^{592,593}. The key goal is to refine our microscopic or phenomenological understanding of these exotic quantum states, and develop predictors to find promising materials candidates within the vast space of possible compounds. Here, the FIBs excels as a versatile patterning tool that is ideal for rapid processing of non-standard materials⁵⁹⁴, as it a) avoids exposure to wet chemistry compared to resist-based lithography; b) can operate with crystallites and microparticles that do not resemble polished wafers; and c) enables 3D structure control that is critical to many electronically 3D quantum materials. The operational goal of this research is to fabricate hybrid structures that join micro-/nanostructures of a quantum material to a Si chip of conventional architecture, both to demonstrate advanced functionalities and to probe the underlying novel physics.

Quantum systems generically respond strongly to changes in their boundary conditions, in this case, their physical shape. FIBs enable the sculpting of non-trivial boundary conditions in crystals, which has been used to elucidate the unconventional superconductivity of Sr_2RuO_4 ^{525,526}, Josephson-vortices in strongly layered high- T_c superconductors and their excitations^{527,528}, quasiparticle transport in ultra-clean metals⁵²⁹, and the magnetic exchange bias in time-reversal symmetry breaking topological semi-metals⁵⁹⁵. Reducing the sample size to the micron scale further enhances the contribution of surface properties to the overall physics. This is particularly important in the quest to probe the contribution of topologically protected surface states which have been proposed to enable novel electronic and spintronic appli-

cations in topological semi-metals^{530–533}. Controlling the motion of Abrikosov lattices by surface structuring⁵⁴¹ allows the control of the motion of the vortices and can be used to build vortex diodes^{542,543}. FIB processing allows to enhance the edge quality of structures which is a prerequisite for the fabrication of efficient SSPDs⁴⁸⁵. The flexibility of FIB processing enabled this process on the top of an optical fiber⁴⁸⁶.

Subtractive FIB processing has also been applied in the fields of spintronics and magnonics. Examples include application to guiding and control of propagating spin waves, which has been enabled using Ga-FIB⁵²⁴ processing. High resolution metal free FIB processing using GFIS enables the fine tuning of the interaction of spin waves across gaps⁵²¹.

Not all applications of the FIBs aim to alter the material. There is a wide class of experiments that aim at probing bulk properties of novel materials which are difficult to access in their native form, for example microcrystals that are too small for conventional measurements. This has allowed insights into microscopic effects on critical charge transport in iron-based superconductors^{534,535}, the determination of topological bandstructures in microcrystals⁵³⁶, or the switchability of anti-ferromagnetic states under the high current densities achievable in FIBs machined crystals^{596,597}. The rich physical responses of quantum materials tend to be rooted in the competition of multiple electronic ground states, which leads to a strong (and potentially discontinuous) change of their properties under weak applied stimuli⁵⁹⁸. One can hardly overstate the importance of residual stress in the samples, with a famous example being the enigma of the “3K phase” of superconductivity in Sr_2RuO_4 which originated from mismatch strain⁵³⁷. Here a crucial advantage of FIBs over mechanical techniques of sample preparation such as polishing or wire sawing is its kinetic nature, which results in samples of low residual stress. Alternatively, the precision control over the physical shape of a sample has enabled microscopic control over desired strain fields and their gradients, which imprint correlation landscapes into the quantum materials^{538,539}.

6. FIB processing in the semiconductor industry

In the field of semiconductor processing, FIBs are most relevant during debugging of new products and for identifying production errors in the context of circuit editing and fault isolation, as well as the repair of photomasks. Among other applications, FIBs have been used for failure analysis, fault isolation, TEM sample preparation, mask repair and backside circuit edit^{568,599,600}. The ongoing scaling of the transistor fin, gate, and interconnect via linear and volumetric shrinking as well as the introduction of new transistor technologies led to a reduction of the critical length scale from 22 nm in 2012 to the current 3 nm technology node to be introduced by all major

manufacturers between 2022 and 2024^{601–603}.

FIBs have been used since the 1980s for mask repair, initially using LMIS and LMAIS based Ga and Au ions⁵¹⁰. However, staining from implanted ions was quickly identified as a problem limiting the application⁵¹¹. Latter, the application of GFIS based H^+ , H_2^+ , N_2^+ , and He^+ for phase shift mask and EUV mask repair was investigated by Aramaki *et al.*^{54,517}, Edinger *et al.*⁵¹⁸. For H_2^+ the minimal repairable dimension is reported to be 11 nm, which is half of what could be achieved using electron beams⁵¹⁶. The application of FIBID was investigated early on for adding missing material to masks and repairing pin holes by Cleaver *et al.*⁵¹² using Ga ions and a carbon deposit. This has been extended to other precursors for deposition and the application of etching gases such as Br_2 and Cl_2 for accelerated material removal⁵¹³ in eUV masks.

For circuit edit and fault isolation applications, gallium was used initially⁵¹⁴ but later Ne-GFIS based FIB processing was employed and resulted in minimal trench widths for high aspect ratio vias of 14 nm⁵¹⁹ and comparable or less collateral damage compared to Ga as measured via changes to ring oscillator timing⁵²⁰. Recently, also hydrogen GFIS based delayering has been used successfully⁶⁰⁴. However, other source technologies, e.g., Chromium based MOTIS⁶⁰⁵, also show potential for circuit edit applications⁶⁰⁶. In general it is found that lower energies will be required while still maintaining a suitably high resolution beam.

To better understand the effects of the beam profile on the achievable mill resolution, in particular for the important case of via fabrication, approaches have been developed to elucidate the probe current distribution^{607,608}. The latter is of importance for the fabrication of the high aspect holes created by milling—in many cases with a stationary beam. For via formation applications during which a good signal to noise ratio is required for reliable endpoint detection, a new figure of merit—SE yield per sputtered atom—can be defined. Here, GFIS based He and Ne based milling promises a spatial and temporal precision compared to Ga based FIB processing⁶⁰⁹. However, GFIS based milling suffers from the formation of gas bubbles and the creation of defects far below the milled surface⁶¹⁰.

7. Summary and outlook

As an all-in-one processing tool, it has been shown how FIBs can provide a versatile method for flexible and fast prototyping of nanostructures and devices by top-down fabrication.

To further advance these developments, FIB technology needs to improve not only lateral resolution but also the in-situ control over the material removal process itself. Critical issues include material selectivity and increasing the signal to noise ratio of the SE monitoring during milling of high aspect ratio structures. How-

ever, FIB top-down nanofabrication is intrinsically limited by the fact that the associated chemical species and energetic particles cause structural and chemical damage or changes, such as amorphization or poisoning. While traditional Ga-FIB still represents the FIB standard, some of the above mentioned fundamental limitations may be resolved by using other ion sources such as GFIS, MOTIS, LOTIS, multicusp plasma ion sources⁷² or LMAIS (see e.g. Section II A).

Additionally, leveraging FIB-based top-down nanofabrication as a practical option will only be achieved when increased reproducibility and throughput are consolidated.

These challenges can be addressed by advances in software and hardware tools that enable, for example, modeling-informed automated operation, thus allowing scale up or in line integration of FIB processing in the whole (nano)-fabrication routine. Theoretical knowledge, modelling and simulation tools that provide precise descriptions of FIB modifications to materials, from the atomic to the microscopic scale, are a prerequisite for predictive design and realization of tailored properties and functionalities in nanostructured surfaces and operating devices. At the same time, there are opportunities for coordinated FIB system development based on the experimental needs.

The strong interest within emerging fields such as quantum technology, as well as novel miniaturized platforms in the fields of microfluidics for lab-on-a-chip or organ-on-a-chip developments would benefit from synergies of theory groups and tool makers within the FIB application community.

B. Engineering materials properties through defects

In addition to the subtractive nanofabrication applications described above, site-specific and dose-controlled irradiation of samples with the FIB is used to tune material properties in spatially defined regions down to the nanoscale and even down to the single-atom level, without surface erosion or deposition. These applications are based on the local introduction of varying concentrations of defects (vacancies, dopants, and dopant-vacancy complexes), controlled by the dose.

1. Basics of irradiation-induced defect creation

A common technique used to create defects in crystals relies on bombardment with high energy ions or electrons^{211,611,612}, and in some cases photons, protons or

neutrons⁶¹³. For example, tuning the fluorescence properties or the refractive index of a material for optical applications by bombardment with ions is a well-established technique^{614,615}. Ion implanters are often employed for such applications. Since these deliver broad beams with spot sizes in the millimeter regime, a lithographically defined mask is needed when higher spatial resolution is required. However, the large collision cascades that are inherent to both high energy ion beams and light ion bombardment make mask design rather challenging. This is where FIB processing comes into play.

As described in Section III, the incident ion induces a collision cascade in the solid with a size that is determined by the target material and the ion's kinetic energy, as defined by the primary beam voltage. In a simplified picture, when a recoil is generated, it leaves behind a vacancy and forms an interstitial when it comes to rest⁶¹⁶. In reality, defect clusters and amorphous pockets may form depending on the target material⁶¹⁷ and the ion mass and energy⁶¹⁸. Such larger defects are usually undesirable for defect engineering as their properties are less well defined than those of simple defects. They are best avoided by using light ions which cause more dilute collision cascades than heavier ions due to the lower nuclear stopping power, and the recoils are less energetic because of the unequal masses of ion and target atoms. In addition, light ions cause less sputtering, which is considered an unwanted effect in defect engineering. Still, the applied ion doses and beam parameters have to be carefully adjusted. Considering the example of He⁺ ion irradiation of silicon and copper substrates, Livengood *et al.*⁶¹⁰ differentiate the various defect regimes according to dose, ranging from individual point defects at low fluence, to extended subsurface microbubbles at very high fluence. While the picture will vary somewhat for other ion-substrate combinations, the same overall trends apply.

Table VI gives the reader a flavor of the breadth of FIB-based defect engineering applications, categorized according to the specific materials property engineered (electrical, ferroelectric, magnetic, optical, quantum optical, chemical, thermal, and mechanical). Further examples can be found in the review articles from Gierak⁶¹⁹, Orús, Córdoba, and De Teresa⁶²⁰, and Allen⁴³⁴. In the remainder of this section we focus on those applications in Table VI that are concerned with engineering of electronic, magnetic, optical and quantum(-optical) properties, as well as tuning of low-dimensional materials (in particular, thin films and 2D materials), and the study of irradiation damage mechanisms (e.g. the formation of gas nanobubbles).

Table VI: Overview of FIB-based property engineering applications, in which fine control over the ion dose, beam energy, and irradiated regions enables local tuning of material properties.

Engineered Property	Experiment	Ion	Material/Device
Electrical & electronic	Conductivity tuning	He	graphene ^{621–625} , few-layer/monolayer MoS ₂ ^{626–628} , epitaxial MoS ₂ ⁶²⁹ , few-layer/monolayer WSe ₂ ^{627,630} , monolayer WSe ₂ ⁶²⁷ , InGaZnO thin film ⁶³¹
		Ga	AlGaAs/GaAs quantum wires ^{632–634} , GaAs quantum constrictions ⁶³⁵ , GaN nanowires ⁶³⁶ , 2D MoSe ₂ /graphene heterostructure ⁶³⁷ , MoSi superconducting thin film ⁶³⁸ , In ₂ O ₃ thin film ⁶³⁹ , Al ₂ O ₃ film ⁶⁴⁰ , ZnO and VO ₂ ⁶⁴¹
	Formation of tunnel barriers	He	superconducting electronic circuitry including nanoSQUIDs in YBCO ^{642–646} , MgB ₂ ⁶⁴⁷
		Ga	single-walled CNT ⁶⁴⁸ , nanoSQUID in Nb ⁵⁰⁵
	Tuning thermoelectric properties	He	MoSe ₂ thin films ⁶⁴⁹
	Tuning superconductivity	He	pinning vortices ⁶⁵⁰
	Pinning ferroelectric domains ferroelectric phase change	He	PbZr _{0.2} Ti _{0.8} O ₃ thin film ⁶⁵¹ , multilayer MoTe ₂ flake ⁶⁵²
		He	induced ferroelectricity in HfO ₂ ⁶⁵³ , conversion to paraelectric phase ⁶⁵⁴
Ga	HfO ₂ thin film ⁶⁵⁵ , damage in ferroelectric capacitors ^{656,657}		
Magnetic	Tuning magnetic anisotropy	He	Co/Pt multilayers ⁶⁵⁸ , Ir ₁₇ Mn ₈₃ /Co ₇₀ Fe ₃₀ bilayer ⁶⁵⁹ , Co-based thin-film stack ^{660,661} , Co/Pt/Ru multilayer system ⁶⁶²
		Ga	skymions in Pt/Co/MgO thin film ⁶⁶³ , and in Pt/Co ₆₀ Fe ₂₅ B ₁₅ /MgO thin film ⁶⁶⁴
	Ga	CoPt multilayers ⁶⁶⁵ , Fe ₇₈ Ni ₂₂ thin film ⁶⁶⁶ , Ir/Co/Pt multilayers ⁶⁶⁷	
	Ga	skymions in FeGe thin plate ⁶⁶⁸ , and in Co/Pt multilayers ^{669–671}	
	Tuning metamagnetic transition temp. FIB-induced ferromagnetism	Si/Ge	Bi and Ga substituted YIG ⁶⁷²
	He	FeRh thin film ⁶⁷³	
Ga	Fe ₆₀ Al ₄₀ alloy ⁶⁷⁴ and Fe ₇₈ Ni ₂₂ on copper ⁶⁷⁵		
Ne	Fe ₆₀ Al ₄₀ thin film ^{522,676}		
Magnonic	Ga	patterned Fe ₇₈ Ni ₂₂ films ⁶⁶⁶ , spin wave optical elements in YIG ⁶⁷⁷	
Optical	Tuning photoluminescence	He	SiN _x membrane ⁶⁷⁸ , monolayer MoSe ₂ ⁶⁷⁹ , InGaAs/GaAs quantum well ⁶⁸⁰ , reducing parasitic fluorescence in hBN ⁶⁸¹
	Tuning of passive optical components	Ga	AlGaAs/GaAs and GaInAsP/InP quantum wells ⁶⁸²
		He	plasmonic resonance in graphene nanostructures ⁶⁸³ , Bragg grating in silica nanofiber ⁶⁸⁴
		Li	Si microdisc nanophotonic resonator ⁶⁸⁵
Ga	ZnSe quantum dot micropillar cavities ⁶⁸⁶ , periodic poling of LiNb waveguide ⁶⁸⁷		
Quantum	Creation of quantum emitters	He	NVcenters in diamond with substitutional nitrogen ^{688,689} , Si vacancy centers in SiC ^{690,691} , luminescent defects in monolayer MoS ₂ ^{692,693}
		Bi	qubits in silicon and germanium ⁶⁹⁴
		Li	Si vacancy centers in SiC ⁶⁹⁵
		Si	Si vacancy centers in diamond ⁶⁹⁶ and diamond nanostructures ⁶⁹⁷ , W and G centers in silicon ⁶⁹⁸
		Ge	Ge vacancy centers in diamond ⁶⁹⁹
		Ga	luminescent defects in hBN ^{700,701} , monolayer WSe ₂ ⁷⁰² , MoS ₂ and WS ₂ ⁷⁰³
		Sb, Si	deterministic single-atom doping ⁷⁰⁴
		Xe	recoil implantation of color centers into diamond ⁷⁰⁵ , spin defects in hBN ⁷⁰⁶ , water assisted fabrication of extended defects in hBN ⁷⁰⁷

continued on the next page.

Table VI: continued

Engineered Property	Experiment	Ion	Material/Device
Chemical	Enhancing chemical etch rates	He	Si ₃ N ₄ thin film ⁷⁰⁸ , SiO ₂ thin film ⁷⁰⁹ , mono-/bilayer MoS ₂ ⁷¹⁰
	Enhancing catalytic activity	He	MoS ₂ and MoSe ₂ flakes ⁷¹¹
		He	epitaxial graphene on SiC ⁷¹²
	Nucleation of growth	Ga	InAs dots on GaAs ⁷¹³ , Ge dots on Si ^{714,715}
		Co	CoSi ₂ nanowires in Co-saturated silicon ⁷¹⁶
	Functionalization	Ga	graphene (fluorination using XeF ₂) ⁷¹⁷
Tuning surface wettability	Ga	molecular self-assembled monolayer ⁷¹⁸	
Thermal	Reducing thermal conductivity	He	Si nanowires ⁷¹⁹ , Si membrane ⁷²⁰ , VO ₂ nanowires ⁷²¹ , Bi ₂ Te ₃ nanoribbons ⁷²²
Mechanical	Tuning Young's modulus	He	monolayer MoSe ₂ ⁶⁷⁹
		Ga	polymer ⁷²³ , hydrogels ⁷²⁴
	Gas bubble effects	He	nanobubble superlattice in Cu ⁷²⁵ , nanobubbles in Si ⁷²⁶ , diamond ⁷²⁷ , Eurofer steel ⁷²⁸ , W ⁷²⁹ , ultrafine-grained W and W-Cu nanocomposite ⁷³⁰

2. Electronic applications

FIBs have been used from the beginning to manufacture electronic devices at the nanoscale. An early example is the fabrication of GaAs quantum wires⁶³² and the slightly later fabrication of a quantum wire transistor⁶³⁴ by Ga-FIB. Recently, a focused Ga ion beam was employed for the fabrication of a lateral diode based on a 2D heterostructure from MoSe₂ and graphene⁶³⁷. The preferential sputtering of Se transformed the top MoSe₂ locally into a quasimetallic state generating a pn junction with rectification performance comparable to that of a vertical diode. The above examples have in common that material needed to be removed by the FIB beam. Indeed, subtractive materials modification was more prevalent initially, but the engineering of electrical materials properties without intentional surface modification has recently become more and more important.

Here, light—and possibly—inert ion beams are of relevance due to their high resolution for creating defect based devices. Furthermore, ion beams of electronically active elements (e.g., P, Sb, As, ...) have the potential for interesting applications. A prime example is the fabrication of nanometer-sized insulating tunnel junctions in the thin-film high-temperature superconductor yttrium barium copper oxide (YBCO) using line irradiation with the He⁺ FIB⁶⁴². Similar tunneling junctions have also been created in other materials such as Nb⁵⁰⁵ and MgB₂⁶⁴⁷.

Due to the nanoscale beam diameter achievable with FIBs and in particular with GFIS based FIBs, they are the ideal tools for the fabrication of single quantum dots, tunneling devices and single electron transistors. This has been demonstrated by the fabrication of single electron transistors in Si/SiO₂ stacks³⁷⁵ and the fabrication of single quantum dots in carbon nanotubes (CNTs)⁶⁴⁸.

The fabrication of single electrically active quantum

dots in Si is a new challenge where some progress has been recently achieved^{258,704}. While these works are a clear demonstration of the placement accuracy for single or a few ions achievable with FIB, both approaches rely on the implantation of the donor atoms (Sb or P) into an active detector which also doubles as the host for the quantum device.

3. Modification of magnetic materials

Ions have been used for many decades for the modification of magnetic materials⁷³¹. To achieve this sort of modification complex and expensive masking processes have to be used unless one employs a focused beams of ions which can modify the magnetic properties locally with nm precision. In 1989 Ishii, Nonaka, and Hatakeyama⁶⁷² used Si and Ge from a LMAIS FIB to create nucleation sites for controlled switching of the magnetization in Bi and Ga substituted yttrium iron garnet (YIG) films. Ga FIB processing was used for the read/write heads⁷³² required for magnetic hard disks but also for modern approaches such as magnetic random access memories (MRAMs) composed of magnetic multilayer structures⁷³³. The FIB-induced local change in magnetic anisotropy was used to create isolated tracks of single domain islands in recording media⁷³⁴ and to control injection location and field dependency of magnetic domain walls in multilayers with perpendicular magnetic anisotropy using focused Ga and He ions⁶⁵⁸. In the case of Co nanowires fabricated by FEBID, irradiation with focused Ga ions allowed modification of the propagation speed of the magnetic domain wall⁷³⁵. In some materials, focused ion-beams can be used to generate ferromagnetism in selected regions, such as in paramagnetic FeAl alloys. The spatially resolved creation of disorder-induced ferromagnetism by focused Ga-FIB beam modi-

fication has been demonstrated by Menéndez *et al.*⁶⁷⁴. A spatial resolution of below 100 nm could thus be achieved with the possibility of erasing the pattern by annealing. Later Fe₆₀Al₄₀ was studied in depth for order-disorder phase transitions and ferromagnetic resonance (FMR) in magnetically written single objects⁵²² induced by focused Ne irradiation⁶⁷⁶.

Paramagnetic regions in non-magnetic materials can also be created by FIB processing as done for InGaAs using a focused Ga ion beam to create a spin filter device⁷³⁶. The continued quest for an increase in storage density in combination with novel data processing approaches (i.e. neuromorphic computing) triggered the development of advanced patterning of complex magnetic alloys and multilayer systems^{737–739}. In these systems various interactions due to the intrinsic anisotropy or lattice and system geometry may lead to topologically protected spin configurations such as skyrmions or controlled formation and transport of spin waves. Here, FIB stands out as it enables tuning of magnetic anisotropy landscapes without any topographical changes of the devices. This was demonstrated for the nucleation control of skyrmions in Co/Pt multilayers using Ga⁺ FIB⁶⁷⁰ and He⁺ FIB⁶⁶⁹, and the patterning of skyrmion racetracks in a Pt/Co/MgO thin film using the He⁺ FIB⁶⁶³. Patterning dots as nucleation sites within a low-dose racetrack using He⁺ FIB processing could realize both deterministic generation and movement of skyrmions with nanometric precision⁶⁶⁴. Finally, spin-wave optical components such as graded-index lenses for applications in magnonics can be created by ion-induced modification of the local magnetization in YIG, which corresponds to an effective refractive index for spin wave propagation. Here, focused Ga ions of 50 keV were employed and the penetration depth of about 100 nm allowed for an effective index of up to 1.8 comparable to light-based optics. Since this depth was only one third of the actual device thickness the much lighter He is expected to significantly improve the optical device performance⁶⁷⁷.

4. Optical applications

Typical applications of ion implantation in optics comprise the local change of refractive index and the creation of fluorescence⁷⁴⁰. However, since FIB processing is serial and the penetration depth is limited, it is mostly interesting in cases where a small number of ions needs to be placed with high spatial accuracy. One especially interesting example in that respect is the tuning and imaging of resonant optical modes in a silicon disc resonator with focused Li ion beams⁶⁸⁵. Here, an extremely low beam current of 1 pA at 3.9 kV acceleration voltage was used to radially raster scan in ion pulses of ≈ 3000 ions while the transmitted light through a critically coupled waveguide was monitored. The optical shifts could be attributed to an ion damage related contribution and a rapid thermal and, thus, reversal response. Using the knowledge about

this time-varying response, imaging of different optical modes could be achieved with minimum device degradation⁶⁸⁵.

The spatial accuracy of defect creation of the maskless process becomes especially beneficial in the field of quantum optics. Here, a defect in an otherwise ideally perfect crystal can take the role of an artificial atom emitting quantum light. The most popular example for this kind of a defect-based quantum emitter is the nitrogen vacancy (NV) center in diamond that are routinely fabricated using ion implanters⁷⁴¹ but were also realized by He ion beam processing^{688,689}. FIB implantation of Si ions has been used to realize nearly lifetime-limited single silicon vacancy (SiV) quantum emitters in diamond nanostructures⁶⁹⁷. This maskless creation of SiV centres in diamond nanocavities has been proven to occur with ≈ 32 nm lateral precision and < 50 nm positioning accuracy, and has been envisioned as promising for the development of scalable solid-state quantum information processors. Focused Si ions at 35 keV with 5 nm to 10 nm beam diameter were also used to fabricate V_{Si}^- defects in 4H-SiC. Starting from 40 ions per spot single emitters were found⁷⁴². A comparative study by the same author using hydrogen, helium and carbon showed that helium produced the highest defect concentration, while the lowest brightness of the emitters was observed for carbon⁷⁴³. In additions Li ions have been employed for the creation of silicon vacancies in silicon carbide⁶⁹⁵. Recently an electron beam ion source with focusing capability was shown to induce Ar⁸⁺ ion implantation for NV-creation in diamond⁷⁴⁴. A particularly interesting study made use of focused Xe ion for recoil implantation of targeted group IV dopants in a deposited surface layer⁷⁰⁵. Thereby, Pb, Sn, Ge and Si color centers in diamond could be fabricated with a spatial accuracy of better than 50 nm in combination with an ultra-shallow doping profile. In the case of silicon Si and C FIB implantation has been employed very recently to create single defects in a spatially resolved way for their application as quantum emitters in the telecom window⁶⁹⁸.

In parallel, 2D materials have been heavily explored for usable quantum emitters e.g. sources of single photons⁷⁴⁵. In that context, ion irradiation can be used to not only tailor the optical properties of 2D systems⁷⁴⁶, but also to produce defects which possess the desired characteristics^{747,748}. In particular, He ion beam processing was successfully used for the site-selective creation of defects in MoS₂. While the actual type of the defects is still to be investigated (being true for most of the luminescent defects in 2D materials) they are expected to cause highly localized trapping potentials for exciton emission. Encapsulation with hBN led to very narrow linewidths of the emission lines in the visible range 100 meV–220 meV below the neutral exciton⁶⁹³. He irradiation was also shown to result in a five-fold reduction of background and parasitic fluorescence resulting in isolation of bright and stable quantum emitters in hBN⁶⁸¹. Recent results on Ga ion beam patterning indicate that the lumines-

cent defect formation is positively correlated to material swelling instead of material removal by milling⁷⁰¹. This helps to explain earlier results on the generation of defects based on Ga FIB where it was not clear whether the single photon emission was actually generated inside the milled holes, at their edges or in the damaged region near the edges⁷⁰⁰.

5. Property engineering of low-dimensional materials

In general, 2D materials such as graphene and atomically thin transition-metal dichalcogenides are expected to play an important role in the realization of future electronic and optoelectronic devices and there exists a significant body of work in which FIB-based defect engineering has been used to tune the unique properties of these materials. In fact, as can be seen in Table VI, the majority of materials that are used in FIB-based defect engineering work are indeed low-dimensional (thin films, 2D materials, and nanowires). The simple reason for this is that typical FIB instruments deliver beams with energies of several tens of keV, which limits the ion penetration depth. For example, in most materials the maximum penetration depth of the ubiquitous 30 keV Ga⁺ ion beam is around 60 nm, which severely limits possibilities for property engineering of bulk materials. Here, light ions such as He⁺ and Ne⁺ bring benefit, as these ions can travel deeper into the sample while leaving the surface largely intact due to significantly reduced surface sputtering. In contrast, increase in ion energy normally gives rise to a drop in defect production in 2D materials⁷⁴⁹, so that lower energies are more suitable for efficient modification of 2D materials.

An example of FIB-based defect engineering of a low-dimensional material is the use of the He⁺ FIB to tune the electrical resistivity of 2D MoS₂⁶²⁶. In the cited work, the electrical resistivity of the MoS₂ monolayer was tuned from semiconducting to insulating depending on the vacancy defect concentration, as controlled by the irradiation dose. Above a certain threshold dose, total amorphization (i.e. disordering) of the material occurs. By irradiating samples locally in specific patterns with fluences below the total amorphization threshold, the FIB can be used to tune the defect density and hence electrical conductivity in spatially defined regions at the nanoscale. For example, using the He⁺ FIB and a line irradiation strategy, also on a 2D MoS₂ sample, a neuromorphic memtransistor device has been demonstrated⁶²⁸. Similarly, Ga-FIB has been used for defect creation in supported graphene with MD simulations providing a pathway for reducing the extension of the damage region by irradiation under an angle⁷⁵⁰. He⁺ FIB line irradiation has been used to isolate narrow widths of graphene, thus creating graphene nanoribbons⁷⁵¹. This enables the opening up of a bandgap in graphene, where tuning of the bandgap size (directly related to the nanoribbon width) is a key step towards the use of graphene in electronic ap-

plications. It should be noted that the minimum achievable nanoribbon width is limited by the influence of the backscattered ions from the substrate³³⁵, as discussed in Section III B 3.

Other defect engineering applications concerning 2D materials include use of the He⁺ FIB to create localized defects in graphene to serve as nucleation points for epitaxial growth of hexagonal boron nitride⁷¹² and localized fluorination of graphene using Ga⁺ FIB irradiation with the simultaneous flow of XeF₂ gas⁷¹⁷. An example of defect engineering of a 1D structure is the use of the He⁺ FIB to induce regions of local disorder in a silicon nanowire in order to tune the thermal conductivity along its length⁷¹⁹.

6. Study of irradiation damage mechanisms

Fundamental curiosity and the need for experimentally straightforward replacements for long-term reactor-based irradiation experiments have resulted in FIB instruments being used for the systematic study of irradiation effects on structural materials. In order to simulate irradiation damage caused by α particles, for example, He⁺ ions are a convenient species to use. A further advantage of using He⁺ ions is that fundamental studies of irradiation effects can be made while avoiding alloying effects and grain boundary embrittlement, as can occur with a metallic ion species such as gallium⁵⁶⁵.

A phenomenon that was discovered several decades ago is the formation of helium nanobubbles upon He⁺ ion irradiation of various metal targets. These nanobubbles form as a result of vacancy defects and helium interstitials that diffuse and recombine to produce gas clusters. However, fundamental studies of the resulting changes in the mechanical properties of the target material were for a long time confined to the use of large-scale ion accelerators and plasma devices. The introduction of the He⁺ FIB changed this, enabling the first systematic dose-controlled irradiation studies. Using the He⁺ FIB, gas bubble phenomena that had been observed in large-scale experiments have been reproduced with much greater control over the experimental conditions. Initial He⁺ FIB studies in this area used silicon targets, mostly driven by the need of the semiconductor industry to evaluate the invasiveness of He⁺ FIB processing⁶¹⁰. Later studies have included the investigation of helium gas-bubble superlattices, using single-crystal copper as a simple model system and probing the effect of the superlattice on the mechanical properties of the host material using in-situ TEM nanoindentation⁷²⁵. Since samples are irradiated with the He⁺ FIB on the nanoscale, individual grains and grain boundaries can be targeted in polycrystalline samples⁷⁵². By increasing the dose, the coalescence of nanobubbles to form crack planes that ultimately result in blistering and delamination can also be studied with a level of control that was previously unattainable⁷⁵³. Furthermore, irradiation-induced

mechanical property changes of a number of materials that are directly relevant for nuclear applications have been investigated using the He⁺ FIB method combined with nanoindentation, for example in studies of Eurofer steel⁷²⁸, tungsten⁷²⁹, ultrafine-grained tungsten and a tungsten-copper nanocomposite⁷³⁰.

Finally, helium gas bubble effects have also been employed for nanofabrication tasks, using patterning with the He⁺ FIB at high dose for localized subsurface swelling to deform surfaces and thereby create 3D nanostructures such as nanopyramids and nanohemispheres^{754–756}.

7. Outlook

Ion beam processing is well-established for material modification and property engineering at the microscopic scale. Recently, strong efforts are underway to further down-scaling with the ultimate goal of creating single defects or implanting single impurity atoms for quantum technology applications. The intrinsically stochastic nature of both ion creation from most source types and of ion-solid interaction in the sample poses a severe challenge. Hence, the deterministic implantation of single ions either in the bulk or at a surface pushes the technique to its fundamental limits in terms of spatial resolution and controllability.

There are two fundamentally different approaches. One is to count the ions that are incident on the surface, the other is to reliably detect the ion impact event, ideally in an universal manner. The first approach can be realized by using an Paul ion trap as a deterministic source of a single ion^{757,758}. While the presence of the ion can be unambiguously proven, ejecting the ion and loading the trap again is time-consuming and using ion-optical elements to spatially localize the impact event causes significant losses. Given that the probabilities for the creation of specific defects is usually low and highly material dependent (see also Section III B) this approach is appealing but technologically extremely demanding. Alternatively, ion columns may be equipped with image charge detectors that count ions from different types of ion sources. The beam is directed towards the sample only if an ion is detected. Thereby, limited detection efficiencies can be mitigated since all non-detected ions are blanked^{166,759}. The drawback of this technique is the large charge state that is necessary for detection such as e.g. 18+ for the case of Ar ions created by an electron beam ion trap (EBIT) source⁷⁵⁹. This requirement excludes light ions by construction and represents severe technological challenges for column design. The second approach, the detection of the ion impact event, could in principle work for any ion source. Promising attempts combine an on-chip IBIC detector with a plasma ion source and a near-surface aperture realized into an AFM cantilever²⁵⁸. Here, the aperture scanning realizes the spatial localization^{760–762} and thus allows use of various types of ion sources, including broad beam implanters.

While this is an important step for all quantum devices that tolerate a nearby pn-junction and amplifier, other device concepts e.g. in photonic quantum technology require truly sample agnostic detector concepts. The conventional SE detectors (Everhart-Thornley, CMOS, see also Section II C) may work as such but suffer from their strong dependence on the SE yield which is unknown for most materials and is, in addition, very surface dependent. These quests are combined with the need for a better understanding and prediction of SE generation and expected detection yields, and for advancing SE detectors exceeding 97% detection efficiency^{694,763}. Instead of detecting all ion impact events (that come with a small probability of creating the target defect) one may instead detect device function in-situ while shooting ions at the target locations. A combination of short dwell times at extremely low current results in a Poissonian probability of either one or zero ions per shot and the process may be stopped once the device is operable. Here, the technological challenge comprises the co-integration of an extremely sensitive fluorescence detection setup⁷⁶⁴. In conclusion, several promising development routes are currently pursued showing first exciting results. Which of the approaches, either modifying the ion supply towards being deterministic or enhancing the detection capabilities towards single-ion sensitivity or even a combined technology, will finally succeed is still open.

C. FIB-based imaging and tomography

In addition to imaging ever smaller features in samples down to atomic resolution as achieved by aberration-corrected TEM, imaging complex systems is becoming increasingly important. To understand data transmission in a brain or chemical energy storage in a battery, one needs to capture the “big picture” ideally in three dimensions rather than resolving individual atoms. This is where FIB-based techniques come into play, either by imaging of radiation-sensitive biological samples by light ions or 3D imaging by tomography where focused ion beam slicing is typically combined with SEM imaging.

1. A brief history of FIB-based imaging and analysis

The enormous potential of electron microscopy for imaging the structure of matter became clear immediately after the invention of the TEM in 1932⁷⁶⁵ and soon thereafter first images of bacteria^{766,767} and virus particles⁷⁶⁸ proved the same for the life-sciences. The introduction of ion microscopy for structural imaging, however, took much longer. Pioneering work was done in the 1970s by the Levi-Setti group who experimented with a scanning transmission ion microscope using up to 65 keV H₂⁺ ions from a GFIS and published images of myofibrils from rabbit muscle³⁶. However, since the achievable lateral resolution of ion microscopy had always been

inferior to that of electron microscopy, ion microscopy had not been used for high-resolution imaging until the early 2000s when the HIM was invented^{19,23} (see Section IV C 2).

The breakthrough, or in Ballerini *et al.*⁷⁶⁹'s words, "the revolution in ultra-microscopy" occurred around the same time when ion microscopic techniques finally became well accepted means for sub-cellular (chemical-)imaging. On one hand, ion beams from liquid metal based sources could now be focused down to better than 10 nm⁷⁷⁰. On the other hand, the idea to use the ion beam "like a tiny scalpel which slices away layers of the sample [and] to exploit this destruction to gain high-resolution three-dimensional structural, morphological, and chemical information"⁷⁶⁹ was brought to the life sciences⁷⁶⁹ and other fields, like energy materials⁷⁷¹. The following years saw the commercialisation of dual beam systems, in the following referred to as FIB-SEM. These usually consist of a field emission SEMs used for high-resolution imaging coupled with a Ga FIB column for sectioning. At the same time significant progress in 3D image segmentation and reconstruction was made⁷⁷² which paved the way for 3D structural imaging of complex specimens. One of the first reported FIB tomography investigations was presented by Inkson, Mulvihill, and Möbus⁷⁷¹ in the year 2001 on the "3D characterization of a metallic nanocomposite". After that, FIB tomography became a more and more common tool in various fields of research such as metallurgy^{82,567,773}, energy research⁷⁷⁴, geology⁷⁷⁵, biology, and medicine⁷⁷⁶. Especially in the latter fields a major step forward in the preservation of ultra-structure was to develop cryo-workflows for cryo-FIB-SEM tomography^{777,778}. Recently FIB has even been applied to paleontology samples⁷⁷⁹.

2. HIM—A tool for imaging of the tiniest living objects

SEM is a standard method for imaging biological specimens. Samples are usually coated with a conductive layer to prevent charging under the beam. Technically, SEM imaging without a conductive layer is possible if the accelerating voltage of the electron beam is reduced below 1 kV. However, the downside of using lower electron voltages is increased chromatic aberration and reduced depth of field⁷⁸⁰. Basically, HIM and SEM are comparable in function and application, so HIM can be considered complementary to SEM in the field of life science. However, compared to the SEM, HIM has some significant advantages: a larger depth of field, less sample damage, higher surface contrast (especially for light elements like carbon) and sub-nanometer image resolution. A particularly important advantage of HIM is the built-in charge compensation with an electron flood gun which allows for investigating non-conductive biological samples without having to coat them with a conductive layer. This is important as metallic coatings can alter and conceal nanoscopic sample features such as virus particles

or the cell membrane topography. FIB images can also be generated by the detection of back-scattered ions, to make material contrasts visible. However, He backscattering in a HIM is particularly well-suited as it provides sufficient back scattering yields and minimizes damage (see also Section II C). So far, this has rarely been used in the life sciences. However, Bidlack *et al.*¹⁶⁰ stated, that backscattered ion (BI) imaging could improve the visualization of immuno-gold labels in cells as they show the same contrast using the ETD. Ma *et al.*¹⁵⁹ used BI imaging to detect different concentrations of colloidal nanoparticles in cells.

a. Preparation of the specimen Since the sample requirements of HIM—samples should be dry and vacuum-compatible—are almost identical to those of electron microscopy, established protocols from SEM provide a good basis for HIM as well. In general the preparation involves 1) chemical fixation with aldehydes (e.g. formaldehyde or glutaraldehyde) 2) optional post-fixation with strong oxidising agents (e.g. osmium tetroxide), 3) dehydration in a graded series of an organic solvent (e.g. methanol, ethanol or acetone) and finally 4) drying (e.g. critical point drying). Instead of dehydration and drying of the sample, the application of ionic liquids has been proposed as an alternative⁷⁸¹ and successfully applied for imaging bacterial bio-films with the HIM⁷⁸². As mentioned before, because of the possibility to compensate charging in the HIM no metallisation of the sample surface is needed. This allows for analysing the sample in a more pristine state.

b. Viruses Sharma *et al.*⁷⁸³ investigated the interactions of viruses and their hosts in sediment and microbial mat samples. In the same manner, HIM has been shown to be a powerful tool to investigate bacteriophages (i.e. viruses that attack bacteria) and their interactions with their host cells. Both Leppänen *et al.*⁷⁸⁴ and You *et al.*⁷⁸⁵ published high-resolution HIM images of T4-phage infected *E. coli* bacteria and Vinner *et al.*⁷⁸⁶ visualized phage Felix O1 infected Salmonella bacteria. How those and other microscope images contributed to our understanding of bacteriophages was recently reviewed in more detail by Almeida *et al.*⁷⁸⁷. Frese *et al.*⁷⁸⁸ and Barreto-Vieira *et al.*⁷⁸⁹ recently reported the first visualization of SARS-CoV-2 virus particles by HIM, demonstrating significant topographical differences from previously published SEM images of sputter-coated samples. Looking ahead, the HIM could be used, for example, to examine phage-infected cells by milling inside them or to create 3D images by projections. In addition, the HIM can be used to better understand the spread of viral particles through other organisms, as it is possible to easily wash away, for example, lightly attached phages through the preparation.

c. Single-celled organisms HIM is an excellent tool for viewing single-celled organisms such as bacteria, archaea, yeast, micro-algae, protozoa and the like at a resolution close to that of TEM without having to embed and section the samples. In their 2013 paper Joens

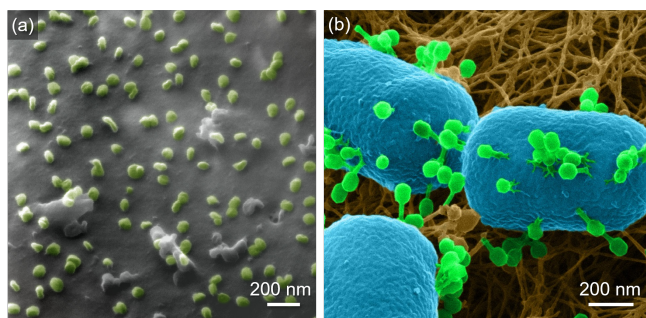


Figure 18. (a) SARS-CoV-2 virus particles on the cell membrane of a vero E6 cell. (b) T4-phage infected *E. coli* bacteria on a fibrous agar surface. (a) Copyright ©2021 Freese *et al.*⁷⁸⁸, distributed under the terms and conditions of the Creative Commons Attribution License.

*et al.*⁷⁸⁰ employed HIM for the first time for imaging of microbes, namely iron-oxidising bacteria. In particular for viewing bacteria on non-conductive surfaces with a strong topography, charge-compensation and large depth-of-field render HIM an excellent tool. The first HIM images of a culture of archaea were published by Chen *et al.*⁷⁹⁰ where HIM proved particularly useful for investigation of alleged cell budding of *Ca. A. ethanivorans*. Furthermore, HIM has been utilized by Said, Chatzinotas, and Schmidt⁷⁹¹ to image infections of bacteria with the bacterial predator *Bdellovibrio bacteriovorus*. Owing to its “large depth of field, the efficient charge compensation and strong edge contrast” HIM is particularly suitable for imaging biofilms which often show strong topography and tend to charge up under charged particle beams⁷⁸². HIM of bacterial biofilms was published by LeTourneau *et al.*⁷⁹² (rhizobacteria), by Belianinov *et al.*⁷⁹³ (*Geobacter sulfurreducens*) and Schmidt, Byrne, and Maasilta⁷⁸² (*Pseudomonas putida*). Further HIM studies on biofilms comprise imaging of microbial mats from hot springs in the Indian Himalayas by Sharma *et al.*⁷⁸³ and investigations of micro-algal biofilms with regard to architecture and phosphorus distribution by Moreno Osorio *et al.*⁷⁹⁴. Other potential applications of HIM imaging of microbiological objects include investigations of biofilms in different environments, for example on medical implants or in bio-reactors, to name a few. Furthermore, HIM will be an excellent technique to study phage-infection or predation by protists or bacteria in environmental bacterial biofilms. One can also perceive HIM investigations into the complex interplay of microbes with plants or fungi. A recent example of such a complex system is given by You *et al.*⁷⁸⁵ where HIM was used to analyse phage co-transport on hyphal-riding bacteria.

d. Cells, tissues, immuno-gold labelling To date, the HIM has been used in many studies to investigate whole cells and nanoscopic cell structures, including plant⁷⁹⁴, animal⁷⁹⁵ and human cells^{796,797}. In the study of nanoscopic cell structures, which are usually distorted

or obscured by metallic coatings, charge compensation allows visualization of topographical structures that would not be observable in SEM. For the first time, Schürmann *et al.*⁷⁹⁸ visualized lipid nanodomains in cell membranes of neurons, which were demonstrated to be concealed under a 10 nm gold coating. Sato, Sato, and Ogawa⁷⁹⁹ have shown that immuno-gold-tagged antibodies can be resolved within cells to identify specific organelles. For the first time, they demonstrated the detection of ionoluminescence from ZnO nanoparticles in biological specimens using HIM. When imaging animal nanostructures such as insect wings, the superior depth of field of the HIM has proven advantageous^{800,801}. Joens *et al.*⁷⁸⁰ demonstrated that the mouth cavity of a nematode can be dissected using the focused neon beam in HIM with minimal thermal damage to the cutting surface.

e. HIM in correlative workflows Besides structural analysis the life science applications also require tools for investigations into the chemical composition on the subcellular level. In general there are two possibilities to overcome the chemical blindness of the HIM. On the one hand detectors such as SIMS (cf. Subsection II C) can be installed directly on the tool and be used for in-situ correlative investigations as has been shown for *E. coli* cells incubated with TiO₂ nanoparticles¹⁵⁶. On the other hand HIM can be embedded into correlative work-flows with micro-analytical tools such as SIMS and EDS or fluorescence microscopy in combination with fluorescent markers (see also Section II F). A recently published example shows how HIM in correlation with the aforementioned techniques was used to analyse a resin-embedded soil sample with regard to roots, sediments, soil-organic matter and bacteria⁸⁰². In the future we expect to see applications of correlative microscopy with the HIM for instance to analyze bio-mineralization processes, to solve ecological questions in environmental microbiology, in plant- and soil science and many more. Owing to its possibility to image non-conductive samples almost destruction-free HIM may also become a central high-resolution technique in correlative workflows for structural and chemical analysis of biological specimens.

3. FIB-based tomography in the life sciences

Three-dimensional nano-imaging of biological objects has become more and more important with respect to, for instance, structural investigations into 3D cell-architecture, the ultra-structure of cell components, cell-to-cell interactions, analysis of tissues and the structure of bio-films, to name a few. Until the early 2000s investigations into the ultra-structure of micrometer-sized biological objects such as resin-embedded tissues or cells in three dimensions were carried out by serial block-face SEM⁸⁰³ or serial sectioning TEM⁸⁰⁴. Whilst a very high lateral resolution can be achieved by this approach, depth resolution is limited by the achievable thickness of the slices. Alternatively serial block-face SEMs with a mi-

rotome fitted into the analysis chamber can be used for tomographic imaging of resin-embedded samples. However, in this technique the depth resolution is also limited by the minimal thickness of the removed material.

With the advent of fine-focused ion beams (mainly Ga⁺-based), micro-tomography of biological objects made a great leap as it allows for better controlled and much finer removal of material from the blocks⁸⁰⁵. As one of the first examples of FIB micro-tomography, Balcerini *et al.*⁷⁶⁹ investigated the internal structure of yeast cells by *in-situ* FIB-sectioning followed by FIB-imaging using (negatively charged) secondary ions and secondary electrons. Soon thereafter the image resolution could be further improved by employing dual-beam FIB-SEM systems where the specimen is FIB-sectioned and electron-imaged. The use of oxygen ions from an PFIB seems to reduce curtaining and other artifacts, allowing the faster fabrication of smoother surfaces for the imaging step⁸⁰⁶. The basic workflow for FIB-SEM analysis of a resin-embedded biological specimen consists of repeated FIB-milling of a trench and SEM-imaging of the facet followed by 2D image-stack registration and finally 3D reconstruction as depicted in Figure 19.

In order to obtain sufficient contrast in the SEM images the sample is usually stained with heavy metals. Pioneering work was done by Drobne *et al.*⁸⁰⁸ who investigated the digestive system of a crustacean by FIB-SEM and discussed the possible imaging modes. In order to achieve better contrast, Leser *et al.*⁸⁰⁹ systematically investigated different OsO₄ and uranylacetate staining techniques and concluded that for plastic resin embedded samples the OTOTO method (OsO₄ / thiocarbonylhydrazide / OsO₄ / thiocarbonylhydrazide / OsO₄) in combination with back-scattered electron imaging provides best results. Other protocols involve a combination of potassium ferrocyanide, OsO₄ and uranylacetate and were successfully applied on brain⁸¹⁰ and bone tissue⁸¹¹ as well as for the investigation of the interaction of CNTs with lung tissue⁸¹². A detailed description of standard protocols for FIB-SEM on dried as well as plastic resin embedded (tissue) samples can be found in the work of Drobne⁸¹³. An alternative preparation method for FIB-SEM investigation of cells on surfaces does not require resin embedding and full impregnation but is based on thin layer plastification of the samples⁸¹¹.

It is well known that dehydration and embedding in plastic resins introduces artifacts and may destroy the ultra-structure of cell components. These can be partially avoided by high-pressure or plunge freezing of the sample followed by cryo-substitution of water and slow infiltration with an epoxy-resin. FIB-SEM imaging of the embedded sample, however, is then done at room temperature, as described, for instance, by Schmid *et al.*⁸¹⁴ for samples of the nitrate-reducing and iron-oxidising bacteria BoFeN1³. However, by the early 2000s it became

clear that the ultra-structure of cells could be preserved even better if full cryo-workflows, where a plunge- or high-pressure frozen specimen (still hydrated) is imaged at cryogenic temperatures, were employed. As a first step towards cryo-FIB-SEM Marko *et al.*⁸¹⁵ explored the possibilities of “thinning of vitreously frozen biological specimens for [...] TEM” by cryo-FIB milling of plunge-frozen water at different temperatures and concluded that A) the experiments will have to be done below −135 °C to avoid devitrification and B) that “FIB-milling of vitreous ice does not induce heating sufficient to cause devitrification”. In 2006, Heymann *et al.*⁷⁷⁷ published SEM data of plunge-frozen and FIB-milled yeast cells as well as SEM and TEM images of FIB-milled lamella of plunge-frozen tumor tissue. Although the frozen samples were not stained at all sufficient contrast for SEM imaging with secondary electrons was gained “by a combination of sublimation at the surface and metal deposition on the exposed surface”. Similar work was done by Hayles *et al.*⁷⁷⁸ who used a GIS system to deposit platinum onto frozen samples of yeast cells and a petal epidermis sample of *Nicotinia tabaccum*. A recent overview over techniques for “cryo-FIB-SEM cross-sectioning of frozen, hydrated life science samples” was published by Hayles and De Winter⁸¹⁶.

Another leap forward was the development of correlative confocal laser scanning and FIB-SEM tomography using fluorescent dyes, high-pressure freezing and cryo-substitution embedding⁸¹⁷ which has paved the way for promising 3D-correlative light-electron microscopy techniques. One of those is the location of protein complexes in living cells at ultra-high resolution. For that Gorelick *et al.*⁸¹⁸ developed the photon ion electron microscope (PIE-scope) which employs “integrated cryo-correlative light and FIB-SEM microscopy” and “enables direct and rapid isolation of cellular regions containing protein complexes of interest”. Another example is the recently published 3D-correlative workflow combining super-resolution light microscopy and FIB-SEM using reactive oxygen FIB spin milling to study embedded cultured cells⁸¹⁹.

Driven by questions in cell biology and connectomics, strategies have been developed to scan large volumes at high spatial resolution using FIB-SEM. For that, Xu *et al.*⁸²⁰ developed an improved FIB-SEM analysis technique with automated recovery from beam/system malfunctions that allowed them to image one third of a fruit fly’s brain at a depth resolution of 8 nm. In order to scan large volumes of hard materials such as bone heavier ions with stronger milling capacity can be used as demonstrated by Binkley *et al.*⁸²¹ who employed Xe-ions from a plasma source to obtain a tomogram of human bone by FIB-SEM.

³ This is the same culture as used by Joens *et al.*⁷⁸⁰ for HIM

imaging, see Section IV C 2 c

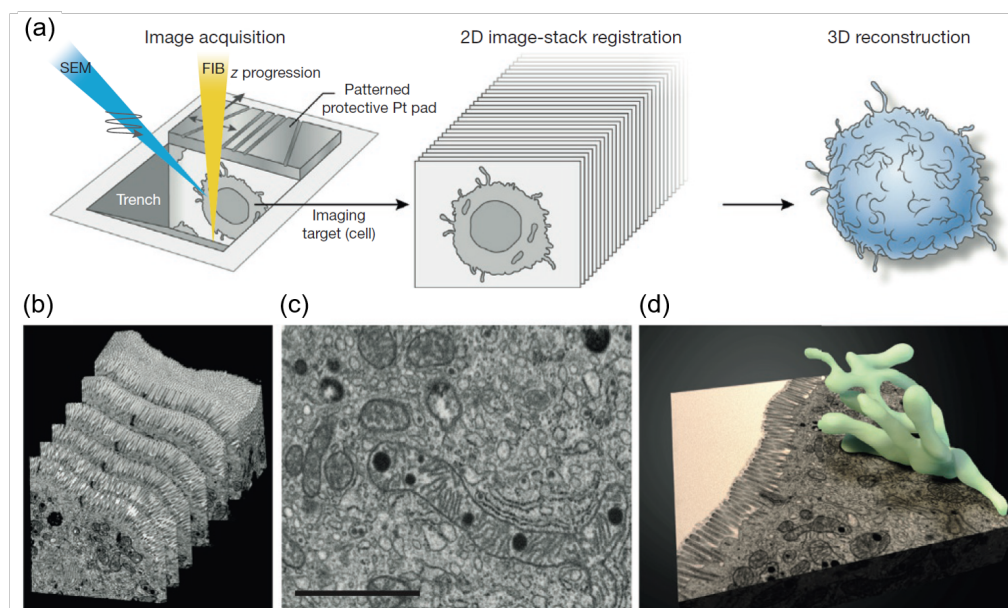


Figure 19. Illustration of the basic workflow for FIB-SEM: a) repeated FIB-milling of a trench followed by SEM imaging, image-stack registration and reconstruction reproduced from Narayan and Subramaniam⁸⁰⁵ b-d) Example of a mouse intestinal sample, reproduced from Hartnell *et al.*⁸⁰⁷

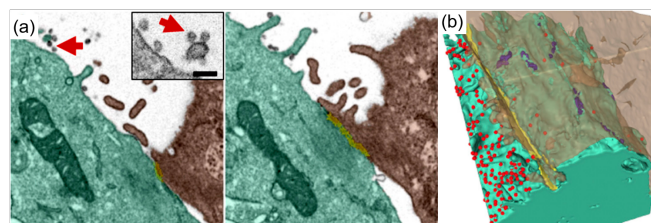


Figure 20. (a) FIB-SEM images of two 8 nm slices showing two contacted (yellow) Vero E6 cells (green, brown) and SARS-CoV-2 particles in the extracellular space (arrows). Inset scale bar: 200 nm. (b) 3D reconstruction of the plasma membranes of the two cells shown in (a). The junction-mediated contact between the cells is coloured in yellow. The virus particles are depicted in red and show a different density on either side of the junction. Data reproduced from Baena *et al.*⁸²².

In the context of the CoVid-19 pandemic FIB-SEM tomography proved a valuable tool to understand the microscopic mechanisms of the disease. Baena *et al.*⁸²² employed FIB-SEM to analyse how SARS-CoV-2 spreads from infected cells to new hosts as shown in Figure 20. Using a combination of TEM-tomography and FIB-SEM Cortese *et al.*⁸²³ were able to visualise morphological changes of SARS-CoV-2-infected lung cells. In a recent study on the frequently observed infection of the human kidney by SARS-CoV-2 FIB-SEM was used to image virus-particles in vacuoles⁸²⁴.

4. FIB-based tomography of energy materials

One of the very first applications of FIB tomography in energy materials research was presented by Wilson *et al.*⁸⁴³ in 2006. They investigated a solid oxide fuel cell anode based on yttrium stabilized zirconia (YSZ) and demonstrated how to separate the YSZ from the Ni and pore structure in a three-dimensional reconstruction of their sample. The presented detail of the 3D structure enabled them to quantify important structural features such as volume fractions, surfaces and even information about the so-called three-phase boundary.

In 2010, Ostadi *et al.*⁷⁷⁴ investigated a microporous layer (MPL) used in a hydrogen-powered proton exchange membrane fuel cell (PEMFC). FIB tomography was used to complement the X-ray tomographic investigations of the fuel cell electrode structure in order to record the nanostructure of the microporous layer (MPL), which can hardly be resolved with standard X-ray imaging equipment due to the limited spatial resolutions of $\approx 1 \mu\text{m}$ compared to FIB tomography ($\approx 10 \text{ nm}$). The porous MPL structure was reconstructed three-dimensionally and the porosity and pore size distribution analyzed. The obtained 3D data set were used as input for simulation of a single-phase flow through the MPL with lattice Boltzmann techniques.

In the same year Zils *et al.*⁸⁴⁴ have demonstrated how FIB tomography can be used to study fabrication-structure-properties relationships (i.e. how material manufacturing parameters are related to the 3D features in the structure). For the development of catalyst electrode materials for PEMFC, they compared the pore size dis-

Table VII. Overview of FIB based imaging and analysis in the life sciences.

	Application	Technique	Experiment
molecules	localisation of proteins	cryo-FIB-SEM HIM & LSM ToF-SIMS	protein-detection in vitrified HeLa-cells using gold-conjugated antibodies against RNA polymerase II ⁸²⁵ detection of quantum-dot labelled proteins ⁸²⁶ detection of proteins on DNA bio-sensor chip ⁸²⁷
	metabolic imaging	OrbiSIMS	imaging of the distribution of neurotransmitters in mouse hippocampus ⁸²⁸ 3D metabolic imaging of <i>Paramecium caudatum</i> using orbitrap-MS coupled to TOF-SIMS ⁸²⁹
virus- & nano-particles	virus imaging	HIM	imaging of bacteriophage-infection ^{783,784} , and transport by bacteria ⁷⁸⁵ imaging of SARS-CoV-2 infected vero-cells ^{788,830}
	nano-particle – cell interactions	FIB-SEM HIM HIM-SIMS ToF-SIMS	investigations into SARS-CoV-2 viral density at cell-cell contacts ⁸²² investigation of biogenic nanoparticles by HIM-SIMS ⁸³¹ 3D-imaging of nanoparticles in an algal bio-film ⁸³²
cell-level	imaging of microbial cells & 3D remodelling	HIM FIB-SEM cryo-FIB-SEM	Joens <i>et al.</i> ⁷⁸⁰ , Chen <i>et al.</i> ⁷⁹⁰ Ballerini <i>et al.</i> ⁷⁶⁹ , Drobne <i>et al.</i> ⁸⁰⁸ , Decelle <i>et al.</i> ⁸³³ Heymann <i>et al.</i> ⁷⁷⁷ , Hayles <i>et al.</i> ⁷⁷⁸
	imaging of mammalian cells	HIM	imaging of mitotic HeLa cells ⁷⁸⁰ , visualisation of lipid nanodomains in human neural stem-cells ⁷⁹⁸
	sub-cellular element mapping	nanoSIMS, ToF-SIMS PIXE	mapping of nitrogen/phosphorus ratio in a photosymbiotic <i>Acantharia</i> -microalgae system ⁸³³ elemental analysis of hair, skin, nervous tissue ⁸³⁴ identification of Ni-U-phosphate deposits in bacteria ⁸³⁵
	metabolic activity measurements	nanoSIMS	Musat <i>et al.</i> ⁸³⁶ , Calabrese <i>et al.</i> ⁸³⁷
	biomarker imaging of single cells	ToF-SIMS	Leefmann <i>et al.</i> ⁸³⁸
	bio-films	HIM	
	chemical analysis of bio-films	ToF-SIMS	Moreno <i>et al.</i> ⁸³⁹
	bacterial predators	HIM	imaging of the different stages of the life-cycle of <i>Bdellovibrio bacteriovorus</i> ⁷⁹¹
	geomicrobiology	HIM HIM & ToF-SIMS	imaging of iron-oxidising bacteria ^{780,840} iron corrosion by methanogens ⁸⁴¹
	bio-mineralisation	ToF-SIMS	Laufer <i>et al.</i> ⁸⁴²
anti-microbial properties of surfaces	HIM milling	investigation of the anti-bacterial properties of the nanostructures on dragonfly wings ⁸⁰¹	

tribution and porosity for different catalyst electrode materials and related the 3D structural features to the performance of the materials. Schulenburg *et al.*⁸⁴⁵ have used FIB tomography to study the degradation effects in the 3D structure of carbon based fuel cell electrodes after several start-stop cycles. They found a breakdown of the entire nanoporous structure, which could lead to a significant reduction in the supply of reaction gases to the catalyst. In combination with other (X-ray based) tomographic imaging techniques and structural modelling, FIB tomography can also be used for correlative tomographic imaging⁸⁴⁶ to fill in missing information at the nanometer scale and to produce multiscale 3D data covering structural features at a broad length scale. Zielke *et al.*⁸⁴⁷ have shown how FIB tomography can be used

to supplement the information missing in synchrotron tomography data due to the limited spatial resolution. The high-resolution 3D data obtained with FIB was used to create a structural model at the nanometer scale, which was used to fill the synchrotron data set with nanometer detail⁸⁴⁷. In a recent study Paulisch *et al.*⁸⁴⁸ used FIB tomography to analyze the complex three-dimensional path network inside silver gas diffusion electrodes (Figure 21). 3D data acquired with FIB tomography can also be used for mathematical modeling of 3D structures of energy materials⁸⁴⁹. The artificially computer created (modelled) 3D structures can be later used for the development of digital twins and for future virtual materials design.

Today, FIB tomography can be seen as an established

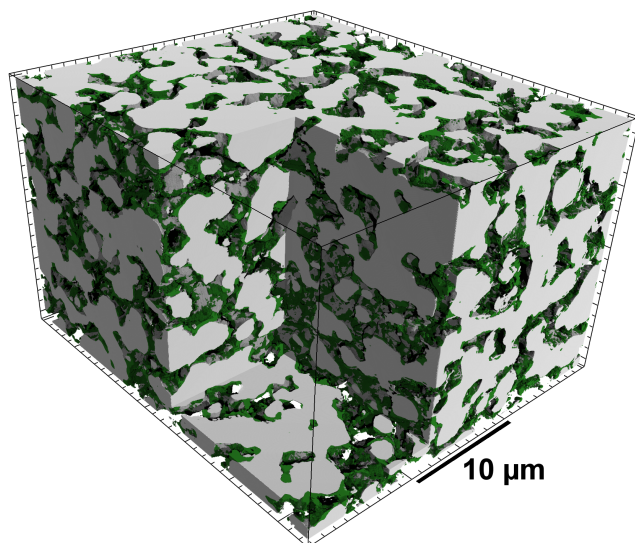


Figure 21. FIB tomography of a silver electrode: grey: silver gas diffusion electrode, green: binder/PTFE. Only the 3D image can reveal the complex paths inside the pore system (Paulisch *et al.*⁸⁴⁸)

tool for the study of materials in energy research, especially for battery materials^{850–860}, fuel cells^{861–864}, electrolyzers^{865–868} and catalytic materials^{869–872}.

FIB tomography is also useful to study materials that are relatively sensitive to ion beam damage. For example Dong *et al.* were recently able to resolve the inner structure of Lithium dendrites with FIB tomography⁸⁷³. The study revealed new details about the correlation between Li dendrite growth conditions and their 3D morphology. For such sensitive samples, cryo-FIB tomography has recently become increasingly popular as radiation damage can be significantly reduced at low temperatures^{873–876}.

5. Data processing of FIB-based tomographies

With the growing volume of data, the analysis of large tensors containing mostly grey scale information is becoming increasingly challenging. Sophisticated analysis requires data classification, i.e. assigning a class to each point. This is particularly challenging for FIB-based tomography, where a measurement contains a large number of classes, but in addition artefacts need to be detected and addressed.

Here, machine learning approaches, especially easy-to-use mostly random forest based tools such as Ilastik⁸⁷⁷ or the trainable Weka segmentation⁸⁷⁸, become more and more established for image annotation and classification.

One of the major issues in tomographic imaging of porous materials is the problem of separating the foreground from the background. If possible, pore infiltration using carbon-based resins is therefore carried out. Silicone-based resins are frequently used for energy mate-

rials due to their generally high carbon content⁸⁷⁹. Due to sample alteration or inaccessibility of pore systems, sample infiltration is often either impossible or undesirable. Thus, when the ion beam cuts through a pore, the electron beam always also illuminates the background of the pore. In such cases a 3D reconstruction can no longer be done in a simple way, because only the foreground around the pore edges of the samples represents the actual material distribution. To address this issue the optimized algorithm of Salzer *et al.*⁸⁸⁰ incorporates information from all sequentially measured layers, resulting in the first good reconstructions on suitable single phase porous samples. Meanwhile, numerous other techniques have been developed, resulting in better and more reliable results^{881–883}. Machine learning tools have recently been developed for this purpose^{884–886}. Osenberg *et al.*⁸⁸⁷ have shown a way to combine two different signals (In-Lens and back scattering) together with a machine learning algorithm to obtain better results for the separation of foreground and background in case of NMC battery electrode materials. However, despite much progress, the general problem is still not completely solved for all types of material structures.

6. Outlook

During the past twenty years FIB-SEM has become a well established technique for investigations into the three-dimensional structure of complex specimens, often with fully established cryo-workflows.

Further improvements in sample preparation and control of heat generation under the ion beam could enable precise nanometer-scale cutting with the ion beam to study the internal structure of biological samples, but also reduce artefacts in tomography of energy materials, as these may consist of fine and heat-sensitive components such as polymers.

In parallel, the ever growing and complex data volumes demand more and more automated analysis pipelines. To make this possible, standardised data and metadata formats are needed. The combination of standardised data sets and high quality individual image classifications, generated e.g. based on random forest models, would then allow for the compilation of diverse training sets to train deep learning models.

With sufficient training data, neural networks such as the U-Nets⁸⁸⁸ can be trained and applied to data that is very different from the original training set itself⁷⁷⁹.

On the instrument side, great progress has been made in increasing the accessible volumes in FIB-based tomographies through the use of plasma sources for heavy noble gases, especially xenon. Together with advances in automation of data acquisition and analysis, tomographies of cubic millimeter volumes with a spatial resolution of several 10 nm are now possible. Finally, complex data from different experimental sources with different lateral resolution and complementary information can be

made available to the research community in large multiscale atlases. This is celebrated in a particularly impressive way in the life sciences, where, for example, Ga FIB-SEM was used to map and reconstruct the connectome of the *Drosophila* fly brain^{820,889}. Also in terms of open data, life science offers the prime example with the virtual fly brain⁸⁹⁰ and the fly brain atlas⁸⁹¹, a digital twin of *Drosophila*'s brain combining huge amounts of data from different sources and methods in an easily accessible way. Creating and analyzing such massive data in an automated way is based on the rapid development of machine learning, which will be one of the key factors for the future evolution of FIB technologies.

D. Elemental Analysis using SIMS

While many correlative imaging approaches—mostly based on FIB-SEM instruments—do exist, SIMS in the FIB is the only relevant ion beam based analysis method used to date. However, the combination of SIMS and FIB is also often found in dedicated SIMS instruments^{892,893}. These implementations may provide better SIMS performance (mass resolution, sensitivity, ...) due to the use of—often two—dedicated FIB beams and a highly optimized mass spectrometer but lack the versatility that a FIB instrument equipped with a SIMS add-on can provide. Today GFIS based FIB instruments provide the highest spatial resolution for SIMS applications^{83,894}. However, recently also a LOTIS based FIB-SIMS instrument has been introduced⁸⁹⁵.

1. Overview

SIMS consists in irradiating the sample with a finely focused beam of ions (the so-called primary ions) and extracting, mass-filtering and detecting the ions sputtered from the sample surface (the so-called secondary ions). SIMS is a powerful technique for analysing surfaces owing in particular to its ability to detect all elements from hydrogen (H) to uranium (U), its excellent sensitivity, its high dynamic range and its ability to differentiate between isotopes. SIMS offers four main analysis modes, namely mass spectrum acquisition, depth profiling, 2D imaging and 3D imaging. In addition, SIMS does not require any complex sample preparation (in contrast to techniques such as EDS or electron energy loss spectroscopy (EELS) performed on TEM or APT).

Therefore, equipping FIB-based instruments with a SIMS system adds unique analytical capabilities for 3D chemical characterisation. Furthermore, the availability of SIMS on FIB instruments offers unique workflows for multimodal analytics by correlating the SIMS data with other imaging/analytical techniques available on these FIB platforms (e.g. SE-imaging, EDS, EBSD, etc.).

2. Applications in materials science

SIMS on FIB(-SEM) instruments has been applied to a number of topics in materials science, in particular for the nano-characterization of complex 3D architectures and compositions. Microelectronic devices are a typical example in this context, where 2D or even 3D SIMS imaging provide the required information with unique lateral and depth resolution⁸⁹⁶. Figure 22 shows as an example a 3D analysis of a fin field-effect transistor (FinFET)⁸⁶. The spatial resolution of this 3D SIMS map obtained with a magnetic sector SIMS system installed on a HIM is better than 15 nm. Such 3D maps can be used for end pointing and circuit editing applications.

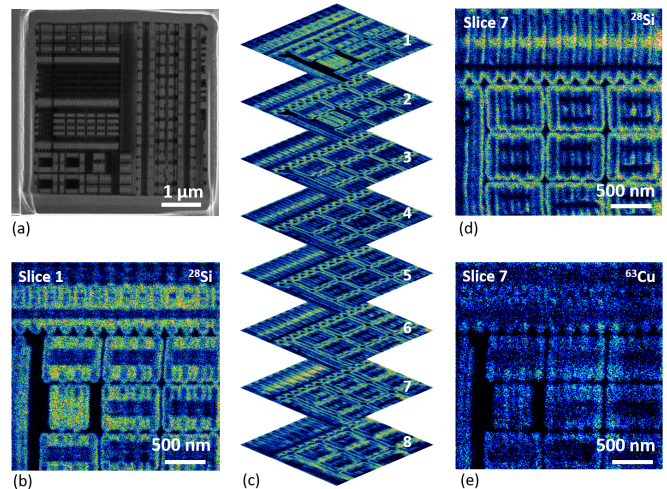


Figure 22. SE and SIMS images of a FinFET obtained on a HIM equipped with a magnetic sector SIMS system. The SE image was taken with a 25 keV He^+ beam (a) and the SIMS images of the ^{28}Si and ^{63}Cu were acquired with a 20 keV Ne^+ beam (b to e) in the zone identified by the white square on the SE image (a). Eight successive SIMS images (noted 1 to 8, (c)) were taken on the same area (FOV $3\ \mu\text{m} \times 3\ \mu\text{m}$) allowing to determine the 3D composition of the FinFET. Image (b) corresponds to the top surface (first slice) and the images (d) and (e) correspond to the 7th slice; reproduced from⁸⁶

There are also a number of examples where FIB based SIMS has been used as a major asset in the development of technologies in the fields of photovoltaics and battery materials. The latest advances in photovoltaic conversion technologies are based on thin films, whether second generation, such as copper indium gallium selenide (CIGS), or third generation dye-based, such as lead halide perovskites, and their development requires a very comprehensive understanding in order to correlate structure and chemical composition with performance and ageing. FIB based SIMS studies allowed addressing many questions related to the chemical heterogeneity of grains⁸⁹⁷ and grain boundaries^{97,898}, precipitation of secondary phases (e.g. PbI_2), or chemical and structural modification at the interfaces with charge-collecting electrodes⁸⁹⁹⁻⁹⁰¹. These optimizations have helped realize new photovoltaic

cells with an efficiency approaching 25%.

In batteries, SIMS technology allows the detection of lithium (in addition to any other elements of interest) with a very high sensitivity. Therefore the Li gradient can be mapped over several orders of magnitude and at highest spatial resolution across the different surfaces and interfaces in batteries^{97,151,902–906}.

Further examples of application of FIB-SIMS in materials science include petroleum based polyolefin plastics⁸⁸, polyester and melamine resins⁹⁰⁷, the investigation of alloys and superalloys^{908–910}, the study of nanoparticles^{911–914}, the investigation of chemical inhomogeneities in grain sizes between 50 nm and 200 nm in Delafossite materials⁹¹⁵, oxygen diffusion in grain boundaries⁹¹⁶ the distribution of rare earths in optical fibres^{917,918} and characterizing thin films^{150,919}.

3. Applications in life sciences

Ion-microscopy has been used for chemical micro-analytics and imaging of biological specimens since the 1970s when high-energy PIXE was found to be a valuable application of ion-beams to determine trace elements in tissue section⁹²⁰. By the beginning of the 1990s accelerator-based proton beams could be focused down to 1 μm and were ready for elemental mapping of trace elements in biological specimens⁸³⁴. The development of high-brightness LMIS in the second-half of the 1970s³¹ also allowed for introducing medium-energy (<100 keV) ion-beam microprobe-techniques to bio-imaging and micro-analysis; in particular in the field of SIMS^{921,922}. Already at that time it turned out that SIMS is advantageous for biological applications because of its low detection limits but also its sensitivity to different isotopes of chemical elements.

Hence, In the life sciences numerous exciting studies based on imaging SIMS exist⁹²³. For example, FIB-SIMS has been used to study the spatially resolved chemical signatures of the surface and the interior of mammalian individual cells⁹²⁴ and bone tissue⁹²⁵. The Cameca nanoSIMS—a sector-field secondary ion mass spectrometer with about 50 nm lateral resolution—is an important tool for sub-cellular chemical and isotopic micro-analysis in the analytical toolbox of the life sciences⁹²⁶. It was designed to achieve a mass resolution high enough to detect the stable isotopes of elements such as carbon and nitrogen (¹³C and ¹⁵N) which are commonly used for isotope-labelling experiments⁸³⁶. Furthermore, time-of-flight mass spectrometer based SIMS techniques for 2D and 3D imaging are becoming increasingly important in the life sciences^{794,923}. Metabolic imaging on a sub-cellular level and a mass-resolution of 240,000 was recently achieved by combining TOF-SIMS with an orbitrap mass-analyzer⁸²⁸. It was the application of gas field-ionization source that allowed to focus ion beams to sub-nanometer spots. HIMs equipped with SIMS spectrometers are not chemically-blind anymore and provide a new

possibility to study bio-mineralisation processes such as tooth or bone formation as well as microbial corrosion, and many others in FIB-SIMS. Being implemented in the scanning helium ion microscope this technique paved the way for numerous high-resolution analyses of micro-organisms, viruses, cells, small animals, plants etc.⁷⁸². The development of SIMS spectrometers for the HIM not only added micro-analytical capabilities to the HIM but also significantly improved the lateral resolution of SIMS in general.

Recent examples of such applications include the localisation and identification of silver nanoparticles and nanowires in intestinal or alveolar cell cultures^{912,927} and the characterisation of biogenic nanoparticles produced by bacteria⁸³¹.

A recently developed GFIS based variant of the standard HIM enables correlative imaging using SE, STIM¹⁰⁹, and SIMS signals¹⁵⁶.

This was used to perform a correlative SE, STIM¹⁰⁹ and SIMS investigation of thin tissue sections of *Daphnia magna* exposed to TiO₂ nanoparticles (Figure 23)¹⁵⁶. In this nano-toxicological test study the machine demonstrated excellent contrast on biological structures as well as on the incorporated inorganic nanoparticles, e.g. the particles were shown to accumulate in the gut without penetration of the epithelial barrier¹⁵⁶.

In future one may anticipate novel SIMS approaches for biological questions. On the one hand the very high mass resolution of OrbiSIMS does allow for chemical micro-mapping of complex bio-molecules in cells and tissues, albeit with a very limited lateral resolution in the μm range. On the other hand LOTIS systems provide high brightness ion beams with extremely low spot sizes that enable high speed SIMS at high sensitivity such that relatively large volumes of biological samples can be chemically mapped.

Considering the prospects offered by novel highest brightness ion sources delivering reactive species such as Cs⁺ and cryo-capabilities on the FIB platforms, one of the most exciting applications of FIB based SIMS in life sciences will become subcellular imaging, allowing for instance the investigation of accumulations of metals, ingulfed nanoparticles or drugs in the different cellular structures.

FIB-SIMS providing high spatial resolution analytical and structural data can be a valuable tool in various fields beyond materials and life sciences, such as soil science⁹²⁸, geology⁸⁷ and cosmochemistry^{929,930}. It has been also used for the analysis of cultural heritage objects^{931–933}.

4. Outlook

Elemental analysis using FIB-SIMS can still continue the trend towards even higher lateral and spatial resolutions. The resolution is no longer mainly limited by the pure beam size. In HIM, lateral resolution is mainly limited by the low signal yield and destructive nature

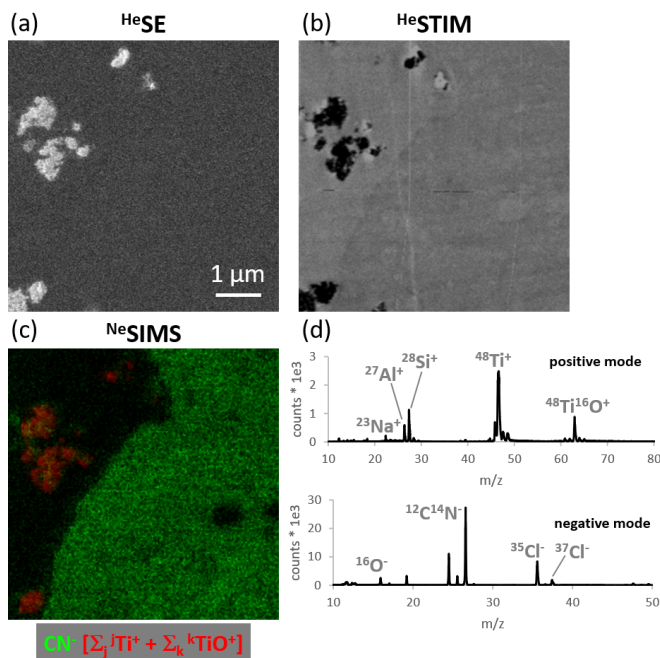


Figure 23. npSCOPE correlative high resolution imaging and nano-analytics on keratinocyte cell cultures exposed to 30 nm Si-Al-TiO₂ nanoparticles. (a) SE imaging (HeSE), (b) HeSTIM bright field imaging, (c) SIMS false color image of CN (green) and Ti-species (red), (d) SIMS spectrum (NeSIMS). SE: FOV 15 × 15 μm, (1024 × 1024) pixel, dwell time 1 μs; STIM: FOV 8 × 8 μm, beam current 2 pA, dwell time 400 μs, (512 × 512) pixel; SIMS negative mode: FOV 8 × 8 μm, magnetic field 300 mT, dwell time 9000 μs, (256 × 256) pixel; SIMS positive mode: FOV 8 × 8 μm, magnetic field 325 mT, dwell time 4000 μs, (256 × 256) pixel.

of SIMS. To obtain the smallest possible detection limits, as much signal as possible must be extracted from the sputtered volume. One possibility is the use of other projectile ions which achieve a higher useful yield of sputtered ions. However, most ions only achieve a higher yield of either positive or negative ions. Higher yields of positive ions, which are particularly suitable for the detection of metal elements, are achieved by projectiles on ions with high electro-negativity such as oxygen or halogen ions. Future developments could therefore be achieved by smaller spot sizes from plasma FIBs or the use of ILIS for FIBs. Higher yields of negative ions are achieved by using projectiles that lower the work function of the sample surface. Recent developments in the direction will already be possible in the near future by using SIMS spectrometers on FIBs using LOTIS⁸⁹⁵. Alternatively, the use of precursor gases could also increase the yield of ions.

One obvious approach to increase the ion yield and therefore also the spatial resolution is to further develop SNMS for FIBs. A major drawback of SIMS is the difficult quantification due to the matrix effect. The use of lasers for post-ionization reduces the dependence of the ionization process at the sample surface to controlled,

sample-independent ionization by photons. Due to the required high laser intensity, SNMS is only possible in pulsed operation. This inevitably requires pulsing of the primary ion beam. For this reason, a combination with TOF spectrometers is advantageous and obvious. Post-ionization with focused electron beams is also conceivable, although experimental preliminary work in this area remains rare.

Another problem of elemental analysis in FIBs is the sample intermixing behavior from the primary ions used. To achieve the highest possible beam resolutions, comparatively high energies in the range of 20 keV to 50 keV are typically used. The high energy has the disadvantage of a long range of ions in the target compared to low energy argon, which is commonly used for depth profiling with SIMS. This quickly leads to mixing of deeper layers and therefore to decreasing depth resolution with increasing sputter depth⁹³⁴. High spatial resolution could be achieved in the future by using projectile ions with high atomic number and/or small projectile energy per nucleon. Cs from LOTIS FIBs or Xe from GFIS FIBs could provide both small beam sizes and good depth resolutions. Alternatively, the energy per nucleon is also reduced by using cluster ions such as bismuth or gold clusters from LMAIS.

Small cluster ions⁹³⁵, reactive projectile ions, or laser post-ionization can also reduce fragmentation of molecules—another aim for future developments. The fragmentation of molecules would need to be understood both theoretically and experimentally in order to deduce the molecular composition of the sample from measured spectra. The creation of molecular fragmentation databases for typically used ion energies and projectiles would enable fingerprinting in the future.

Another focus is of course the further development of spectrometers. Important is the complete detection of all sputtered ions which is currently already possible by the use of TOF spectrometers or magnetic sectors with large area MCP. A possible further development would be the combination of fib with spectrometers that can separate isobars. The results already shown with Orbitraps, for example, are very promising⁸²⁸.

What has already been shown individually, in the perfect machine all parameters such as spatial resolution, mass resolution, detection limit as well as measurement time should be optimized simultaneously. In addition, an in-situ combination of elemental analysis in the FIB with other, for example, electron beam-based analytical methods would be beneficial. The combination with focused electron beams would also be possible for charge compensation of insulating sample surfaces. In-situ AFM would allow the correlation of the acquired signal versus fluence with true sputtering depths. The reconstruction of measured signals from three-dimensional volumes will continue to be a very difficult task in the future, which could be facilitated by the use of electron beams and AFM.

Last but not least, most element analysis methods like

SIMS require vacuum levels better than ultra-high vacuum (UHV) in the FIB. This is a prerequisite that is not always given so far and that should be considered by all manufacturers in the future because of its high relevance.

E. Applications of gas-assisted FIB processing

Direct bottom-up writing of nanostructures with a focused ion beam is powerful, flexible, and conceptually simple, but at the same time extremely complex in the chemical and physical processes involved. In addition to the surface processes and electron-driven chemistry that also occur in direct writing with electron beams, competition with physical sputtering, and thermal or ion-induced structural changes contribute here to the shape and microstructure of the deposit. Hence, FIBID strongly depends on multiple growth conditions such as ion species, acceleration voltage, ion beam current, ion dose, beam dwell time, scanning strategy, substrate type (insulating or conductive), GIS nozzle position, precursor molecule (vapour pressure, sticking coefficient to the surface, residence time, non-hazardous), precursor temperature, base and process pressure in the vacuum chamber among others. This makes FIBID of functional nanostructures highly dependent on the experience of the particular user and calls for both, better theoretical understanding and empirical modeling tools that generate patterns based on few calibration routines, thus enabling also less experienced users to fabricate complex nanostructures. Table VIII provides an overview on the fields where gas-assisted FIB processing has been employed so far.

1. Basics of ion-induced chemistry

Ion-molecule reactions have been studied in the context of FIBID, which involves decomposition of the precursor on the substrate surface during ion bombardment. In FIBID of metal nanostructures from organometallic precursors, the deposited material is composed of the metal(s) and contamination from nonvolatile ligand-derived decomposition byproducts. Ion-induced chemistry during FIBID is only partially understood but has been postulated to involve ion-molecule collisions with the precursor, reactions with low energy secondary electrons produced by impact of ions with the substrate, and thermal processes driven by dissipation of collision energy (see also Figure 14).^{396,995} An additional feature of FIBID is the concomitant sputtering of material from the surface that competes with deposition. Although preferential sputtering of ligand-derived atoms can purify the material under appropriate conditions,^{413,996} etching of the metal will also occur and the choice of reaction conditions is critical to obtaining deposits with high metal content. Broad application of FIBID will require development of custom precursors that undergo well-understood and efficient ion-induced decomposition

to metal atoms and volatile byproducts. In addition to the standard physical properties common to all deposition methods that involve gas phase delivery of reactants to the substrate (volatility, thermal stability, ready availability, etc.), mechanism-based design^{995,997} of FIBID precursors will require a fundamental understanding of ion-molecule reactions on the surface. Much of the current understanding of these processes comes from model studies of FIBID carried out by ion bombardment of a few monolayers of precursor molecules on a substrate in ultra-high vacuum (UHV)^{995,997}. Although there are differences between FIBID and its UHV models (the UHV environment is cleaner than standard HV FIBID deposition conditions, the UHV studies are carried out at lower temperatures, and the ion source is more diffuse), UHV studies can be used to identify ligands that dissociate from the complex and ultimately desorb cleanly from the surface during ion-molecule reactions. Purification of deposits by sputtering away ligand-derived contaminants can also be modeled in UHV. Additional mechanistic information has been obtained in gas phase studies of ion-molecule collisions between organometallic precursors and ions of different masses and energies⁹⁹⁸.

As an example, a study of the reactions of $\text{Ru}(\text{CO})_4\text{I}_2$ with 860 eV Ar^+ ions on a surface in UHV demonstrated that the initial reaction was loss of all four CO ligands to form adsorbed RuI_2 ⁴¹³. Additional ion exposure resulted in sputtering of iodine from the surface at a rate five times faster than sputtering of Ru. These results suggest that proper optimization of FIBID conditions could result in deposition of high metal content Ru from this precursor. This study also highlights the difference in the charged-particle induced reactivity between FIBID and FEBID, as modeling of the FEBID process in UHV with 500 eV electrons results in loss of the CO ligands, but not the iodide, to afford RuI_2 as the final product⁹⁹⁹. Rapid loss of all of the carbonyl ligands was also observed upon ion bombardment (860 eV) in a UHV model study of the heterobimetallic precursor $(\eta^5\text{-C}_5\text{H}_5)\text{Fe}(\text{CO})_2\text{Re}(\text{CO})_5$ ⁹⁹⁶. In contrast to the electron-induced chemistry of this complex under the same conditions, the ion beam slowly removed the remaining carbon from the cyclopentadienyl ligand by sputtering, leaving behind non-stoichiometric Fe/Re material.

Additional information on ion-molecule reactions was obtained during studies of FIBID of gold from $(\text{CH}_3)_2\text{Au}(\text{hfac})$ (hfac = hexafluoroacetylacetonate) with He^+ , Ne^+ , Ar^+ , Kr^+ , or Xe^+ at energies of 2 keV to 100 keV^{414,1000}. The decomposition yield from the precursor increased with increasing ion mass and energy, consistent with a binary collision model for decomposition. The authors concluded that the FIBID process was driven by energy deposition from ion-surface collisions. These results have implications for ion source choice in FIBID, because the mass variation in ions impacts the deposition chemistry through differences in secondary electron yields, sputter yields and ion implantation yields. Ar^+ and Ne^+ generate sufficient secondary

Table VIII. Overview of applications of gas-assisted FIB-processing, in which gaseous precursor compounds are locally dissociated by the ion beam to grow nanostructures.

Property	Target Application	Ion	Deposit Geometry & Precursor
Electrical & electronic	Electrical connections	He	semiconducting nanowires from CpPtMe ₃ ⁹³⁶ , metallic Co lines from Co ₂ (CO) ₈ ⁹³⁷
		Ne	metallic nanowires from CpPtMe ₃ ⁹³⁶
		Ga	conducting nanowires from CpPtMe ₃ ^{938,939} and MeCpPtMe ₃ ⁹⁴⁰⁻⁹⁴² , C ₇ H ₇ F ₆ O ₂ Au ^{943,944} , Co(CO) ₃ NO ⁹⁴⁵ , C ₁₀ H ₁₃ CuF ₆ O ₂ Si ⁹⁴⁶ ; W(CO) ₆ contacts to Co and Cu nanowires ⁹⁴⁷⁻⁹⁴⁹ , Pt based sidewall contacts using MeCpPtMe ₃ to MoSi layer stack ⁹⁵⁰
	Insulating barriers	Si	thin layer from tetramethoxysilane (Si(OCH ₃) ₄) ⁹⁵¹
		Ga	thin layer from tetramethoxysilane ^{952,953} and pentamethylcyclopentasiloxane ⁹⁵⁴
	Superconductivity		He
		Ga	planar nanowires W(CO) ₆ ⁹⁵⁹⁻⁹⁶⁹ and Nb(NMe ₂) ₃ (N- <i>t</i> -Bu) ^{970,971} , arrays of JJs from Nb(NMe ₂) ₃ (N- <i>t</i> -Bu) ⁹⁷² , 3D SQUID from W(CO) ₆ ⁹⁷³ , WC nanoSQUID ⁹⁷⁴
Magnetic	Nanomagnets	He	nanowires from Co ₂ (CO) ₈ ⁹³⁷
		Ga	nanoparticles from Co ₂ (CO) ₈ ⁹⁷⁵ , nanowires from Co(CO) ₃ NO ⁹⁴⁵ and from Co ₂ (CO) ₈ ⁹⁷⁶
	Tips for magnetic force microscopy Nanomagnetic probes	Ga	deposition of thin layer by milling Co ₇₁ Cr ₁₇ Pt ₁₂ target ⁹⁷⁷
		Ga	filling FIB milled trenches with tungsten ⁹⁷⁸ , Hall-probes from Co ₂ (CO) ₈ ⁹⁷⁹
Optical	Photonic cavities / waveguides	Ga	deposition of defects in etch mask for photonic crystal ⁹⁸⁰
	Fresnel zone plates	Ga	Deposition of the central Pt beamstop ⁴⁸⁰
	Chiral photonic nano-antennas	Ga	helices from MeCpPtMe ₃ ⁹⁸¹⁻⁹⁸³ and from phenanthrene ⁹⁸⁴
	Chiral plasmonic nano-antennas	Ga	helices from phenanthrene covered with gold ^{985,986}
	Chiral biosensing	Ga	helix arrays from MeCpPtMe ₃ coated with poly- <i>o</i> -phenylenediamine ⁹⁸⁷
Mechanical	AFM tips	He	hammerhead probes from MeCpPtMe ₃ ⁹⁸⁸
	Tunable elastic moduli	Ga	core-shell pillars and springs from phenanthrene ^{989,990} metal containing pillars and springs from phenanthrene and ferrocene ⁹⁹¹ , MeCpPtMe ₃ ⁹⁹² , W(CO) ₆ ⁹⁹³ , tetramethylcyclotetrasiloxane (TMCTS) and oxygen (O ₂) ⁹⁹⁴

electrons at low beam energies (30 eV) but have a shallower beam penetration depth than He⁺, leading to lower ion-substrate interactions. Heavier ions have higher sputtering yields, which can remove light atom impurities but at the cost of deposition rates, as the target material will also be sputtered away^{53,1001}.

Gas phase studies of reactions of Fe(CO)₅ with He, Ne, Ar and Kr ions of varying charge and energy⁹⁹⁸ also demonstrated facile loss of CO ligands upon ion-molecule collision. The distribution of fragment ions from CO loss, Fe(CO)_{5-x} where x=1 to 5, was dependent on the ion mass and the energy transfer in the collision. Under these conditions, light ions such as He⁺ resulted in electronic excitation with low fragmentation efficiency. Heavier ions yielded more extensive CO dissociation from energy transfer and nuclear stopping. The highest extent of CO loss occurred upon collision with Ne⁺, where both electron transfer and energy transfer were significant. It was pointed out that the gas phase results may not accu-

rately predict behavior on a surface during FIBID due to the heat sink behavior of the substrate. However, more efficient fragmentation upon impact with heavier ions is to be expected. Although there is not yet an extensive set of privileged ligands for FIBID, some preliminary conclusions about ion-molecule chemistry of organometallic precursors on substrate surfaces can be drawn from the mechanistic studies described above:⁹⁹⁵ 1) to minimize ligand-derived contamination in deposits, ligands should be small and few in number; 2) CO ligands can be removed quite easily by ions; 3) halide ligands can be removed by sputtering, but more slowly than CO; 4) carbon derived from anionic π -facial ligands such as cyclopentadienyl and allyl can be removed by sputtering but it is also slow and competes with removal of metal.

Table IX. Overview on various precursor ion combinations and the resulting electrical properties.

Material	Precursor material	Ion	Shape	Composition (mol %)	Microstructure	Electric behavior	ρ_{RT} ($\mu\Omega$ cm)	ρ_{RT} bulk ($\mu\Omega$ cm)	Ref.
Platinum	MeCpPtMe ₃	Ga ⁺	planar	Pt:C:Ga:O 22:60:11:7	5–10 nm sized nanocrystals	Metal	700	10.4	941
	CpPtMe ₃	Ga ⁺	planar	Pt:C:Ga:O 46:24:28:2	Amorphous	Metal	70–700		940
	MeCpPtMe ₃	Ga ⁺	planar	Pt:C:Ga 17:72:11	≈3 nm sized nanocrystals	Metal	800		942
	MeCpPtMe ₃	Ne ⁺	planar	Pt:C 17:83	≈4.5 nm sized nanocrystals	Metal	600		936
	MeCpPtMe ₃	He ⁺	planar	Pt:C 16:84	≈3 nm sized nanocrystals	Semiconductor	180000		936
Gold	C ₇ H ₇ F ₆ O ₂ Au	Ga ⁺	planar	Au:C:Ga 50:35:15	—	Metal	500–1500	2.4	943
	C ₇ H ₇ F ₆ O ₂ Au	Ga ⁺	planar	Au:C:Ga:O 75:<5:20:<5	—	Metal	500–1300		944
Cobalt	Co ₂ (CO) ₈	Ga ⁺	planar	—	—	Metal	189	6	975
	Co ₂ (CO) ₈	Ga ⁺	planar	—	amorphous	Metal	19–38		976
	Co(CO) ₃ NO	Ga ⁺	planar	Co:C:Ga:N:O 54:7:9:13:17	>20 nm sized nanocrystals	Metal	189		945
	Co ₂ (CO) ₈	He ⁺	planar	—	6 nm sized nanocrystals	Metal	64–116		937
Copper	C ₁₀ H ₁₃ CuF ₆ O ₂ Si	Ga ⁺	planar	Cu:C 55:45	20 nm sized nanocrystals	Metal	50	1.7	946
Tungsten	W(CO) ₆	Ga ⁺	planar	W:C:Ga 40:40:20	Amorphous	Superconductor below 5.2 K	200	5.6	959,960
	W(CO) ₆	Ga ⁺	planar	W:C:Ga:O 40:43:10:7	1–2 nm sized nanocrystals	Superconductor below 4.2–5.1 K	275		967
	W(CO) ₆	Ga ⁺	planar	W:C:Ga:O 53:34:11:2	≈1 nm sized nanocrystals	Superconductor below 5–5.5 K	100–350		964
	W(CO) ₆	He ⁺	3D	W:C:O 72:20:8	20–30 nm sized nanocrystals	Superconductor below 6.2–7.1 K	398		955–957
Niobium	Nb(NMe ₂) ₃ (N-t-Bu)	Ga ⁺	planar	Nb:C:Ga:N 29:43:15:13	15–20 nm sized nanocrystals	Superconductor below 5.0 K	550	15	970
	Nb(NMe ₂) ₃ (N-t-Bu)	Ga ⁺	3D	—	15–20 nm sized nanocrystals	Superconductor below 8.1 K	380		970

2. Nanostructures for electronics

The ease to directly write functional structures with different conductivity regimes render FIBID a powerful tool in electronic applications. At least three different electric conductivity regimes are reported for materials grown using FIBID: semiconducting, metallic and superconducting at low temperature. In this regard, semiconducting and metallic platinum (Pt), gold (Au), cobalt (Co) and copper (Cu) based deposits were grown using a variety of precursor compounds (cf. Table IX) mostly under use of Ga ions. Thus, Ga⁺ FIB is the ionic species used in the process when no other is mentioned. As the actual content of carbon as well as the micro-structure

of the deposit depends on the actual growth conditions, this offers an efficient way to tune electrical and electronic behavior. Examples include Pt⁹⁴¹ and Au^{943,944} for which the conductivity increases with thickness for the as-grown material. Pt-based deposits below 50 nm in thickness behave as semiconductors; for 50 nm in thickness and above, they behave as metals⁹⁴⁰ (reaching the threshold of 3000 $\mu\Omega$ cm for metallic conduction¹⁰⁰²) with metallic content <33 at % and exhibiting fcc Pt nanocrystals with diameters from 5 nm to 10 nm embedded in an amorphous carbon matrix⁹⁴². Additionally, using Ne⁺ FIB, Pt deposits behave as metals whereas they behave as semiconductors using He⁺ FIB⁹³⁶. In the case of gold-based deposits, its high gold content (75 at. % Au) allows

obtaining metallic deposits with ρ_{RT} around $500 \mu\Omega \text{ cm}$ but still two orders of magnitude above the bulk resistivity.

As-grown^{975,1003} and annealed⁹⁴⁵ Co deposits (50 at % Co) are ferromagnetic with $\rho_{RT} = 189 \mu\Omega \text{ cm}$ and $62 \mu\Omega \text{ cm}$ (ρ_{RT} Co bulk = $6 \mu\Omega \text{ cm}$), respectively. Using He^+ FIB, metallic Co 10 nm-wide lines were grown with similar ρ_{RT} values⁹³⁷. Cu deposits behave as metals with 55 at % Cu and 20 nm-sized crystals embedded in an amorphous C matrix and their conductivity increasing with the ion beam current⁹⁴⁶.

Other interesting materials deposited with FIBID exhibited metallic behavior at room temperature, while at low temperature they transitioned to the superconducting state. This is the case for superconducting tungsten (W) and niobium (Nb) based nanostructures grown using $\text{W}(\text{CO})_6$ and $\text{Nb}(\text{Nme}_2)_3(\text{N}-t\text{-Bu})$ as precursor materials, respectively. Particularly, WC- and NbC- deposits behave as superconductors below 4.2 K to 5.1 K^{959,960,964,967} (T_c W bulk = 15 mK) and 5 K⁹⁷⁰ (T_c Nb bulk = 9.7 K), respectively.

On the other hand, freestanding 3D NbC nanowires exhibit a broadened superconducting transition between 4 K and 11 K. The composition is around 40 at % to 50 at % W for WC deposits, and 29 at % Nb for NbC deposits and their microstructure has short-range order (1 nm-sized crystals) for the former and 15 nm to 20 nm-sized crystals of fcc NbC phase for the latter. It is worth mentioning that reasonably high values of the superconducting parameters are found for WC nanostructures, such as the upper critical magnetic field $B_{c2}(2\text{K}) = 7 \text{ T} - 8.5 \text{ T}$ ^{965,967} and critical current density $J_c(2\text{K}) = 0.01 \text{ MA cm}^{-2} - 0.1 \text{ MA cm}^{-2}$ ^{959,961-963,967}. For narrower nanostructures ($\leq 50 \text{ nm}$ in width), finite size effects which are key to their application to superconducting circuits, have been studied. This includes a magnetic field-driven reentrance of the superconductivity⁹⁶⁶, the occurrence of non-local voltages^{968,969}, and electric field-induced control of superconductivity⁹⁵⁸. He^+ FIB enabled the growth of fancied shaped 3D WC nanosuperconductors with outstanding capabilities ($T_c = 6.2 \text{ K} - 7.1 \text{ K}$, $B_{c2}(0) = 12 \text{ T} - 15 \text{ T}$), such as hollow nanowires (32 nm in diameter and an aspect ratio of ≈ 200)^{955,957} and nano-helices (100 nm in diameter, and an aspect ratio of ≈ 65)⁹⁵⁶ (Figure 24), cf. Fig. 24. These nanostructures exhibit a metallic content of 70 at % W and consist of 20 nm to 30 nm-sized fcc WC_{1-x} crystals.

3. Nanostructures for mechanics

One of the main advantages of FIBID is the capability of directly writing high-aspect ratio structures onto any substrate topography. When it comes to mechanical applications, this would allow to place dedicated tips on top of AFM cantilevers and place springs into pre-fabricated mechanical devices. A recent review by Utke *et al.*¹⁰⁰⁴, summarizes the mechanical properties

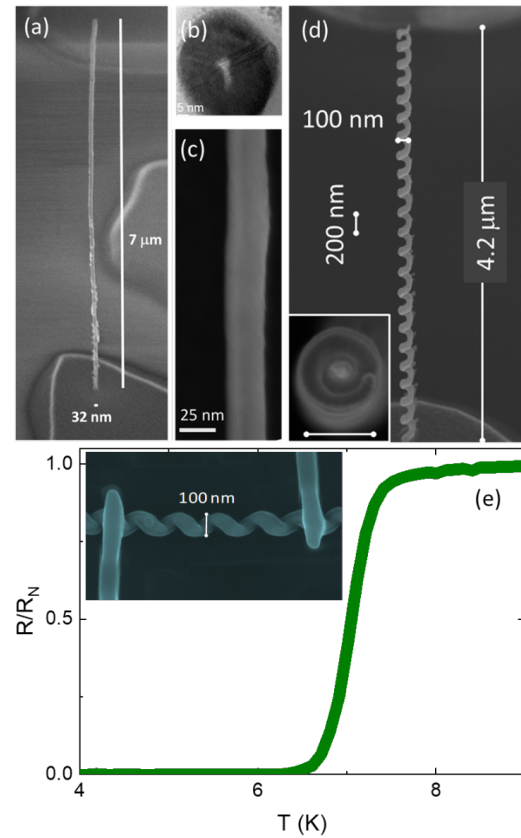


Figure 24. Focused ion beam-induced deposition. (a) SEM image of a hollow crystalline W-C 3D superconducting nanopillar grown by He^+ FIBID. (b) Cross-sectional TEM image of the hollow nanowire. (c) High-magnification SEM image of (a). Adapted with permission from Córdoba *et al.*⁹⁵⁵ ©(2018) American Chemical Society. (d) Superconducting W-C 3D nano-helix grown by He^+ FIBID. Inset shows its top view. (e) Superconducting transition of the nano-helix. Inset shows the nano-helix contacted for the electrical transport measurements. Adapted with permission from Córdoba *et al.*⁹⁶⁸ ©(2019) American Chemical Society.

of all bottom-up grown FIBID pillars and springs. All were deposited by Ga^+ ions (mostly within the range of 10 keV to 30 keV ion energy, 0.5 pA to 9 pA beam current). The most interesting finding was that the gallium-FIBID pillars tend to grow as core-shell structures. Using phenanthrene ($\text{C}_{14}\text{H}_{10}$), the elastic moduli of the hydrogenated carbonaceous material were $\approx 300 \text{ GPa}$ (stiff core with Ga implantation, low H content) and $\approx 30 \text{ GPa}$ (soft shell, presumably high H content)^{989,990}. Depending on the inner diameter of the core and the thickness of the shell, the total elastic modulus ranges between these boundary values. Metal containing pillars with $< 40 \text{ at} \%$, i.e. below percolation, are dominated in their mechanical properties by the co-deposited carbonaceous matrix¹⁰⁰⁴. Larger metal contents in pillars and elastic moduli sum up as follows (metal at.% / elastic modulus normalized to pure metal): Fe (21 at.% / 0.4)⁹⁹¹, Pt (60 at.% /

0.8)⁹⁹², W (80 at.% / 0.4)⁹⁹³, SiO₂ (95 at.% / 0.8)⁹⁹⁴. The non-correlation between metal content and elastic pillar modulus may be due to Ga implantation, which softens the metals. Furthermore, the carbonaceous matrix stiffens or softens the pillar depending on its sp² vs. sp³ hybridization ratio and its hydrogen content. So far, FIBID is typically not used as method to obtain high-aspect ratio scanning probe tips, in contrast to FEBID, see review of Plank *et al.*¹⁰⁰⁵. This can be attributed to Ga-implantation and pulsed irradiation conditions being compulsory to avoid milling instead of tip (pillar) growth. Both make the process difficult to control in material and smallest tip apexes. Only one example employed He-FIBID for the fabrication of hammerhead probes for 3D AFM measurements⁹⁸⁸. The same applies to strain sensors based on piezoresistive granular material where only FEBID is presently used¹⁰⁰⁶. Changing to He or other ion species FIBID⁴¹⁵ these issues might be mitigated in future.

4. Nanostructures for photonics and plasmonics

FIBID represents a powerful nanofabrication tool to explore new optical properties at the nanoscale thanks to its unique design flexibility^{267,1007,1008}. The local nature of FIBID allows the growth of photonic structures on different material substrates¹⁰⁰⁹, opening the path to the fabrication of a number of optical elements such as optical waveguides, Fresnel lenses⁴⁸⁰, or nanosensors.

One especially interesting example combines large area laser interference lithography to fabricate a large area photonic crystal with with focused ion beam deposition to define defects forming a multimode waveguide⁹⁸⁰.

In particular, under optimized parameter conditions, it is possible to make planar structures evolve along the third dimension, thus manufacturing free-standing nanostructures for more exotic optical properties. For example, 3D chiral nano-helices, prototyped by FIBID, have shown tunable chiroptical response at optical frequencies^{982,983}, (Figure 25(a)), have been used as sub-wavelength circular polarization optics (Figure 25(b))⁹⁸⁵, have been exploited in compact and miniaturized high-sensitivity biosensors⁹⁸⁷, and have been integrated on the apex of background-free and broadband chiroptical probes¹⁰¹⁰.

The wide gamut of available gas precursors enables the deposition of metal and dielectric materials, for the emerging field of photonic resonant nanostructures³⁹⁶. On the other hand, pure and homogeneous compositions are intrinsically hindered by all the species involved in the deposition process, such as incomplete dissociation of the precursor molecules and the residual contamination of CO and CO₂ present in the vacuum chamber causing carbon percentage content in the nanostructure, and implanted ions, causing absorption losses and in some cases, material damage. As a result, FIBID deposits exhibit either a nanocrystalline and composite structure^{940,942,1011}

or a core/shell architecture, depending on the precursor properties and on the ion beam irradiation conditions¹⁰¹². Beyond purification approaches, mostly used for FEBID and which might alter the nanostructure dimensions^{1013–1016}, or reduced implantation effects which require the employment of cryo-FIBID^{259,260,968}, promising strategies are also post-processing coating methods. In the case of complex 3D shapes, even conformal coverage can be obtained combining FIBID with glancing angle deposition of metals^{985,1010}, cyclic voltammetry coating of polymers⁹⁸⁷ and atomic layer deposition of oxides¹⁰¹⁷. Also, the core-shell architecture, resulting from the Ga scattering into a lower molecular weight matrix can be controlled to engineer specific optical effects^{1018,1019}. Other strategies may come from the exploitation of newly explored ion beam sources, such as alloy sources⁴⁴, smaller ion sources⁴¹⁶, and plasmonic metal sources¹⁰²⁰.

5. Outlook

Focused ion beams are a flexible and versatile tool for gas-assisted processing, but have been much less used than focused electron beams. The reason for this may be the dominance of Ga ions, which are not only implanted into bottom-up grown structures and cause significant physical sputtering, but can also trigger undesirable chemical and physical side effects. In addition, there is still no research in precursor development specifically for FIBID. On the other hand, ions may offer the opportunity to obtain purer and denser materials due to their higher mass. Here, ion beams from noble gases, which are chemically inert, are of particular interest. While several studies already present promising results for FIBID using He and Ne ion beams (cf. Table VIII), until now no experiments with plasma sources for FIB using beams of argon, krypton or xenon have been published yet.

F. Novel and unconventional approaches in FIB processing

Apart from removing material, introducing dopants or creating defects, the interaction between ions and solids can be used to change materials chemically or morphologically. Such ‘non-standard’ approaches include FIB-induced cross-linking or dissociation in different types of organic and metal-organic surface layers but also the trigger of self-organization processes. Furthermore, ‘standard’ FIB procedures can be combined with other nanofabrication techniques to mitigate specific limitations.

1. Resist patterning by FIB

The goal of lithography using resists is to induce a chemical change in the exposed resist layer to render

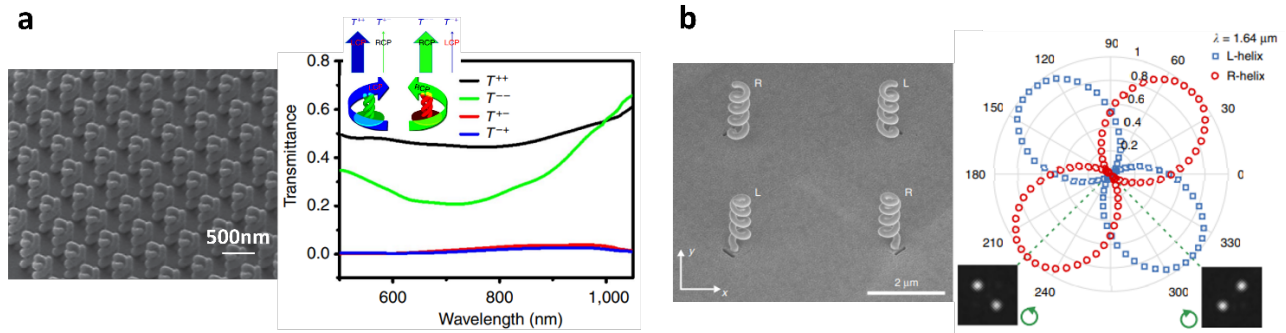


Figure 25. Example of photonic nanostructures realized via FIBID and related optical properties. (a) SEM image of an array of intertwined nano-helices and the related transmission spectra for T_{++} , T_{--} , T_{+-} , T_{-+} for right and left circularly polarized incident light (RCP and LCP, respectively). The inset represents a scheme of the handedness of incident and transmitted circular polarization. Adapted from Esposito *et al.*⁹⁸³. (b) SEM of subwavelength optical device made of helices with opposite handedness (L and R) coupled with orthogonal apertures. This system allows to convert an incoming light beam into four beams of tunable polarizations and intensities. The related graph represents the helicity analysis of the device recorded measuring the transmitted power after placing a rotating quarter-wave plate and a fixed polarizer in front of the detector and measuring the transmitted power. The insets show the image of the device when the quarter waveplate rotates at ± 45 degree. Adapted from Wang *et al.*⁹⁸⁵

it either soluble (positive tone resist) or insoluble (negative tone resist) to the subsequent development step. Resist-based nanopatterning techniques based on photons (optical lithography (OL)) and electrons (EBL) are common in industry, with the main properties being, respectively, the high throughput and the high resolution¹⁰²¹. With the aim of getting a higher throughput than EBL as well as keeping a high resolution, pioneer studies demonstrated the use of Ga-FIB to expose resists^{33,1022–1024}. Ions have the advantage over electrons that due to their mass they do not induce backscattering from the underlying substrate and therefore reduce unintended exposure of neighboring pixels (known as the proximity effect). For example, line widths with resolution better than 100 nm and with sensitivity of 8×10^{11} ions/cm² were found using a commercial negative resist and 30 kV Ga FIB irradiation¹⁰²³. In addition, line widths with resolution better than 30 nm and with sensitivity of 1×10^{13} ions/cm² were achieved using the positive poly(methyl methacrylate) (PPMA) resist and 50 kV Ga FIB irradiation¹⁰²². Moreover, by means of a 50 kV Ga FIB irradiation of the negative PPSQ resist, sensors based on sub-100 nm tunnelling tips were fabricated¹⁰²⁴. Yet, Ga FIB, practically presents drawbacks like beam sputtering of the resist and a relatively large beam spot size (several nanometers) with its significant beam tails. Compared to the significant developments of EBL in the following years this hampered further use of focused ion irradiation for resist exposure until the advent of the HIM. Helium ion beam lithography (HIBL) combines a better focused probe with low sputter yield, high resist sensitivity and a reduced proximity effect¹⁰²⁵.

First studies published in 2009 already highlighted the potential of HIBL for sub-10 nm patterning due to the small ion beam spot (<1 nm) and the low proximity effect^{1026,1027}. In both cases, the hydrogen silsesquiox-

ane (HSQ) negative resist was used. An ion dose of $31 \mu\text{C cm}^{-2}$ was required for complete exposure¹⁰²⁷ (see Fig. 26). Compared to EBL using HSQ, a factor of 4 lower dose is therefore required in HIBL. Thus, HIBL can provide, simultaneously, a similar resolution and a better throughput than EBL.

Such good resolution on HSQ was subsequently employed as a mould for nanoimprint¹⁰²⁹. Some examples of high resolution HIBL are presented in Fig. 26. The 3D nanofabrication of complex crosslinked HSQ nanostructures such as embedded nanochannels and suspended grids was demonstrated using two different exposure configurations¹⁰³⁰. Due to the large depth of field in HIBL, large-area dense patterns were achieved on HSQ as well as exposures on tilted surfaces¹⁰³¹. On the other hand, the use of Ne for HSQ exposure has been found to be interesting giving its trade-off between high resolution and dose efficiency¹⁰³².

Sub-10 nm resolution was also obtained on a fullerene-based resist and $40 \mu\text{C cm}^{-2}$ He⁺ irradiation dose, three orders of magnitude lower compared to a similar process by EBL¹⁰³³. Likewise, sub-10 nm resolution was achieved on an alumina-based resist and the pattern was later transferred to Si, with an aspect ratio of 10, by means of a low-bias reactive ion etching process¹⁰³⁴. Recent work has made use of a metalorganic negative-tone resist, Cr₈F₈(pivalate)₁₆, which is capable of sub-10 nm resolution and requires low He⁺ irradiation dose around 20 pC/cm (three orders of magnitude lower compared to a similar process by EBL), being used on Si and W substrates and with good behaviour against a subsequent dry etching process¹⁰³⁵. Interestingly, hybrid organic-inorganic resists based on Ni perform well in HIBL, requiring 22 $\mu\text{C/cm}^2$ He⁺ irradiation dose and producing sub-10 nm resolution with low line and width roughness¹⁰³⁶.

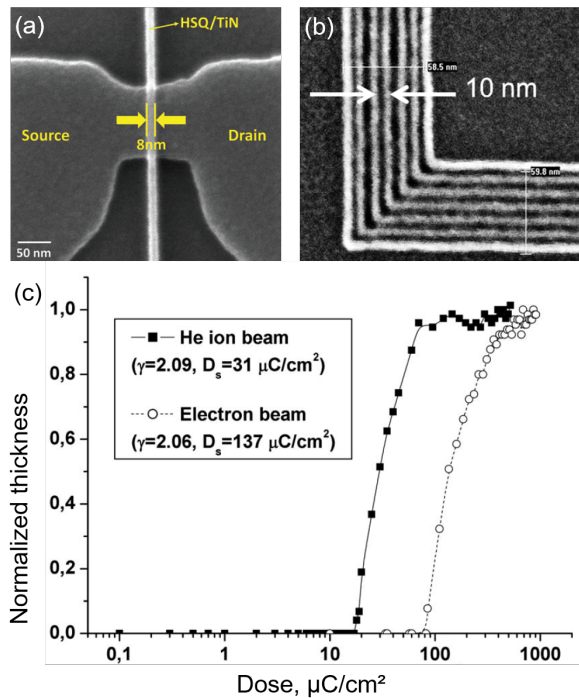


Figure 26. (a) 8 nm-wide HSQ lines nanopatterned by HIBL and used as hard masks for subsequent etching of TiN gate metals. Reprinted from Chang *et al.*¹⁰²⁸; (b) High-resolution dense nanopatterns written on HSQ by HIBL. Reprinted from Li, Wu, and Stanley Williams¹⁰²⁹; (c) Comparison of the required charge dose in HIBL and EBL using the HSQ resist. Reprinted from Sidorkin *et al.*¹⁰²⁷.

Additionally, HIBL has demonstrated good performance in combination with lift-off processes, in particular with Au, which has been used to fabricate plasmonic nanoantenna¹⁰³⁷. Remarkably, a very low ion dose of $6 \mu\text{C}/\text{cm}^2$ is required to expose by HIBL a new resist composed of a radiation-sensitive monomer (MAPDST) with an organic functionality (TIPMA)¹⁰³⁸. Recently, 8 nm-wide HSQ lines were nanopatterned by HIBL and used as hard masks for subsequent etching of TiN gate metals¹⁰²⁸ (see Fig. 26). The comparison of He irradiation for PMMA exposure compared to irradiation by heavier ions has also been described¹⁰³⁹.

A different approach consists on the direct He and Ne milling of HSQ or PMMA resists previously patterned by standard EBL of HIBL, which can be for instance used for repairing purposes¹⁰⁴⁰. Moreover, HIBL has been proposed as a method for the (pre-)screening of EUV resists on fundamental properties¹⁰⁴¹.

In general, it can be stated that HIBL is very promising for high-resolution resist-based nanopatterning due to the low proximity effect¹⁰⁴² and the lower ion dose required in comparison with EBL¹⁰²⁷, so, a broader use of HIBL in coming years can be anticipated. More detailed discussions on this topic can be found in existing review articles^{434,1025,1043}.

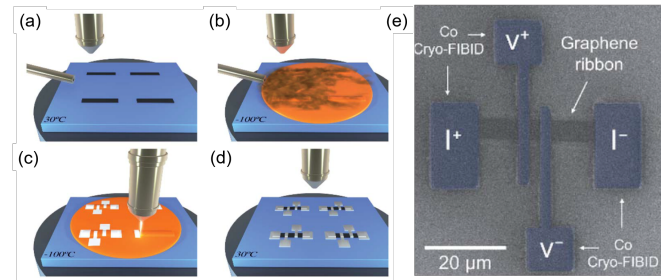


Figure 27. Cryo-FIBID process used to grow electrical contacts on 2D materials (e.g. graphene). (a) Deposition of the material on a Si/SiO₂ substrate. (b) Aperture of GIS on the cooled substrate, giving rise to a precursor condensed layer. (c) Focused ion beam irradiates the condensed layer with the wanted pattern. (d) Substrate heating up to 30 °C producing the sublimation of the non-irradiated condensed layer. (e) Artificially coloured SEM micrograph of the measured graphene ribbon with four electrical contacts grown by Co Cryo-FIBID technique. Reprinted from Salvador-Porroche *et al.*²⁶².

2. Cryo-FIBID

In the past, it was found that electron or ion irradiation of Sn-based precursors condensed on a substrate at 120 K produced deposits that could show metallic behaviour¹⁰⁴⁴. The topic was recently revived through the use of Ga-FIB to dissociate the W(CO)₆ condensed precursor under -100°C , giving rise to W-C nanodeposits that can exhibit metallic resistivity with the great advantage of the low ion dose required compared to the standard process at room temperature (a 600 times lower dose)⁹⁶⁸. This technique, coined Cryo-FIBID, calls for a thickness of the condensed precursor layer comparable to the ion penetration length, so that the deposit does not lift off when heating back to room temperature^{259,260}. Subsequently, Cryo-FIBID was carried out using the (CH₃)₃Pt(CpCH₃) precursor²⁶¹, but the obtained Pt-C deposits were less conductive than the W-C ones.

So far, the best results of Cryo-FIBID have been achieved using the Co₂(CO)₈ precursor²⁶². In this case, the Ga dose required is only $15 \mu\text{C cm}^{-2}$ and the obtained metallic resistivity is low and equals $200 \mu\Omega \text{ cm}$. With these extraordinary properties, it is possible to write electrical contacts directly on a micro-/nanostructure in an ultra-fast way, as sketched in Fig. 27, and applied to grow electrical contacts onto materials such as graphene, as shown in Figure 27b.

Interestingly, the burden of using an expensive and bulky cryogenic module to decrease the substrate temperature in a Cryo-FIBID experiment can be circumvented by means of a cheap, vibration-free and compact thermoelectric plate. In fact, recent process optimization has been carried out to successfully implement Cryo-FIBID using a thermoelectric plate for the W(CO)₆ precursor under -60°C , the lowest temperature achievable in standard commercial thermoelectric plates¹⁰⁴⁵. The obtained

resistivity, $620 \mu\Omega \text{ cm}$, is even lower than that obtained when the Cryo-FIBID is performed at -100°C . This is indeed a promising route to make Cryo-FIBID popular and available on any FIB chamber.

One can tentatively foresee that further Cryo-FIBID studies will stem from (a) the use of alternative and promising precursors for metallic deposits in condensed form^{996,1046}; (b) the Cryo-FIBID process optimization on thermoelectric plates, widely available on FIB chambers¹⁰⁴⁵; and (c) the application of Cryo-FIBID to directly create electrical contacts in an ultra-fast way onto 2D materials²⁶² and onto ion-sensitive materials.

3. FIB irradiation of metalorganic spin-coated layers

Although spin-coated layers such as resists are typically used as sacrificial material in a multi-step patterning process, it was proposed that metalorganic spin-coated layers could be directly patterned by means of ion irradiation, producing metallic structures based on Pd^{514,1047}, Ir¹⁰⁴⁸ and Au¹⁰⁴⁹. However, post-annealing treatments were required to achieve metallic resistivity values, which limited the interest of this approach. As a consequence, this approach was not further developed, in sharp contrast to other techniques such as multi-step resist-based EBL processing, FIBID, etc. Similarly, the use of electron irradiation on Pd-based spin-coated layers led to nanopatterned structures that required a post-annealing step to achieve metallic resistivity and thus had limited reach¹⁰⁵⁰.

However, recent process optimization using Pd-based spin-coated layers in combination with either focused electron¹⁰⁵¹ or focused ion irradiation¹⁰⁵² has led to the development of a single-step process that allows the direct (nano)patterning of metallic micro- and nanostructures at the wafer level. Due to the simplicity of the process, together with its high resolution and its implementation at the wafer level, it is tempting to foresee its wide application in nanoelectronics when electrical contacts or conductive structures need to be patterned.

4. FIB-induced mass transport

Ion irradiation can also cause a change in a material's structure by inducing mass transport along its surface or between layers, including variations such as atomic mixing or stress⁴³⁴. A further example is the formation of self-organized ripples on the surface of semiconductors depending on the angle of incidence of the ions and the ion fluence. This particular effect has been attributed to a trade-off between surface roughening by sputtering and surface smoothing due to beam-induced mass redistribution¹⁰⁵³. Again, the fact that these material modifications can be achieved with the FIB on the nanometer scale, with flexible patterning and processing simplicity,

is what sets the FIB approach apart from broad-beam methods.

5. Hybrid fabrication and heterogeneous integration

Despite the flexibility of FIB-based processing, the intrinsically low throughput of serial processing with the FIB means that large-scale patterning remains elusive. A way to overcome this limitation is by combining the FIB-based step with other lithography methods, using the so-called 'Mix and Match' approach. For example, FIB patterning has been combined with nanoimprint lithography (NIL)^{1029,1054}. An imprint template prepared with FIB on a HSQ resist was transferred by UV nanoimprint on a resist, remarkably, preserving the 4 nm half-pitch lines resolution¹⁰²⁹. Miniaturized fluidic channels for single molecule analysis consisting in complex, multilevel, multiscale fluidic circuits can be patterned as a simple, two-minute imprinting step. The stamp by direct FIB milling is the key aspect and allowed patterning of nanochannels with different cross sections and depths, all at once with 3D transient inlets¹⁰⁵⁴. Alternatively, the fabrication of complex and high fidelity plasmonic nanostructures was achieved by combining EBL and Au-FIB demonstrating both planar and 3D nanostructures with extreme patterning accuracy over large areas with minimal amount of defects or errors¹⁰²⁰. Optical lithography in combination with FIB milling allowed the fabrication of nanochannels in silicon-glass microfluidic chips. Used to study of ion transport, the microfluidic chips consisted in a system of nanochannels connecting two independent volumes¹⁰⁵⁵.

FIB techniques have also been combined with other processing methods, offering improved versatility in terms of the material to be processed and reducing total processing times. For example, direct patterning of inorganic hardmask layers has been demonstrated using FIB milling and FIBID combined with reactive ion etching (RIE), comparing favorably with the much more complex and material-limited resist-based lithography techniques that are conventionally used in this area¹⁰⁵⁶. FIB patterning of molds was also applied for later HFCVD growth of diamond nanocone arrays¹⁰⁵⁷. A further promising application is the use of the FIB as a post-processing tool in complementary metal-oxide-semiconductor (CMOS) chip manufacture. This extends the semiconductor industry's conventional use of the FIB as a debugging and inspection tool, to the top-down FIB-based integration of novel semiconductor circuitry such as nanometer-scale mechanical devices^{1058,1059}. In combination with new (nano)-electronic materials, such as single walled CNT, it has also been shown that there is low, amendable damage to electrical circuits when some FIB patterning process is addressed after the fabrication of field-effect transistor (FET)^{1060,1061}.

6. Outlook

In terms of applications, machining based on FIB goes far beyond a purely top-down approach, but can be used to trigger chemical processes and combined with various other nanofabrication techniques. Device fabrication based on unconventional processing steps, as well as original combinations or alternative advanced sequences may further gain in importance since these can mitigate typical limitations in either FIB processing or other nanofabrication techniques. It is hard to foresee in which way such unconventional processing techniques will develop, but they will certainly benefit from the progress in other FIB techniques, like e.g. from new insights in ion-induced chemical processes, novel precursor materials as well as novel ion species and accessible energy ranges.

V. ROADMAP

Focused ion beams can be considered an all-in-one tool for studying and modifying microscopic matter. For example, there is no other way to image corona virus particles and create Josephson junctions with the same tool as it can be done with a He FIB.

Based on the previous sections describing the current state of instrumentation, theory, and applications of focused ion beam technology, we can now ask where to go with FIB? The short answer is it depends. There are many avenues to pursue. This article, and this section in particular, is intended to provide the long answer.

Figure 28 provides an overview of the fields that drive various FIB techniques, and the resulting challenges and demands for further development of tools, interfaces, and accessories as well as process modeling and fundamental understanding. All of these developments are driven by established or newly emerging research fields that require FIB as a tool for any or all of the following: localized and comprehensive analytics, material modification, and advanced device fabrication.

To account for the complexity of the field without getting buried in details, this section is structured along the lines of important future developments. These can be traced back to the selection of key drivers, each of which is based on different FIB techniques, brings its own challenges, and requires different actions to move forward. A short description of the drivers is followed by an evaluation of the needs of the user community based on a survey. The questions were answered by more than 50 scientists across all research fields who are part of a network established under the European COST Action CA19140 FIT4Nano (www.fit4nano.eu). The developments necessary for future progress were then derived and described in terms of their challenges and potential.

A. Drivers for future applications

The drivers for FIB technologies span a wide variety of areas of science and technology. Currently, the semiconductor industry is the largest driver, demanding process automation, modelling and big data analysis. In general, the drivers split into two overlapping areas. In the first, FIB is mainly used for analytical purposes, providing access to a wealth of physical properties, thereby increasing knowledge of material phenomena. In the second, FIB enables rapid, flexible device prototyping and stimulates novel device development.

A prime example of FIB-based analysis is health and environmental research, which often requires large volume 3D tomographic analysis of cells and tissues under cryogenic conditions, driving the need for increased processing speed, advanced cryo capabilities and automation. One potential way to achieve this is cryo-plasma FIB milling for faster removal of bulk material as discussed in Section IV D. Cryogenic processes are further complicated by insufficient vacuum levels in the sample chamber of current dual beam instruments. A better vacuum, as has been demonstrated in the past, leads to less contamination¹¹⁹ and in the case of cryo-FIB also to less water condensation on the target structure.

Multimodal imaging approaches and the identification of the target area for e.g. TEM lamella preparation are currently hindered by the very different contrast mechanisms in the fluorescence light microscope and the SEM in the FIB/SEM tool, a problem that will require improved correlative techniques as well as more advanced data analysis and management.

In materials science, FIB techniques such as cross sectioning, tomography and sample fabrication, e.g. for TEM and APT studies or ex-situ characterisation of physical properties, have become established standards that now would benefit from powerful process automation. Increasingly, cryo-FIB techniques are also being applied to beam-sensitive samples that are relevant to energy-technology applications such as novel battery materials, calling for the cryo-related developments listed above.

In a broader context, FIB-research into quantum and 2D materials, as well as other novel and functional materials, can largely be subsumed under materials science as well, but should be recognised as a driver of “non-conventional” FIB opportunities in their own right. In this respect, the growing interest in 3D quantum materials is driving the need for rapid and high-precision patterning of large 3D structures from novel materials. This could be achieved by combining process modelling with an easy-to-use interface for 3D shape definition and calculation of the required beam and patterning parameters. In addition, chemical dimensions can be integrated into patterning through the development of novel ion sources. In particular, oxygen is an important tuning parameter for the electronic structure of many quantum materials. At a more fundamental level, the maskless approach of

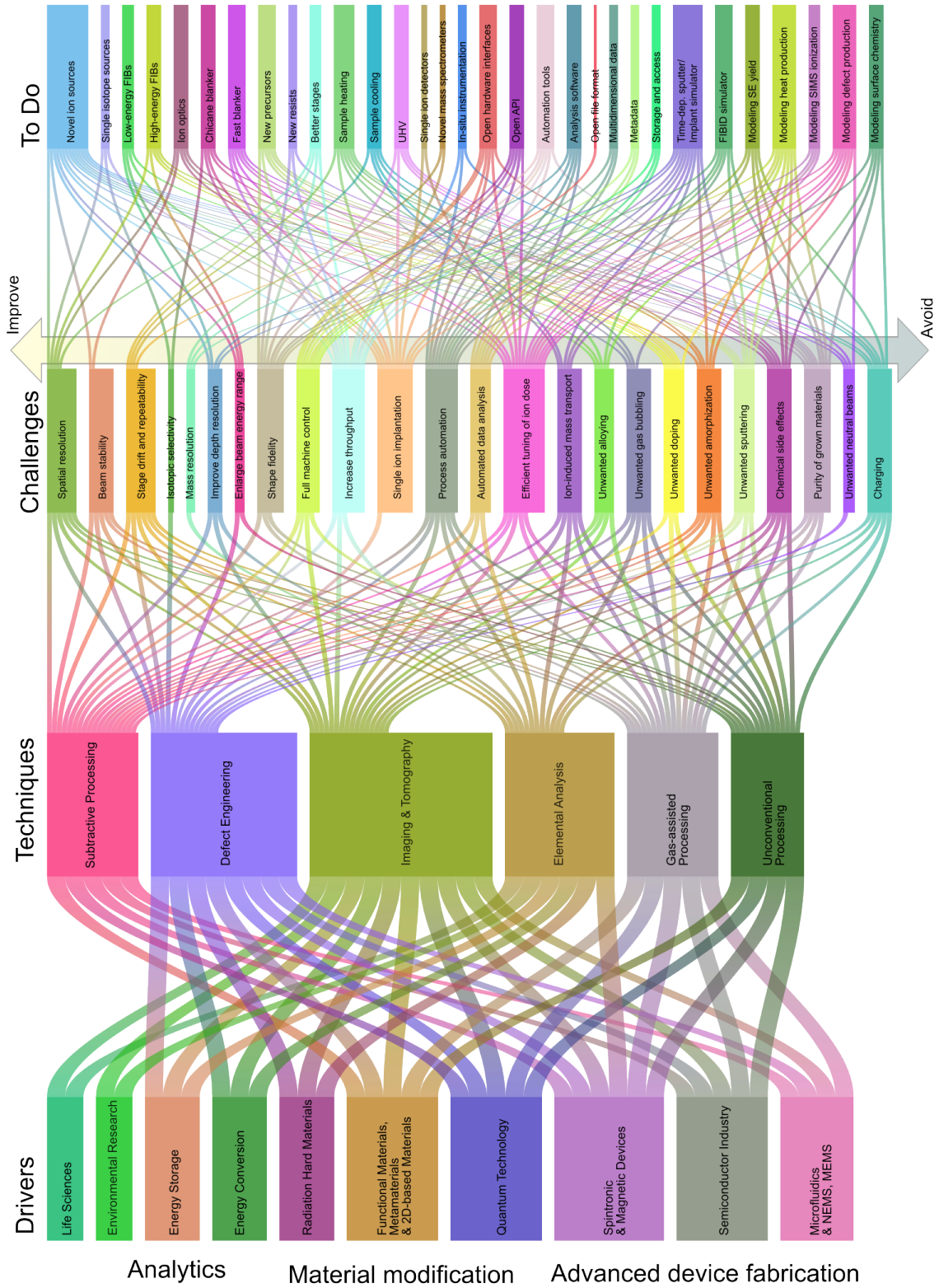


Figure 28. Sankey diagram

focused ion beam processing renders it an ideal technique for the highly precise creation of defects at the exact location where they are needed. This is driven by applications in quantum technology, where defects in an otherwise perfect crystal can act as quantum emitters or, if they carry spin information, as qubits. On the theoretical side, single-ion implementation requires a deeper understanding of the mechanisms of defect formation and the evolution of their local environment, which determines their physical properties.

In terms of instrumentation, the technological challenge is to place individual ions in a (quasi-)deterministic manner and detect them with near-uniform efficiency. Certain defect types may require a specific ion for which stable ion columns need to be developed. The implantation depth is controlled by the mass and energy of the incident ions. Quantum emitters in photonic chip architectures are usually intended to be below the surface (10 to 100 nm) to reduce dephasing. Therefore, the currently available energy ranges of tens of keV are mostly well suited. A higher primary beam energy would only be required to achieve the desired implantation depth for spatially resolved heavy element implantation. This poses challenges for the power supplies and electrical isolation in the ion optical column and elsewhere. If guest atoms are to be implanted into 2D materials instead, e.g. high resolution flexible area doping, lower energies would be highly desired. In this context low energy means less than 100 eV to ensure a significant number of replacement collisions in which the ion replaces the target atom and not just sputters it, leaving behind a vacancy (cf. Section III B). Deceleration lenses in the final stage of the beam focusing or reverse sample biasing might be used for the reduction of the primary energy (see also Section V C). Detection of the primary ion itself or the resulting interaction with the substrate (SE or IBIC) might be achieved by different approaches that are still under development (cf. the Outlook of Section IV B).

B. The generic needs of the community

Focused ion beam systems have become ubiquitous in scientific research and industrial processing, but the market is heavily dominated by Ga ion beam columns. While Ga represents a good compromise between spatial resolution and sputtering yield for many material systems, other systems require different beam parameters and/or suffer from Ga contamination. In our survey, the participants were therefore asked in which areas they conduct research and upon which material systems and/or devices they focus. The corresponding results and percentages thus reflect the experiences of this particular groups of users. As expected, Figure 29 shows that material science, physics and engineering are the most prominent research areas in the FIB community. Fields such as biology, medicine and earth science may be underrepresented in these statistics as connecting to scientists with

other backgrounds turned out to be challenging. Therefore, it would be interesting to repeat the survey with a larger number of participants that are statistically representative. Following the main research fields, the most commonly addressed material systems are 2D materials and semiconductors. Here, the community would certainly benefit from other ion types such as noble gas ions that neither remain in the material (as traps or deep levels) nor undergo chemical reactions or change the phase distribution (such as in Ga-containing direct semiconductors). Specifically, 2D materials will require low ion energies while maintaining spatial resolution.

The typical problems encountered by FIB users (see Fig. 30) show a clear trend, with surface damage, unwanted implantation and contamination being the most dominant problems. The last point on contamination is mostly related to the typical vacuum operating range around $10^{-6} - 10^{-7}$ mbar and the associated residual gases in the vacuum chamber. In this pressure range, a monolayer still forms on the substrate per second, and with a typical water content of around 60% in the residual gas, most surfaces will contain a double layer of water molecules, adding chemical interactions. The hydrocarbons from the residual gas are decomposed by the ion beam and can form a carbonaceous layer on the sample, depending on the ratio of sputtering to deposition yield. Particularly with light ions, even a small amount of contamination can result in greatly reduced net sputtering rates or, in extreme cases, net contamination deposition. Here, a significant improvement of the vacuum level towards an ultra-high vacuum chamber would be an important option. Since some of the contamination is introduced with the sample, a dedicated load lock for plasma cleaning of samples prior to FIB processing would be an ideal complement. Other unwanted chemical side-effects may occur within the sample and be mitigated by more inert ion species. However, unwanted physical side-effects such as interlayer mixing or dealloying are difficult to avoid as their reduction requires a significant reduction in primary ion energies. Therefore, on a shorter time scale, these effects can be better taken into account by process modelling.

Problems with long patterning times are either due to the available beam current range or to stability problems of the system. In particular, the mechanical stages suffer from drift over time and from inaccuracies in exact positioning. In principle, laser interferometric stages solve this problem. However, most FIB systems require the sample to be tilted for FIB processing. Here, novel system designs with an upright FIB column are of great value. Interestingly, the questions about target energies and lateral and vertical resolution more or less correspond to what is currently technologically available. This makes sense in that users aim for what is feasible with their instruments. Only a few users were interested in depositing single molecules or removing single atoms. Currently, however, such approaches are beyond the technological limits of commercial systems and therefore require

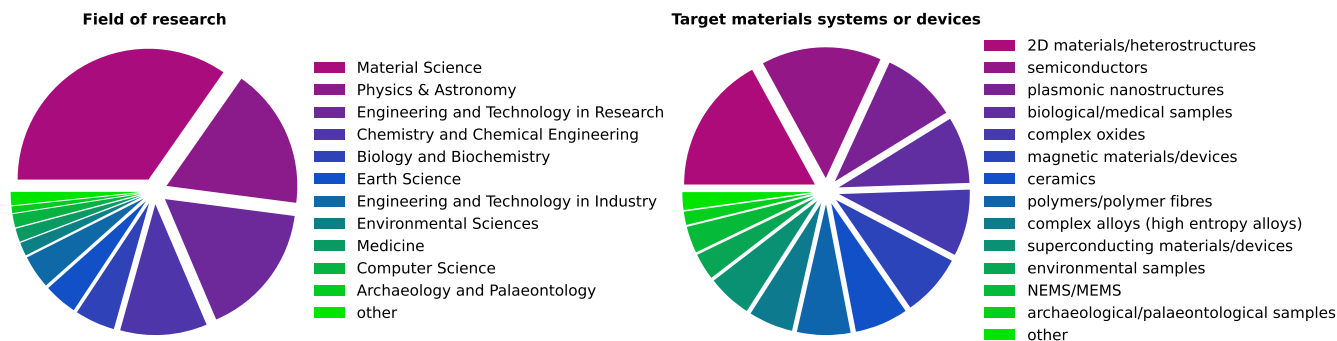


Figure 29. Results of a non-representative survey on (left) the fields of research and (right) the target materials systems or devices being investigated or addressed.

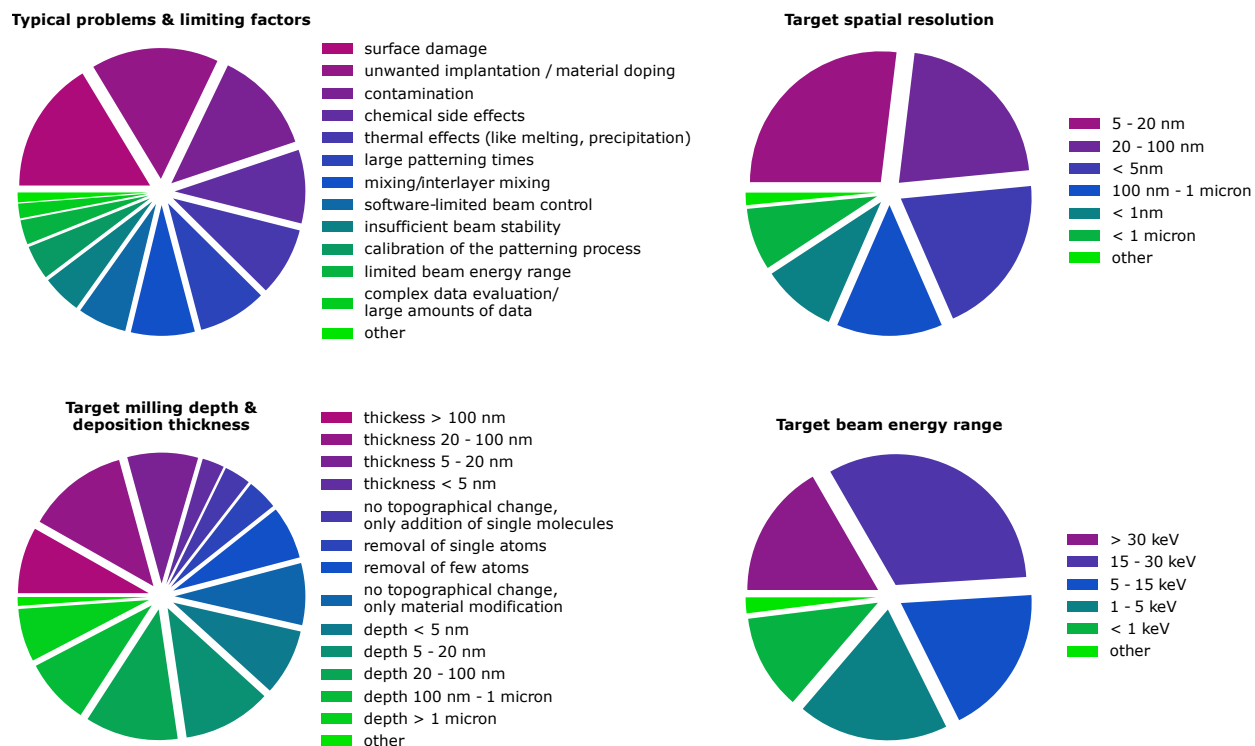


Figure 30. Results of a non-representative survey on (top left) the typical problems and limiting factors in FIB processing, and on the target spatial resolution (top right), milling depth and deposition thickness (bottom left), and primary ion energy range (bottom right)

developments that have yet to be made available to the user community.

C. Important future developments

Having discussed the needs and wants in terms of future applications and user experiences, we now turn to specific technologies that need to be developed. Therefore, Figure 28 is broken up into subplots based on the

to-do pillars. This allows us to trace the impact of certain developments on specific challenges that are solved, techniques that are enabled and drivers that underlie their importance.

1. Ion beam generation and transport

a. Novel source types including single isotope sources
Sources are key for the further development of FIBs.

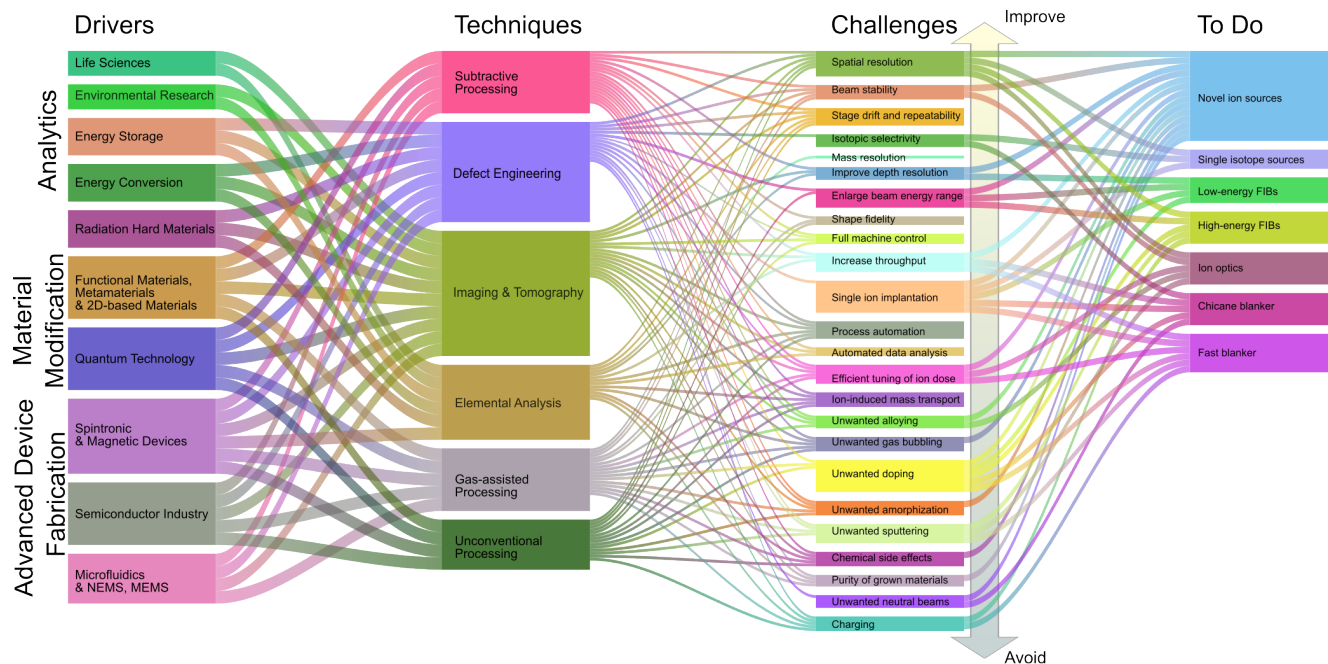


Figure 31. Developments that are required with respect to the generation and transport of focused ion beams

Figure 31 displays the corresponding technological challenges together with their connection to the drivers for which they are required.

The most important challenge concerns the development of novel sources, in particular, high brightness and light element sources that are crucial for high resolution imaging and nanostructuring applications. Here, the further development of GFIS based sources to gases other than He, Ne, and N₂ is desired. The first steps in this direction have been taken by various researchers by testing GFIS based emission from hydrogen¹⁰⁶², Xe⁵⁷, and Kr⁵⁸. However, the heavier noble gases possess numerous isotopes in sometimes nearly equal proportions. This might affect the resolution if the ion optical column is not well shielded from magnetic fields, as magnetic fields present in the column may split the ion beam according to the mass of the containing isotopes. Solutions to this problem, other than shielding, include the addition of a Wien filter or preferably the use of isotopically clean source gases. The use of isotopically pure source materials is also interesting for LMAIS and is already done routinely by many manufacturers of Ga-LMIS and Au-GeSi LMAIS. Such single isotope sources might also be of interest in the context of single ion implantation, local isotope enrichment and other applications. Again, these developments will require new ion optical columns which can reduce or correct the aberration induced by the Wien filter. Alternatively, newly developed MOTIS or LOTIS sources are able to reach high brightness with a number of interesting ion types^{27,66,1063}. However, fundamentally new concepts based e.g. on insulator on conductor ion sources¹⁰⁶⁴ and other ideas for new sources with a

currently very low technology readiness level (TRL) may have a high potential for their application as high brightness sources.

Heavy and reactive ion sources are interesting when it comes to applications such as SIMS but also for low penetration depth high sputtering uses in semiconductor device debugging. Here, ions from group 1 and group 17 in the periodic table are of key interest, due to their reactivity. However, while successful attempts have been made in the past with group 1 elements^{27,43,66,1063} no significant efforts have been undertaken for the development of sources based on group 17 elements such as fluorine or iodine. A possible approach for the fabrication of reactive ion sources which contain group 17 elements could be the application of ILIS sources with suitable salts⁵¹. One of the intrinsic issues of the ILIS technology is the requirement of switching the polarity of the extracted ion beam to keep the source composition in balance. While this is usually considered a nuisance, it can become an advantage, if by using clever chemistry, ion beams suitable for performing SIMS with both polarities can be extracted. However, collateral damage by the reactive ions to ion optical elements needs to be considered and avoided as much as possible. Such efforts in source technology need to be accompanied by a careful review of the other parts inside the FIB tool and in particular the ion optical column. The first commercially available FIB systems combining reactive ion species with SIMS spectrometers are entering the market now.

For more general applications and in combination with reactive gas flooding, LMAIS based sources have a high potential. An example of a useful source for SIMS appli-

cations is the GaBiLi-source^{43,1065}, which provides heavy Bi atoms and small Bi clusters for milling, and a reactive Li ion beam for analysis. Switching between two sorts of ion beams can be automated and requires only a few seconds. For the future, new alloy concepts which include heavier reactive species are desired. However, to date only Au-Si, Au-Ge, Au-Ge-Si and Ga-Bi-Li alloy based LMAIS are commercially available.

An aspect that is becoming more and more important for users is to increase the uptime of the instrument by decreasing maintenance needs. For example, LMIS and LMAIS lifetimes could be increased by increasing the reservoir size of the liquid metal/alloy, and the lifetimes of apertures could be increased by adjusting the material and thickness of the aperture strip, as well as the number of apertures incorporated.

b. Ion optics for low and high energy ion beams With the reduction of dimensions and the increase of complexity of the (3D-)architectures of devices and samples in general, the interactions between the primary ions and the sample become more critical, in terms of both the penetration depth and the ion straggle inside the material.

The key way to reduce these effects is to decrease the energy of the beam. However, the transport of a low-energy beam is thus more complex (see also Section II B). To solve the issues related to the transportation of low-energy ion beams, in particular in terms of chromatic aberrations, specific optics have to be designed¹⁰⁶⁶.

Furthermore, reducing the energy spread of the ions generated in the ion source becomes mandatory, whether it be by developing new types of ion sources, or by filtering the energy, or by adding elements to correct chromatic aberrations. These extra elements like energy-filters and chromatic aberration correctors are, in general, complex to produce and to align and tune¹⁰⁶⁶, which is adding a lot of complexity to the new systems that should be completely automated. Finally, this trend toward low energies not only poses challenges to optics, but also to electronics in terms of stability and precision. In particular, the FIB-based debugging and mask repair needed by the semiconductor industry⁵¹⁹ will benefit from the combination of some of the developments discussed above. Here, a low energy heavy ion beam with high resolution is desired. While the need for high resolution is obvious, the other two requirements ensure minimal penetration depth of the ion beam and thus minimal damage to underlying layers and structures. These low energy ion beam developments are also needed to enable experiments aimed at increasing the understanding of doping of 2D materials. For the controlled and spatially resolved doping of 2D materials—or surfaces—energies below 100 eV are required (see also Section III A). Such an ion source will require an exceptional small energy spread (comparable to that of a LOTIS or GFIS) to ensure that controlled placement of ions with a kinetic energy as low as a few tens of eV is possible.

For high resolution imaging as well as the deep place-

ment of heavy atom donors or single atoms for quantum technology applications, higher energy beams are required. While for higher energies the technological challenge is moderate, the increased size of the electrical isolation and power supplies will set extra constraints on the achievable resolution (since they may act as additional noise sources).

c. Fast beam control and blanking For high resolution resist patterning, demanding FIBID applications and SII, fast beam blankers are required to avoid unintended irradiation or growth during the actual beam blanking. Standard FIB blankers can typically achieve rise times on the order of 20 ns to 100 ns. However, for the abovementioned applications, rise times below 10 ns are desirable and have been demonstrated in the past⁹⁹.

Different source technologies usually also create an undesired beam of neutrals as an unwanted side effect. These neutrals result from collisions of energetic ions with neutral gas atoms. The latter are present as a result of the ion source technology that is used or, in general, due to an insufficient vacuum level in the source or ion optical column. Roughly estimated, the relative numbers of neutrals are e.g. 1 per 1000 ions in a GFIS column. Since the neutrals are not influenced by electromagnetic ion optical components and cannot even be blanked away, they may cause a broad background especially for long overall processing times. This is especially detrimental in applications where high dose markers are required to subsequently find and characterize a few or single ion impacts at specific target locations. To stop the neutral beam, an obstacle can be introduced in the central part of the column, which is bypassed by the (electrically charged) ions with the help of several deflectors. Such chicane blankers or similar solutions will be required to avoid unwanted exposure and irradiation in applications such as resist patterning, and in most applications of defect engineering of material properties, including SII.

2. Accessories and complementary instrumentation

a. Ion-induced chemistry As outlined in Figure 32, the application of FIB-induced deposition, gas-assisted etching, and resist-based lithography (all involving ion-induced chemistry), could be enhanced greatly by the development of more advanced modeling tools, new gaseous precursors and new resists.

In the case of beam-induced deposition, new precursor chemistries that enable higher deposit purity (e.g. for plasmonic applications) and superior resistivity (e.g. for circuit edit applications) are needed. The prerequisite for the development of these precursors is a deeper understanding of the ion-molecule reactions that occur during the deposition process³⁹⁶. For high-purity metallic deposits, the precursor molecule will ideally be fully decomposed so that only the desired metal component is deposited and the ligand fragments are pumped away. Similarly, in the case of gas-assisted etching, the pre-

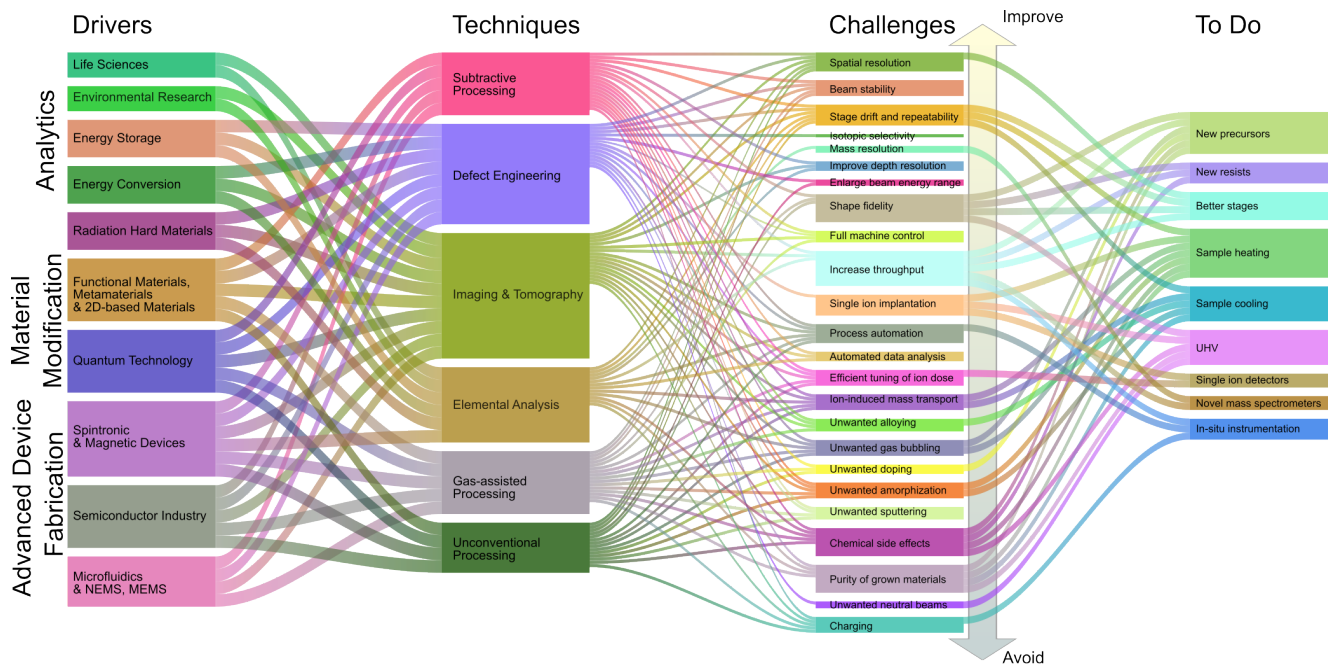


Figure 32. Developments that are required with respect to accessories and complementary instrumentation

cursor molecules should undergo ligand loss to generate empty coordination sites that bind with the substrate to enhance the rate of removal of substrate atoms without forming a residue of nonvolatile reaction products. Once the fundamentals of beam-induced chemical reactions are better understood (including aspects such as the effect of beam-heating), researchers will be better poised to develop simulation tools to enable the prediction and design of more complex deposition and etching scenarios. The development of these simulation tools will also rely on input from systematic parameter optimization, where automated beam control and data analysis will play a key role.

A common but generally undesired effect from ion-induced chemistry is the deposition of a thin carbon film over ion-irradiated regions, arising due to residual hydrocarbon species on the sample surface and in the microscope chamber¹⁰⁶⁷. This effect can be minimized by e.g. plasma cleaning samples before loading into the microscope or working in ultrahigh vacuum. Other unwanted beam-induced effects that can occur during intentional deposition processes include implantation of the ions themselves into a deposit during the growth process, or concurrent milling of the deposit. To minimize these problems, it is desirable to increase the deposition rate, so that a lower total ion dose is needed for the process. Recently it has been shown that cryogenic cooling of the substrate is one way to increase deposition rates, which could be investigated further⁹⁶⁸. However, it is worth mentioning at least one application where a balance between deposition and concurrent milling by the primary ion beam is actually desired, namely the formation of

high-aspect-ratio hollow nanopillar deposits with unique electronic properties using the helium FIB⁹⁵⁵. Overall, fine control over the rate of deposition should prove highly beneficial for future applications.

For resist-based lithography, further development of resists specifically for ion-induced chemistry is needed. It has already been shown that resists tend to be much more sensitive to ions than electrons, but so far most resist development has still been for EBL. In order to optimize resists for lithography using different ion species, a deeper understanding of the ion-resist interaction process is required¹⁰³⁹. Consequently, the full potential of FIB-based lithography has yet to be realized, even though high resolution patterning with dramatically reduced proximity effects compared with EBL has been demonstrated. HIBL in particular has shown great promise for high-resolution patterning^{1026,1027}.

b. Adapted sample environments Sample heating during FIB processing has found uses for decades, including reduction of ion beam induced amorphization during light ion FIB processing. Quasi-local heating with an infrared laser¹⁰⁶⁸ and homogeneous heating using a heating stage³²⁴ have been both tested. However, the latter approach in particular suffers from sample drift induced by the high thermal mass of the sample heater. In this context, low drift implementations with lower power requirements are required to protect the rest of the system from overheating (e.g. piezo motors in the stage and ion optical components in the pole piece) and to allow faster heating ramps¹⁰⁶⁹. Also FIBID-related applications could benefit from new simple heating stages for exploring in-situ annealing of the deposited structures.

On the other side, cooling may be interesting as well in the context of sample amorphization, surface microstructure formation and for applications using FIBID or HIBL. Often temperatures slightly below 0°C are sufficient to avoid the formation of eutectic phases or phase separation. In the same manner, molecular desorption rates may be tuned by either decreasing or increasing the temperature by only few tens of Kelvin. Hence, for many experiments with a smaller temperature range to bridge, Peltier based solutions are possible¹⁰⁴⁵. A much clearer requirement for cooling comes from biological applications, and cryo-stages as part of an entire cryo-workflow are available (see Section IV C for examples). However, because of the required piping and shielding, these systems can suffer from reduced imaging performance and limitations on sample geometry and accessories in the FIB chamber.

Nevertheless, it is expected that specialized FIB instruments dedicated to the handling of biological or other sensitive samples will become available. These devices will require special load locks for vacuum and/or cryo transfer. Replacement of the SEM column with a fluorescence light microscope might open a unique pathway to a dedicated but cost efficient system for the preparation of TEM lamella in biology, medicine and related fields. A comparable triple beam system has been presented recently¹⁰⁷⁰. Having a well established method from the field of biology available to find the region of interest and analyze suitable portions after FIB processing in-situ will also allow new and more efficient workflows.

Additional developments will be related to the continued integration of sample cleaning options based on UV light or remote plasma, as well as the combination of ion beam based sample processing with direct laser milling¹⁰⁷¹. Products integrating the latter technology with FIB-based processing became available only recently, and the work flows and possibilities require further investigation. In general, cooling would particularly benefit from better vacuum conditions, as less condensation of background gases would be expected.

c. Analytical add-on systems for FIB platforms Analytical and other support systems can be split into several subgroups which sometimes are exclusive but more often can be combined to allow new multidimensional data sets.

A number of *true* ion beam analytical methods have been implemented or are interesting candidates for a future implementation. The general trends are better spatial resolution in 3D, higher sensitivity (and hence lower detection limits) and better quantification of results. These include IL¹⁴³ and RBS¹¹³ which have been explored by many researchers but are not available commercially. In IL the luminescence of excited target atoms, defects or recoiled ions is detected using parabolic mirrors and a combination of gratings and lenses to obtain spectral information that allows the identification of the emission source. In contrast, RBS measures the energy and scattering angle of backscattered ions and allows the

standard free and depth resolved elemental analysis of samples. While RBS has been largely abandoned due to fundamental problems related to the high number of multiple and double scattering events, IL has still potential in such important fields as geology, mineralogy and biology, as well as in research involving nanoparticles for various intentional and unintentional applications (i.e. nanotoxocology).

A promising approach appears to be SIMS, which allows high spatial resolution in 3D and also high sensitivity. It is noteworthy that resolution and sensitivity affect one another and hence efforts to improve performance should consider both. Here, realistic expectations are particularly important, as for some methods (e. g. GFIS or LOTIS based SIMS) a simultaneous increase in both is impossible as the reduced sampling volume statistically does not contain any atoms of the target species. However, other new approaches such as optical characterization of the sputtered material¹⁰⁷² can be feasible for certain applications.

There has been debate about the potential use of detecting X-rays as a signal for ion-induced processes. While it is not done on a regular basis, some publications indicate that it could be possible¹³⁹. However, the observed X-rays were not generated by the interaction of the primary ion beam with the sample as intended. Instead, non-conductive samples are positively charged and backscattered ions release SE from different places in the chamber. These SE are then accelerated toward the positively charged sample surface and generate X-rays with ‘unexpected’ peaks caused by random interaction with the chamber parts. Correspondingly, a conductive sample exhibits no X-ray generation¹⁰⁷³ because the inelastic interactions in the stopping power that are responsible for X-ray generation depend on velocity and not on energy. As stated in Joy *et al.*¹⁰⁷³, a primary energy of about 53 MeV for He is required to excite the same X-ray lines as can be obtained using a 6 keV electron beam. Unfortunately, these energies are out of reach for conventional FIB systems and thus remain elusive to the related high energy ion beam technique PIXE. In contrast to X-ray spectroscopy, the generation and detection of Auger electrons is indeed possible for low-energy ions. The mechanism of Auger electron generation is attributed to the creation of core-hole vacancies in both the projectile ions and the substrate atoms. Thus, the Auger signal stems from both colliding particles and results in spectra with rich features that can be quantitatively evaluated as has been shown for the case of incident Au⁺ and Si⁺⁺ ion beams¹³⁶.

Another analytical approach is based on the observation of ion beam-induced effects. One example is monitoring the electrical properties of nanostructured samples. Properties that can be derived from the electrical measurements (e. g. magnetization via the measurement of a Hall voltage) can also be evaluated in these experiments. Various surface characterization techniques (e. g. AFM) and in-situ mechanical testing also belong to this

category. The benefit of performing these methods in-situ is not only control of the environment but also the possibility of high resolution imaging that enables immediate quality control of the measurement. In all cases open hard- and software APIs are required for the implementation of these approaches.

3. Automation and data management

Figure 33 shows the technological developments required in terms of automation and data management. Both categories are rapidly growing in importance due to the sheer volume of samples and data that need to be processed. Because of recent developments in machine learning and artificial intelligence, there is enormous potential to facilitate the daily work of researchers and users. However, the black-box nature of such routines requires awareness and regular cross-checking of both the training data used and the results obtained.

a. Open interfaces to hard- and software In recent decades, science has increasingly moved towards openness and transparency. Today, both are often prerequisites for receiving taxpayers' money for scientific research. The idea of sharing not only raw data but also task-specific developments in terms of machine operation and data evaluation holds great potential. Instead of developing isolated solutions specific to particular research groups, which often become obsolete or are lost after the original developers leave, a larger community can maintain and further develop methods much more efficiently. In addition, the overall speed of development is significantly increased, as people first look for existing data and tools before "reinventing the wheel".

Open access to data and non-proprietary development are already standard in many scientific fields, but the more technologically sophisticated and commercially valuable scientific work becomes, the more conflicts over intellectual property, licenses or potential patents can arise.

Nevertheless, the major tool manufacturers have recognized the opportunity that lies in opening up their machines for modification by users. Because everyday users want to get the ultimate performance, the most efficient use of instrument time and the most insight from the data generated, they are a key resource for driving future developments. The more people who are involved in and benefit from an active user community, the better for manufacturers' sales figures, even if new technological developments do not have immediate impact on a patent or a price tag. Hence, what users need are open hardware interfaces to get real-time signals or to add their own components. Even more important is a full-fledged API that allows control of all the system parameters accessible in the user interface (UI) and ideally others in a developer mode. In this respect, UI development on the manufacturer side must be a compromise between the needs of technicians, who require easy-to-use software,

and scientists, who require full access.

For users at intermediate skill levels, this can be bridged well by certain automation tools that are already included in some devices. Here, routines that have already been executed can be stored and modified in a quasi-graphical approach, removing the hurdle of programming in a text box. Although it is particularly important in the life sciences and environmental research, all branches of materials science, including battery and energy conversion, also increasingly rely on the rapid recording of tomographic data based on SE images and analytical signals from EDS or EBSD. A high degree of automation, high precision, and repeatable sample and add-on manipulation are prerequisite for such workflows.

In the future these tools should be complemented by machine learning algorithms that help with experimental control and real-time data analysis. Integration of an active learning UI (human in the loop)¹⁰⁷⁴ for continuous improvement of the supporting machine learning algorithms would then allow easy continuous training and thus automatic control and/or optimization of processing based on predefined quality parameters or figures of merit. Such feedback control would also be beneficial for advanced patterning tasks, where modeling-informed pattern generation and optimization could be coupled fully automatically with FIB-processing.

b. Data access and management Similarly, all data generated must be open. Manufacturers' proprietary file formats can be useful if they offer additional functionality or easier access to data analysis. However, it is a big problem if there is no way to access the raw unprocessed data. In the future, a standardized and multidimensional open file format especially for correlative image and spectroscopy data would be highly desirable. HDF5 would be such an option, where HDF stands for hierarchical data format and allows raw data to be stored in image or spectroscopy file formats (such as tiff or binary files) with metadata and all other types of information in a structured way¹⁰⁷⁵. However, this would require that instrument manufacturers agree on such a uniform standard, possibly following the development in neutron, X-ray and muon research with the HDF5-based data format neXus¹⁰⁷⁶. In general, open data enable platform- and tool-independent analysis as well as correlation with data from other sources. In addition, image processing tools developed for other purposes, that may be based on completely different data generation platforms, can be used and further developed for analysis. A prime example is the open source and platform-independent image processing software ImageJ and its derivatives^{204,1077,1078}, that can already be extended by a variety of community-developed plug-ins as well as further adapted and integrated into other programs via its API. Here again, machine learning has proven to be extremely powerful in automated data evaluation, especially for large and complex data sets from correlative measurements or tomography. For example, external libraries for image classification and analysis such as scikit-learn¹⁰⁷⁹, Tensor-

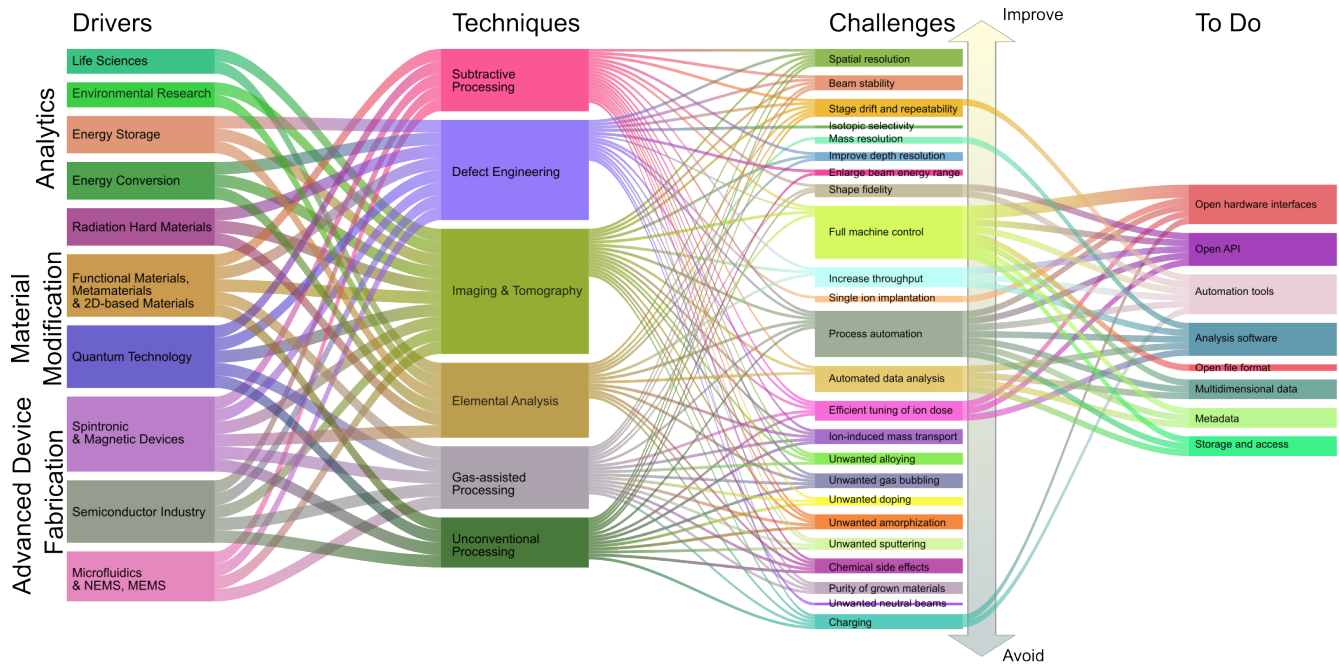


Figure 33. Developments that are required with respect to automation and data management

flow¹⁰⁸⁰, PyTorch¹⁰⁸¹, dragonfy¹⁰⁸² and Ilastik⁸⁷⁷ are already available, actively developed and becoming easier to use. Since data analysis in science varies greatly depending on the application, it often requires a tailored approach. As a result, machine learning-based solutions are also very diverse, with application to problems including simple data noise reduction, the broad field of feature recognition and data reduction, super resolution imaging, and full quantification. The integration or linking of different methods and data streams, from which the increasingly popular machine learning approaches benefit greatly, requires open interfaces. Therefore, tool manufacturers should not aim to develop closed all-in-one tools for data analysis and automation, but should instead provide the necessary infrastructure that allows users to efficiently develop what they need themselves.

Ultimately, protocols will need to be defined to preprocess raw data into a relevant part for storage and discard another part in order to be able to store and access at least some of the data that are generated. Hierarchical and structured data can help here to manage and sort data to provide “useful” raw data for further processing both internally and externally, while avoiding or at least minimising the typical data graveyards.

4. Process modeling

Process simulation plays a key role in technology development for integrated circuits (ICs)^{1083,1084}. Together with other types of simulation, it is considered one of the drivers of Moore’s law, the exponential growth of the

number of devices per IC. It is also heavily used beyond traditional device scaling (“Beyond CMOS” and “More than Moore”¹⁰⁸⁵). In spite of FIB processes sharing a lot of physics and chemistry with IC processes, process simulation is much less used in the FIB community. This is partly due to the hefty price tag for commercial simulation tools used in the IC business, and partly due to the much smaller industry behind FIB activities. Nevertheless, the success of process simulation in IC development demonstrates its potential for the development of FIB related processes.

a. From BCA to sputter simulation The simulation program most widely used by the FIB community is TRIM²¹⁸. As mentioned in Section III A 2, TRIM allows the calculation of range and damage statistics, in addition to rough estimates of sputtering yields in 1D amorphous targets. Its success is based on the fact that it provides reasonable estimates for any ion–target combination, and on the availability of a convenient user interface. Other BCA simulation tools that allow consideration of dynamic changes to the target and additional target types (2D and 3D and/or crystalline targets), would certainly benefit from more intuitive user interfaces. Work toward this goal has recently been reported for one particular code¹⁰⁸⁶ and could probably be transferred to other codes with moderate effort. This would promote adoption of a wider range of codes by the community.

b. Continuum modeling and approaches towards FIBID modeling As discussed in Sections III D 1 and III D 3, continuum simulations of surface evolution are hampered by the need for various input parameters

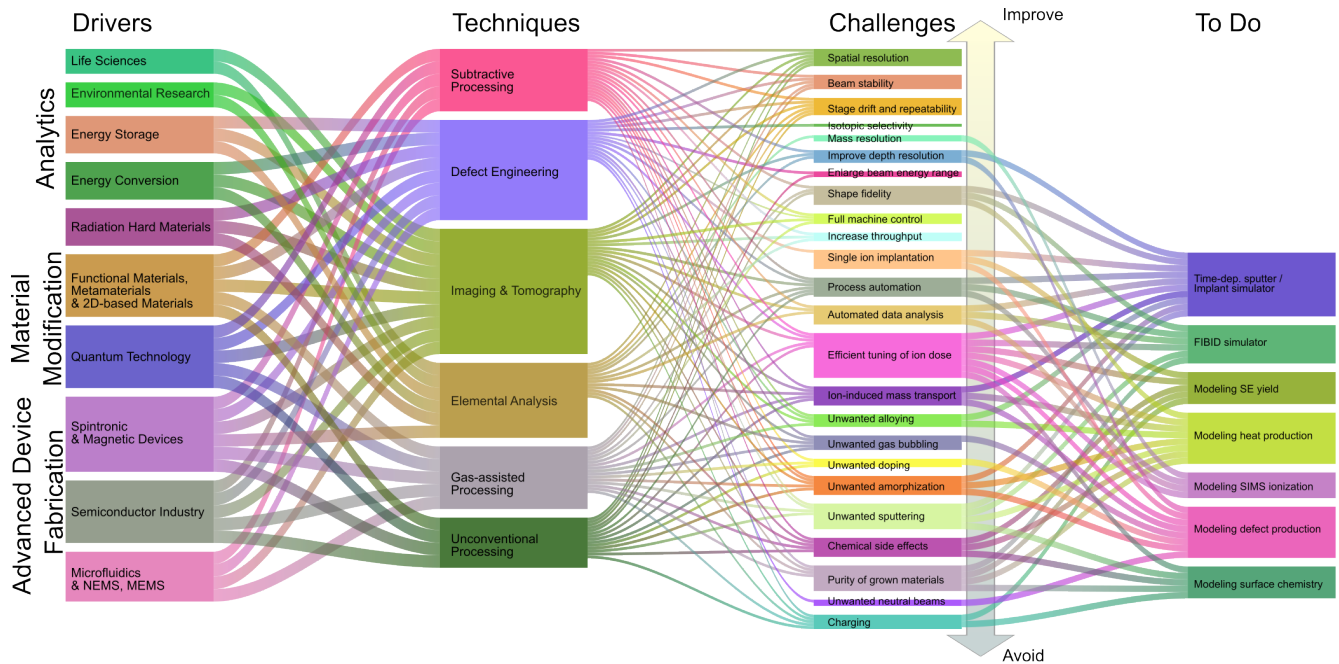


Figure 34. Developments that are required with respect to process modeling

and neglect of processes taking place below the surface. However, they are still useful for qualitative investigations. Wider applicability is expected from coupling BCA with continuum simulations, which could include surface diffusion and reactions, heat transport and/or relaxation of density changes. This could pave the way for accurate and general process simulation of FIB processes, although physical and chemical parameters will still be an issue. Input from more fundamental methods or strategies for experimental parameter determination will be required. The former is already standard in IC process simulation, while an example of the latter in the context of FEBID⁴³² can be found in use of tilted nanowires on a pedestal for model calibration.

As an alternative to physico-chemical modeling, deep learning has opened up new possibilities in many fields of research. In FIB technology, a neural network has been trained on a set of binary design patterns, corresponding SEM images, and ion beam parameters used in their production¹⁰⁸⁷. The trained network was then able to accurately predict the outcome for previously unseen designs in nearly real time. This approach holds promise for process control and, in a more general setup, for reducing the number of trial and error iterations in the fabrication of nanostructures.

Another desired feature is the implementation of SE generation into BCA codes. This will allow more accurate interpretation of FIB images and will foster model development for precursor dissociation in FIBID processes. Also SII may benefit when detecting single ion impacts by the secondary electron detector.

c. Addressing the gap in understanding Having discussed the modelling of the effects of FIB on various materials at the binary collision level of theory, we now consider applications of more advanced computational techniques to the FIB simulations. The most important fundamental issues which cannot be addressed at the BCA level are:

- Accurate description of the energy loss by the energetic ion accounting for its charge state and the electronic structure of the target
- Production of defects in the irradiated material accounting for the electronic excitations
- Evolution of the atomic structure of the target over macroscopic time scales at room and elevated temperatures during the annealing
- Effects of defects and impurities on the mechanical, electronic, optical and magnetic properties of the irradiated system

To attack these problems, different simulation techniques and setups should be used. Ultimately, the simulations can be divided into three groups: modeling of the collision, evolution of the system after the ion impact and assessment of the influence of defects on materials properties.

With regard to the computational techniques, increasingly powerful computers allow for the simulation of larger systems and longer times. These advances will lead to more widespread use of MD and kMC simulations to shed light on specific FIB-related applications,

or to explore the physics of ion-target interaction in general. Their usage can be extended to areas currently only accessible to BCA-type simulations. In addition, new developments in computational techniques widen the range of applicability of these methods. For example, MD simulations with ML interatomic potentials trained by DFT calculations (cf. Section III B 2) raise the accuracy and reliability of MD predictions to DFT level while being applicable to much larger systems.

d. Approaches to bridging scale mismatch Combinations of various techniques in a single run, e.g., first-principles approaches with ML potential MD, or analytical potential MD with BCA methods, help elucidate irradiation effects in various situations such as in strongly non-uniform systems when the main focus is on the description of damage production with high precision in one of the subsystems, or over longer time scales. Examples are the response of 2D materials on substrates^{335,1088} or the evolution of the target under high-dose FIB irradiation.

In addition, computers with massively parallel architecture and recent development of Ehrenfest dynamics allow prediction of the energy transfer from the ion to the target through ballistic collisions and electronic excitations, and its dissipation in the target involving defect formation without any empirical parameters. In particular, the direct juxtaposition of experimental data and corresponding simulation results on passing ions through atomically thin targets (e.g., graphene and other 2D materials) should shed light on the mechanisms of ion neutralization and energy transfer. Indeed, if the initial/final charge states of the ion and its kinetic energy are known, along with the scattering angle, this information can be correlated with impact parameter-dependent results of atomistic simulations carried out using TDDFT-based Ehrenfest dynamics combined with the assumption that nuclei are classical particles.

TDDFT-based Ehrenfest dynamics can also improve parametrization of two-temperature models, bridging the gap between different approaches in multi-scale atomistic simulations. Though very useful, their application will remain limited to small systems for quite some time.

e. Current limitations and challenges While significant progress has been made, there are still challenges in development of the more advanced methods and their applications to irradiation simulations. For example, one of the challenges is simulations of the ions passing through 2D materials discussed above, and interpretation of the theoretical results. After passing through the target, the ion may be in a mixed charge state because the nuclei move in an average potential created by the electron subsystem, which can be in an excited state. In particular, in the experiment a hydrogen atom (proton) which has passed through the target can be in charge states zero or plus one, while non-integral charge localized around the atom can be found in the simulations. This problem is related to the fundamental question of the connection between quantum-mechanical averages and ob-

servable quantities, and requires careful analysis in the context of ion-target interaction.

At the same time, there are also challenges in the methodology. As an example, the common computational schemes of DFT codes fail at small separations between the nuclei, when atom cores overlap. Even for full-electron codes, numerical instabilities in the eigenvalue solvers are expected at small interatomic distances. There are other challenges related to spin-polarization energies of atoms, as recent calculations³⁴¹ indicated.

As for the long-term evolution of the system after irradiation, e.g., post-treatments such as annealing at temperatures of several hundred Kelvin over hours, this problem cannot be attacked using MD either with DFT or ML/analytical potentials. The bottleneck is the large number of computational steps to be done. Parallelization can resolve the issue of the system size (more atoms, more processors so that ultimately each processor calculates forces acting on one specific atom), and thus reduce the cost of the time step up to a certain minimum. However, the time step in MD simulations should still be at the atomic scale (normally a few femtoseconds), which indicates that still $\sim 10^{15}$ steps must be done to simulate one second of the physical time. Even if each time step is $\sim 10^{-4}$ second (a typical value for a system comprised from less than 100 atoms), the total CPU time will be several years. In some cases (e.g., migration of point defects and their annealing in crystalline solids), kMC simulations may provide insights into the evolution of the system at the macroscopic time scale, but kMC can hardly be applied to systems with a high degree of amorphization or when the atomic structure of the system substantially changes during annealing.

Assessment of the effects of defects on the properties of materials is in a much better situation. DFT-based approaches make it possible to calculate the electronic and magnetic properties of the system with defects and directly juxtapose the results of calculations with the experimental data. In particular, insights into the optical properties and exciton binding energies of defective materials have recently been obtained¹⁰⁸⁹, and PL spectra of materials with defects as single-photon emitters were calculated^{748,1090–1093}.

VI. EXECUTIVE SUMMARY AND PERSPECTIVE

A focused ion beam (FIB) instrument employs a finely focused beam of ions with an energy of typically 2 keV to 30 keV that is scanned across a sample to effect modifications with nanometer-scale resolution. The technique relies on the transfer of energy from the energetic primary ion to target atoms during elastic nuclear collisions, resulting in the displacement of these substrate atoms and potentially their removal from the sample. As such it comprises an universal tool for all areas of research that enables comprehensive analyzes, maskless local material changes and rapid prototyping of devices.

The aim of this document is to provide an overview of the current state of the art of FIB technology, its applications and important tool developments, all of which require attention by researchers and technologists developing new FIB-based workflows and instrumentation. As such, this document can serve as an important reference work for students, FIB users, academic and commercial developers of related technologies, and funding agencies. It includes overview tables, providing a bird's eye view of the relevant works in this field. New developments in the various driving fields of research pose new challenges for FIB techniques, for which we propose targeted solutions and a list of technical developments that will be required.

From an instrumentation point of view, the ubiquitous gallium FIB is an excellent tool for the preparation of both transmission electron microscope (TEM) samples and functional nanostructures. However, FIB sources for ions of other elements are becoming increasingly common and provide additional degrees of freedom for the fabrication of new meta- and functional materials. In fact, liquid metal alloy ion sources (LMAISs) and gas field-ionization sources (GFISs) were used even before the gallium liquid metal ion source (LMIS) started to control the market. Newer developments include the plasma focused ion beam (PFIB) using electron cyclotron resonance (ECR) or inductively coupled plasma (ICP) sources, which has quickly gained relevance due to its ability to remove large volumes of material while maintaining a lateral resolution sufficient for many applications. Combined with the very recent addition of the magneto-optical trap ion source (MOTIS), about two thirds of the elements of the periodic table can now be used for FIB applications (see Fig. 1 and Tab. I). New applications related to e.g. health, quantum technology, as well as energy conversion and storage, present new challenges to existing techniques that will require innovations in ion sources, beam transport and detectors (see Fig. 31). Low energy FIBs (≤ 1 keV) are particularly relevant for the semiconductor industry, quantum technology, and applications based on low dimensional materials. New developments related to heavy and unconventional ion beams are important for single ion implantation (SII) and analytical applications such as secondary ion mass spectrometry (SIMS).

An important technique that has strong overlap with theory and simulation is gas-assisted processing, usually referred to as focused ion beam-induced deposition (FIBID). This is the nanometer-scale counterpart to industrial and consumer 3D printing. The variety of precursor gases (see Tab. IX) and the patterning flexibility of the FIB enable the fabrication of nanoscale devices with special properties and geometries for emerging applications (see Figs. 24 and 25). Here, an in-depth understanding of the complex processes related to precursor gas flow, surface diffusion of molecular species, and modeling of the generation of secondary particles are needed for accurate process simulation.

Simulations and process modeling are also relevant for other FIB applications, such as subtractive processing

and defect engineering. Applicability, however, will also require an extension of the existing knowledge on ion-solid interactions into the energy range relevant for FIB applications. This knowledge transfer would be particularly helpful for calculations of the production rate of charged secondary particles, especially secondary electrons (SEs). The yield of SEs is relevant for several applications, including SII and also general imaging and analysis. For analysis applications, robust models for the prediction of secondary ion (SI) yields are needed. In addition to addressing these fundamental questions, efforts are required in the areas of process modelling and shape prediction for additive and subtractive patterning. Here, open application programming interfaces (APIs) and open source software in combination with machine learning (ML) will enable better control over the focused ion beams, which will in turn allow higher precision, resulting in faster and more reproducible device fabrication.

New software and computing technologies also enable the creation and evaluation of large data sets that are mostly generated via FIB-based analytical methods, e.g. FIB-SIMS and serial sectioning. ML algorithms can aid with the acquisition, alignment, and segmentation of these usually multidimensional data sets. Drivers for these techniques are health, energy storage and conversion, meta- and functional materials, and the semiconductor industry. Currently, biological applications are also driving this field through the use of FIB-based tomography to generate nanoscale 3D representations of samples, e.g. the fly brain^{890,891}, enabling new insight into the microscopic structures responsible for cognitive processes.

As the applications of FIB processing are extremely diverse, it will not be a single technological development that brings a breakthrough. Instead, numerous advances will be needed in order to address the challenges that have been identified. New developments will often impact several scientific fields, as can be seen from the overview graph in Fig. 28. Therefore, we look to an exciting future where FIB processing will grow in importance and open new avenues in many areas of science and technology, spanning quantum technology to the life sciences.

ACKNOWLEDGEMENTS

This publication is based upon work from the COST Action FIT4NANO CA19140, supported by COST (European Cooperation in Science and Technology) <https://www.cost.eu/>. Financial support from COST Action CA19140 is acknowledged <http://www.fit4nano.eu/>. The authors would like to thank the FIT4NANO members for participating in the survey that forms part of Section VB, as well as for input provided during in-person meetings and online discussion. The writing of this document and the implementation of FIT4NANO also benefitted greatly from the guidance and support of

worldwide FIB manufacturers and add-on producers, including (in alphabetical order) Carl Zeiss AG, Kleindiek Nanotechnik GmbH, NenoVision s.r.o., RAITH GmbH, Tescan Orsay Holding a.s., and Thermo Fisher Scientific.

AUTHOR CONTRIBUTIONS

Katja Höfflich: Conceptualization (equal); Data curation (equal); Writing—Section 4: Applications (leading), Section 5: Roadmap (leading); Writing—review & editing (equal); Visualization (leading). **Gregor Hlawacek:** Conceptualization (leading); Funding acquisition (leading); Writing—original draft (equal); Writing—review & editing (equal); Visualization (equal); **Gerhard Hobler:** Conceptualization (equal); Writing—Section 3: Simulation Approaches (leading); Writing—review & editing (equal). **Frances Allen:** Writing—Section 4: Applications (leading); Writing—review & editing (leading). **Tom Wirtz:** Conceptualization (equal); Writing—Section 2: Instrumentation (leading); Writing—review & editing (equal). **Gemma Rius:** Conceptualization (equal); Data curation (leading); Writing—original draft (equal); Writing—review & editing (equal); Visualization (equal). **Lisa McElwee-White:** Writing—original draft (equal); Writing—review & editing (leading). **Lothar Bischoff, Olivier de Castro, Rosa Córdoba, Anne Delobbe, Flyura Djurabekova, Peter Dunne, Natalie Freese, Armin Göhlhäuser, Nico Klingner, Arkady V. Krasheninnikov, Ingo Manke, Mariachiara Manoccio, Paul Mazarov, Johann Michler, Philip Moll, Oleksandr V. Dobrovolskiy, Wolfhard Möller, Markus Osenberg, Francesc Pérez-Murano, Patrick Philip, Matthias Schmidt, José María de Teresa, Ivo Utke, Florian Vollnhals:** Writing—original draft (equal).

REFERENCES

- ¹ESA, “Lisa factsheet,” online (2023), https://www.esa.int/Science_Exploration/Space_Science/LISA_factsheet.
- ²M. Tajmar, A. Genovese, and W. Steiger, “Indium field emission electric propulsion microthruster experimental characterization,” *Journal of Propulsion and Power* **20**, 211–218 (2004).
- ³D. Bock and M. Tajmar, “Highly miniaturized fep propulsion system (nanofep) for attitude and orbit control of cubesats,” *Acta Astronautica* **144**, 422–428 (2018).
- ⁴J. Mayer, L. A. Giannuzzi, T. Kamino, and J. Michael, “TEM sample preparation and FIB-induced damage,” *MRS Bulletin* **32**, 400–407 (2007).
- ⁵C. Berger, N. Premaraj, R. B. G. Ravelli, K. Knoops, C. López-Iglesias, and P. J. Peters, “Cryo-electron tomography on focused ion beam lamellae transforms structural cell biology,” *Nat. Methods* **20**, 499–511 (2023).
- ⁶T. J. Prosa and D. J. Larson, “Modern focused-ion-beam-based site-specific specimen preparation for atom probe tomography,” *Microsc. Microanal.* **23**, 194–209 (2017).
- ⁷V. N. Tondare, “Quest for high brightness, monochromatic noble gas ion sources,” *J. Vac. Sci. Technol. A* **23**, 1498 (2005).

- ⁸D. Langmuir, “Theoretical limitations of cathode-ray tubes,” *Proceedings of the IRE* **25**, 977–991 (1937).
- ⁹A. N. Zorzos and P. C. Lozano, “The use of ionic liquid ion sources in focused ion beam applications,” *Journal of Vacuum Science & Technology B: Microelectronics and Nanometer Structures* **26**, 2097–2102 (2008).
- ¹⁰L. Bischoff, P. Mazarov, L. Bruchhaus, and J. Gierak, “Liquid metal alloy ion sources—An alternative for focussed ion beam technology,” *Appl. Phys. Rev.* **3**, 021101 (2016).
- ¹¹L. W. Swanson, “Use of the liquid metal ion source for focused beam applications,” *Applied Surface Science* **76–77**, 80–88 (1994).
- ¹²O. Physics, “Orsay physics datasheet chroma exb,” (2021).
- ¹³S. Bauerdick, L. Bruchhaus, P. Mazarov, A. Nadzeyka, R. Jede, J. Fridmann, J. E. Sanabia, B. Gila, and B. R. Appleton, “Multispecies focused ion beam lithography system and its applications,” *Journal of Vacuum Science & Technology B, Nanotechnology and Microelectronics: Materials, Processing, Measurement, and Phenomena* **31**, 06F404 (2013).
- ¹⁴P. C. Lozano, “Energy properties of an EMI-im ionic liquid ion source,” *Journal of Physics D: Applied Physics* **39**, 126–134 (2005).
- ¹⁵T. P. Fedkiw and P. C. Lozano, “Development and characterization of an iodine field emission ion source for focused ion beam applications,” *Journal of Vacuum Science & Technology B: Microelectronics and Nanometer Structures* **27**, 2648 (2009).
- ¹⁶N. S. Smith, W. P. Skoczylas, S. M. Kellogg, D. E. Kinion, P. P. Tesch, O. Sutherland, A. Aanesland, and R. W. Boswell, “High brightness inductively coupled plasma source for high current focused ion beam applications,” *Journal of Vacuum Science & Technology B: Microelectronics and Nanometer Structures* **24**, 2902 (2006).
- ¹⁷B. V. Leer and M. Dutka, “Latest developments in multiple ion species plasma FIB technology,” *Microscopy and Microanalysis* **25**, 570–571 (2019).
- ¹⁸O. Physics, “Orsay physics datasheet ifib,” online (2021), <https://www.orsayphysics.com/fib>.
- ¹⁹B. W. Ward, J. A. Notte, and N. P. Economou, “Helium ion microscope: A new tool for nanoscale microscopy and metrology,” *Journal of Vacuum Science & Technology B: Microelectronics and Nanometer Structures* **24**, 2871 (2006).
- ²⁰R. Hill and F. H. M. Faridur Rahman, “Advances in helium ion microscopy,” *Nuclear Instruments and Methods in Physics Research Section A: Accelerators, Spectrometers, Detectors and Associated Equipment* **645**, 96–101 (2011).
- ²¹J. Notte and J. Huang, “The helium ion microscope,” in *Helium Ion Microscopy*, edited by G. Hlawacek and A. Göhlhäuser (Springer International Publishing, Cham, 2016) pp. 3–30.
- ²²N. Ernst, G. Bozdech, H. Schmidt, W. Schmidt, and G. L. Larkins, “On the full-width-at-half-maximum of field ion energy distributions,” *Applied Surface Science* **67**, 111–117 (1993).
- ²³G. Hlawacek and A. Göhlhäuser, eds., *Helium Ion Microscopy* (Springer International Publishing, 2016).
- ²⁴R. H. Livengood, S. Tan, R. Hallstein, J. Notte, S. McVey, and F. F. Rahman, “The neon gas field ion source—a first characterization of neon nanomachining properties,” (Elsevier BV, 2011) pp. 136–140.
- ²⁵N. Klingner, G. Hlawacek, P. Mazarov, W. Pilz, F. Meyer, and L. Bischoff, “Imaging and milling resolution of light ion beams from helium ion microscopy and FIBs driven by liquid metal alloy ion sources,” *Beilstein Journal of Nanotechnology* **11**, 1742–1749 (2020).
- ²⁶A. V. Steele, A. Schwarzkopf, J. J. McClelland, and B. Knuffman, “High-brightness Cs focused ion beam from a cold-atomic-beam ion source,” *Nano Futures* **1**, 015005 (2017).
- ²⁷G. ten Haaf, S. Wouters, D. Nijhof, P. Mutsaers, and E. Vredendregt, “Measurements of the energy distribution of a high brightness rubidium ion beam,” *Ultramicroscopy* **190**, 12–20 (2018).

- ²⁸E. Moufarej, M. Vielle-Grosjean, G. Khalili, A. J. McCulloch, F. Robicheaux, Y. J. Picard, and D. Comparat, "Forced field ionization of Rydberg states for the production of monochromatic beams," *Phys. Rev. A* **95**, 043409 (2017).
- ²⁹L. van Kouwen and P. Kruit, "Brightness measurements of the nano-aperture ion source," *Journal of Vacuum Science & Technology B* **36**, 06J901 (2018).
- ³⁰J. A. van Kan, R. Pang, T. Basu, Y. Dou, Gokul, N. Tarino, J. Tregidga, S. C. Roy, and H. M. Tan, "Considerations for the nano aperture ion source: Geometrical design and electrical control," *Review of Scientific Instruments* **91**, 013310 (2020).
- ³¹V. E. Krohn and G. R. Ringo, "Ion source of high brightness using liquid metal," *Applied Physics Letters* **27**, 479–481 (1975).
- ³²R. Clappitt, K. L. Aitken, and D. K. Jefferies, "Abstract: Intense field-emission ion source of liquid metals," *Journal of Vacuum Science and Technology* **12**, 1208–1208 (1975).
- ³³R. L. Seliger, J. W. Ward, V. Wang, and R. L. Kubena, "A high-intensity scanning ion probe with submicrometer spot size," *Applied Physics Letters* **34**, 310–312 (1979).
- ³⁴E. W. Müller, "Das Feldionenmikroskop," *Zeitschrift für Phys.* **131**, 136–142 (1951).
- ³⁵R. Levi-Setti, "Proton scanning microscopy: feasibility and promise," *Scanning Electron Microscopy* **7**, 125–134 (1974).
- ³⁶W. H. Escovitz, T. R. Fox, and R. Levi-Setti, "Scanning transmission ion microscope with a field ion source," *Proceedings of the National Academy of Sciences* **72**, 1826–1828 (1975).
- ³⁷G. I. Taylor, "Disintegration of water drops in an electric field," *Proceedings of the Royal Society of London. Series A. Mathematical and Physical Sciences* **280**, 383–397 (1964).
- ³⁸P. Mazarov, A. D. Wieck, L. Bischoff, and W. Pilz, "Alloy liquid metal ion source for carbon focused ion beams," *Journal of Vacuum Science & Technology B: Microelectronics and Nanometer Structures* **27**, L47 (2009).
- ³⁹L. Bischoff, W. Pilz, P. Mazarov, and A. D. Wieck, "Comparison of bismuth emitting liquid metal ion sources," *Applied Physics A: Materials Science and Processing* **99**, 145–150 (2010).
- ⁴⁰L. Bruchhaus, P. Mazarov, L. Bischoff, J. Gierak, A. D. Wieck, and H. Hövel, "Comparison of technologies for nano device prototyping with a special focus on ion beams: A review," *Applied Physics Reviews*, *Applied Physics Reviews* **4**, 011302 (2017).
- ⁴¹W. Pilz, P. Laufer, M. Tajmar, R. Böttger, and L. Bischoff, "Polyatomic ions from a high current ion implanter driven by a liquid metal ion source," *Review of Scientific Instruments* **88**, 123302 (2017).
- ⁴²J. Gierak, P. Mazarov, L. Bruchhaus, R. Jede, and L. Bischoff, "Review article: Review of electrohydrodynamical ion sources and their applications to focused ion beam technology," *Journal of Vacuum Science & Technology B* **36**, 06J101 (2018).
- ⁴³W. Pilz, N. Klingner, L. Bischoff, P. Mazarov, and S. Bauerdick, "Lithium ion beams from liquid metal alloy ion sources," *Journal of Vacuum Science & Technology B* **37**, 021802 (2019).
- ⁴⁴L. Bischoff, N. Klingner, P. Mazarov, W. Pilz, and F. Meyer, "Boron liquid metal alloy ion sources for special focused ion beam applications," *Journal of Vacuum Science & Technology B* **38**, 042801 (2020), arXiv:2004.12722.
- ⁴⁵P. A. Mazarov, V. G. Dudnikov, and A. B. Tolstoguzov, "Electrohydrodynamic emitters of ion beams," *Uspekhi Fizicheskikh Nauk* **190**, 1293–1333 (2020).
- ⁴⁶L. Bischoff, N. Klingner, P. Mazarov, K. Lenz, R. Narkowicz, W. Pilz, and F. Meyer, "Dysprosium liquid metal alloy ion source for magnetic nanostructures," *Journal of Vacuum Science & Technology B* **40**, 052802 (2022).
- ⁴⁷P. Lozano and M. Martínez-Sánchez, "Ionic liquid ion sources: suppression of electrochemical reactions using voltage alternation," *Journal of Colloid and Interface Science* **280**, 149–154 (2004).
- ⁴⁸P. Lozano and M. Martínez-Sánchez, "Ionic liquid ion sources: Characterization of externally wetted emitters," *J. Colloid Interface Sci.* **282**, 415–421 (2005).
- ⁴⁹D. Krejci, F. Mier-Hicks, R. Thomas, T. Haag, and P. Lozano, "Emission characteristics of passively fed electrospray microthrusters with propellant reservoirs," *Journal of Spacecraft and Rockets* **54**, 447–458 (2017).
- ⁵⁰C. Perez-Martinez, S. Guilet, N. Gogneau, P. Jegou, J. Gierak, and P. Lozano, "Development of ion sources from ionic liquids for microfabrication," *Journal of Vacuum Science & Technology B, Nanotechnology and Microelectronics: Materials, Processing, Measurement, and Phenomena* **28**, L25–L27 (2010).
- ⁵¹S. Guilet, C. Perez-Martinez, P. Jegou, P. Lozano, and J. Gierak, "Ionic liquid ion sources for silicon reactive machining," *Microelectron. Eng.* **88**, 1968–1971 (2011).
- ⁵²A. B. Tolstogouzov, S. F. Belykh, V. S. Gurov, A. A. Lozovan, A. I. Taganov, O. M. N. D. Teodoro, A. A. Trubitsyn, and S. P. Chenakin, "Ion-beam sources based on room-temperature ionic liquids for aerospace applications, nanotechnology, and microprobe analysis (review)," *Instruments and Experimental Techniques* **58**, 1–14 (2015).
- ⁵³G. Hlawacek, V. Veligura, R. van Gastel, and B. Poelsema, "Helium ion microscopy," *Journal of Vacuum Science & Technology B* **32**, 020801 (2014).
- ⁵⁴F. Aramaki, T. Ogawa, O. Matsuda, T. Kozakai, and Y. Sugiyama, "Development of new FIB technology for EUVL mask repair," *Proceedings of SPIE The International Society for Optical Engineering* , 7969 (2011).
- ⁵⁵M. E. Schmidt, A. Yasaka, M. Akabori, and H. Mizuta, "Nitrogen gas field ion source (GFIS) focused ion beam (FIB) secondary electron imaging: A first look," *Microscopy and Microanalysis* **23**, 758–768 (2017).
- ⁵⁶M. E. Schmidt, M. Akabori, and H. Mizuta, "Nitrogen ion microscopy," in *Ion Beam Applications* (InTech, 2018).
- ⁵⁷W.-c. Lai, C.-y. Lin, W.-T. Chang, P.-c. Li, T.-Y. Fu, C.-S. Chang, T. T. Tsong, and I.-S. Hwang, "Xenon gas field ion source from a single-atom tip," *Nanotechnology* **28**, 255301 (2017).
- ⁵⁸H. Shichi, S. Matsubara, and T. Hashizume, "Characteristics of krypton ion emission from a gas field ionization source with a single atom tip," *Japanese Journal of Applied Physics* **56** (2017), 10.7567/JJAP.56.06GC01.
- ⁵⁹C. Lejeune and F. Prangere, "UN MODÈLE SIMPLE déCRIVANT LES PROPRIÉTÉS DE LA déCHARGE d'UNE SOURCE DU TYPE DUOPLASMATRON," *Le Journal de Physique Colloques* **29**, C3–90–C3–92 (1968).
- ⁶⁰R. W. Boswell, N. S. Smith, P. P. Tesch, and N. P. Martin, "RF system, magnetic filter, and high voltage isolation for an inductively coupled plasma ion source," patent US20140077699 (Oregon Physics LLC, 2014).
- ⁶¹P. Sortais, T. Lamy, J. Médard, J. Angot, L. Latrasse, and T. Thuillier, "Ultracompact/ultralow power electron cyclotron resonance ion source for multipurpose applications," *Review of Scientific Instruments* **81**, 02B314 (2010).
- ⁶²J. L. Hanssen, J. J. McClelland, E. A. Dakin, and M. Jacka, "Laser-cooled atoms as a focused ion-beam source," *Phys. Rev. A* **74**, 063416 (2006).
- ⁶³B. J. Claessens, M. P. Reijnders, G. Taban, O. J. Luiten, and E. J. D. Vredenburg, "Cold electron and ion beams generated from trapped atoms," *Phys. Plasmas* **14**, 093101 (2007).
- ⁶⁴J. L. Hanssen, S. B. Hill, J. Orloff, and J. J. McClelland, "Magneto-Optical-Trap-Based, High Brightness Ion Source for Use as a Nanoscale Probe," *Nano Lett.* **8**, 2844–2850 (2008).
- ⁶⁵L. Kime, A. Fioretti, Y. Bruneau, N. Porfido, F. Fuso, M. Viteau, G. Khalili, N. Šantić, A. Gloter, B. Rasser, P. Suardraud, P. Pillet, and D. Comparat, "High-flux monochromatic ion and electron beams based on laser-cooled atoms," *Phys. Rev. A* **88**, 033424 (2013).
- ⁶⁶B. Knuffman, A. V. Steele, and J. J. McClelland, "Cold atomic beam ion source for focused ion beam applications," *J. Appl. Phys.* **114**, 044303 (2013).

- ⁶⁷G. ten Haaf, S. H. W. Wouters, S. B. van der Geer, E. J. D. Vredenburg, and P. H. a. Mutsaers, "Performance predictions of a focused ion beam from a laser cooled and compressed atomic beam," *Journal of Applied Physics* **116**, 244301 (2014), [arXiv:1410.4362](https://arxiv.org/abs/1410.4362).
- ⁶⁸J. J. McClelland, A. V. Steele, B. Knuffman, K. A. Twedt, A. Schwarzkopf, and T. M. Wilson, "Bright focused ion beam sources based on laser-cooled atoms," *Appl. Phys. Rev.* **3**, 011302 (2016).
- ⁶⁹W. Schnitzler, G. Jacob, R. Fickler, F. Schmidt-Kaler, and K. Singer, "Focusing a deterministic single-ion beam," *New Journal of Physics* **12**, 065023 (2010).
- ⁷⁰M. A. Levine, R. E. Marrs, J. R. Henderson, D. A. Knapp, and M. B. Schneider, "The electron beam ion trap: A new instrument for atomic physics measurements," *Physica Scripta* **T22**, 157–163 (1988).
- ⁷¹X. Xu, R. Pang, P. S. Raman, R. Mariappan, A. Khursheed, and J. A. van Kan, "Fabrication and development of high brightness nano-aperture ion source," *Microelectronic Engineering* **174**, 20–23 (2017).
- ⁷²Q. Ji, X. Jiang, T.-J. King, K.-N. Leung, K. Standiford, and S. B. Wilde, "Improvement in brightness of multicusp-plasma ion source," *J. Vac. Sci. Technol. B* **20**, 2717 (2002).
- ⁷³A. B. Tolstoguzov, S. F. Belykh, G. P. Gololobov, V. S. Gurov, S. I. Gusev, D. V. Suvorov, A. I. Taganov, D. J. Fud, Z. Ai, and C. S. Liu, "Ion-beam sources based on solid electrolytes for aerospace applications and ion-beam technologies (review)," *Instruments and Experimental Techniques* **61**, 159–172 (2018).
- ⁷⁴M. Nojima, H. Mita, and K. Hara, "Mass separation of water cluster ion beam using two rotating electric fields and sputtering of a polymer thin film," (Surface Science Society Japan, 2020) pp. 101–105.
- ⁷⁵D. S. Jun, V. G. Kutchoukov, and P. Kruit, "Ion beams in SEM: An experiment towards a high brightness low energy spread electron impact gas ion source," *Journal of Vacuum Science & Technology B, Nanotechnology and Microelectronics: Materials, Processing, Measurement, and Phenomena* **29**, 06F603 (2011).
- ⁷⁶J. Orloff, *Handbook of Charged Particle Optics*, 2nd ed. (CRC Press, 2009).
- ⁷⁷H. Liebl, *Applied Charged Particle Optics*, 1st ed. (Springer, Berlin, Heidelberg, 2008).
- ⁷⁸J. Orloff, *Charged particle optics*, 2nd ed. (CRC Press, 2009).
- ⁷⁹H. Rose, *Geometrical Charged-Particle Optics*, 2nd ed. (Springer, 2009).
- ⁸⁰T. E. Everhart and R. F. M. Thornley, "Wide-band detector for micro-microampere low-energy electron currents," *Journal of Scientific Instruments* **37**, 246–248 (1960).
- ⁸¹G. McMahon, J. Nxumalo, and M. Phaneuf, "Applications of a Novel FIB-SIMS Instrument in SIMS Image Depth Profiling," *Microscopy and Microanalysis* **8**, 1212–1213 (2002).
- ⁸²A. J. Kubis, G. J. Shiflet, R. Hull, and D. N. Dunn, "Focused ion-beam tomography," *Metallurgical and Materials Transactions A* **35**, 1935–1943 (2004).
- ⁸³N. Klingner, R. Heller, G. Hlawacek, S. Facsko, and J. von Borany, "Time-of-flight secondary ion mass spectrometry in the helium ion microscope," *Ultramicroscopy* **198**, 10–17 (2019).
- ⁸⁴T. Wirtz, N. Vanhove, L. Pillatsch, D. Dowsett, S. Sijbrandij, and J. Notte, "Towards secondary ion mass spectrometry on the helium ion microscope: An experimental and simulation based feasibility study with He⁺ and Ne⁺ bombardment," *Applied Physics Letters* **101**, 1–5 (2012).
- ⁸⁵T. Wirtz, O. De Castro, J. N. Audinot, and P. Philipp, "Imaging and Analytics on the Helium Ion Microscope," *Annual Review of Analytical Chemistry* **12**, 523–543 (2019).
- ⁸⁶J.-N. Audinot, P. Philipp, O. D. Castro, A. Biesemeier, Q. H. Hoang, and T. Wirtz, "Highest resolution chemical imaging based on secondary ion mass spectrometry performed on the helium ion microscope," *Reports on Progress in Physics* **84**, 105901 (2021).
- ⁸⁷M. R. Ball, R. J. M. Taylor, J. F. Einsle, F. Khanom, C. Guillermier, and R. J. Harrison, "Helium ion microscope – secondary ion mass spectrometry for geological materials," *Beilstein Journal of Nanotechnology* **11**, 1504–1515 (2020).
- ⁸⁸O. S. Ovchinnikova, N. Borodinov, A. A. Trofimov, S. T. King, M. Lorenz, W. Lamberti, D. Abmayr, and A. V. Ievlev, "Helium ion microscopy with secondary ion mass spectrometry for nanoscale chemical imaging and analysis of polyolefins," *ACS Applied Polymer Materials* **3**, 3478–3484 (2021).
- ⁸⁹F. A. Stevie, "Focused Ion Beam Secondary Ion Mass Spectrometry (FIB-SIMS)," in *Introduction to Focused Ion Beams* (Springer US, Boston, MA, 2005) pp. 269–280.
- ⁹⁰F. Kollmer, W. Paul, M. Krehl, and E. Niehuis, "Ultra high spatial resolution SIMS with cluster ions - approaching the physical limits," *Surface and Interface Analysis* **45**, 312–314 (2013).
- ⁹¹S. Kim, A. Trofimov, F. Khanom, L. Stern, W. Lamberti, R. Colby, D. Abmayr, A. Belianinov, and O. S. Ovchinnikova, "High Resolution Multimodal Chemical Imaging Platform for Organics and Inorganics," *Analytical Chemistry* **91**, 12142–12148 (2019).
- ⁹²R. J. Chater, A. J. Smith, and G. Cooke, "Simultaneous detection of positive and negative secondary ions," *J. Vac. Sci. Technol. B: Microelectron. Nanometer Struct.* **34**, 03H122 (2016).
- ⁹³R. H. Brugge, R. J. Chater, J. A. Kilner, and A. Aguadero, "Experimental determination of Li diffusivity in LLZO using isotopic exchange and FIB-SIMS," *Journal of Physics: Energy* **3**, 034001 (2021).
- ⁹⁴S. Hayashi, N. Tsuji, S. Nishinomiya, and N. Kubota, "Development of FIB-TOF-SIMS Apparatus to Evaluate Suspended Particulate Matters," Tech. Rep. (Nippon Steel, 2011).
- ⁹⁵F. A. Stevie, L. Sedlacek, P. Babor, J. Jiruse, E. Principe, and K. Klosova, "FIB-SIMS quantification using TOF-SIMS with Ar and Xe plasma sources," *Surface and Interface Analysis* **46**, 285–287 (2014).
- ⁹⁶J. A. Whitby, F. Östlund, P. Horvath, M. Gabureac, J. L. Riegerer, I. Utke, M. Hohl, L. Sedláček, J. Jiruše, V. Friedli, M. Bechelany, and J. Michler, "High Spatial Resolution Time-of-Flight Secondary Ion Mass Spectrometry for the Masses: A Novel Orthogonal ToF FIB-SIMS Instrument with In Situ AFM," *Advances in Materials Science and Engineering* **2012**, 1–13 (2012).
- ⁹⁷L. Pillatsch, F. Östlund, and J. Michler, "FIBSIMS: A review of secondary ion mass spectrometry for analytical dual beam focussed ion beam instruments," *Progress in Crystal Growth and Characterization of Materials* **65**, 1–19 (2019).
- ⁹⁸W. D. Rickard, S. M. Reddy, D. W. Saxey, D. Fougereuse, N. E. Timms, L. Daly, E. Peterman, A. J. Cavosie, and F. Jourdan, "Novel Applications of FIB-SEM-Based ToF-SIMS in Atom Probe Tomography Workflows," *Microscopy and Microanalysis* **26**, 750–757 (2020).
- ⁹⁹N. Klingner, R. Heller, G. Hlawacek, J. von Borany, N. J., J. Huang, and S. Facsko, "Nanometer scale elemental analysis in the helium ion microscope using time of flight spectrometry," *Ultramicroscopy* **162**, 91–97 (2016), 1510.04594.
- ¹⁰⁰K. Nagata, K.-i. Bajo, S. Itose, M. Matsuya, M. Ishihara, K. Uchino, and H. Yurimoto, "Aberration-corrected focused ion beam for time-of-flight secondary neutral mass spectrometry," *Applied Physics Express* **12**, 085005 (2019).
- ¹⁰¹K.-i. Bajo, S. Itose, M. Matsuya, M. Ishihara, K. Uchino, M. Kudo, I. Sakaguchi, and H. Yurimoto, "High spatial resolution imaging of helium isotope by TOF-SNMS," *Surface and Interface Analysis* **48**, 1190–1193 (2016).
- ¹⁰²S. Ebata, M. Ishihara, K. Uchino, S. Itose, M. Matsuya, M. Kudo, K.-i. Bajo, and H. Yurimoto, "Development of laser ionization mass nanoscope (LIMAS)," *Surface and Interface Analysis* **44**, 635–640 (2012).
- ¹⁰³A. R. Hall, "In Situ Thickness Assessment During Ion Milling of a Free-Standing Membrane Using Transmission Helium Ion Microscopy," *Microscopy and Microanalysis* **19**, 740–744 (2013).

- ¹⁰⁴D. Emmrich, A. Beyer, A. Nadzeyka, S. Bauerdick, J. C. Meyer, J. Kotakoski, and A. Gözlhäuser, “Nanopore fabrication and characterization by helium ion microscopy,” *Applied Physics Letters* **108**, 163103 (2016).
- ¹⁰⁵T. J. Woehl, R. M. White, and R. R. Keller, “Dark-Field Scanning Transmission Ion Microscopy via Detection of Forward-Scattered Helium Ions with a Microchannel Plate,” *Microscopy and Microanalysis* **22**, 544–550 (2016).
- ¹⁰⁶K. L. Kavanagh, C. Herrmann, and J. Notte, “Camera for transmission He⁺ ion microscopy,” *J. Vac. Sci. Technol. B: Microelectron. Nanometer Struct.* **35**, 1–5 (2017).
- ¹⁰⁷J. Wang, S. H. Huang, C. Herrmann, S. A. Scott, F. Schietekatte, and K. L. Kavanagh, “Focussed helium ion channeling through Si nanomembranes,” *J. Vac. Sci. Technol. B: Microelectron. Nanometer Struct.* **36**, 1–5 (2018).
- ¹⁰⁸K. L. Kavanagh, A. Bunevich, and M. R. Motapothula, “Transmission Helium Ion Microscopy of Graphene,” (2020), arXiv:2004.01682 [physics.app-ph].
- ¹⁰⁹E. Serralta, N. Klingner, O. De Castro, M. Mousley, S. Eswara, S. Duarte Pinto, T. Wirtz, and G. Hlawacek, “Scanning transmission imaging in the helium ion microscope using a microchannel plate with a delay line detector,” *Beilstein Journal of Nanotechnology* **11**, 1854–1864 (2020).
- ¹¹⁰J. Notte, R. Hill, S. M. McVey, R. Ramachandra, B. Griffin, and D. Joy, “Diffraction Imaging in a He + Ion Beam Scanning Transmission Microscope,” *Microscopy and Microanalysis* **16**, 599–603 (2010).
- ¹¹¹S. Sijbrandij, B. Thompson, J. Notte, B. W. Ward, and N. P. Economou, “Elemental analysis with the helium ion microscope,” *J. Vac. Sci. Technol. B: Microelectron. Nanometer Struct.* **26**, 2103–2106 (2008).
- ¹¹²S. Sijbrandij, J. Notte, L. Scipioni, C. Huynh, and C. Sanford, “Analysis and metrology with a focused helium ion beam,” *J. Vac. Sci. Technol. B: Microelectron. Nanometer Struct.* **28**, 73–77 (2010).
- ¹¹³R. Heller, N. Klingner, and G. Hlawacek, “Backscattering Spectrometry in the Helium Ion Microscope: Imaging Elemental Compositions on the nm Scale,” in *Helium ion microscopy*, edited by G. Hlawacek and A. Gözlhäuser (Springer International Publishing Switzerland, 2016) pp. 265–295.
- ¹¹⁴D. C. Bell, “Contrast Mechanisms and Image Formation in Helium Ion Microscopy,” *Microscopy and Microanalysis* **15**, 147–153 (2009).
- ¹¹⁵J. W. Rabalais, *Principles and applications of ion scattering spectrometry: surface chemical and structural analysis* (Wiley, 2002) p. 344.
- ¹¹⁶S. Abo, T. Azuma, T. Lohner, F. Wakaya, and M. Takai, “Study on spatial resolution of three-dimensional analysis by full count TOF-RBS with beryllium nanoprobe,” *Nuclear Instruments and Methods in Physics Research Section B: Beam Interactions with Materials and Atoms* **273**, 266–269 (2012).
- ¹¹⁷R. van Gastel, G. Hlawacek, S. Dutta, and B. Poelsema, “Backscattered helium spectroscopy in the helium ion microscope: Principles, resolution and applications,” *Nuclear Instruments and Methods in Physics Research Section B: Beam Interactions with Materials and Atoms* **344**, 44–49 (2015).
- ¹¹⁸G. Hlawacek, V. Veligura, S. Lorbek, T. F. Mocking, A. George, R. van Gastel, H. J. W. Zandvliet, and B. Poelsema, “Imaging ultra thin layers with helium ion microscopy: Utilizing the channeling contrast mechanism,” *Beilstein Journal of Nanotechnology* **3**, 507–512 (2012).
- ¹¹⁹V. Veligura, G. Hlawacek, R. van Gastel, H. J. W. Zandvliet, and B. Poelsema, “Channeling in helium ion microscopy: Mapping of crystal orientation,” *Beilstein Journal of Nanotechnology* **3**, 501–506 (2012).
- ¹²⁰H. Hijazi, M. Li, D. Barbacci, A. Schultz, R. Thorpe, T. Gustafsson, and L. C. Feldman, “Channeling in the helium ion microscope,” *Nuclear Instruments and Methods in Physics Research Section B: Beam Interactions with Materials and Atoms* **456**, 92–96 (2019).
- ¹²¹R. van Gastel, G. Hlawacek, H. J. W. Zandvliet, and B. Poelsema, “Subsurface analysis of semiconductor structures with helium ion microscopy,” *Microelectronics Reliability* **52**, 2104–2109 (2012).
- ¹²²G. Hlawacek, V. Veligura, R. van Gastel, and B. Poelsema, “Channeling and Backscatter Imaging,” in²³, Chap. 9, pp. 205–224.
- ¹²³N. Stehling, R. Masters, Y. Zhou, R. O’Connell, C. Holland, H. Zhang, and C. Rodenburg, “New perspectives on nano-engineering by secondary electron spectroscopy in the helium ion and scanning electron microscope,” *MRS Communications* **8**, 226–240 (2018).
- ¹²⁴R. C. Masters, A. J. Pearson, T. S. Glen, F.-C. Sasam, L. Li, M. Dapor, A. M. Donald, D. G. Lidzey, and C. Rodenburg, “Sub-nanometre resolution imaging of polymer–fullerene photovoltaic blends using energy-filtered scanning electron microscopy,” *Nature Communications* **6**, 6928 (2015).
- ¹²⁵A. E. Anikeva, Y. V. Petrov, and O. F. Vyvenko, “Secondary electron energy distribution from insulators in helium ion microscope,” in *AIP Conference Proceedings* (2019) p. 020001.
- ¹²⁶T. Suzuki, M. Kudo, Y. Sakai, and T. Ichinokawa, “Material Contrast of Scanning Electron and Ion Microscope Images of Metals,” *Microscopy Today* **16**, 6–10 (2008).
- ¹²⁷N. T. H. Farr, G. M. Hughes, and C. Rodenburg, “Monitoring Carbon in Electron and Ion Beam Deposition within FIB-SEM,” *Materials* **14**, 3034 (2021).
- ¹²⁸Y. Petrov, A. Anikeva, and O. Vyvenko, “Helium ion beam induced electron emission from insulating silicon nitride films under charging conditions,” *Nuclear Instruments and Methods in Physics Research Section B: Beam Interactions with Materials and Atoms* **425**, 11–17 (2018).
- ¹²⁹Y. Petrov and O. Vyvenko, “Secondary electron emission spectra and energy selective imaging in helium ion microscope,” in *Proc. SPIE 8036*, edited by M. T. Postek, D. E. Newbury, S. F. Platek, D. C. Joy, and T. K. Mangel (2011) p. 80360O.
- ¹³⁰R. Ramachandra, B. Griffin, and D. Joy, “A model of secondary electron imaging in the helium ion scanning microscope,” *Ultramicroscopy* **109**, 748–757 (2009).
- ¹³¹A. J. Pearson, S. A. Boden, D. M. Bagnall, D. G. Lidzey, and C. Rodenburg, “Imaging the bulk nanoscale morphology of organic solar cell blends using helium ion microscopy,” *Nano Letters* **11**, 4275–4281 (2011).
- ¹³²M. Polak, “Ion-excited low-energy Auger electron emission from Ti and TiNi.pdf,” *Journal of Physics: Condensed Matter* **7**, 5275–5279 (1995).
- ¹³³R. Whaley and E. W. Thomas, “Auger spectra induced by Ne + and Ar + impact on Mg, Al, and Si,” *Journal of Applied Physics* **56**, 1505–1513 (1984).
- ¹³⁴F. Xu, P. Riccardi, A. Oliva, and A. Bonanno, “Ar L-shell and metal M-shell Auger electron emission for 14 keV Ar⁺ ion impact on Ca, Sc, Ti, V, Cr, Fe, Co, Ni, and Cu,” *Nuclear Instruments and Methods in Physics Research Section B: Beam Interactions with Materials and Atoms* **78**, 251–254 (1993).
- ¹³⁵T. E. Gallon, K. Orgassa, and J. A. D. Matthew, “Low-energy Auger electron emission from titanium induced by ion bombardment,” *Journal of Physics: Condensed Matter* **7**, 8539–8546 (1995).
- ¹³⁶H. Parvaneh and R. Hull, “Examination of ion-induced Auger electron spectra of Ti, Cr and Co in a mass-selecting Focused Ion Beam with a gold–silicon liquid metal source,” *Vacuum* **110**, 69–73 (2014).
- ¹³⁷A. Y. Pereyaslavtsev and A. V. Naumkin, “Ion-induced Auger electrons contrast on cross-beam systems,” *Semiconductor Science and Technology* **34**, 124005 (2019).
- ¹³⁸L. A. Giannuzzi, “Particle-induced x-ray analysis using focused ion beams,” *Scanning* **27**, 165–169 (2006).
- ¹³⁹L. A. Giannuzzi and B. P. Gorman, “Particle-induced x-ray emission in stainless steel using 30keV Ga⁺ focused ion beams,” *J. Vac. Sci. Technol. A: Vac. Surf. Films* **27**, 668–671 (2009).

- ¹⁴⁰T. M. W. Franklin, *Scanning Ionoluminescence Microscopy with a Helium Ion Microscope*, Ph.D. thesis, University of Southampton (2012).
- ¹⁴¹V. Veligura, G. Hlawacek, R. van Gastel, H. J. W. Zandvliet, and B. Poelsema, “A high resolution ionoluminescence study of defect creation and interaction,” *Journal of Physics: Condensed Matter* **26**, 165401 (2014).
- ¹⁴²V. Veligura, *Material characterization and modification using helium ion microscopy: various examples*, Ph.D. thesis, University Twente, Enschede, Netherlands (2014).
- ¹⁴³V. Veligura and G. Hlawacek, “Ionoluminescence,” in *Helium ion microscopy*, edited by G. Hlawacek and A. Gözlhäuser (Springer International Publishing Switzerland, 2016) pp. 325–351.
- ¹⁴⁴V. Veligura, G. Hlawacek, U. Jahn, R. van Gastel, H. J. W. Zandvliet, and B. Poelsema, “Creation and physical aspects of luminescent patterns using helium ion microscopy,” *Journal of Applied Physics* **115**, 183502 (2014).
- ¹⁴⁵S. Ogawa, T. Iijima, S. Awata, R. Sugie, N. Kawasaki, and Y. Otsuka, “Characterization of Damage in SiO₂ during Helium Ion Microscope Observation by Luminescence and TEM-EELS,” *Microscopy and Microanalysis* **18**, 814–815 (2012).
- ¹⁴⁶A. R. Waugh, A. R. Bayly, M. Walls, P. Vohralik, and D. Fathers, “RECENT DEVELOPMENTS IN THE APPLICATION OF LIQUID METAL ION SOURCES TO SIMS,” *Le Journal de Physique Colloques* **47**, C2-133–C2-136 (1986).
- ¹⁴⁷R. J. Chater, B. A. Shollock, D. S. McPhail, A. J. Smith, and G. Cooke, “Differentially pumped quadrupole SIMS probe on FIB-based and two-beam microscopes,” *Surface and Interface Analysis* **46**, 372–374 (2014).
- ¹⁴⁸A. Priebe, I. Utke, L. Pethö, and J. Michler, “Application of a gas-injection system during the FIB-TOF-SIMS analysis—influence of water vapor and fluorine gas on secondary ion signals and sputtering rates,” *Analytical Chemistry* **91**, 11712–11722 (2019).
- ¹⁴⁹A. Priebe, L. Pethö, and J. Michler, “Fluorine gas coinjection as a solution for enhancing spatial resolution of time-of-flight secondary ion mass spectrometry and separating mass interference,” *Analytical Chemistry* **92**, 2121–2129 (2020).
- ¹⁵⁰A. Priebe, E. Huszar, M. Nowicki, L. Pethö, and J. Michler, “Mechanisms of fluorine-induced separation of mass interference during TOF-SIMS analysis,” *Analytical Chemistry* **93**, 10261–10271 (2021).
- ¹⁵¹A. Priebe, J. Sastre, M. H. Futscher, J. Jurczyk, M. V. P. dos Santos, Y. E. Romanyuk, and J. Michler, “Detection of Au⁺ ions during fluorine gas-assisted time-of-flight secondary ion mass spectrometry (TOF-SIMS) for the complete elemental characterization of microbatteries,” *ACS Applied Materials & Interfaces* **13**, 41262–41274 (2021).
- ¹⁵²G. Frache, B. E. Adib, J.-N. Audinot, and H.-N. Migeon, “Evaluation of ionization yields under gallium bombardment,” *Surface and Interface Analysis* **43**, 639–642 (2010).
- ¹⁵³P. Philipp, T. Wirtz, H.-N. Migeon, and H. Scherrer, “SIMS analysis with neutral cesium deposition: Negative secondary ion sensitivity increase and quantification aspects,” *International Journal of Mass Spectrometry* **253**, 71–78 (2006).
- ¹⁵⁴F. Draude, S. Galla, A. Pelster, J. Tentschert, H. Jungnickel, A. Haase, A. Manton, A. F. Thünemann, A. Taubert, A. Luch, and H. F. Arlinghaus, “ToF-SIMS and laser-SNMS analysis of macrophages after exposure to silver nanoparticles,” *Surface and Interface Analysis* **45**, 286–289 (2012).
- ¹⁵⁵M. Franzmann, H. Bosco, L. Hamann, C. Walther, and K. Wendt, “Resonant laser-SNMS for spatially resolved and element selective ultra-trace analysis of radionuclides,” *Journal of Analytical Atomic Spectrometry* **33**, 730–737 (2018).
- ¹⁵⁶O. D. Castro, A. Biesemeier, E. Serralta, O. Bouton, R. Barrahna, Q. H. Hoang, S. Cambier, T. Taubitz, N. Klingner, G. Hlawacek, S. D. Pinto, P. Gnauck, F. Lucas, C. Bebeacua, and T. Wirtz, “npSCOPE: A new multimodal instrument for in situ correlative analysis of nanoparticles,” *Analytical Chemistry* **93**, 14417–14424 (2021).
- ¹⁵⁷F. Vollnhals, J.-N. Audinot, T. Wirtz, M. Mercier-Bonin, I. Fourquaux, B. Schroepel, U. Kraushaar, V. Lev-Ram, M. H. Ellisman, and S. Eswara, “Correlative microscopy combining secondary ion mass spectrometry and electron microscopy: Comparison of Intensity-Hue-Saturation and laplacian pyramid methods for image fusion,” *Anal. Chem.* **89**, 10702–10710 (2017).
- ¹⁵⁸G. Hlawacek, M. Jankowski, H. Wormeester, R. van Gastel, H. J. W. Zandvliet, and B. Poelsema, “Visualization of steps and surface reconstructions in Helium Ion Microscopy with atomic precision,” *Ultramicroscopy* **162**, 17–24 (2015), [arXiv:1505.00020](https://arxiv.org/abs/1505.00020).
- ¹⁵⁹X. Ma, R. Hartmann, D. J. de Aberasturi, F. Yang, S. J. H. Soenen, B. B. Manshian, J. Franz, D. Valdeperez, B. Pelaz, N. Feliu, N. Hampp, C. Riethmüller, H. Vieker, N. Frese, A. Gözlhäuser, M. Simonich, R. L. Tanguay, X.-J. Liang, and W. J. Parak, “Colloidal gold nanoparticles induce changes in cellular and subcellular morphology,” *ACS Nano* **11**, 7807–7820 (2017).
- ¹⁶⁰F. B. Bidlack, C. Huynh, J. Marshman, and B. Goetze, “Helium ion microscopy of enamel crystallites and extracellular tooth enamel matrix,” *Frontiers in Physiology* **5**, 1–10 (2014).
- ¹⁶¹C. Langlois, T. Douillard, H. Yuan, N. P. Blanchard, A. Descamps-Mandine, B. Van de Moortèle, C. Rigotti, and T. Epicier, “Crystal orientation mapping via ion channeling: An alternative to EBSD,” *Ultramicroscopy* **157**, 65–72 (2015).
- ¹⁶²C. Rodenburg, M. A. E. Jepson, S. A. Boden, and D. M. Bagnall, “Helium ion microscopy and energy selective scanning electron microscopy – two advanced microscopy techniques with complementary applications,” *Journal of Physics: Conference Series* **522**, 012049 (2014).
- ¹⁶³Y. V. Petrov and O. F. Vyvenko, “Secondary Electron Generation in the Helium Ion Microscope: Basics and Imaging,” in ²³, Chap. 5, pp. 119–146.
- ¹⁶⁴Y. V. Petrov, O. F. Vyvenko, and A. S. Bondarenko, “Scanning helium ion microscope: Distribution of secondary electrons and ion channeling,” *J. Surf. Investig.* **4**, 792–795 (2010).
- ¹⁶⁵H. Parvaneh and R. Hull, “Ion-induced Auger Electron Spectroscopy as a Potential Route to Chemical Focused-Ion Beam Tomography,” *Microscopy and Microanalysis* **20**, 310–311 (2014).
- ¹⁶⁶P. Räcke, R. Staacke, J. W. Gerlach, J. Meijer, and D. Spemann, “Image charge detection statistics relevant for deterministic ion implantation,” *Journal of Physics D: Applied Physics* **52**, 305103 (2019).
- ¹⁶⁷P. Räcke, J. Meijer, and D. Spemann, “Image charge detection of ion bunches using a segmented, cryogenic detector,” *Journal of Applied Physics* **131**, 204502 (2022).
- ¹⁶⁸T. Schenkel, A. Persaud, S. J. Park, J. Nilsson, J. Bokor, J. A. Liddle, R. Keller, D. H. Schneider, D. W. Cheng, and D. E. Humphries, “Solid state quantum computer development in silicon with single ion implantation,” *Journal of Applied Physics* **94**, 7017–7024 (2003).
- ¹⁶⁹J. C. McCallum, D. N. Jamieson, C. Yang, A. D. Alves, B. C. Johnson, T. Hopf, S. C. Thompson, and J. A. van Donkelaar, “Single-ion implantation for the development of si-based MOS-FET devices with quantum functionalities,” *Advances in Materials Science and Engineering* **2012**, 1–10 (2012).
- ¹⁷⁰T. Hopf, C. Yang, S. M. Hearne, D. N. Jamieson, E. Gauja, S. E. Andresen, and A. S. Dzurak, “Low-noise detection system for the counted implantation of single ions in silicon,” *IEEE Transactions on Nuclear Science* **55**, 812–816 (2008).
- ¹⁷¹B. C. Johnson, G. C. Tettamanzi, A. D. C. Alves, S. Thompson, C. Yang, J. Verduijn, J. A. Mol, R. Wacquez, M. Vinet, M. Sanquer, S. Rogge, and D. N. Jamieson, “Drain current modulation in a nanoscale field-effect-transistor channel by single dopant implantation,” *Applied Physics Letters* **96**, 264102 (2010).

- ¹⁷²S. Robson, P. Räcke, A. Jakob, N. Collins, H. Firgau, V. Schmitt, V. Mourik, A. Morello, E. Mayes, D. Spemann, and D. Jamieson, “Near-surface electrical characterization of silicon electronic devices using focused keV-range ions,” *Physical Review Applied* **18**, 034037 (2022).
- ¹⁷³L. A. Giannuzzi, B. I. Prenzler, and B. W. Kempshall, “Ion-solid interactions,” in ⁵⁶⁸, Chap. 2, pp. 13–52.
- ¹⁷⁴N. Yao, *Sci. Technol.*, edited by N. Yao (Cambridge University Press, Cambridge, 2007) p. 395.
- ¹⁷⁵R. GmbH, “Raith laser interferometer stage,” (2021).
- ¹⁷⁶I. Utke, S. Moshkalev, and P. Russell, eds., *Nanofabrication using focused ion and electron beams* (Oxford University Press, 2012).
- ¹⁷⁷A. Götzhäuser and G. Hlawacek, “HIM of Biological Samples,” in ²³, Chap. 7, pp. 173–185.
- ¹⁷⁸D. J. Stokes, T. Vystavel, and F. Morrissey, “Focused ion beam (FIB) milling of electrically insulating specimens using simultaneous primary electron and ion beam irradiation,” *Journal of Physics D: Applied Physics* **40**, 874–877 (2007).
- ¹⁷⁹F. J. Timmermans and C. Otto, “Contributed review: Review of integrated correlative light and electron microscopy,” *Review of Scientific Instruments* **86**, 011501 (2015).
- ¹⁸⁰R. Langford and C. Clinton, “In situ lift-out using a FIB-SEM system,” *Micron* **35**, 607–611 (2004).
- ¹⁸¹J. B. Pawley, “A dual needle piezoelectric micromanipulator for the scanning electron microscope,” *Review of Scientific Instruments* **43**, 600–602 (1972).
- ¹⁸²C. Shi, D. K. Luu, Q. Yang, J. Liu, J. Chen, C. Ru, S. Xie, J. Luo, J. Ge, and Y. Sun, “Recent advances in nanorobotic manipulation inside scanning electron microscopes,” *Microsystems & Nanoengineering* **2** (2016), 10.1038/micronano.2016.24.
- ¹⁸³C. Jiang, H. Lu, H. Zhang, Y. Shen, and Y. Lu, “Recent advances on in situ SEM mechanical and electrical characterization of low-dimensional nanomaterials,” *Scanning* **2017**, 1–11 (2017).
- ¹⁸⁴H. Stegmann, H. Dömer, R. Rosenkranz, and E. Zschech, “Efficient target preparation by combined pulsed laser ablation and FIB milling,” *Microscopy and Microanalysis* **17**, 658–659 (2011).
- ¹⁸⁵N. Stephant, R. Grissa, F. Guillou, M. Bretaudeau, Y. Borjon-Piron, J. Guillet, and P. Moreau, “New airtight transfer box for SEM experiments: Application to lithium and sodium metals observation and analyses,” *Micron* **110**, 10–17 (2018).
- ¹⁸⁶S. H. Andany, G. Hlawacek, S. Hummel, C. Brillard, M. Kangül, and G. E. Fantner, “An atomic force microscope integrated with a helium ion microscope for correlative nanoscale characterization,” *Beilstein Journal of Nanotechnology* **11**, 1272–1279 (2020), arXiv:2004.00536 [physics.ins-det].
- ¹⁸⁷H. D. Wanzenböck and S. Wai, “Focused ion beam lithography,” in *Recent Advances in Nanofabrication Techniques and Applications* (InTech, 2011).
- ¹⁸⁸M. Jamali, I. Gerhardt, M. Rezai, K. Frenner, H. Fedder, and J. Wrachtrup, “Microscopic diamond solid-immersion-lenses fabricated around single defect centers by focused ion beam milling,” *Review of Scientific Instruments* **85**, 123703 (2014).
- ¹⁸⁹R. Cui, M. Shalaginov, and A. V. Kildishev, “Nanocraft-fibstream: Focused ion beam stream file generator,” (2017).
- ¹⁹⁰V. Deinhart, L.-M. Kern, J. N. Kirchof, S. Juergensen, J. Sturm, E. Krauss, T. Feichtner, S. Kovalchuk, M. Schneider, D. Engel, B. Pfau, B. Hecht, K. I. Bolotin, S. Reich, and K. Höflich, “The patterning toolbox FIB-o-mat: Exploiting the full potential of focused helium ions for nanofabrication,” *Beilstein Journal of Nanotechnology* **12**, 304–318 (2021).
- ¹⁹¹G. Lalev, S. Dimov, J. Kettle, F. van Delft, and R. Minev, “Data preparation for focused ion beam machining of complex three-dimensional structures,” *Proceedings of the Institution of Mechanical Engineers, Part B: Journal of Engineering Manufacture* **222**, 67–76 (2008).
- ¹⁹²A. Svintsov, S. Zaitsev, G. Lalev, S. Dimov, V. Velkova, and H. Hirshy, “FIB sputtering optimization using Ion Reverse Software,” *Microelectronic Engineering* **86**, 544–547 (2009).
- ¹⁹³H.-B. Kim, “Multiple surface driving method for the accurate sculpting of predefined arbitrary surfaces in the micro/nano regime,” *Microelectronic Engineering* **91**, 14–18 (2012).
- ¹⁹⁴D. D. Felicis, M. Z. Mughal, and E. Bemporad, “A method to improve the quality of 2.5 dimensional micro-and nanostructures produced by focused ion beam machining,” *Micron* **101**, 8–15 (2017).
- ¹⁹⁵F. Niessen and M. J. B. Nancarrow, “Computer-aided manufacturing and focused ion beam technology enable machining of complex micro- and nano-structures,” *Nanotechnology* **30**, 435301 (2019).
- ¹⁹⁶S. Lindsey, S. Waid, G. Hobler, H. D. Wanzenböck, and E. Bertagnolli, *Nucl. Instrum. and Meth. Phys. Res. B* **341**, 77–83 (2014).
- ¹⁹⁷L. Scipioni, L. Stern, and J. Notte, “Applications of the helium ion microscope,” *Microscopy Today* **15**, 12–15 (2007).
- ¹⁹⁸S. A. Boden, T. M. Franklin, L. Scipioni, D. M. Bagnall, and H. N. Rutt, “Ionoluminescence in the Helium Ion Microscope,” *Microscopy and Microanalysis* **18**, 1253–1262 (2012).
- ¹⁹⁹T. L. Burnett, S. A. McDonald, A. Gholinia, R. Geurts, M. Janus, T. Slater, S. J. Haigh, C. Ornek, F. Almuaili, D. L. Engelberg, G. E. Thompson, and P. J. Withers, “Correlative tomography,” *Scientific Reports* **4** (2014), 10.1038/srep04711.
- ²⁰⁰L. Holzer and M. Cantoni, “Review of FIB tomography,” in ¹⁷⁶, Chap. 11, pp. 410–435.
- ²⁰¹D. Andersen, H. Chen, S. Pal, L. Cressa, O. D. Castro, T. Wirtz, G. Schmitz, and S. Eswara, “Correlative high-resolution imaging of hydrogen in mg₂ni hydrogen storage thin films,” *International Journal of Hydrogen Energy* **48**, 13943–13954 (2023).
- ²⁰²P. Parlanti and V. Cappello, “Microscopes, tools, probes, and protocols: A guide in the route of correlative microscopy for biomedical investigation,” *Micron* **152**, 103182 (2022).
- ²⁰³T. Ando, S. P. Bhamidimarri, N. Brending, H. Colin-York, L. Collinson, N. D. Jonge, P. J. de Pablo, E. Debroye, C. Eggeling, C. Franck, M. Fritzsche, H. Gerritsen, B. N. G. Giepmans, K. Grunewald, J. Hofkens, J. P. Hoogenboom, K. P. F. Janssen, R. Kaufmann, J. Klumperman, N. Kurniawan, J. Kusch, N. Liv, V. Parekh, D. B. Peckys, F. Rehfeldt, D. C. Reutens, M. B. J. Roeflaers, T. Salditt, I. A. T. Schaap, U. S. Schwarz, P. Verkade, M. W. Vogel, R. Wagner, M. Winterhalter, H. Yuan, and G. Zifarelli, “The 2018 correlative microscopy techniques roadmap,” *Journal of Physics D: Applied Physics* **51**, 443001 (2018).
- ²⁰⁴J. Schindelin, I. Arganda-Carreras, E. Frise, V. Kaynig, M. Longair, T. Pietzsch, S. Preibisch, C. Rueden, S. Saalfeld, B. Schmid, J.-Y. Tinevez, D. J. White, V. Hartenstein, K. Eliceiri, P. Tomancak, and A. Cardona, “Fiji: an open-source platform for biological-image analysis,” *Nature Methods* **9**, 676–682 (2012).
- ²⁰⁵F. Rohde, U.-D. Braumann, and M. Schmidt, “Correlia: an ImageJ plug-in to co-register and visualise multimodal correlative micrographs,” *Journal of Microscopy* **280**, 3–11 (2020).
- ²⁰⁶M. Schmidt, F. Rohde, and U.-D. Braumann, “Visualization and co-registration of correlative microscopy data with the ImageJ plug-in correlia,” in *Methods in Cell Biology* (Elsevier, 2021) pp. 353–388.
- ²⁰⁷COMULIS, “Correlated multimodal imaging in life sciences,” online (2023).
- ²⁰⁸BIII, “Bioimage informatics index,” online (2023), <https://biii.eu>.
- ²⁰⁹F. Lutter, P. Stahlhut, K. Dremel, S. Zabler, J. Fell, H.-G. Herrmann, and R. Hanke, “Combining X-ray Nano Tomography with focused ion beam serial section imaging — Application of correlative tomography to integrated circuits,” *Nuclear Instruments and Methods in Physics Research Section B: Beam Interactions with Materials and Atoms* **500-501**, 10–17 (2021).
- ²¹⁰R. Smith, ed., *Atomic and Ion Collisions in Solids and at Surfaces: Theory, Simulation and Applications* (Cambridge Uni-

- versity Press, Cambridge, 1997).
- ²¹¹A. V. Krashennnikov and K. Nordlund, "Ion and electron irradiation-induced effects in nanostructured materials," *J. Appl. Phys.* **107**, 071301 (2010).
- ²¹²K. Nordlund, "Historical review of computer simulation of radiation effects in materials," *Journal of Nuclear Materials* **520**, 273–295 (2019).
- ²¹³K. Nordlund and F. Djurabekova, "Multiscale modelling of irradiation in nanostructures," *Journal of Computational Electronics* **13**, 122–141 (2014).
- ²¹⁴W. Eckstein, *Computer Simulation of Ion-Solid Interactions* (Springer, Berlin, 1991).
- ²¹⁵J. F. Ziegler, J. P. Biersack, and U. Littmark, *The Stopping and Range of Ions in Solids* (Pergamon Press, New York, 1985).
- ²¹⁶W. D. Wilson, L. G. Haggmark, and J. P. Biersack, "Calculation of Nuclear Stopping, Ranges, and Straggling in the Low-Energy Region," *Phys. Rev. B* **15**, 2458–2468 (1977).
- ²¹⁷J. Lindhard and M. Scharff, "Energy Dissipation by Ions in the keV Region," *Phys. Rev.* **124**, 128–130 (1961).
- ²¹⁸J. F. Ziegler, "Particle interactions with matter," (2013).
- ²¹⁹O. S. Oen and M. T. Robinson, "Computer studies of the reflection of light ions from solids," *Nucl. Instrum. Meth.* **132**, 647–653 (1976).
- ²²⁰P. Sigmund, "Energy density and time constant of heavy-ion-induced elastic-collision spikes in solids," *Appl. Phys. Lett.* **25**, 169–171 (1974).
- ²²¹P. Sigmund, "Theory of Sputtering. I. Sputtering Yield of Amorphous and Polycrystalline Targets," *Phys. Rev.* **184**, 383–416 (1969).
- ²²²G. Hobler and G. Betz, "On the useful range of application of molecular dynamics simulations in the recoil interaction approximation," *Nucl. Instrum. Meth. Phys. Res. B* **180**, 203–208 (2001).
- ²²³G. Hobler and K. Nordlund, "Channeling maps for Si ions in Si: Assessing the binary collision approximation," *Nucl. Instrum. Meth. Phys. Res. B* **449**, 17–21 (2019).
- ²²⁴W. Eckstein and H. M. Urbassek, "Computer Simulation of the Sputtering Process," in *R. Behrisch, W. Eckstein (eds.), Sputtering by Particle Bombardment* (Springer, 2007) pp. 21–31.
- ²²⁵K. Schlueter, K. Nordlund, G. Hobler, M. Balden, F. Granberg, O. Flinck, T. da Silva, and R. Neu, "Absence of a Crystal Direction Regime in which Sputtering Corresponds to Amorphous Material," *Phys. Rev. Lett.* **125**, 225502 (2020), publisher: American Physical Society.
- ²²⁶J. P. Biersack and W. Eckstein, "Sputtering Studies with the Monte Carlo Program TRIM.SP," *Appl. Phys. A* **34**, 73–94 (1984).
- ²²⁷M. Posselt, "Dynamic simulation of damage accumulation during implantation of BF₂⁺ molecular ions into crystalline silicon," *Nucl. Instrum. Meth. Phys. Res. B* **102**, 167–172 (1995).
- ²²⁸G. Hobler, A. Simionescu, L. Palmetshofer, C. Tian, and G. Stingeder, "Boron Channeling Implantations in Silicon: Modeling of Electronic Stopping and Damage Accumulation," *J. Appl. Phys.* **77**, 3697–3703 (1995).
- ²²⁹J. P. Biersack and L. G. Haggmark, "A Monte Carlo Computer Program for the Transport of Energetic Ions in Amorphous Targets," *Nucl. Instrum. Meth.* **174**, 257–269 (1980).
- ²³⁰J. Ziegler, *SRIM - The Stopping and Range of Ions in Matter* (Lulu Press Co., 860 Aviation Parkway; Suite 300, Morrisville, NC 27560, USA, 2015).
- ²³¹W. Möller, W. Eckstein, and J. Biersack, "Tridyn - Binary collision simulation of atomic collisions and dynamic composition changes in solids," *Computer Physics Communications* **51**, 355–368 (1988).
- ²³²W. Möller and W. Eckstein, "Tridyn — A TRIM simulation code including dynamic composition changes," *Nuclear Instruments and Methods in Physics Research Section B: Beam Interactions with Materials and Atoms* **2**, 814–818 (1984).
- ²³³W. Eckstein, A. Mutzke, R. Dohmen, and R. Schneider, "SDTrimSP: A Monte-Carlo Code for Calculating Collision Phenomena in Randomized Targets," Tech. Rep. (Max-Planck-Institut für Plasmaphysik, 2007).
- ²³⁴H. Hofsäss and A. Stegmaier, "Binary collision approximation simulations of ion solid interaction without the concept of surface binding energies," *Nuclear Instruments and Methods in Physics Research Section B: Beam Interactions with Materials and Atoms* **517**, 49–62 (2022).
- ²³⁵M. Posselt, "Computer Simulation of Channeling Implantation at High and Medium Energies," *Nucl. Instrum. Meth. Phys. Res. B* **80/81**, 28–32 (1993).
- ²³⁶G. Hobler, "Monte Carlo Simulation of Two-Dimensional Implanted Dopant Distributions at Mask Edges," *Nucl. Instrum. Meth. Phys. Res. B* **96**, 155–162 (1995).
- ²³⁷G. Hobler and D. Kovac, "Dynamic binary collision simulation of focused ion beam milling of deep trenches," *Nucl. Instrum. Meth. Phys. Res. B* **269**, 1609–1613 (2011).
- ²³⁸G. Hobler, "Combined binary collision and continuum mechanics model applied to focused ion beam milling of a silicon membrane," *Nuclear Instruments and Methods in Physics Research Section B: Beam Interactions with Materials and Atoms Proceedings of the 12th International Conference on Computer Simulation of Radiation Effects in Solids, Alacant, Spain, 8-13 June, 2014*, **352**, 22–26 (2015).
- ²³⁹A. Mutzke and R. Schneider, "SDTrimSP-2D: Simulation of Particles Bombarding on a Two Dimensional Target, Version 1.0," Tech. Rep. IPP 12/4 (Max-Planck-Institut für Plasmaphysik, 2009).
- ²⁴⁰F. Schiettekatte, "Fast Monte Carlo for ion beam analysis simulations," *Nucl. Instrum. Meth. Phys. Res. B* **226**, 1880–1885 (2008).
- ²⁴¹F. Schiettekatte and M. Chicoine, "Spectrum simulation of rough and nanostructured targets from their 2D and 3D image by Monte Carlo methods," *Nuclear Instruments and Methods in Physics Research Section B: Beam Interactions with Materials and Atoms The 22nd International Conference on Ion Beam Analysis (IBA 2015)*, **371**, 106–110 (2016).
- ²⁴²M. L. Nietiadi, L. Sandoval, H. M. Urbassek, and W. Möller, "Sputtering of Si nanospheres," *Phys. Rev. B* **90**, 045417 (2014).
- ²⁴³C. Borschel and C. Ronning, "Ion beam irradiation of nanostructures – A 3D Monte Carlo simulation code," *Nucl. Instrum. Meth. Phys. Res. B* **269**, 2133–2138 (2011).
- ²⁴⁴Y. G. Li, Y. Yang, M. P. Short, Z. J. Ding, Z. Zeng, and J. Li, "IM3D: A parallel Monte Carlo code for efficient simulations of primary radiation displacements and damage in 3D geometry," *Scientific Reports* **5**, 18130 (2015).
- ²⁴⁵U. v. Toussaint, A. Mutzke, and A. Manhard, "Sputtering of rough surfaces: a 3D simulation study," *Phys. Scr.* **2017**, 014056 (2017).
- ²⁴⁶W. Möller, "TRI3DYN - Collisional computer simulation of the dynamic evolution of 3-dimensional nanostructures under ion irradiation," *Nucl. Instrum. Meth. Phys. Res. B* **322**, 23–33 (2014).
- ²⁴⁷H. Holland-Moritz, J. Graupner, W. Möller, C. Pacholski, and C. Ronning, "Dynamics of nanoparticle morphology under low energy ion irradiation," *Nanotechnology* **29**, 314002 (2018).
- ²⁴⁸W. Möller, A. Johannes, and C. Ronning, "Shaping and compositional modification of zinc oxide nanowires under energetic manganese ion irradiation," *Nanotechnology* **27**, 175301 (2016).
- ²⁴⁹D. A. Smith, D. C. Joy, and P. D. Rack, "Monte Carlo simulation of focused helium ion beam induced deposition," *Nanotechnology* **21**, 175302 (2010).
- ²⁵⁰R. Timilsina and P. D. Rack, "Monte Carlo simulations of nanoscale focused neon ion beam sputtering," *Nanotechnology* **24**, 495303 (2013).
- ²⁵¹R. Timilsina, D. A. Smith, and P. D. Rack, "A comparison of neon versus helium ion beam induced deposition via Monte

- Carlo simulations,” *Nanotechnology* **24**, 115302 (2013).
- ²⁵²R. Timilsina, S. Tan, R. Livengood, and P. D. Rack, “Monte Carlo simulations of nanoscale focused neon ion beam sputtering of copper: elucidating resolution limits and sub-surface damage,” *Nanotechnology* **25**, 485704 (2014).
- ²⁵³K. Mahady, S. Tan, Y. Greenzweig, R. Livengood, A. Raveh, and P. Rack, “Monte Carlo simulations of nanoscale Ne + ion beam sputtering: investigating the influence of surface effects, interstitial formation, and the nanostructural evolution,” *Nanotechnology* **28**, 045305 (2017).
- ²⁵⁴K. T. Mahady, S. Tan, Y. Greenzweig, A. Raveh, and P. D. Rack, “Simulating advanced focused ion beam nanomachining: a quantitative comparison of simulation and experimental results,” *Nanotechnology* **29**, 495301 (2018).
- ²⁵⁵K. Mahady, S. Tan, Y. Greenzweig, A. Raveh, and P. Rack, “Monte Carlo Simulation of Nanoscale Material Focused Ion Beam Gas-Assisted Etching: Ga+ and Ne+ Etching of SiO₂ in the Presence of a XeF₂ Precursor Gas,” *Nanoscale Adv.* **1**, 3584–3596 (2019).
- ²⁵⁶“Ion Beam Software,” ().
- ²⁵⁷H. Hofsäss, K. Zhang, and A. Mutzke, “Simulation of ion beam sputtering with SDTrimSP, TRIDYN and SRIM,” *Applied Surface Science* **310**, 134–141 (2014).
- ²⁵⁸A. M. Jakob, S. G. Robson, V. Schmitt, V. Mourik, M. Posselt, D. Spemann, B. C. Johnson, H. R. Firtg, E. Mayes, J. C. McCallum, A. Morello, and D. N. Jamieson, “Deterministic shallow dopant implantation in silicon with detection confidence upper-bound to 99.85% by ion–solid interactions,” *Advanced Materials* **34**, 2103235 (2021).
- ²⁵⁹J. D. Teresa, P. Orús, R. Córdoba, and P. Philipp, “Comparison between focused electron/ion beam-induced deposition at room temperature and under cryogenic conditions,” *Micromachines* **10**, 799 (2019), number: 12 Publisher: Multidisciplinary Digital Publishing Institute.
- ²⁶⁰J. M. D. Teresa, P. Orús, R. Córdoba, and P. Philipp, “Erratum: De teresa, j.m. et al. comparison between focused electron/ion beam-induced deposition at room temperature and under cryogenic conditions. micromachines 2019, 10, 799,” *Micromachines* **11**, 211 (2020).
- ²⁶¹A. Salvador-Porroche, S. Sangiao, P. Philipp, P. Cea, and J. M. D. Teresa, “Optimization of Pt-C Deposits by Cryo-FIBID: Substantial Growth Rate Increase and Quasi-Metallic Behaviour,” *Nanomaterials* **10**, 1906 (2020), number: 10 Publisher: Multidisciplinary Digital Publishing Institute.
- ²⁶²A. Salvador-Porroche, S. Sangiao, C. Magén, M. Barrado, P. Philipp, D. Belotcerkovtceva, M. V. Kamalakar, P. Cea, and J. M. D. Teresa, “Highly-efficient growth of cobalt nanostructures using focused ion beam induced deposition under cryogenic conditions: application to electrical contacts on graphene, magnetism and hard masking,” *Nanoscale Advances* **3**, 5656–5662 (2021), publisher: RSC.
- ²⁶³H.-B. Kim, G. Hobler, A. Steiger, A. Lugstein, and E. Bertagnolli, “Level set approach for the simulation of focused ion beam processing on the micro/nano scale,” *Nanotechnology* **18**, 265307 (2007).
- ²⁶⁴C. Ebm and G. Hobler, “Assessment of approximations for efficient topography simulation of ion beam processes: 10 keV Ar on Si,” *Nucl. Instrum. Meth. Phys. Res. B* **267**, 2987–2990 (2009).
- ²⁶⁵C. Ebm, G. Hobler, S. Waid, and H. D. Wanzenboeck, “Quantitative simulation of ion-beam induced deposition of nanostructures,” *J. Vac. Sci. Technol. B* **29**, 011031 (2011).
- ²⁶⁶S. Lindsey and G. Hobler, “The significance of redeposition and backscattering in nanostructure formation by focused ion beams,” *Nucl. Instrum. Meth. Phys. Res. B* **282**, 12–16 (2012).
- ²⁶⁷P. Li, S. Chen, H. Dai, Z. Yang, Z. Chen, Y. Wang, Y. Chen, W. Peng, W. Shan, and H. Duan, “Recent advances in focused ion beam nanofabrication for nanostructures and devices: fundamentals and applications,” *Nanoscale* **13**, 1529–1565 (2021), publisher: The Royal Society of Chemistry.
- ²⁶⁸J. Huang, M. Loeffler, U. Muehle, W. Moeller, J. J. L. Mulders, L. F. T. Kwakman, W. F. Van Dorp, and E. Zschech, “Si amorphization by focused ion beam milling: Point defect model with dynamic BCA simulation and experimental validation,” *Ultramicroscopy* **184**, 52–56 (2018).
- ²⁶⁹T. D. d. l. Rubia, R. S. Averback, R. Benedek, and W. E. King, “Role of thermal spikes in energetic displacement cascades,” *Phys. Rev. Lett.* **59**, 1930–1933 (1987).
- ²⁷⁰E.B. Tadmor and R.E. Miller, *Modeling Materials: Continuum, Atomistic and Multiscale Techniques* (Cambridge University Press, United Kingdom, 2011).
- ²⁷¹S. Ghaderzadeh, M. Ghorbani-Asl, S. Kretschmer, G. Hlawacek, and A. V. Krashennnikov, “Channeling effects in gold nanoclusters under He ion irradiation: Insights from molecular dynamics simulations,” *Nanotechnology* **31**, 035302 (2020).
- ²⁷²M. P. Allen and D. J. Tildesley, *Computer Simulation of Liquids* (Oxford University Press, Oxford, England, 1989).
- ²⁷³A. R. Leach, *Molecular modelling: principles and applications*, 2nd ed. (Pearson Education, Harlow, England, 2001).
- ²⁷⁴K. Nordlund, S. J. Zinkle, A. E. Sand, F. Granberg, R. S. Averback, R. E. Stoller, T. Suzudo, L. Malerba, F. Banhart, W. J. Weber, F. Willaime, S. L. Dudarev, and D. Simeone, “Primary radiation damage: A review of current understanding and models,” *J. Nucl. Mater.* **512**, 450–479 (2018).
- ²⁷⁵K. Nordlund, F. Djurabekova, S. T. Murphy, and D. M. Duffy, “Tools for investigating electronic excitation: experiment and multi-scale modelling,” (COST, Brussels, Belgium, 2021) Chap. Molecular dynamics for radiation effects, pp. 227–259.
- ²⁷⁶S. Plimpton, “Fast parallel algorithms for short-range molecular dynamics,” *J. Comput. Phys.* **115**, 468–472 (1995).
- ²⁷⁷A. P. Thompson, H. M. Aktulga, R. Berger, D. S. Bolintineanu, W. M. Brown, P. S. Crozier, P. J. in ’t Veld, A. Kohlmeyer, S. G. Moore, T. D. Nguyen, R. Shan, M. J. Stevens, J. Tranchida, C. Trott, and S. J. Plimpton, “LAMMPS - a flexible simulation tool for particle-based materials modeling at the atomic, meso, and continuum scales,” *Comp. Phys. Comm.* **271**, 108171 (2022).
- ²⁷⁸W. Smith and T. Forester, “Dl_poly_2.0: A general-purpose parallel molecular dynamics simulation package,” *Journal of Molecular Graphics* **14**, 136–141 (1996).
- ²⁷⁹F. Granberg, K. Nordlund, M. Ullah, K. Jin, C. Lu, H. Bei, L. Wang, F. Djurabekova, W. Weber, and Y. Zhang, “Mechanism of radiation damage reduction in equiatomic multicomponent single phase alloys,” *Phys. Rev. Lett.* **116**, 135504 (2016).
- ²⁸⁰C. Becquart, K. Decker, C. Domain, J. Ruste, Y. Souffez, J. Turbatte, and J. Duysen, “Massively parallel molecular dynamics simulations with eam potentials,” *Radiat. Eff. Defect Solid* **142**, 9–21 (1997).
- ²⁸¹D. de la Rubia and M. Guinan, “Progress in the development of a molecular dynamics code for high-energy cascade studies,” *J. Nucl. Mater.* **174**, 151–157 (1990).
- ²⁸²H. Berendsen, D. van der Spoel, and R. van Drunen, “Gromacs: A message-passing parallel molecular dynamics implementation,” *Computer Physics Communications* **91**, 43–56 (1995).
- ²⁸³J. Phillips, R. Braun, W. Wang, J. Gumbart, E. Tajkhorshid, E. Villa, C. Chipot, R. Skeel, L. Kalé, and K. Schulten, “Scalable molecular dynamics with NAMD,” *Journal of Computational Chemistry* **26**, 1781–1802 (2005), eprint: <https://onlinelibrary.wiley.com/doi/pdf/10.1002/jcc.20289>.
- ²⁸⁴G. Kresse and J. Furthmüller, “Efficiency of ab-initio total energy calculations for metals and semiconductors using a plane-wave basis set,” *Comput. Mater. Sci.* **6**, 15–50 (1996).
- ²⁸⁵P. Giannozzi, S. Baroni, N. Bonini, M. Calandra, R. Car, C. Cavazzoni, D. Ceresoli, G. L. Chiarotti, M. Cococcioni, I. Dabo, A. D. Corso, S. d. Gironcoli, S. Fabris, G. Fratesi, R. Gebauer, U. Gerstmann, C. Gougoussi, A. Kokalj, M. Lazzeri, L. Martin-Samos, N. Marzari, F. Mauri, R. Mazzarello, S. Paolini, A. Pasquarello, L. Paulatto, C. Sbraccia, S. Scandolo, G. Sclauzero, A. P. Seitsonen, A. Smogunov,

- P. Umari, and R. M. Wentzcovitch, "QUANTUM ESPRESSO: a modular and open-source software project for quantum simulations of materials," *J. Phys.: Condens. Matter* **21**, 395502 (2009).
- ²⁸⁶D. S. Sholl and J. A. Steckel, *Density Functional Theory, A Practical Introduction* (Wiley, Hoboken, NJ, 2009).
- ²⁸⁷A. J. Cohen, P. Mori-Sánchez, and W. Yang, "Challenges for density functional theory," *Chemical Reviews* **112**, 289–320 (2012).
- ²⁸⁸D. Golze, M. Dvorak, and P. Rinke, "The gw compendium: A practical guide to theoretical photoemission spectroscopy," *Frontiers in Chemistry* **7** (2019), 10.3389/fchem.2019.00377.
- ²⁸⁹F. Gao, H. Xiao, X. Zu, M. Posselt, and W. J. Weber, "Defect-enhanced charge transfer by ion-solid interactions in SiC using large-scale ab initio molecular dynamics simulations," *Phys. Rev. Lett.* **103**, 027405 (2009).
- ²⁹⁰G. Shchygol, A. Yakovlev, T. Trnka, A. C. T. van Duin, and T. Verstraelen, "ReaxFF Parameter Optimization with Monte-Carlo and Evolutionary Algorithms: Guidelines and Insights," *Journal of Chemical Theory and Computation* **15**, 6799–6812 (2019).
- ²⁹¹L. Angibaud, L. Briquet, P. Philipp, T. Wirtz, and J. Kieffer, "Parameter optimization in molecular dynamics simulations using a genetic algorithm," *Nuclear Instruments and Methods in Physics Research, Section B: Beam Interactions with Materials and Atoms* **269**, 1559–1563 (2011).
- ²⁹²A. Jaramillo-Botero, S. Naserifar, and W. A. Goddard, "General Multiobjective Force Field Optimization Framework, with Application to Reactive Force Fields for Silicon Carbide," *Journal of Chemical Theory and Computation* **10**, 1426–1439 (2014).
- ²⁹³M. Dittner, J. Müller, H. M. Aktulga, and B. Hartke, "Efficient global optimization of reactive force-field parameters," *Journal of Computational Chemistry* **36**, 1550–1561 (2015).
- ²⁹⁴H. R. Larsson, A. C. T. van Duin, and B. Hartke, "Global optimization of parameters in the reactive force field ReaxFF for SiOH," *Journal of Computational Chemistry* **34**, 2178–2189 (2013).
- ²⁹⁵J. P. Larentzos, B. M. Rice, E. F. C. Byrd, N. S. Weingarten, and J. V. Lill, "Parameterizing Complex Reactive Force Fields Using Multiple Objective Evolutionary Strategies (MOES). Part 1: ReaxFF Models for Cyclotrimethylene Trinitramine (RDX) and 1,1-Diamino-2,2-dinitroethene (FOX-7)," *Journal of Chemical Theory and Computation* **11**, 381–391 (2015).
- ²⁹⁶D. Furman, B. Carmeli, Y. Zeiri, and R. Kosloff, "Enhanced Particle Swarm Optimization Algorithm: Efficient Training of ReaxFF Reactive Force Fields," *Journal of Chemical Theory and Computation* **14**, 3100–3112 (2018).
- ²⁹⁷H. Nakata and S. Bai, "Development of a new parameter optimization scheme for a reactive force field based on a machine learning approach," *Journal of Computational Chemistry* **40**, 2000–2012 (2019).
- ²⁹⁸M. Y. Sengul, Y. Song, N. Nayir, Y. Gao, Y. Hung, T. Dasgupta, and A. C. T. van Duin, "INDEEDopt: a deep learning-based ReaxFF parameterization framework," *Computational Materials* **7**, 1–9 (2021).
- ²⁹⁹"LAMMPS Benchmarks," ().
- ³⁰⁰J. Schneider, J. Hamaekers, S. T. Chill, S. Smidstrup, J. Bulin, R. Thesen, A. Blom, and K. Stokbro, "ATK-ForceField: a new generation molecular dynamics software package," *Modelling Simul. Mater. Sci. Eng.* **25**, 085007 (2017).
- ³⁰¹J. E. Lennard-Jones, "Cohesion," *Proceedings of the Physical Society* **43**, 461–482 (1931).
- ³⁰²M. S. Daw and M. I. Baskes, "Embedded-atom method: Derivation and application to impurities, surfaces, and other defects in metals," *Phys. Rev. B* **29**, 6443–6453 (1984).
- ³⁰³F. H. Stillinger and T. A. Weber, "Computer simulation of local order in condensed phases of silicon," *Physical Review B* **31**, 5262–5271 (1985).
- ³⁰⁴J. Tersoff, "New empirical approach for the structure and energy of covalent systems," *Physical Review B* **37**, 6991–7000 (1988).
- ³⁰⁵B. van Beest and G. Kramer, "Force Fields for Silicas and Aluminophosphates Based on Ab Initio Calculations," *Phys. Rev. Lett.* **64**, 1955–1958 (1990).
- ³⁰⁶B. R. Brooks, C. L. Brooks III, A. D. Mackerell Jr., L. Nilsson, R. J. Petrella, B. Roux, Y. Won, G. Archontis, C. Bartels, S. Boresch, A. Caffisch, L. Caves, Q. Cui, A. R. Dinner, M. Feig, S. Fischer, J. Gao, M. Hodoscek, W. Im, K. Kuczera, T. Lazaridis, J. Ma, V. Ovchinnikov, E. Paci, R. W. Pastor, C. B. Post, J. Z. Pu, M. Schaefer, B. Tidor, R. M. Venable, H. L. Woodcock, X. Wu, W. Yang, D. M. York, and M. Karplus, "CHARMM: The biomolecular simulation program," *Journal of Computational Chemistry* **30**, 1545–1614 (2009), [_eprint: https://onlinelibrary.wiley.com/doi/pdf/10.1002/jcc.21287](https://onlinelibrary.wiley.com/doi/pdf/10.1002/jcc.21287).
- ³⁰⁷M. I. Baskes, "Modified embedded-atom potentials for cubic materials and impurities," *Phys. Rev. B* **46**, 2727–2742 (1992).
- ³⁰⁸J. Yu, S. B. Sinnott, and S. R. Phillpot, "Charge optimized many-body potential for the Si/SiO₂ system," *Physical Review B - Condensed Matter and Materials Physics* **75**, 1–13 (2007).
- ³⁰⁹A. C. T. Van Duin, S. Dasgupta, F. Lorant, and W. A. Goddard, "ReaxFF: A reactive force field for hydrocarbons," *Journal of Physical Chemistry A* **105**, 9396–9409 (2001), [arXiv:1011.1669v3](https://arxiv.org/abs/1011.1669v3).
- ³¹⁰L. Huang and J. Kieffer, "Molecular dynamics study of cristobalite silica using a charge transfer three-body potential: Phase transformation and structural disorder," *Journal of Chemical Physics* **118**, 1487–1498 (2003).
- ³¹¹C. Becker, Z. Trautt, and L. Hale, "NIST interatomic potentials repository," (2010), type: dataset.
- ³¹²"OpenKIM - Knowledgebase of Interatomic Models," online (2023), <https://openkim.org/>.
- ³¹³J. Behler, "Perspective: Machine learning potentials for atomistic simulations," *J. Chem. Phys.* **145**, 170901 (2016), publisher: American Institute of Physics.
- ³¹⁴Y. Mishin, "Machine-learning interatomic potentials for materials science," *Acta Materialia* **214**, 116980 (2021).
- ³¹⁵T. L. Jacobsen, M. Jorgensen, and B. Hammer, "On-the-fly machine learning of atomic potential in density functional theory structure optimization," *Physical Review Letters* **120**, 026102 (2018), publisher: American Physical Society.
- ³¹⁶J. Vandermause, S. B. Torrisi, S. Batzner, Y. Xie, L. Sun, A. M. Kolpak, and B. Kozinsky, "On-the-fly active learning of interpretable bayesian force fields for atomistic rare events," *npj Computational Materials* **6** (2020), 10.1038/s41524-020-0283-z.
- ³¹⁷A. P. Bartok, R. Kondor, and G. Csanyi, "Gaussian approximation potentials: The accuracy of quantum mechanics, without the electrons," *Phys. Rev. Lett.* **104**, 136403 (2010).
- ³¹⁸J. Byggmästar, A. Hamedani, K. Nordlund, and F. Djurabekova, "Machine-learning interatomic potential for radiation damage and defects in tungsten," *Physical Review B* **100**, 144105 (2019).
- ³¹⁹J. Byggmästar, K. Nordlund, and F. Djurabekova, "Modeling refractory high-entropy alloys with efficient machine-learned interatomic potentials: Defects and segregation," *Phys. Rev. B* **104**, 104101 (2021).
- ³²⁰J. F. Ziegler and J. P. Biersack, "The stopping and range of ions in matter," (Springer US, Boston, MA, 1985) pp. 93–129.
- ³²¹K. Nordlund, N. Runeberg, and D. Sundholm, "Repulsive interatomic potentials calculated using Hartree-Fock and density-functional theory methods," *Nucl. Instr. Meth. Phys. Res. B* **132**, 45–54 (1997).
- ³²²K. Nordlund, J. Keinonen, and T. Mattila, "Formation of ion irradiation-induced small-scale defects on graphite surfaces," *Phys. Rev. Lett.* **77**, 699 (1996).
- ³²³C. Fridlund, A. Lopez-Cazalilla, K. Nordlund, and F. Djurabekova, "Deformations related to atom mixing in Si/SiO₂/Si nanopillars under high-fluence broad-beam

- irradiation," *Phys. Rev. Mater.* **5**, 083606 (2021).
- ³²⁴X. Xu, K.-H. Heinig, W. Möller, H.-J. Engelmann, N. Klingner, A. Gharbi, R. Tiron, J. von Borany, and G. Hlawacek, "Morphology modification of Si nanopillars under ion irradiation at elevated temperatures: plastic deformation and controlled thinning to 10 nm," *Semiconductor Science and Technology* **35**, 015021 (2019).
- ³²⁵K. Das, J. B. Freund, and H. T. Johnson, "Mechanisms of material removal and mass transport in focused ion beam nanopore formation," *Journal of Applied Physics* **117**, 085304 (2015).
- ³²⁶K. Das, H. T. Johnson, and J. B. Freund, "Atomic-scale thermocapillary flow in focused ion beam milling," *Physics of Fluids (1994-present)* **27**, 052003 (2015).
- ³²⁷E. Holmström, J. Kotakoski, L. Lechner, U. Kaiser, and K. Nordlund, "Atomic-scale effects behind structural instabilities in Si lamellae during ion beam thinning," *AIP Advances* **2**, 012186–012186–13 (2012).
- ³²⁸P. R. Barry, P. Philipp, T. Wirtz, and J. Kieffer, "Mechanisms of silicon sputtering and cluster formation explained by atomic level simulations," *Journal of Mass Spectrometry* **49**, 185–194 (2014).
- ³²⁹D. A. Newsome, D. Sengupta, H. Foroutan, M. F. Russo, and A. C. T. Van Duin, "Oxidation of silicon carbide by O₂ and H₂O: A ReaxFF reactive molecular dynamics study, part i," *Journal of Physical Chemistry C* **116**, 16111–16121 (2012).
- ³³⁰A. Hamedani, J. Byggmästar, F. Djurabekova, G. Alahyarizadeh, R. Ghaderi, A. Minuchehr, and K. Nordlund, "Insights into the primary radiation damage in silicon by machine learning interatomic potential," *Mater. Res. Lett.* **8**, 364–372 (2020).
- ³³¹E. Holmström, A. Kuronen, and K. Nordlund, "Threshold defect production in silicon determined by density functional theory molecular dynamics simulations," *Phys. Rev. B* **78**, 045202 (2008).
- ³³²M. Ghorbani-Asl, S. Kretschmer, D. E. Spearot, and A. V. Krasheninnikov, "Two-dimensional MoS₂ under ion irradiation: from controlled defect production to electronic structure engineering," *2D Materials* **4**, 25078 (2017).
- ³³³S. Ghaderzadeh, S. Kretschmer, M. Ghorbani-Asl, G. Hlawacek, and A. V. Krasheninnikov, "Atomistic simulations of defect production in monolayer and bulk hexagonal boron nitride under low- and high-fluence ion irradiation," *Nanomaterials* **11** (2021), 10.3390/nano11051214.
- ³³⁴O. Lehtinen, J. Kotakoski, A. V. Krasheninnikov, A. Tolvanen, K. Nordlund, and J. Keinonen, "Effects of ion bombardment on a two-dimensional target: Atomistic simulations of graphene irradiation," *Physical Review B* **81**, 153401 (2010), publisher: American Physical Society.
- ³³⁵S. Kretschmer, M. Maslov, S. Ghaderzadeh, M. Ghorbani-Asl, G. Hlawacek, and A. V. Krasheninnikov, "Supported Two-Dimensional Materials under Ion Irradiation: The Substrate Governs Defect Production," *ACS Applied Materials & Interfaces* **10**, 30827–30836 (2018).
- ³³⁶M. Kalbac, O. Lehtinen, A. V. Krasheninnikov, and J. Keinonen, "Ion-irradiation-induced defects in isotopically-labeled two layered graphene: Enhanced in-situ annealing of the damage," *Advanced Materials* **25**, 1004–1009 (2013).
- ³³⁷S. Standop, O. Lehtinen, C. Herbig, G. Lewes-Malandrakis, F. Craes, J. Kotakoski, T. Michely, A. V. Krasheninnikov, and C. Busse, "Ion impacts on graphene/ir(111): Interface channeling, vacancy funnels, and a nanomesh," *Nano Letters* **13**, 1948–1955 (2013).
- ³³⁸O. Lehtinen, J. Kotakoski, A. V. Krasheninnikov, and J. Keinonen, "Cutting and controlled modification of graphene with ion beams," *Nanotechnology* **22**, 175306 (2011).
- ³³⁹W. Li and J. Xue, "Ion implantation of low energy Si into graphene: Insight from computational studies," *RSC Advances* **5**, 99920–99926 (2015).
- ³⁴⁰M. Tripathi, A. Markevich, R. Böttger, S. Facsko, E. Besley, J. Kotakoski, and T. Susi, "Implanting Germanium into Graphene," *ACS Nano* **12**, 4641–4647 (2018).
- ³⁴¹S. Kretschmer, S. Ghaderzadeh, S. Facsko, and A. V. Krasheninnikov, "Threshold Ion Energies for Creating Defects in 2D Materials from First-Principles Calculations: Chemical Interactions Are Important," *J. Phys. Chem. Lett.* **13**, 514–519 (2022), publisher: American Chemical Society.
- ³⁴²D. Cai, N. Grønsbech-Jensen, C. M. Snell, and K. M. Beardmore, "Phenomenological electronic stopping-power model for molecular dynamics and Monte Carlo simulation of ion implantation into silicon," *Phys. Rev. B* **54**, 17147–17157 (1996).
- ³⁴³H. Y. Chan, K. Nordlund, H. J. L. Gossmann, M. Harris, N. J. Montgomery, C. P. A. Mulcahy, S. Biswas, M. P. Srinivasan, F. Benistant, C. M. Ng, and L. Chan, "Molecular dynamics with phase-shift-based electronic stopping for calibration of ion implantation profiles in crystalline silicon," *Thin Solid Films Proceedings of The International Conference on Materials for Advanced Technologies (ICMAT 2005) Symposium H: Silicon Microelectronics: Processing to Packaging ICMAT 2005 Symposium H The International Conference on Materials for Advanced Technologies (ICMAT 2005) Symposium H: Silicon Microelectronics: Processing to Packaging*, **504**, 121–125 (2006).
- ³⁴⁴L. Sandoval and H. M. Urbassek, "Influence of electronic stopping on sputtering induced by cluster impact on metallic targets," *Phys. Rev. B* **79**, 144115 (2009).
- ³⁴⁵E. Zarkadoula, S. L. Daraszewicz, D. M. Duffy, M. A. Seaton, I. T. Todorov, K. Nordlund, M. T. Dove, and K. Trachenko, "Electronic effects in high-energy radiation damage in iron," *J. Phys.: Condens. Matter* **26**, 085401 (2014), publisher: IOP Publishing.
- ³⁴⁶A. Meftah, F. Brisard, J. M. Costantini, E. Dooryhee, M. Hage-Ali, M. Hervieu, J. P. Stoquert, F. Studer, and M. Toulemonde, "Track formation in SiO₂ quartz and the thermal-spike mechanism," *Physical Review B* **49**, 12457–12463 (1994).
- ³⁴⁷T. Jarrin, N. Richard, J. Teunissen, F. Da Pieve, and A. Hémerlyck, "Integration of electronic effects into molecular dynamics simulations of collision cascades in silicon from first-principles calculations," *Phys. Rev. B* **104**, 195203 (2021), publisher: American Physical Society.
- ³⁴⁸E. Runge and E. K. U. Gross, "Density-Functional Theory for Time-Dependent Systems," *Phys. Rev. Lett.* **52**, 997–1000 (1984), publisher: American Physical Society.
- ³⁴⁹A. Lim, W. M. C. Foulkes, A. P. Horsfield, D. R. Mason, A. Schleife, E. W. Draeger, and A. A. Correa, "The electron elevator: excitations across the band gap via a dynamical gap state," *Phys. Rev. Lett.* **116**, 043201 (2016).
- ³⁵⁰A. Tamm, G. Samolyuk, A. A. Correa, M. Klintonberg, A. Aabloo, and A. Caro, "Electron-phonon interaction within classical molecular dynamics," *Phys. Rev. B* **94**, 024305 (2016).
- ³⁵¹Sand Andrea E., Ullah Rafi, and Correa Alfredo A., "Heavy ion ranges from first-principles electron dynamics," *npj Computational Materials* **5**, 43 (2019).
- ³⁵²R. Darkins, P.-W. Ma, S. Murphy, and D. Duffy, "Simulating electronically driven structural changes in silicon with two-temperature molecular dynamics," *Physical Review B: Condensed Matter and Materials Physics* **98**, 024304 (2018).
- ³⁵³A. V. Krasheninnikov, Y. Miyamoto, and D. Tománek, "Role of electronic excitations in ion collisions with carbon nanostructures," *Physical Review Letters* **99**, 016104 (2007).
- ³⁵⁴A. Ojanpera, A. V. Krasheninnikov, and M. Puska, "Electronic stopping power from first-principles calculations with account for core electron excitations and projectile ionization," *Physical Review B* **89**, 035120 (2014).
- ³⁵⁵A. A. Correa, J. Kohanoff, E. Artacho, D. Sánchez-Portal, and A. Caro, "Nonadiabatic forces in ion-solid interactions: The initial stages of radiation damage," *Physical Review Letters* **108**, 213201 (2012).
- ³⁵⁶R. Ullah, E. Artacho, and A. A. Correa, "Core electrons in the electronic stopping of heavy ions," *Physical Review Letters* **121**, 116401 (2018).

- ³⁵⁷C.-W. Lee and A. Schleife, “Hot-electron-mediated ion diffusion in semiconductors for ion-beam nanostructuring,” *Nano Letters* **19**, 3939–3947 (2019).
- ³⁵⁸S. Kretschmer, T. Lehnert, U. Kaiser, and A. V. Krasheninnikov, “Formation of Defects in Two-Dimensional MoS₂ in the Transmission Electron Microscope at Electron Energies below the Knock-on Threshold: The Role of Electronic Excitations,” *Nano Letters* **20**, 2865–2870 (2020).
- ³⁵⁹H. Zhang, Y. Miyamoto, and A. Rubio, “Ab-initio Simulation of Helium-Ion Microscopy Images: The Case of Suspended Graphene,” *Physical Review Letters* **109**, 265505 (2012).
- ³⁶⁰G. Henkelman, B. P. Uberuaga, and H. Jonsson, “A climbing image nudged elastic band method for finding saddle points and minimum energy paths,” *The Journal of Chemical Physics* **113**, 9901–9904 (2000).
- ³⁶¹A. F. Voter, “INTRODUCTION TO THE KINETIC MONTE CARLO METHOD,” in *Radiation Effects in Solids*, NATO Science Series No. 235, edited by K. E. Sickafus, E. A. Kotomin, and B. P. Uberuaga (Springer Netherlands, 2007) pp. 1–23.
- ³⁶²A. Chatterjee and D. G. Vlachos, “An overview of spatial microscopic and accelerated kinetic Monte Carlo methods,” *Journal of Computer-Aided Materials Design* **14**, 253–308 (2007).
- ³⁶³C. S. Becquart, N. Mousseau, and C. Domain, “1.24 - kinetic monte carlo simulations of irradiation effects,” in *Comprehensive Nuclear Materials (Second Edition)*, edited by R. J. Konings and R. E. Stoller (Elsevier, Oxford, 2020) second edition ed., pp. 754–778.
- ³⁶⁴I. Martin-Bragado, R. Borges, J. P. Balbuena, and M. Jaraiz, “Kinetic Monte Carlo simulation for semiconductor processing: A review,” *Progress in Materials Science* **92**, 1–32 (2018).
- ³⁶⁵A.F. Voter, F. Montalenti, and T.C. Germann, “Extending the Time Scale in Atomistic Simulation of Materials,” *Ann. Rev. Mater. Res.* **32**, 321–346 (2002).
- ³⁶⁶H. Xu, Y. N. Osetsky, and R. E. Stoller, “Self-evolving atomistic kinetic Monte Carlo: fundamentals and applications,” *Journal of physics-condensed matter* **24**, 375402 (2012).
- ³⁶⁷Y. Zhou, K. Jolley, R. Phillips, R. Smith, and H. Wu, “Modelling defect evolution in irradiated graphite,” *Carbon* **154**, 192–202 (2019).
- ³⁶⁸C. Scott, S. Blackwell, L. Vernon, S. Kenny, M. Walls, and R. Smith, “Atomistic surface erosion and thin film growth modelled over realistic time scales,” *The Journal of Chemical Physics* **135**, 174706 (2011), publisher: American Institute of Physics.
- ³⁶⁹L. Malerba, C. Becquart, M. Hou, and C. Domain, “Comparison of algorithms for multiscale modelling of radiation damage in Fe–Cu alloys,” *Philosophical Magazine* **85**, 417–428 (2005), publisher: Taylor & Francis _eprint: <https://doi.org/10.1080/02678370412331320242>.
- ³⁷⁰I. Martin-Bragado and V. Moroz, “Facet formation during solid phase epitaxy regrowth: A lattice kinetic Monte Carlo model,” *Applied Physics Letters* **95**, 123123–123123–3 (2009).
- ³⁷¹N. Klingner, K.-H. Heinig, D. Tuchsolski, W. Möller, R. Hübner, L. Bischoff, G. Hlawacek, and S. Facsko, “Epitaxial lateral overgrowth of tin spheres driven and directly observed by helium ion microscopy,” *The Journal of Physical Chemistry C* **126**, 16332–16340 (2022).
- ³⁷²R. Böttger, K.-H. Heinig, L. Bischoff, B. Liedke, and S. Facsko, “From holes to sponge at irradiated ge surfaces with increasing ion energy - an effect of defect kinetics?” *Applied Physics A* **113**, 53–59 (2013).
- ³⁷³Z. Yang, M. A. Lively, and J. P. Allain, “Kinetic monte carlo simulation of self-organized pattern formation induced by ion beam sputtering using crater functions,” *Physical Review B* **91**, 075427 (2015).
- ³⁷⁴J. Kotakoski, C. H. Jin, O. Lehtinen, K. Suenaga, and A. V. Krasheninnikov, “Electron knock-on damage in hexagonal boron nitride monolayers,” *Physical Review B* **82**, 113404 (2010).
- ³⁷⁵X. Xu, T. Prüfer, D. Wolf, H.-J. Engelmann, L. Bischoff, R. Hübner, K.-H. Heinig, W. Möller, S. Facsko, J. v. Borany, and G. Hlawacek, “Site-controlled formation of single Si nanocrystals in a buried SiO₂ matrix using ion beam mixing,” *Beilstein J. Nanotechnol.* **9**, 2883–2892 (2018), publisher: Beilstein-Institut.
- ³⁷⁶C. Domain, C. Becquart, and L. Malerba, “Simulation of radiation damage in fe alloys: An object kinetic monte carlo approach,” *Journal of Nuclear Materials* **335**, 121–145 (2004).
- ³⁷⁷M. Aboy, L. Pelaz, E. Bruno, S. Mirabella, and S. Boninelli, “Kinetics of large B clusters in crystalline and preamorphized silicon,” *J. Appl. Phys.* **110**, 073524 (2011).
- ³⁷⁸H. Runge, “Distribution of Implanted Ions under Arbitrarily Shaped Mask Edges,” *Phys. Stat. Sol. A* **39**, 595–599 (1977).
- ³⁷⁹M. J. Vasile, R. Nassar, and J. Xie, “Focused ion beam technology applied to microstructure fabrication,” in *Papers from the Japan/U.S. workshop on formation of ion nanobeams*, Vol. 16 (AVS, Osaka (Japan), 1998) pp. 2499–2505.
- ³⁸⁰J.A. Sethian, *Level Set Methods and Fast Marching Methods*, Cambridge Monographs on Applied and Computational Mathematics (Cambridge University Press, 1999).
- ³⁸¹G. Hobler, T. Zahel, S. Lindsey, “PyTopSim,” (2011).
- ³⁸²K. P. Müller, U. Weigmann, and H. Burghause, “Simulation of focused ion beam milling,” *Microelectronic Engineering* **5**, 481–489 (1986).
- ³⁸³F. Itoh, A. Shimase, and S. Haraichi, “Two-Dimensional Profile Simulation of Focused Ion-Beam Milling of LSI,” *J. Electrochem. Soc.* **137**, 983–988 (1990).
- ³⁸⁴I. V. Katardjiev, G. Carter, M. J. Nobes, S. Berg, and H.-O. Blom, “Three-dimensional simulation of surface evolution during growth end erosion,” *J. Vac. Sci. Technol. A* **12**, 61–68 (1994).
- ³⁸⁵E. Platzgummer, A. Biedermann, H. Langfischer, S. Eder-Kapl, M. Kueimmel, S. Cernusca, H. Loeschner, C. Lehrer, L. Frey, A. Lugstein, and E. Bertagnolli, “Simulation of ion beam direct structuring for 3D nanoimprint template fabrication,” *Microelectron. Eng.* **83**, 936–939 (2006).
- ³⁸⁶H.-B. Kim, G. Hobler, A. Lugstein, and E. Bertagnolli, “Simulation of ion beam induced micro/nano fabrication,” *J. Microelectromech. Microeng.* **17**, 1178–1183 (2007).
- ³⁸⁷H.-B. Kim, G. Hobler, A. Steiger, A. Lugstein, and E. Bertagnolli, “Full three-dimensional simulation of focused ion beam micro/nanofabrication,” *Nanotechnology* **18**, 245303 (2007).
- ³⁸⁸O. Ertl, L. Filipović, and S. Selberherr, “Three-Dimensional Simulation of Focused Ion Beam Processing Using the Level Set Method,” in *Proc. SISPAD 2010* (IEEE, 2010) pp. 49–52.
- ³⁸⁹J. Sun, X. Luo, J. Ritchie, W. Chang, and W. Wang, “An investigation of redeposition effect for deterministic fabrication of nanodots by focused ion beam,” *Precision Engineering* **36**, 31–36 (2012).
- ³⁹⁰N. I. Borgardt, R. L. Volkov, A. V. Rumyantsev, and Y. A. Chaplygin, “Simulation of material sputtering with a focused ion beam,” *Tech. Phys. Lett.* **41**, 610–613 (2015).
- ³⁹¹A. V. Rumyantsev, N. I. Borgardt, R. L. Volkov, and Y. A. Chaplygin, “Study of silicon dioxide focused ion beam sputtering using electron microscopy imaging and level set simulation,” *Vacuum* **202**, 111128 (2022).
- ³⁹²C. Cupak, P. S. Szabo, H. Biber, R. Stadlmayr, C. Grave, M. Fellingner, J. Brötzner, R. A. Wilhelm, W. Möller, A. Mutzke, M. V. Moro, and F. Aumayr, “Sputter yields of rough surfaces: Importance of the mean surface inclination angle from nano- to microscopic rough regimes,” *Applied Surface Science* **515**, 151204 (2021).
- ³⁹³R. M. Bradley and H. Hofsäss, “Nanoscale patterns produced by self-sputtering of solid surfaces: The effect of ion implantation,” *J. Appl. Phys.* **120**, 074302 (2016).
- ³⁹⁴E. Mutunga, R. Winkler, J. Sattelkow, P. D. Rack, H. Plank, and J. D. Fowlkes, “Impact of Electron-Beam Heating during 3D Nanoprinting,” *ACS Nano* **13**, 5198–5213 (2019), publisher: American Chemical Society.

- ³⁹⁵A. Wolff, N. Klingner, W. Thompson, Y. Zhou, J. Lin, Y. Peng, J. Ramshaw, and Y. Xiao, "Modelling of focused ion beam induced increases in sample temperature: a case study of heat damage in biological samples," *Journal of Microscopy* **272**, 47–59 (2018), eprint: <https://onlinelibrary.wiley.com/doi/pdf/10.1111/jmi.12731>.
- ³⁹⁶I. Utke, P. Hoffmann, and J. Melngailis, "Gas-assisted focused electron beam and ion beam processing and fabrication," *J Vac Sci Technol B: Microelectron Nanometer Struct* **26**, 1197 (2008).
- ³⁹⁷I. Utke, "Continuum Models for One Adsorbate Species," in *Nanofabrication Using Focused Ion and Electron Beams: Principles and Applications*, edited by I. Utke, S. Moshkalev, and P. Russell (Oxford University Press, 2012) pp. 248–285.
- ³⁹⁸M. Toth, C. Lobo, V. Friedli, A. Szkudlarek, and I. Utke, "Continuum models of focused electron beam induced processing," *Beilstein J. Nanotechnol.* **6**, 1518–1540 (2015), publisher: Beilstein-Institut.
- ³⁹⁹K. Mahady, S. Tan, Y. Greenzweig, R. Livengood, A. Raveh, J. D. Fowlkes, and P. Rack, "Monte Carlo simulations of secondary electron emission due to ion beam milling," *Journal of Vacuum Science & Technology B* **35**, 041805 (2017).
- ⁴⁰⁰H. D. Hagstrum, "Theory of Auger Ejection of Electrons from Metals by Ions," *Phys. Rev.* **96**, 336–365 (1954), publisher: American Physical Society.
- ⁴⁰¹H. D. Hagstrum, "Theory of Auger Neutralization of Ions at the Surface of a Diamond-Type Semiconductor," *Phys. Rev.* **122**, 83–113 (1961), publisher: American Physical Society.
- ⁴⁰²M. Bercx, B. Partoens, and D. Lamoen, "Quantitative modeling of secondary electron emission from slow-ion bombardment on semiconductors," *Phys. Rev. B* **99**, 085413 (2019), publisher: American Physical Society.
- ⁴⁰³I. Utke, P. Swiderek, K. Höflich, K. Madajska, J. Jurczyk, P. Martinović, and I. B. Szymańska, "Coordination and organometallic precursors of group 10 and 11: Focused electron beam induced deposition of metals and insight gained from chemical vapour deposition, atomic layer deposition, and fundamental surface and gas phase studies," *Coordination Chemistry Reviews* , 213851 (2022).
- ⁴⁰⁴D. Sanz-Hernández and A. Fernández-Pacheco, "Modelling focused electron beam induced deposition beyond Langmuir adsorption," *Beilstein J. Nanotechnol.* **8**, 2151–2161 (2017), publisher: Beilstein-Institut.
- ⁴⁰⁵J. Bishop, C. J. Lobo, A. Martin, M. Ford, M. Phillips, and M. Toth, "Role of Activated Chemisorption in Gas-Mediated Electron Beam Induced Deposition," *Phys. Rev. Lett.* **109**, 146103 (2012), publisher: American Physical Society.
- ⁴⁰⁶I. Utke, "Febip codes," <https://www.empa.ch/web/s206/febip-codes> (2023).
- ⁴⁰⁷V. Friedli and I. Utke, "Optimized molecule supply from nozzle-based gas injection systems for focused electron- and ion-beam induced deposition and etching: simulation and experiment," *J. Phys. D Appl. Phys.* **42**, 125305 (2009).
- ⁴⁰⁸R. M. Thorman, P. Ragesh Kumar T., D. H. Fairbrother, and O. Ingólfsson, "The role of low-energy electrons in focused electron beam induced deposition: four case studies of representative precursors," *Beilstein Journal of Nanotechnology* **6**, 1904–1926 (2015), publisher: Beilstein-Institut.
- ⁴⁰⁹O. Ingólfsson, *Low-energy electrons: Fundamentals and applications* (Pan Stanford Publishing, Singapore, 2019).
- ⁴¹⁰J. A. Spencer, S. G. Rosenberg, M. Barclay, Y.-C. Wu, L. McElwee-White, and D. Howard Fairbrother, "Understanding the electron-stimulated surface reactions of organometallic complexes to enable design of precursors for electron beam-induced deposition," *Appl. Phys. A* **117**, 1631–1644 (2014).
- ⁴¹¹E. Böhrer, J. Warneke, and P. Swiderek, "Control of chemical reactions and synthesis by low-energy electrons," *Chem. Soc. Rev.* **42**, 9219–9231 (2013), publisher: The Royal Society of Chemistry.
- ⁴¹²W. F. v. Dorp, "The role of electron scattering in electron-induced surface chemistry," *Phys. Chem. Chem. Phys.* **14**, 16753–16759 (2012), publisher: The Royal Society of Chemistry.
- ⁴¹³E. Bilgiliyoy, R. M. Thorman, J.-C. Yu, T. B. Dunn, H. Marbach, L. McElwee-White, and D. H. Fairbrother, "Surface Reactions of Low-Energy Argon Ions with Organometallic Precursors," *J. Phys. Chem. C* **124**, 24795–24808 (2020), publisher: American Chemical Society.
- ⁴¹⁴A. D. Dubner, A. Wagner, J. Melngailis, and C. V. Thompson, "The role of the ion-solid interaction in ion-beam-induced deposition of gold," *J. Appl. Phys.* **70**, 665–673 (1991).
- ⁴¹⁵I. Shorubalko, L. Pillatsch, and I. Utke, "Direct-write milling and deposition with noble gases," in ²³, pp. 355–393.
- ⁴¹⁶P. F. A. Alkemade and H. Miro, "Focused helium-ion-beam-induced deposition," *Appl. Phys. A* **117**, 1727–1747 (2014).
- ⁴¹⁷S. Barth, M. Huth, and F. Jungwirth, "Precursors for direct-write nanofabrication with electrons," *J. Mater. Chem. C* **8**, 15884–15919 (2020), publisher: The Royal Society of Chemistry.
- ⁴¹⁸A. Belianinov, M. J. Burch, A. Ievlev, S. Kim, M. G. Stanford, K. Mahady, B. B. Lewis, J. D. Fowlkes, P. D. Rack, and O. S. Ovchinnikova, "Direct Write of 3D Nanoscale Mesh Objects with Platinum Precursor via Focused Helium Ion Beam Induced Deposition," *Micromachines* **11**, 527 (2020), number: 5 Publisher: Multidisciplinary Digital Publishing Institute.
- ⁴¹⁹R. Qin, J. Fu, Z. Yin, and C. Zheng, "Large-scale process optimization for focused ion beam 3-D nanofabrication," *Int J Adv Manuf Technol* **64**, 587–600 (2013).
- ⁴²⁰R. Schmied, B. Chernev, G. Trimmel, and H. Plank, "New possibilities for soft matter applications: eliminating technically induced thermal stress during FIB processing," *RSC Adv.* **2**, 6932–6938 (2012).
- ⁴²¹K.-H. Müller, "Elektronen-Mikroschreiber mit geschwindigkeitsgesteuerter Strahlführung. I," *Optik* **33**, 296–311 (1971).
- ⁴²²С. ЖДАНОВ and В.Н. ВЕРЩЕР, "ИССЛЕДОВАНИЕ МЕХАНИЗМА ОБРАЗОВАНИЯ УГЛЕВОДОРОДНЫХ ЗАГРЯЗНЕНИЙ НА ОБЪЕКТАХ, ОБЛУЧАЕМЫХ ЭЛЕКТРОНАМИ," *ИЗВЕСТИЯ АКАДЕМИИ НАУК СССР* **32**, 1091–1094 (1968).
- ⁴²³V. Aristov, N. Kislov, and I. Khodos, "Direct electron beam-induced formation of nanometer carbon structures in STEM," *Institute of Physics Conference Series* **117**, 775–780 (1991), iSSN: 0373-0751 Issue: 117.
- ⁴²⁴P. Hirsch, M. Kässens, M. Püttmann, and L. Reimer, "Contamination in a scanning electron microscope and the influence of specimen cooling," *Scanning* **16**, 101–110 (1994).
- ⁴²⁵A. Szkudlarek, W. Szmyt, C. Kapusta, and I. Utke, "Lateral resolution in focused electron beam-induced deposition: scaling laws for pulsed and static exposure," *Appl. Phys. A* **117**, 1715–1726 (2014).
- ⁴²⁶C. J. Lobo, M. Toth, R. Wagner, B. L. Thiel, and M. Lysaght, "High resolution radially symmetric nanostructures from simultaneous electron beam induced etching and deposition," *Nanotechnology* **19**, 025303 (2007), publisher: IOP Publishing.
- ⁴²⁷M. Toth, C. J. Lobo, G. Hartigan, and W. Ralph Knowles, "Electron flux controlled switching between electron beam induced etching and deposition," *Journal of Applied Physics* **101**, 054309 (2007), publisher: American Institute of Physics.
- ⁴²⁸R. Winkler, J. Fowlkes, A. Szkudlarek, I. Utke, P. D. Rack, and H. Plank, "The Nanoscale Implications of a Molecular Gas Beam during Electron Beam Induced Deposition," *ACS Appl. Mater. Interfaces* **6**, 2987–2995 (2014), publisher: American Chemical Society.
- ⁴²⁹L. Bernau, M. Gabureac, R. Erni, and I. Utke, "Tunable Nanosynthesis of Composite Materials by Electron-Impact Reaction," *Angewandte Chemie International Edition* **49**, 8880–8884 (2010), eprint: <https://onlinelibrary.wiley.com/doi/pdf/10.1002/anie.201004220>.

- ⁴³⁰C. Lobo and M. Toth, "Continuum Modeling of Electron Beam Induced Process," in *Nanofabrication Using Focused Ion and Electron Beams: Principles and Applications (I. Utke, S. Moshkalev, Ph. Russell, ed.)* (Oxford University Press, 2012) pp. 286–320.
- ⁴³¹C. Fang, Y. Xing, Z. Zhou, Q. Chai, and Q. Chen, "Structural characterization and continuous cellular automata simulation of micro structures by focused Ga ion beam induced deposition process," *Sensors and Actuators A: Physical* **312**, 112150 (2020).
- ⁴³²J. D. Fowlkes, R. Winkler, B. B. Lewis, A. Fernández-Pacheco, L. Skoric, D. Sanz-Hernández, M. G. Stanford, E. Mutunga, P. D. Rack, and H. Plank, "High-Fidelity 3D-Nanoprinting via Focused Electron Beams: Computer-Aided Design (3BD)," *ACS Appl. Nano Mater.* **1**, 1028–1041 (2018), publisher: American Chemical Society.
- ⁴³³R. Winkler, B. Lewis, J. Fowlkes, P. Rack, and H. Plank, "High-Fidelity 3D-Nanoprinting via Focused Electron Beams: Growth Fundamentals," *ACS Appl. Nano Mater.* **1**, 1014–1027 (2018), publisher: American Chemical Society.
- ⁴³⁴F. I. Allen, "A review of defect engineering, ion implantation, and nanofabrication using the helium ion microscope," *Beilstein J. Nanotechnol.* **12**, 633–664 (2021).
- ⁴³⁵J. E. E. Baglin, "Ion beam enabled nanoscale fabrication, surface patterning, and self-assembly," *Applied Physics Reviews* **7**, 011601 (2020).
- ⁴³⁶S. M. Vitale and J. D. Sugar, "Using Xe plasma FIB for High-Quality TEM sample preparation," *Microsc. Microanal.* **1**, 1–13 (2022).
- ⁴³⁷X. L. Zhong, C. A. Wade, P. J. Withers, X. Zhou, C. Cai, S. J. Haigh, and M. G. Burke, "Comparing Xe⁺ pFIB and Ga⁺ FIB for TEM sample preparation of Al alloys: Minimising FIB-induced artefacts," *J. Microsc.* (2020), 10.1111/jmi.12983.
- ⁴³⁸T. C. Pekin, F. I. Allen, and A. M. Minor, "Evaluation of neon focused ion beam milling for TEM sample preparation," *Journal of Microscopy* **264**, 59–63 (2016).
- ⁴³⁹M. K. Miller, K. F. Russell, K. Thompson, R. Alvis, and D. J. Larson, "Review of atom probe FIB-based specimen preparation methods," *Microsc. Microanal.* **13**, 428–436 (2007).
- ⁴⁴⁰J. R. Famelton, G. M. Hughes, C. A. Williams, C. Barbatti, M. P. Moody, and P. A. J. Bagot, "Xenon plasma focussed ion beam preparation of an Al-6XXX alloy sample for atom probe tomography including analysis of an α -Al(Fe,Mn)Si dispersoid," *Mater. Charact.* **178**, 111194 (2021).
- ⁴⁴¹J. E. Halpin, R. W. H. Webster, H. Gardner, M. P. Moody, P. A. J. Bagot, and D. A. MacLaren, "An in-situ approach for preparing atom probe tomography specimens by xenon plasma-focussed ion beam," *Ultramicroscopy* **202**, 121–127 (2019).
- ⁴⁴²F. Allen, J. Notte, D. Xia, P. Blanchard, R. Zhang, A. Minor, and N. Sanford, "Neon-FIB for the fabrication of tips for atom probe tomography and electron tomography," *Microsc. Microanal.* **26**, 184 (2020).
- ⁴⁴³T. L. Burnett, R. Kelley, B. Winiarski, L. Contreras, M. Daly, A. Gholinia, M. G. Burke, and P. J. Withers, "Large volume serial section tomography by Xe plasma FIB dual beam microscopy," *Ultramicroscopy* **161**, 119–129 (2016).
- ⁴⁴⁴J. E. Bradby, J. S. Williams, J. Wong-Leung, M. V. Swain, and P. Munroe, "Mechanical deformation in silicon by micro-indentation," *Journal of Materials Research* **16**, 1500–1507 (2001).
- ⁴⁴⁵J. Michler and E. Blank, "Analysis of coating fracture and substrate plasticity induced by spherical indentors: diamond and diamond-like carbon layers on steel substrates," *Thin Solid Films* **381**, 119–134 (2001).
- ⁴⁴⁶M. D. Uchic, D. M. Dimiduk, J. N. Florando, and W. D. Nix, "Sample dimensions influence strength and crystal plasticity," *Science* **305**, 986–989 (2004).
- ⁴⁴⁷J. R. Greer, W. C. Oliver, and W. D. Nix, "Size dependence of mechanical properties of gold at the micron scale in the absence of strain gradients," *Acta Materialia* **53**, 1821–1830 (2005).
- ⁴⁴⁸S. J. Lloyd, A. Castellero, F. Giuliani, Y. Long, K. K. McLaughlin, J. M. Molina-Aldareguia, N. A. Stelmashenko, L. J. Vandeperre, and W. J. Clegg, "Observations of nanoindentations via cross-sectional transmission electron microscopy: a survey of deformation mechanisms," *Proceedings of the Royal Society A: Mathematical, Physical and Engineering Sciences* **461**, 2521–2543 (2005).
- ⁴⁴⁹D. Kiener, W. Grosinger, G. Dehm, and R. Pippan, "A further step towards an understanding of size-dependent crystal plasticity: In situ tension experiments of miniaturized single-crystal copper samples," *Acta Materialia* **56**, 580–592 (2008).
- ⁴⁵⁰D. E. J. Armstrong, A. J. Wilkinson, and S. G. Roberts, "Measuring anisotropy in young's modulus of copper using microcantilever testing," *Journal of Materials Research* **24**, 3268–3276 (2009).
- ⁴⁵¹J. R. Greer, J.-Y. Kim, and M. J. Burek, "The in-situ mechanical testing of nanoscale single-crystalline nanopillars," *JOM* **61**, 19–25 (2009).
- ⁴⁵²D. Kiener, C. Motz, G. Dehm, and R. Pippan, "Overview on established and novel FIB based miniaturized mechanical testing using in-situ SEM," *International Journal of Materials Research* **100**, 1074–1087 (2009).
- ⁴⁵³F. Östlund, K. Rzepiejewska-Malyska, K. Leifer, L. M. Hale, Y. Tang, R. Ballarini, W. W. Gerberich, and J. Michler, "Brittle-to-ductile transition in uniaxial compression of silicon pillars at room temperature," *Advanced Functional Materials* **19**, 2439–2444 (2009).
- ⁴⁵⁴S. Shim, H. Bei, M. K. Miller, G. M. Pharr, and E. P. George, "Effects of focused ion beam milling on the compressive behavior of directionally solidified micropillars and the nanoindentation response of an electropolished surface," *Acta Materialia* **57**, 503–510 (2009).
- ⁴⁵⁵A. M. Korsunsky, M. Sebastiani, and E. Bemporad, "Residual stress evaluation at the micrometer scale: Analysis of thin coatings by fib milling and digital image correlation," *Surface and Coatings Technology* **205**, 2393–2403 (2010).
- ⁴⁵⁶M. Legros, D. Gianola, and C. Motz, "Quantitative in-situ mechanical testing in electron microscopes," *MRS Bulletin* **35**, 354–360 (2010).
- ⁴⁵⁷D. R. P. Singh, N. Chawla, and Y.-L. Shen, "Focused ion beam (fib) tomography of nanoindentation damage in nanoscale metal/ceramic multilayers," *Materials Characterization* **61**, 481–488 (2010).
- ⁴⁵⁸D. Kiener and A. M. Minor, "Source truncation and exhaustion: Insights from quantitative in situ TEM tensile testing," *Nano Letters* **11**, 3816–3820 (2011).
- ⁴⁵⁹J. Ast, T. Przybilla, V. Maier, K. Durst, and M. Göken, "Microcantilever bending experiments in nial – evaluation, size effects, and crack tip plasticity," *Journal of Materials Research* **29**, 2129–2140 (2014).
- ⁴⁶⁰J.-K. Heyer, S. Brinckmann, J. Pfetzinger-Micklich, and G. Eggeler, "Microshear deformation of gold single crystals," *Acta Materialia* **62**, 225–238 (2014).
- ⁴⁶¹R. Schönggrundner, R. Treml, T. Antretter, D. Kozic, W. Ecker, D. Kiener, and R. Brunner, "Critical assessment of the determination of residual stress profiles in thin films by means of the ion beam layer removal method," *Thin Solid Films* **564**, 321–330 (2014).
- ⁴⁶²J. Schwiedrzik, R. Raghavan, A. Bürki, V. LeNader, U. Wolfram, J. Michler, and P. Zysset, "In situ micropillar compression reveals superior strength and ductility but an absence of damage in lamellar bone," *Nature Materials* **13**, 740–747 (2014).
- ⁴⁶³J. P. Best, J. Zechner, I. Shorubalko, J. V. Oboňa, J. E. Wehrs, M. Morstein, and J. Michler, "A comparison of three different notching ions for small-scale fracture toughness measurement," *Scripta Materialia* **112**, 71–74 (2016).
- ⁴⁶⁴Y. Xiao, J. Wehrs, H. Ma, T. Al-Samman, S. Korte-Kerzel, M. Göken, J. Michler, R. Spolenak, and J. M. Wheeler, "Investigation of the deformation behavior of aluminum micropillars produced by focused ion beam machining using Ga and Xe ions,"

- Scripta Materialia* **127**, 191–194 (2017).
- ⁴⁶⁵J. Ast, M. Ghidelli, K. Durst, M. Göken, M. Sebastiani, and A. M. Korsunsky, “A review of experimental approaches to fracture toughness evaluation at the micro-scale,” *Materials & Design* **173**, 107762 (2019).
- ⁴⁶⁶D. Casari, L. Pethö, P. Schürch, X. Maeder, L. Philippe, J. Michler, P. Zysset, and J. Schwiedrzik, “A self-aligning microtensile setup: Application to single-crystal GaAs microscale tension–compression asymmetry,” *Journal of Materials Research* **34**, 2517–2534 (2019).
- ⁴⁶⁷S. Kalácska, J. Ast, P. D. Ispánovity, J. Michler, and X. Maeder, “3d hr-ebcd characterization of the plastic zone around crack tips in tungsten single crystals at the micron scale,” *Acta Materialia* **200**, 211–222 (2020).
- ⁴⁶⁸B. Bor, D. Giuntini, B. Domènech, A. Plunkett, M. Kampferbeck, T. Vossmeier, H. Weller, I. Scheider, and G. A. Schneider, “Constitutive and fracture behavior of ultra-strong supercrystalline nanocomposites,” *Applied Physics Reviews* **8**, 031414 (2021).
- ⁴⁶⁹E. I. Preiß, B. Merle, Y. Xiao, F. Gannott, J. P. Liebig, J. M. Wheeler, and M. Göken, “Applicability of focused ion beam (fib) milling with gallium, neon, and xenon to the fracture toughness characterization of gold thin films,” *Journal of Materials Research* **36**, 2505–2514 (2021).
- ⁴⁷⁰M. Soleimani, S. P. Maddala, M. Wismans, W.-C. Liao, L. C. A. Breemen, R. A. T. M. Benthem, and H. Friedrich, “In situ fabrication, manipulation, and mechanical characterization of free-standing silica thin films using focused ion beam scanning electron microscopy,” *Advanced Materials Interfaces* **9**, 2102201 (2022).
- ⁴⁷¹A. A. Martin, S. Randolph, A. Botman, M. Toth, and I. Aharonovich, “Maskless milling of diamond by a focused oxygen ion beam,” *Scientific Reports* **5** (2015), 10.1038/srep08958.
- ⁴⁷²M. Langridge, D. Cox, R. Webb, and V. Stolojan, “The fabrication of aspherical microlenses using focused ion-beam techniques,” *Micron* **57**, 56–66 (2014).
- ⁴⁷³P. Scholz, C. Gallrapp, U. Kerst, T. Lundquist, and C. Boit, “Optimizing focused ion beam created solid immersion lenses in bulk silicon using design of experiments,” *Microelectronics Reliability* **50**, 1441–1445 (2010).
- ⁴⁷⁴J. P. Hadden, J. P. Harrison, A. C. Stanley-Clarke, L. Marseglia, Y.-L. D. Ho, B. R. Patton, J. L. O’Brien, and J. G. Rarity, “Strongly enhanced photon collection from diamond defect centers under microfabricated integrated solid immersion lenses,” *Applied Physics Letters* **97**, 241901 (2010).
- ⁴⁷⁵L. Marseglia, J. P. Hadden, A. C. Stanley-Clarke, J. P. Harrison, B. Patton, Y.-L. D. Ho, B. Naydenov, F. Jelezko, J. Meijer, P. R. Dolan, J. M. Smith, J. G. Rarity, and J. L. O’Brien, “Nanofabricated solid immersion lenses registered to single emitters in diamond,” *Applied Physics Letters* **98**, 133107 (2011).
- ⁴⁷⁶I. Bayn, B. Meyler, J. Salzman, and R. Kalish, “Triangular nanobeam photonic cavities in single-crystal diamond,” *New Journal of Physics* **13**, 025018 (2011).
- ⁴⁷⁷J. M. Kindem, A. Ruskuc, J. G. Bartholomew, J. Rochman, Y. Q. Huan, and A. Faraon, “Control and single-shot readout of an ion embedded in a nanophotonic cavity,” *Nature* **580**, 201–204 (2020).
- ⁴⁷⁸T. Zhong, J. M. Kindem, J. G. Bartholomew, J. Rochman, I. Craiciu, E. Miyazono, M. Bettinelli, E. Cavalli, V. Verma, S. W. Nam, F. Marsili, M. D. Shaw, A. D. Beyer, and A. Faraon, “Nanophotonic rare-earth quantum memory with optically controlled retrieval,” *Science* **357**, 1392–1395 (2017).
- ⁴⁷⁹T. Zhong, J. Rochman, J. M. Kindem, E. Miyazono, and A. Faraon, “High quality factor nanophotonic resonators in bulk rare-earth doped crystals,” *Optics Express* **24**, 536 (2016).
- ⁴⁸⁰K. Keskinbora, C. Grévent, U. Eigenthaler, M. Weigand, and G. Schütz, “Rapid prototyping of fresnel zone plates via direct Ga⁺ ion beam lithography for high-resolution x-ray imaging,” *ACS Nano* **7**, 9788–9797 (2013).
- ⁴⁸¹J. Riedrich-Möller, C. Arend, C. Pauly, F. Mücklich, M. Fischer, S. Gsell, M. Schreck, and C. Becher, “Deterministic coupling of a single silicon-vacancy color center to a photonic crystal cavity in diamond,” *Nano Letters* **14**, 5281–5287 (2014).
- ⁴⁸²M. Rakhlin, S. Sorokin, D. Kazanov, I. Sedova, T. Shubina, S. Ivanov, V. Mikhailovskii, and A. Toropov, “Bright single-photon emitters with a CdSe quantum dot and multimode tapered nanoantenna for the visible spectral range,” *Nanomaterials* **11**, 916 (2021).
- ⁴⁸³K. Sloyan, H. Melkonyan, H. Apostoleris, M. S. Dahlem, M. Chiesia, and A. A. Ghaferi, “A review of focused ion beam applications in optical fibers,” *Nanotechnology* **32**, 472004 (2021).
- ⁴⁸⁴P. Romagnoli, M. Maeda, J. M. Ward, V. G. Truong, and S. N. Chormaic, “Fabrication of optical nanofibre-based cavities using focussed ion-beam milling: a review,” *Applied Physics B* **126** (2020), 10.1007/s00340-020-07456-x.
- ⁴⁸⁵Y. P. Korneeva, N. Manova, I. Florya, M. Y. Mikhailov, O. Dobrovolskiy, A. Korneev, and D. Y. Vodolazov, “Different single-photon response of wide and narrow superconducting Mo_xSi_{1-x} strips,” *Phys. Rev. Appl.* **13**, 024011 (2020).
- ⁴⁸⁶G. Bachar, I. Baskin, O. Shtempluck, and E. Buks, “Superconducting nanowire single photon detectors on-fiber,” *Appl. Phys. Lett.* **101**, 262601 (2012).
- ⁴⁸⁷M. Sivijs, M. Duwe, B. Abel, and C. Ropers, “Extreme-ultraviolet light generation in plasmonic nanostructures,” *Nature Physics* **9**, 304–309 (2013).
- ⁴⁸⁸L. Ding, J. Qin, S. Guo, T. Liu, E. Kinzel, and L. Wang, “Resonant effects in nanoscale bowtie apertures,” *Scientific Reports* **6** (2016), 10.1038/srep27254.
- ⁴⁸⁹J.-T. Lv, Y. Yan, W.-K. Zhang, Y.-H. Liu, Z.-Y. Jiang, and G.-Y. Si, “Plasmonic nanoantennae fabricated by focused ion beam milling,” *International Journal of Precision Engineering and Manufacturing* **16**, 851–855 (2015).
- ⁴⁹⁰R. Kullock, M. Ochs, P. Grimm, M. Emmerling, and B. Hecht, “Electrically-driven yagi-uda antennas for light,” *Nature Communications* **11** (2020), 10.1038/s41467-019-14011-6.
- ⁴⁹¹A. Kriesch, S. P. Burgos, D. Ploss, H. Pfeifer, H. A. Atwater, and U. Peschel, “Functional plasmonic nanocircuits with low insertion and propagation losses,” *Nano Letters* **13**, 4539–4545 (2013).
- ⁴⁹²P. Mühlischlegel, H.-J. Eisler, O. J. F. Martin, B. Hecht, and D. W. Pohl, “Resonant optical antennas,” *Science* **308**, 1607–1609 (2005).
- ⁴⁹³C. Cherqui, Y. Wu, G. Li, S. C. Quillin, J. A. Busche, N. Thakkar, C. A. West, N. P. Montoni, P. D. Rack, J. P. Camden, and D. J. Masiello, “STEM/EELS imaging of magnetic hybridization in symmetric and symmetry-broken plasmon oligomer dimers and all-magnetic fano interference,” *Nano Letters* **16**, 6668–6676 (2016).
- ⁴⁹⁴D. Simeone, M. Esposito, M. Scuderi, G. Calafiore, G. Palermo, A. D. Luca, F. Todisco, D. Sanvitto, G. Nicotra, S. Cabrini, V. Tasco, A. Passaseo, and M. Cuscunà, “Tailoring electromagnetic hot spots toward visible frequencies in ultra-narrow gap Al₂O₃ bowtie nanoantennas,” *ACS Photonics* **5**, 3399–3407 (2018).
- ⁴⁹⁵H. Kollmann, X. Piao, M. Esmann, S. F. Becker, D. Hou, C. Huynh, L.-O. Kautschor, G. Bösker, H. Vieker, A. Beyer, A. Götzhäuser, N. Park, R. Vogelgesang, M. Silies, and C. Lienau, “Toward plasmonics with nanometer precision: Non-linear optics of helium-ion milled gold nanoantennas,” *Nano Letters* **14**, 4778–4784 (2014).
- ⁴⁹⁶Y. Wang, M. Abb, S. A. Borden, J. Aizpurua, C. H. de Groot, and O. L. Muskens, “Ultrafast nonlinear control of progressively loaded, single plasmonic nanoantennas fabricated using helium ion milling,” *Nano Letters* **13**, 5647–5653 (2013).
- ⁴⁹⁷M. Melli, A. Polyakov, D. Gargas, C. Huynh, L. Scipioni, W. Bao, D. F. Ogletree, P. J. Schuck, S. Cabrini, and A. Weber-Bargioni, “Reaching the theoretical resonance quality factor limit in coaxial plasmonic nanoresonators fabricated by helium

- ion lithography," *Nano Letters* **13**, 2687–2691 (2013).
- ⁴⁹⁸C. Hahn, A. Hajebifard, and P. Berini, "Helium focused ion beam direct milling of plasmonic heptamer-arranged nanohole arrays," *Nanophotonics* **9**, 393–399 (2020).
- ⁴⁹⁹A. Hajebifard, C. Hahn, J. Walia, H. Suleman, F. Variola, A. Weck, and P. Berini, "Fano resonances in nanohole oligomers in a gold film," *Journal of Applied Physics* **129**, 033103 (2021).
- ⁵⁰⁰Y. Fu, X. Hu, C. Lu, S. Yue, H. Yang, and Q. Gong, "All-optical logic gates based on nanoscale plasmonic slot waveguides," *Nano Letters* **12**, 5784–5790 (2012).
- ⁵⁰¹C. Rewitz, G. Razinskas, P. Geisler, E. Krauss, S. Goetz, M. Pawłowska, B. Hecht, and T. Brixner, "Coherent control of plasmon propagation in a nanocircuit," *Physical Review Applied* **1**, 014007 (2014).
- ⁵⁰²P. Geisler, G. Razinskas, E. Krauss, X.-F. Wu, C. Rewitz, P. Tuchscherer, S. Goetz, C.-B. Huang, T. Brixner, and B. Hecht, "Multimode plasmon excitation and *In Situ* analysis in top-down fabricated nanocircuits," *Physical Review Letters* **111**, 183901 (2013).
- ⁵⁰³E. Krauss, G. Razinskas, D. Köck, S. Grossmann, and B. Hecht, "Reversible mapping and sorting the spin of photons on the nanoscale: A spin-optical nanodevice," *Nano Letters* **19**, 3364–3369 (2019).
- ⁵⁰⁴O. W. Kennedy, J. Burnett, J. C. Fenton, N. G. N. Constantino, P. A. Warburton, J. J. L. Morton, and E. Dupont-Ferrier, "Tunable Nb superconducting resonator based on a constriction nano-SQUID fabricated with a Ne focused ion beam," *Physical Review Applied* **11**, 014006 (2019).
- ⁵⁰⁵L. Hao, D. C. Cox, and J. C. Gallop, "Characteristics of focused ion beam nanoscale josephson devices," *Superconductor Science and Technology* **22**, 064011 (2009).
- ⁵⁰⁶L. Hao, C. Aßmann, J. C. Gallop, D. Cox, F. Ruede, O. Kazakova, P. Josephs-Franks, D. Drung, and T. Schurig, "Detection of single magnetic nanobead with a nano-superconducting quantum interference device," *Applied Physics Letters* **98**, 092504 (2011).
- ⁵⁰⁷L. Hao, J. C. Macfarlane, J. C. Gallop, D. Cox, J. Beyer, D. Drung, and T. Schurig, "Measurement and noise performance of nano-superconducting-quantum-interference devices fabricated by focused ion beam," *Applied Physics Letters* **92**, 192507 (2008).
- ⁵⁰⁸D. C. Cox, J. C. Gallop, and L. Hao, "Focused ion beam processing of superconducting junctions and SQUID based devices," *Nanofabrication* **1** (2014), 10.2478/nanofab-2014-0005.
- ⁵⁰⁹T. Godfrey, J. C. Gallop, D. C. Cox, E. J. Romans, J. Chen, and L. Hao, "Investigation of dayem bridge NanoSQUIDs made by xe focused ion beam," *IEEE Transactions on Applied Superconductivity* **28**, 1–5 (2018).
- ⁵¹⁰P. J. Heard, "Application of a focused ion beam system to defect repair of VLSI masks," *Journal of Vacuum Science & Technology B: Microelectronics and Nanometer Structures* **3**, 87 (1985).
- ⁵¹¹P. D. Prewett and P. J. Heard, "Repair of opaque defects in photomasks using focused ion beams," *Journal of Physics D: Applied Physics* **20**, 1207–1209 (1987).
- ⁵¹²J. Cleaver, H. Ahmed, P. Heard, P. Prewett, G. Dunn, and H. Kaufmann, "Focused ion beam repair techniques for clear and opaque defects in masks," *Microelectronic Engineering* **3**, 253–260 (1985).
- ⁵¹³T. Liang, A. Stivers, R. Livengood, P.-Y. Yan, G. Zhang, and F.-C. Lo, "Progress in extreme ultraviolet mask repair using a focused ion beam," *Journal of Vacuum Science & Technology B: Microelectronics and Nanometer Structures* **18**, 3216 (2000).
- ⁵¹⁴L. R. Harriott, K. D. Cummings, M. E. Gross, and W. L. Brown, "Decomposition of palladium acetate films with a microfocused ion beam," *Applied Physics Letters* **49**, 1661–1662 (1986).
- ⁵¹⁵A. Wagner, "X-ray mask repair with focused ion beams," *Journal of Vacuum Science & Technology B: Microelectronics and Nanometer Structures* **8**, 1557 (1990).
- ⁵¹⁶F. Aramaki, T. Kozakai, O. Matsuda, O. Takaoka, Y. Sugiyama, H. Oba, K. Aita, and A. Yasaka, "Photomask Repair Technology by using Gas Field Ion Source," *BACUS* **29**, 1–8 (2013).
- ⁵¹⁷F. Aramaki, T. Kozakai, O. Matsuda, A. Yasaka, S. Yoshikawa, K. Kanno, H. Miyashita, and N. Hayashi, "Performance of GFIS mask repair system for various mask materials," in *SPIE Proceedings*, edited by P. W. Ackmann and N. Hayashi (SPIE, 2014).
- ⁵¹⁸K. Edinger, K. Wolff, H. Steigerwald, N. Auth, P. Spies, J. Oster, H. Schneider, M. Budach, T. Hofmann, and M. Waiblinger, "Bringing mask repair to the next level," in *SPIE Proceedings*, edited by P. W. Ackmann and N. Hayashi (SPIE, 2014).
- ⁵¹⁹S. Tan and R. H. Livengood, "Applications of GFIS in Semiconductors," in ²³, Chap. 19, pp. 471–498.
- ⁵²⁰S. Tan, R. Hallstein, R. Livengood, H. Prakasam, L. Patel, O. Nastasescu, and C. Scheffler, "Exploring neon gfis nanomachining applications incircuit edit," in *EIPBN* (2015).
- ⁵²¹V. Iurchuk, J. Pablo-Navarro, T. Hula, R. Narkowicz, G. Hlawacek, L. Körber, A. Kákay, H. Schultheiss, J. Fassbender, K. Lenz, and J. Lindner, "Tailoring crosstalk between localized 1d spin-wave nanochannels using focused ion beams," *Scientific Reports* **13** (2023), 10.1038/s41598-022-27249-w, arXiv:2209.13180 [cond-mat.mes-hall].
- ⁵²²H. Cansever, M. S. Anwar, S. Stienen, K. Lenz, R. Narkowicz, G. Hlawacek, K. Potzger, O. Hellwig, J. Fassbender, J. Lindner, and R. Bali, "Resonance behavior of embedded and freestanding microscale ferromagnets," *Scientific Reports* **12** (2022), 10.1038/s41598-022-15959-0.
- ⁵²³A. Lara, O. V. Dobrovolskiy, J. L. Prieto, M. Huth, and F. G. Aliev, "Magnetization reversal assisted by half antivortex states in nanostructured circular cobalt disks," *Appl. Phys. Lett.* **105**, 182402 (2014).
- ⁵²⁴O. V. Dobrovolskiy, R. Sachser, S. A. Bunyayev, D. Navas, V. M. Bevez, M. Zelent, W. Śmigaj, J. Rychlý, M. Krawczyk, R. V. Vovk, M. Huth, and G. N. Kakazei, "Spin-wave phase inverter upon a single nanodefekt," *Applied Materials & Interfaces* **11**, 17654–17662 (2019).
- ⁵²⁵J. Jang, D. G. Ferguson, V. Vakaryuk, R. Budakian, S. B. Chung, P. M. Goldbart, and Y. Maeno, "Observation of half-height magnetization steps in Sr₂RuO₄," *Science* **331**, 186–188 (2011).
- ⁵²⁶Y. Yasui, K. Lahabi, V. F. Becerra, R. Fermin, M. S. Anwar, S. Yonezawa, T. Terashima, M. V. Milošević, J. Aarts, and Y. Maeno, "Spontaneous emergence of josephson junctions in homogeneous rings of single-crystal Sr₂RuO₄," *npj Quantum Materials* **5** (2020), 10.1038/s41535-020-0223-7.
- ⁵²⁷P. J. W. Moll, X. Zhu, P. Cheng, H.-H. Wen, and B. Batlogg, "Intrinsic josephson junctions in the iron-based multi-band superconductor (V₂Sr₄O₆)Fe₂As₂," *Nature Physics* **10**, 644–647 (2014).
- ⁵²⁸S. Ooi, T. Mochiku, and K. Hirata, "Periodic oscillations of josephson-vortex flow resistance in Bi₂Sr₂CaCu₂O_{8+y}," *Physical Review Letters* **89**, 247002 (2002).
- ⁵²⁹C. Putzke, M. D. Bachmann, P. McGuinness, E. Zhakina, V. Sunko, M. Konczykowski, T. Oka, R. Moessner, A. Stern, M. König, S. Khim, A. P. Mackenzie, and P. J. Moll, "h/e oscillations in interlayer transport of delafossites," *Science* **368**, 1234–1238 (2020).
- ⁵³⁰K. Geishendorf, P. Vir, C. Shekhar, C. Felser, J. I. Facio, J. van den Brink, K. Nielsch, A. Thomas, and S. T. B. Goennenwein, "Signatures of the magnetic entropy in the thermopower signals in nanoribbons of the magnetic Weyl semimetal Co₃Sn₂S₂," *Nano Letters* **20**, 300–305 (2019).
- ⁵³¹P. J. W. Moll, N. L. Nair, T. Helm, A. C. Potter, I. Kimchi, A. Vishwanath, and J. G. Analytis, "Transport evidence for Fermi-arc-mediated chirality transfer in the Dirac semimetal Cd₃As₂," *Nature* **535**, 266–270 (2016).
- ⁵³²J. Gooth, A. C. Niemann, T. Meng, A. G. Grushin, K. Landsteiner, B. Gotsmann, F. Menges, M. Schmidt, C. Shekhar,

- V. Süß, R. Hühne, B. Rellinghaus, C. Felser, B. Yan, and K. Nielsch, “Experimental signatures of the mixed axial-gravitational anomaly in the weyl semimetal NbP,” *Nature* **547**, 324–327 (2017).
- ⁵³³J. Y. Liu, J. Yu, J. L. Ning, H. M. Yi, L. Miao, L. J. Min, Y. F. Zhao, W. Ning, K. A. Lopez, Y. L. Zhu, T. Pillsbury, Y. B. Zhang, Y. Wang, J. Hu, H. B. Cao, B. C. Chakoumakos, F. Balakirev, F. Weickert, M. Jaime, Y. Lai, K. Yang, J. W. Sun, N. Alem, V. Gopalan, C. Z. Chang, N. Samarth, C. X. Liu, R. D. McDonald, and Z. Q. Mao, “Spin-valley locking and bulk quantum hall effect in a noncentrosymmetric dirac semimetal BaMnSb₂,” *Nature Communications* **12** (2021), 10.1038/s41467-021-24369-1.
- ⁵³⁴P. J. W. Moll, R. Puzniak, F. Balakirev, K. Rogacki, J. Karpinski, N. D. Zhigadlo, and B. Batlogg, “High magnetic-field scales and critical currents in SmFeAs(O, F) crystals,” *Nature Materials* **9**, 628–633 (2010).
- ⁵³⁵J. Jaroszynski, F. Hunte, L. Balicas, Y. jung Jo, I. Raičević, A. Gurevich, D. C. Larbalestier, F. F. Balakirev, L. Fang, P. Cheng, Y. Jia, and H. H. Wen, “Upper critical fields and thermally-activated transport of NdFeAsO_{0.7}F_{0.3} single crystal,” *Physical Review B* **78**, 174523 (2008).
- ⁵³⁶H. Yang, M. Schmidt, V. Süß, M. Chan, F. F. Balakirev, R. D. McDonald, S. S. P. Parkin, C. Felser, B. Yan, and P. J. W. Moll, “Quantum oscillations in the type-II dirac semi-metal candidate PtSe₂,” *New Journal of Physics* **20**, 043008 (2018).
- ⁵³⁷Y. Maeno, T. Ando, Y. Mori, E. Ohmichi, S. Ikeda, S. NishiZaki, and S. Nakatsui, “Enhancement of superconductivity of Sr₂RuO₄ to 3 K by embedded metallic microdomains,” *Physical Review Letters* **81**, 3765–3768 (1998).
- ⁵³⁸M. R. van Delft, M. D. Bachmann, C. Putzke, C. Guo, J. A. W. Straquadine, E. D. Bauer, F. Ronning, and P. J. W. Moll, “Controlling superconductivity of CeIrIn₅ microstructures by substrate selection,” *Applied Physics Letters* **120**, 092601 (2022).
- ⁵³⁹M. D. Bachmann, G. M. Ferguson, F. Theuss, T. Meng, C. Putzke, T. Helm, K. R. Shirer, Y.-S. Li, K. A. Modic, M. Nicklas, M. König, D. Low, S. Ghosh, A. P. Mackenzie, F. Arnold, E. Hassinger, R. D. McDonald, L. E. Winter, E. D. Bauer, F. Ronning, B. J. Ramshaw, K. C. Nowack, and P. J. W. Moll, “Spatial control of heavy-fermion superconductivity in CeIrIn₅,” *Science* **366**, 221–226 (2019).
- ⁵⁴⁰A. Pautrat, J. Scola, C. Goupil, C. Simon, C. Villard, B. Domengès, Y. Simon, C. Guilpin, and L. Méchin, “Quantitative analysis of the critical current due to vortex pinning by surface corrugation,” *Phys. Rev. B* **69**, 224504–1–5 (2004).
- ⁵⁴¹O. V. Dobrovolskiy, “Abrikosov fluxonics in washboard nanolandscapes,” *Physica C* **533**, 80–90 (2017).
- ⁵⁴²O. V. Dobrovolskiy and M. Huth, “Dual cut-off direct current-tunable microwave low-pass filter on superconducting Nb microstrips with asymmetric nanogrooves,” *Appl. Phys. Lett.* **106**, 142601–1–5 (2015).
- ⁵⁴³O. V. Dobrovolskiy, E. Begun, M. Huth, and V. A. Shklovskij, “Electrical transport and pinning properties of Nb thin films patterned with focused ion beam-milled washboard nanostructures,” *New J. Phys.* **14**, 113027–1–27 (2012).
- ⁵⁴⁴J. A. Veerman, A. M. Otter, L. Kuipers, and N. F. van Hulst, “High definition aperture probes for near-field optical microscopy fabricated by focused ion beam milling,” *Appl. Phys. Lett.* **72**, 3115–3117 (1998).
- ⁵⁴⁵M. Mivelle, T. S. van Zanten, L. Neumann, N. F. van Hulst, and M. F. Garcia-Parajo, “Ultrabright bowtie nanoaperture antenna probes studied by single molecule fluorescence,” *Nano Lett.* **12**, 5972–5978 (2012).
- ⁵⁴⁶T. H. Taminiou, R. J. Moerland, F. B. Segerink, L. Kuipers, and N. F. van Hulst, “ $\lambda/4$ resonance of an optical monopole antenna probed by single molecule fluorescence,” *Nano Letters* **7**, 28–33 (2006).
- ⁵⁴⁷T. S. van Zanten, M. J. Lopez-Bosque, and M. F. Garcia-Parajo, “Imaging individual proteins and nanodomains on intact cell membranes with a probe-based optical antenna,” *Small* **6**, 270–275 (2010).
- ⁵⁴⁸J. N. Farahani, H.-J. Eisler, D. W. Pohl, M. Pavius, P. Flückiger, P. Gasser, and B. Hecht, “Bow-tie optical antenna probes for single-emitter scanning near-field optical microscopy,” *Nanotechnology* **18**, 125506 (2007).
- ⁵⁴⁹B. Hoffmann, S. Vasant, X.-W. Chen, S. Götzinger, V. Sandoghdar, and S. Christiansen, “Fabrication and characterization of plasmonic nanocone antennas for strong spontaneous emission enhancement,” *Nanotechnology* **26**, 404001 (2015).
- ⁵⁵⁰S. Schmidt, B. Piglosiewicz, D. Sadiq, J. Shirdel, J. S. Lee, P. Vasa, N. Park, D.-S. Kim, and C. Lienau, “Adiabatic nanofocusing on ultrasmooth single-crystalline gold tapers creates a 10-nm-sized light source with few-cycle time resolution,” *ACS Nano* **6**, 6040–6048 (2012).
- ⁵⁵¹J. A. Grant-Jacob, S. Z. Oo, F. Carpignano, S. A. Boden, W. S. Brocklesby, M. D. B. Charlton, and T. Melvin, “Design and fabrication of a 3d-structured gold film with nanopores for local electric field enhancement in the pore,” *Nanotechnology* **27**, 065302 (2016).
- ⁵⁵²B. S. Archanjo, T. L. Vasconcelos, B. S. Oliveira, S. Song, F. I. Allen, C. A. Achete, and P. Ercius, “Plasmon 3D electron tomography and local Electric-Field enhancement of engineered plasmonic nanoantennas,” *ACS Photonics* **7**, 2834–2842 (2018).
- ⁵⁵³S. Geaney, D. Cox, T. Hönlgl-Decrinis, R. Shaikhaidarov, S. E. Kubatkin, T. Lindström, A. V. Danilov, and S. E. de Graaf, “Near-field scanning microwave microscopy in the single photon regime,” *Scientific Reports* **9** (2019), 10.1038/s41598-019-48780-3.
- ⁵⁵⁴A. Meister, M. Liley, J. Brugger, R. Pugin, and H. Heinzelmann, “Nanodispenser for attoliter volume deposition using atomic force microscopy probes modified by focused-ion-beam milling,” *Appl. Phys. Lett.* **85**, 6260–6262 (2004).
- ⁵⁵⁵O. Guillaume-Gentil, E. Potthoff, D. Ossola, C. M. Franz, T. Zambelli, and J. A. Vorholt, “Force-controlled manipulation of single cells: from AFM to FluidFM,” *Trends Biotechnol.* **32**, 381–388 (2014).
- ⁵⁵⁶A. Persaud, S. J. Park, J. A. Liddle, T. Schenkel, J. Bokor, and I. W. Rangelow, “Integration of scanning probes and ion beams,” *Nano Lett.* **5**, 1087–1091 (2005).
- ⁵⁵⁷A. Wang and M. J. Butte, “Customized atomic force microscopy probe by focused-ion-beam-assisted tip transfer,” *Appl. Phys. Lett.* **105**, 053101 (2014).
- ⁵⁵⁸P. Kunicki, T. Angelov, T. Ivanov, T. Gotszalk, and I. Rangelow, “Sensitivity improvement to active piezoresistive AFM probes using focused ion beam processing,” *Sensors* **19** (2019), 10.3390/s19204429.
- ⁵⁵⁹H. Corte-León, L. A. Rodríguez, M. Pancaldi, C. Gatel, D. Cox, E. Snoeck, V. Antonov, P. Vavassori, and O. Kazakova, “Magnetic imaging using geometrically constrained nano-domain walls,” *Nanoscale* **11**, 4478–4488 (2019).
- ⁵⁶⁰J. N. Kirchof, K. Weinel, S. Heeg, V. Deinhart, S. Kovalchuk, K. Höflich, and K. I. Bolotin, “Tunable graphene phononic crystal,” *Nano Letters* **21**, 2174–2182 (2021).
- ⁵⁶¹D. Miller, A. Blaikie, B. Carter, and B. Aleman, “Engineering the modal shape of graphene nanoelectromechanical systems using focused ion beam milling,” in *2018 IEEE 13th Nanotechnology Materials and Devices Conference (NMDC)* (IEEE, 2018).
- ⁵⁶²C. A. Volkert and A. M. Minor, “Focused ion beam microscopy and micromachining,” *MRS Bull.* **32**, 389–399 (2007).
- ⁵⁶³F. Lenrick, M. Ek, D. Jacobsson, M. T. Borgström, and L. R. Wallenberg, “FIB plan and side view cross-sectional TEM sample preparation of nanostructures,” *Microscopy and Microanalysis* **20**, 133–140 (2013).
- ⁵⁶⁴M. Schaffer, B. Schaffer, and Q. Ramasse, “Sample preparation for atomic-resolution STEM at low voltages by FIB,” *Ultramicroscopy* **114**, 62–71 (2012).
- ⁵⁶⁵K. A. Unocic, M. J. Mills, and G. S. Daehn, “Effect of gallium focused ion beam milling on preparation of aluminium thin foils,” *J. Microsc.* **240**, 227–238 (2010).

- ⁵⁶⁶R. Hugo and R. Hoagland, “In-situ TEM observation of aluminum embrittlement by liquid gallium,” *Scripta Materialia* **38**, 523–529 (1998).
- ⁵⁶⁷M. D. Uchic, L. Holzer, B. J. Inkson, E. L. Principe, and P. Munroe, “Three-dimensional microstructural characterization using focused ion beam tomography,” *MRS Bulletin* **32**, 408–416 (2007).
- ⁵⁶⁸L. A. Giannuzzi and F. A. Stevie, *Introduction to Focused Ion Beams*, 1st ed., edited by L. A. Giannuzzi and F. A. Stevie (Kluwer Academic Publishers, Boston, 2005) pp. 1–357.
- ⁵⁶⁹M. D. Uchic and D. M. Dimiduk, “A methodology to investigate size scale effects in crystalline plasticity using uniaxial compression testing,” *Materials Science and Engineering: A* **400-401**, 268–278 (2005).
- ⁵⁷⁰J. Hütsch and E. T. Lilleodden, “The influence of focused-ion beam preparation technique on microcompression investigations: Lathe vs. annular milling,” *Scripta Materialia* **77**, 49–51 (2014).
- ⁵⁷¹L. Novotny and B. Hecht, *Principles of Nano-Optics* (Cambridge University Press, 2012).
- ⁵⁷²F. J. Garcia-Vidal, L. Martin-Moreno, T. W. Ebbesen, and L. Kuipers, “Light passing through subwavelength apertures,” *Reviews of Modern Physics* **82**, 729–787 (2010).
- ⁵⁷³L. Novotny and N. van Hulst, “Antennas for light,” *Nature Photonics* **5**, 83–90 (2011).
- ⁵⁷⁴K. Kneipp, Y. Wang, H. Kneipp, L. T. Perelman, I. Itzkan, R. R. Dasari, and M. S. Feld, “Single molecule detection using surface-enhanced raman scattering (SERS),” *Physical Review Letters* **78**, 1667–1670 (1997).
- ⁵⁷⁵D. Punj, M. Mivelle, S. B. Moparthy, T. S. van Zanten, H. Rigneault, N. F. van Hulst, M. F. García-Parajó, and J. Wenger, “A plasmonic ‘antenna-in-box’ platform for enhanced single-molecule analysis at micromolar concentrations,” *Nature Nanotechnology* **8**, 512–516 (2013).
- ⁵⁷⁶P. Ghenuche, M. Mivelle, J. de Torres, S. B. Moparthy, H. Rigneault, N. F. V. Hulst, M. F. García-Parajó, and J. Wenger, “Matching nanoantenna field confinement to FRET distances enhances forster energy transfer rates,” *Nano Letters* **15**, 6193–6201 (2015).
- ⁵⁷⁷J.-S. Huang, V. Callegari, P. Geisler, C. Brüning, J. Kern, J. C. Prangma, X. Wu, T. Feichtner, J. Ziegler, P. Weinmann, M. Kamp, A. Forchel, P. Biagioni, U. Sennhauser, and B. Hecht, “Atomically flat single-crystalline gold nanostructures for plasmonic nanocircuitry,” *Nature Communications* **1** (2010), 10.1038/ncomms1143.
- ⁵⁷⁸J. Kern, R. Kullock, J. Prangma, M. Emmerling, M. Kamp, and B. Hecht, “Electrically driven optical antennas,” *Nature Photonics* **9**, 582–586 (2015).
- ⁵⁷⁹C. Schörner, S. Adhikari, and M. Lippitz, “A single-crystalline silver plasmonic circuit for visible quantum emitters,” *Nano Letters* **19**, 3238–3243 (2019).
- ⁵⁸⁰M. Ochs, L. Zurak, E. Krauss, J. Meier, M. Emmerling, R. Kullock, and B. Hecht, “Nanoscale electrical excitation of distinct modes in plasmonic waveguides,” *Nano Letters* **21**, 4225–4230 (2021).
- ⁵⁸¹M. Horák, K. Bukvišová, V. Švarc, J. Jaskowiec, V. Krápek, and T. Šikola, “Comparative study of plasmonic antennas fabricated by electron beam and focused ion beam lithography,” *Scientific Reports* **8** (2018), 10.1038/s41598-018-28037-1.
- ⁵⁸²Y. Chen, X. Yang, and J. Gao, “3d janus plasmonic helical nanoapertures for polarization-encrypted data storage,” *Light: Science & Applications* **8** (2019), 10.1038/s41377-019-0156-8.
- ⁵⁸³L. Xia, W. Wu, J. Xu, Y. Hao, and Y. Wang, “3d nanohelix fabrication and 3d nanometer assembly by focused ion beam stress-introducing technique,” in *19th IEEE International Conference on Micro Electro Mechanical Systems* (IEEE, 2006).
- ⁵⁸⁴J. Li and Z. Liu, “Focused-ion-beam-based nano-kirigami: from art to photonics,” *Nanophotonics* **7**, 1637–1650 (2018).
- ⁵⁸⁵O. Scholder, K. Jefimovs, I. Shorubalko, C. Hafner, U. Sennhauser, and G.-L. Bona, “Helium focused ion beam fabricated plasmonic antennas with sub-5 nm gaps,” *Nanotechnology* **24**, 395301 (2013).
- ⁵⁸⁶Y. Chen, K. Bi, Q. Wang, M. Zheng, Q. Liu, Y. Han, J. Yang, S. Chang, G. Zhang, and H. Duan, “Rapid focused ion beam milling based fabrication of plasmonic nanoparticles and assemblies via “sketch and peel” strategy,” *ACS Nano* **10**, 11228–11236 (2016).
- ⁵⁸⁷F. Laible, C. Dreser, D. P. Kern, and M. Fleischer, “Time-effective strategies for the fabrication of poly- and single-crystalline gold nano-structures by focused helium ion beam milling,” *Nanotechnology* **30**, 235302 (2019).
- ⁵⁸⁸Y. Chen, Y. Hu, J. Zhao, Y. Deng, Z. Wang, X. Cheng, D. Lei, Y. Deng, and H. Duan, “Topology optimization-based inverse design of plasmonic nanodimer with maximum near-field enhancement,” *Advanced Functional Materials* **30**, 2000642 (2020).
- ⁵⁸⁹M. Gittinger, K. Höflich, V. Smirnov, H. Kollmann, C. Lienau, and M. Silies, “Strongly coupled, high-quality plasmonic dimer antennas fabricated using a sketch-and-peel technique,” *Nanophotonics* **9**, 401–412 (2020).
- ⁵⁹⁰H. G. Frey, F. Keilmann, A. Kriele, and R. Guckenberger, “Enhancing the resolution of scanning near-field optical microscopy by a metal tip grown on an aperture probe,” *Applied Physics Letters* **81**, 5030–5032 (2002).
- ⁵⁹¹H. G. Frey, S. Witt, K. Felderer, and R. Guckenberger, “High-resolution imaging of single fluorescent molecules with the optical near-field of a metal tip,” *Physical Review Letters* **93**, 200801 (2004).
- ⁵⁹²D. N. Basov, R. D. Averitt, and D. Hsieh, “Towards properties on demand in quantum materials,” *Nature Materials* **16**, 1077–1088 (2017).
- ⁵⁹³F. Giustino, J. H. Lee, F. Trier, M. Bibes, S. M. Winter, R. Valentí, Y.-W. Son, L. Taillefer, C. Heil, A. I. Figueroa, B. Plaçais, Q. Wu, O. V. Yazyev, E. P. A. M. Bakkers, J. Nygård, P. Forn-Díaz, S. D. Franceschi, J. W. McIver, L. E. F. F. Torres, T. Low, A. Kumar, R. Galceran, S. O. Valenzuela, M. V. Costache, A. Manchon, E.-A. Kim, G. R. Schleder, A. Fazzio, and S. Roche, “The 2021 quantum materials roadmap,” *Journal of Physics: Materials* **3**, 042006 (2020).
- ⁵⁹⁴P. J. Moll, “Focused ion beam microstructuring of quantum matter,” *Annual Review of Condensed Matter Physics* **9**, 147–162 (2018).
- ⁵⁹⁵A. Noah, F. Toric, T. D. Feld, G. Zissman, A. Gutfreund, D. Tsruya, T. R. Devidas, H. Alpern, A. Vakahi, H. Steinberg, M. E. Huber, J. G. Analytis, S. Gazit, E. Lachman, and Y. Anahory, “Tunable exchange bias in the magnetic Weyl semimetal $\text{Co}_3\text{Sn}_2\text{S}_2$,” *Physical Review B* **105**, 144423 (2022).
- ⁵⁹⁶N. L. Nair, E. Maniv, C. John, S. Doyle, J. Orenstein, and J. G. Analytis, “Electrical switching in a magnetically intercalated transition metal dichalcogenide,” *Nature Materials* **19**, 153–157 (2019).
- ⁵⁹⁷N. L. Nair, E. Maniv, C. John, S. Doyle, J. Orenstein, and J. G. Analytis, “Author correction: Electrical switching in a magnetically intercalated transition metal dichalcogenide,” *Nature Materials* **19**, 1036–1036 (2020).
- ⁵⁹⁸F. Ronning, T. Helm, K. R. Shirer, M. D. Bachmann, L. Balicas, M. K. Chan, B. J. Ramshaw, R. D. McDonald, F. F. Balakirev, M. Jaime, E. D. Bauer, and P. J. W. Moll, “Electronic in-plane symmetry breaking at field-tuned quantum criticality in CeRhIn_5 ,” *Nature* **548**, 313–317 (2017).
- ⁵⁹⁹J. H. Orloff, M. Utlaut, and L. W. Swanson, *High Resolution Focused Ion Beams: FIB and its Applications* (Springer US, Boston, MA, 2003).
- ⁶⁰⁰T. Gandhi, ed., *Microelectronics failure analysis* (ASM International, 2019).
- ⁶⁰¹TSMC, “3nm technology,” online (2022), https://www.tsmc.com/english/dedicatedFoundry/technology/logic/1_3nm.
- ⁶⁰²Intel, “Intel technology roadmaps and milestones,” online (2022), <https://www.intel.com/content/www/us/en/newsroom/news/intel-technology-roadmaps-milestones>.

- [html#s.tuhd2s](#).
- ⁶⁰³Samsung, “Samsung electronics announces first quarter 2022 results,” online (2022), <https://news.samsung.com/global/samsung-electronics-announces-first-quarter-2022-results>.
- ⁶⁰⁴S. Matsubara, H. Shichi, S. Tanimoto, M. Ikota, and T. Hashizume, “Visualization of 3d structure of semiconductor devices by “dig and see” using GFIS-SIM,” in *Metrology, Inspection, and Process Control for Microlithography XXXIII*, edited by O. Adan and V. A. Ukraintsev (SPIE, 2019).
- ⁶⁰⁵A. V. Steele, B. Knuffman, J. J. McClelland, and J. Orloff, “Focused chromium ion beam,” *Journal of Vacuum Science & Technology B, Nanotechnology and Microelectronics: Materials, Processing, Measurement, and Phenomena* **28**, C6F1–C6F5 (2010).
- ⁶⁰⁶R. Livengood, S. Tan, P. Hack, M. Kane, and Y. Greenzweig, “Focused ion beam circuit edit—a look into the past, present, and future,” *Microscopy and Microanalysis* **17**, 672–673 (2011).
- ⁶⁰⁷S. Tan, R. Livengood, Y. Greenzweig, Y. Drezner, and D. Shima, “Probe current distribution characterization technique for focused ion beam,” *Journal of Vacuum Science & Technology B, Nanotechnology and Microelectronics: Materials, Processing, Measurement, and Phenomena* **30**, 06F606 (2012).
- ⁶⁰⁸S. Tan, R. H. Livengood, Y. Greenzweig, Y. Drezner, R. Hallstein, and C. Scheffler, “Characterization of ion beam current distribution influences on nanomachining,” in *ISTFA 2012* (ASM International, 2012) pp. 436–439.
- ⁶⁰⁹S. Tan, R. Hallstein, R. H. Livengood, and W. Ali, “GFIS in semiconductor applications,” *Microscopy and Microanalysis* **22**, 156–157 (2016).
- ⁶¹⁰R. H. Livengood, S. Tan, Y. Greenzweig, J. A. Notte, and S. McVey, “Subsurface damage from helium ions as a function of dose, beam energy, and dose rate,” *J. Vac. Sci. Technol. B* **27**, 3244 (2009).
- ⁶¹¹H. Bernas, ed., *Materials science with ion beams* (Springer Berlin Heidelberg, 2010).
- ⁶¹²Y. Zhang and W. J. Weber, “Ion irradiation and modification: The role of coupled electronic and nuclear energy dissipation and subsequent nonequilibrium processes in materials,” *Applied Physics Reviews* **7**, 041307 (2020).
- ⁶¹³G. H. Kinchin and R. S. Pease, “The displacement of atoms in solids by radiation,” *Rep. Prog. Phys.* **18**, 1 (1955).
- ⁶¹⁴Y. Morimoto, R. A. Weeks, A. V. Barnes, N. H. Tolk, and R. A. Zuhr, “The effect of ion implantation on luminescence of a silica,” *Journal of Non-Crystalline Solids* **196**, 106–112 (1996).
- ⁶¹⁵F. Chen and F. Schrepel, “Modification of structure and properties of optical crystals,” in *Ion Beam Modification of Solids: Ion-Solid Interaction and Radiation Damage*, edited by W. Wesch and E. Wendler (Springer International Publishing, Cham, 2016) pp. 501–528.
- ⁶¹⁶J. F. Ziegler, Ziegler, and J. P. Biersack, “SRIM – the stopping and range of ions in matter (2010),” *Nucl. Instrum. Methods Phys. Res. B* **268**, 1818–1823 (2010).
- ⁶¹⁷K. Nordlund, M. Ghaly, R. S. Averback, M. Caturla, T. D. d. l. Rubia, and J. Tarus, “Defect production in collision cascades in elemental semiconductors and fcc metals,” *Phys. Rev.* **B 57**, 7556–7570 (1998).
- ⁶¹⁸L. Pelaz, L. A. Marqués, and J. Barbolla, “Ion-beam-induced amorphization and recrystallization of silicon,” *J. Appl. Phys.* **96**, 5947–5976 (2004).
- ⁶¹⁹J. Gierak, “Focused ion beam technology and ultimate applications,” *Semicond. Sci. Technol.* **24**, 043001 (2009).
- ⁶²⁰P. Orús, R. Córdoba, and J. M. De Teresa, “Focused ion beam induced processing,” in *Nanofabrication* (IOP Publishing, 2020) pp. 5–1 to 5–58.
- ⁶²¹S. Nakaharai, T. Iijima, S. Ogawa, S. Suzuki, S.-L. Li, K. Tsukagoshi, S. Sato, and N. Yokoyama, “Conduction tuning of graphene based on defect-induced localization,” *ACS Nano* **7**, 5694–5700 (2013).
- ⁶²²Z. Muktadir, S. Hang, and H. Mizuta, “Defect-induced fermi level pinning and suppression of ambipolar behaviour in graphene,” *Carbon N. Y.* **93**, 325–334 (2015).
- ⁶²³E. N. D. Araujo, J. C. Brant, B. S. Archanjo, G. Medeiros-Ribeiro, F. Plentz, and E. S. Alves, “Patterning graphene with a helium ion microscope: Observation of metal-insulator transition induced by disorder,” *Phys. Rev. B Condens. Matter* **91**, 245414 (2015).
- ⁶²⁴Y. Zhou, P. Maguire, J. Jadwiszczak, M. Muruganathan, H. Mizuta, and H. Zhang, “Precise milling of nano-gap chains in graphene with a focused helium ion beam,” *Nanotechnology* **27**, 325302 (2016).
- ⁶²⁵Y. Naitou and S. Ogawa, “Conductivity change of defective graphene by helium ion beams,” *AIP Adv.* **7**, 045203 (2017).
- ⁶²⁶D. S. Fox, Y. Zhou, P. Maguire, A. O’Neill, C. Ó’Coileáin, R. Gatenby, A. M. Glushenkov, T. Tao, G. S. Duesberg, I. V. Shvets, M. Abid, M. Abid, H.-C. Wu, Y. Chen, J. N. Coleman, J. F. Donegan, and H. Zhang, “Nanopatterning and electrical tuning of MoS₂ layers with a subnanometer helium ion beam,” *Nano Lett.* **15**, 5307–5313 (2015).
- ⁶²⁷M. G. Stanford, P. R. Pudasaini, E. T. Gallmeier, N. Cross, L. Liang, A. Oyedele, G. Duscher, M. Mahjouri-Samani, K. Wang, K. Xiao, D. B. Geohegan, A. Belianinov, B. G. Sumpter, and P. D. Rack, “High conduction hopping behavior induced in transition metal dichalcogenides by percolating defect networks: Toward atomically thin circuits,” *Adv. Funct. Mater.* **27**, 1702829 (2017).
- ⁶²⁸J. Jadwiszczak, D. Keane, P. Maguire, C. P. Cullen, Y. Zhou, H. Song, C. Downing, D. Fox, N. McEvoy, R. Zhu, J. Xu, G. S. Duesberg, Z.-M. Liao, J. J. Boland, and H. Zhang, “MoS₂ memtransistors fabricated by localized helium ion beam irradiation,” *ACS Nano* **13**, 14262–14273 (2019).
- ⁶²⁹S. Parida, Y. Wang, H. Zhao, H. Htoon, T. M. Kucinski, M. Chubarov, T. Choudhury, J. M. Redwing, A. Dongare, and M. T. Pettes, “Tuning of the electronic and vibrational properties of epitaxial MoS₂ through he-ion beam modification,” *Nanotechnology* **34**, 085702 (2022).
- ⁶³⁰M. G. Stanford, P. R. Pudasaini, A. Belianinov, N. Cross, J. H. Noh, M. R. Koehler, D. G. Mandrus, G. Duscher, A. J. Rondinone, I. N. Ivanov, T. Z. Ward, and P. D. Rack, “Focused helium-ion beam irradiation effects on electrical transport properties of few-layer WSe₂: enabling nanoscale direct write homo-junctions,” *Sci. Rep.* **6**, 27276 (2016).
- ⁶³¹M. G. Stanford, J. H. Noh, K. Mahady, A. V. Ievlev, P. Maksymovych, O. S. Ovchinnikova, and P. D. Rack, “Room-Temperature activation of InGaZnO Thin-Film transistors via he⁺ irradiation,” *ACS Appl. Mater. Interfaces* **9**, 35125–35132 (2017).
- ⁶³²Y. Hirayama, S. Tarucha, Y. Suzuki, and H. Okamoto, “Fabrication of a GaAs quantum-well-wire structure by ga focused-ion-beam implantation and its optical properties,” *Physical Review B* **37**, 2774–2777 (1988).
- ⁶³³M. Itoh, T. S. T. Saku, and S. T. S. Tarucha, “High-Mobility quantum wires fabricated by ga focused ion beam shallow implantation,” *Jpn. J. Appl. Phys.* **31**, 4487 (1992).
- ⁶³⁴A. D. Wieck and K. Ploog, “In-plane-gated quantum wire transistor fabricated with directly written focused ion beams,” *Appl. Phys. Lett.* **56**, 928–930 (1990).
- ⁶³⁵Y. Hirayama, T. Saku, and Y. Horikoshi, “Electronic transport through very short and narrow channels constricted in GaAs by highly resistive ga-implanted regions,” *Phys. Rev. B Condens. Matter* **39**, 5535–5537 (1989).
- ⁶³⁶S. Dhara, C. Y. Lu, C. T. Wu, C. W. Hsu, W. S. Tu, K. H. Chen, Y. L. Wang, L. C. Chen, and B. Raj, “Focused ion beam induced nanojunction and defect doping as a building block for nanoscale electronics in GaN nanowires,” *The Journal of Physical Chemistry C* **114**, 15260–15265 (2010).
- ⁶³⁷Y. Liu, Y. Qu, Y. Liu, H. Yin, J. Liu, Y. Tan, and F. Chen, “Direct-Writing of 2D Diodes by Focused Ion Beams,” *Advanced Functional Materials* **31**, 2102708 (2021).

- ⁶³⁸E. Mykkänen, A. Bera, J. S. Lehtinen, A. Ronzani, K. Koppää, T. Hönlgl-Decrinis, R. Shaikhaidarov, S. E. de Graaf, J. Govenius, and M. Prunnila, "Enhancement of Superconductivity by Amorphizing Molybdenum Silicide Films Using a Focused Ion Beam," *Nanomaterials* **10**, 950 (2020).
- ⁶³⁹N. E. Sosa, C. Chen, J. Liu, S. Xie, T. J. Marks, and M. C. Hersam, "Nanoscale structure, composition, and charge transport analysis of transparent conducting oxide nanowires written by focused ion beam implantation," *J. Am. Chem. Soc.* **132**, 7347–7354 (2010).
- ⁶⁴⁰S. Bianconi, M.-S. Park, and H. Mohseni, "Giant conductivity modulation of aluminum oxide using focused ion beam," *ACS Appl. Electron. Mater.* **1**, 1208–1214 (2019).
- ⁶⁴¹H. Mei, A. Koch, C. Wan, J. Rensberg, Z. Zhang, J. Salman, M. Hafermann, M. Schaal, Y. Xiao, R. Wambold, S. Ramathan, C. Ronning, and M. A. Kats, "Tuning carrier density and phase transitions in oxide semiconductors using focused ion beams," *Nanophotonics* **11**, 3923–3932 (2022).
- ⁶⁴²S. A. Cybart, E. Y. Cho, T. J. Wong, B. H. Wehlin, M. K. Ma, C. Huynh, and R. C. Dynes, "Nano josephson superconducting tunnel junctions in YBa₂Cu₃O(7- δ) directly patterned with a focused helium ion beam," *Nat. Nanotechnol.* **10**, 598–602 (2015).
- ⁶⁴³E. Y. Cho, Y. W. Zhou, J. Y. Cho, and S. A. Cybart, "Superconducting nano josephson junctions patterned with a focused helium ion beam," *Appl. Phys. Lett.* **113**, 022604 (2018).
- ⁶⁴⁴B. Müller, M. Karrer, F. Limberger, M. Becker, B. Schröppel, C. J. Burkhardt, R. Kleiner, E. Goldobin, and D. Koelle, "Josephson junctions and SQUIDs created by focused Helium-Ion-Beam irradiation of YBa₂Cu₃O₇," *Phys. Rev. Applied* **11**, 044082 (2019).
- ⁶⁴⁵F. Couëdo, P. Amari, C. Feuillet-Palma, C. Ulysse, Y. K. Srivastava, R. Singh, N. Bergeal, and J. Lesueur, "Dynamic properties of high-*t_c* superconducting nano-junctions made with a focused helium ion beam," *Sci. Rep.* **10**, 10256 (2020).
- ⁶⁴⁶J. C. LeFebvre, E. Cho, H. Li, H. Cai, and S. A. Cybart, "Flux focused series arrays of long josephson junctions for high-dynamic range magnetic field sensing," *Journal of Applied Physics* **131**, 163902 (2022).
- ⁶⁴⁷L. Kasaei, T. Melbourne, V. Manichev, L. C. Feldman, T. Gustafsson, K. Chen, X. X. Xi, and B. A. Davidson, "MgB₂ josephson junctions produced by focused helium ion beam irradiation," *AIP Adv.* **8**, 075020 (2018).
- ⁶⁴⁸K. Maehashi, H. Ozaki, Y. Ohno, K. Inoue, K. Matsumoto, S. Seki, and S. Tagawa, "Formation of single quantum dot in single-walled carbon nanotube channel using focused-ion-beam technique," *Appl. Phys. Lett.* **90**, 023103 (2007).
- ⁶⁴⁹H. J. Kim, N. V. Quang, T. H. Nguyen, S. Kim, Y. Lee, I. H. Lee, S. Cho, M.-J. Seong, K. Kim, and Y. J. Chang, "Tuning of thermoelectric properties of MoSe₂ thin films under helium ion irradiation," *Nanoscale Research Letters* **17** (2022), 10.1186/s11671-022-03665-9.
- ⁶⁵⁰B. Aichner, B. Müller, M. Karrer, V. R. Misko, F. Limberger, K. L. Mletschnig, M. Dosmailov, J. D. Pedarnig, F. Nori, R. Kleiner, D. Koelle, and W. Lang, "Ultradense tailored vortex pinning arrays in superconducting YBa₂Cu₃O_{7-d} thin films created by focused He ion beam irradiation for fluxonics applications," *ACS Appl. Nano Mater.* **2**, 5108–5115 (2019).
- ⁶⁵¹S. Saremi, R. Xu, F. I. Allen, J. Maher, J. C. Agar, R. Gao, P. Hosemann, and L. W. Martin, "Local control of defects and switching properties in ferroelectric thin films," *Phys. Rev. Materials* **2**, 084414 (2018).
- ⁶⁵²D. Seol, S. Kim, W.-S. Jang, Y. Jin, S. Kang, S. Kim, D. Won, C. Lee, Y.-M. Kim, J. Lee, H. Yang, M. S. Jeong, A. Belianinov, A. Tselev, S. Somnath, C. R. Smith, O. S. Ovchinnikova, N. Balke, and Y. Kim, "Selective patterning of out-of-plane piezoelectricity in MoTe₂ via focused ion beam," *Nano Energy* **79**, 105451 (2021).
- ⁶⁵³S. Kang, W.-S. Jang, A. N. Morozovska, O. Kwon, Y. Jin, Y.-H. Kim, H. Bae, C. Wang, S.-H. Yang, A. Belianinov, S. Randalph, E. A. Eliseev, L. Collins, Y. Park, S. Jo, M.-H. Jung, K.-J. Go, H. W. Cho, S.-Y. Choi, J. H. Jang, S. Kim, H. Y. Jeong, J. Lee, O. S. Ovchinnikova, J. Heo, S. V. Kalinin, Y.-M. Kim, and Y. Kim, "Highly enhanced ferroelectricity in HfO₂-based ferroelectric thin film by light ion bombardment," *Science* **376**, 731–738 (2022).
- ⁶⁵⁴A. Belianinov, M. J. Burch, H. E. Hysmith, A. V. Ievlev, V. Iberi, M. A. Susner, M. A. McGuire, P. Maksymovych, M. Chyashnavichyus, S. Jesse, and O. S. Ovchinnikova, "Chemical changes in layered ferroelectric semiconductors induced by helium ion beam," *Scientific Reports* **7** (2017), 10.1038/s41598-017-16949-3.
- ⁶⁵⁵E. Guberna, A. Chouprik, R. Kirtaev, S. Zarubin, I. Margolin, M. Spiridonov, and D. Negrov, "Local ga ion implantation as a source of diverse ferroelectric properties of hafnium oxide," *physica status solidi (RRL) – Rapid Research Letters* **16**, 2100485 (2021).
- ⁶⁵⁶A. Stanishevsky, B. Nagaraj, J. Melngailis, R. Ramesh, L. Khriachtchev, and E. McDaniel, "Radiation damage and its recovery in focused ion beam fabricated ferroelectric capacitors," *Journal of Applied Physics* **92**, 3275–3278 (2002).
- ⁶⁵⁷C. S. Ganpule, A. Stanishevsky, Q. Su, S. Aggarwal, J. Melngailis, E. Williams, and R. Ramesh, "Scaling of ferroelectric properties in thin films," *Applied Physics Letters* **75**, 409–411 (1999).
- ⁶⁵⁸J. H. Franken, M. Hoeijmakers, R. Lavrijsen, J. T. Kohlhepp, H. J. M. Swagten, B. Koopmans, E. van Veldhoven, and D. J. Maas, "Precise control of domain wall injection and pinning using helium and gallium focused ion beams," *J. Appl. Phys.* **109**, 07D504 (2011).
- ⁶⁵⁹H. Huckfeldt, A. Gaul, N. David Mücklich, D. Holzinger, D. Nissen, M. Albrecht, D. Emmrich, A. Beyer, A. Götzhäuser, and A. Ehresmann, "Modification of the saturation magnetization of exchange bias thin film systems upon light-ion bombardment," *J. Phys. Condens. Matter* **29**, 125801 (2017).
- ⁶⁶⁰P. Dunne, C. Fowley, G. Hlawacek, J. Kurian, G. Atcheson, S. Colis, N. Teichert, B. Kundys, M. Venkatesan, J. Lindner, A. M. Deac, T. M. Hermans, J. M. D. Coey, and B. Doudin, "Helium ion microscopy for reduced spin orbit torque switching currents," *Nano Lett.* **20**, 7036–7042 (2020), arXiv:2005.07626 [cond-mat.mes-hall].
- ⁶⁶¹J. Kurian, A. Joseph, S. Cherifi-Hertel, C. Fowley, G. Hlawacek, P. Dunne, M. Romeo, G. Atcheson, J. M. D. Coey, and B. Doudin, "Deterministic multi-level spin orbit torque switching using He⁺ microscopy patterning," *Applied Physics Letters* **122**, 032402 (2023), 2301.02188.
- ⁶⁶²F. Samad, G. Hlawacek, S. S. P. K. Arekapudi, X. Xu, L. Koch, M. Lenz, and O. Hellwig, "Controlled and deterministic creation of synthetic antiferromagnetic domains by focused ion beam irradiation," *Applied Physics Letters* **119**, 022409 (2021).
- ⁶⁶³R. Juge, K. Bairagi, K. G. Rana, J. Vogel, M. Sall, D. Mailly, V. T. Pham, Q. Zhang, N. Sisodia, M. Foerster, L. Aballe, M. Belmeguenai, Y. Roussigné, S. Auffret, L. D. Buda-Prejbeanu, G. Gaudin, D. Ravelosona, and O. Boulle, "Helium ions put magnetic skyrmions on the track," *Nano Lett.* **21**, 2989–2996 (2021).
- ⁶⁶⁴L.-M. Kern, B. Pfau, V. Deinhart, M. Schneider, C. Klose, K. Gerlinger, S. Wittrock, D. Engel, I. Will, C. M. Günther, R. Lieferrink, J. H. Mentink, S. Wintz, M. Weigand, M.-J. Huang, R. Battistelli, D. Metternich, F. Büttner, K. Höflich, and S. Eisebitt, "Deterministic generation and guided motion of magnetic skyrmions by focused He⁺-Ion irradiation," arXiv [cond-mat.mtrl-sci] (2022), arXiv:2202.12057 [cond-mat.mtrl-sci].
- ⁶⁶⁵T. Aign, P. Meyer, S. Lemerle, J. P. Jamet, J. Ferré, V. Mathet, C. Chappert, J. Gierak, C. Vieu, F. Rousseaux, H. Launois, and H. Bernas, "Magnetization reversal in arrays of perpendicularly magnetized ultrathin dots coupled by dipolar interaction," *Physical Review Letters* **81**, 5656–5659 (1998).

- ⁶⁶⁶L. Flajšman, K. Wagner, M. Vaňatka, J. Gloss, V. Křížáková, M. Schmid, H. Schultheiss, and M. Urbánek, “Zero-field propagation of spin waves in waveguides prepared by focused ion beam direct writing,” *Phys. Rev. B Condens. Matter* **101**, 014436 (2020).
- ⁶⁶⁷M. C. H. de Jong, M. J. Meijer, J. Lucassen, J. van Liempt, H. J. M. Swagten, B. Koopmans, and R. Lavrijsen, “Local control of magnetic interface effects in chiral Ir|Co|Pt multilayers using Ga⁺ ion irradiation,” *Physical Review B* **105**, 064429 (2022).
- ⁶⁶⁸K. Shibata, J. Iwasaki, N. Kanazawa, S. Aizawa, T. Tanigaki, M. Shirai, T. Nakajima, M. Kubota, M. Kawasaki, H. S. Park, D. Shindo, N. Nagaosa, and Y. Tokura, “Large anisotropic deformation of skyrmions in strained crystal,” *Nature Nanotechnology* **10**, 589–592 (2015).
- ⁶⁶⁹M. V. Sapozhnikov, Y. V. Petrov, N. S. Gusev, A. G. Temiryazev, O. L. Ermolaeva, V. L. Mironov, and O. G. Udalov, “Artificial dense lattices of magnetic skyrmions,” *Materials* **13**, 99 (2019).
- ⁶⁷⁰K. Fallon, S. Hughes, K. Zeissler, W. Legrand, F. Ajejas, D. Maccariello, S. McFadzean, W. Smith, D. McGrouther, S. Collin, N. Reyren, V. Cros, C. H. Marrows, and S. McVitie, “Controlled individual skyrmion nucleation at artificial defects formed by ion irradiation,” *Small* **16**, e1907450 (2020).
- ⁶⁷¹Y. Hu, S. Zhang, Y. Zhu, C. Song, J. Huang, C. Liu, X. Meng, X. Deng, L. Zhu, C. Guan, H. Yang, M. Si, J. Zhang, and Y. Peng, “Precise tuning of skyrmion density in a controllable manner by ion irradiation,” *ACS Applied Materials & Interfaces* **14**, 34011–34019 (2022).
- ⁶⁷²O. Ishii, K. Nonaka, and I. Hatakeyama, “Magnetization reversal in focussed ion-beam implanted YIG patterns,” *IEEE Translation Journal on Magnetism in Japan* **4**, 197–203 (1989).
- ⁶⁷³C. D. Cress, D. Wickramaratne, M. R. Rosenberger, Z. Hennighausen, P. G. Callahan, S. W. LaGasse, N. Bernstein, O. M. van ’t Erve, B. T. Jonker, S. B. Qadri, J. C. Prestigiacomo, M. Currie, I. I. Mazin, and S. P. Bennett, “Direct-Write of nanoscale domains with tunable metamagnetic order in FeRh thin films,” *ACS Appl. Mater. Interfaces* **13**, 836–847 (2021).
- ⁶⁷⁴E. Menéndez, M. O. Liedke, J. Fassbender, T. Gemming, A. Weber, L. J. Heyderman, K. V. Rao, S. C. Deevi, S. Suriñach, M. D. Baró, J. Sort, and J. Nogués, “Direct magnetic patterning due to the generation of ferromagnetism by selective ion irradiation of paramagnetic FeAl alloys,” *Small* **5**, 229–234 (2008).
- ⁶⁷⁵M. Urbánek, L. Flajšman, V. Křížáková, J. Gloss, M. Horký, M. Schmid, and P. Varga, “Research update: Focused ion beam direct writing of magnetic patterns with controlled structural and magnetic properties,” *APL Materials* **6**, 060701 (2018).
- ⁶⁷⁶F. Röder, G. Hlawacek, S. Wintz, R. Hübner, L. Bischoff, H. Lichte, K. Potzger, J. Lindner, J. Fassbender, and R. Bali, “Direct depth- and lateral- imaging of nanoscale magnets generated by ion impact,” *Sci. Rep.* **5**, 16786 (2015).
- ⁶⁷⁷M. Kiechle, A. Papp, S. Mendisch, V. Ahrens, M. Golibrzuch, G. H. Bernstein, W. Porod, G. Csaba, and M. Becherer, “Spin-wave optics in YIG realized by ion-beam irradiation,” *Small* **2207293** (2023).
- ⁶⁷⁸F. Sawafra, B. Clancy, A. T. Carlsen, M. Huber, and A. R. Hall, “Solid-state nanopores and nanopore arrays optimized for optical detection,” *Nanoscale* **6**, 6991–6996 (2014).
- ⁶⁷⁹V. Iberi, L. Liang, A. V. Ievlev, M. G. Stanford, M.-W. Lin, X. Li, M. Mahjouri-Samani, S. Jesse, B. G. Sumpter, S. V. Kalinin, D. C. Joy, K. Xiao, A. Belianinov, and O. S. Ovchinnikova, “Nanoforging single layer MoSe₂ through defect engineering with focused helium ion beams,” *Sci. Rep.* **6**, 30481 (2016).
- ⁶⁸⁰Y. V. Kapitonov, P. Y. Shapochkin, L. Y. Beliaev, Y. V. Petrov, Y. P. Efimov, S. A. Eliseev, V. A. Lovtcius, V. V. Petrov, and V. V. Ovsyankin, “Ion-beam-assisted spatial modulation of inhomogeneous broadening of a quantum well resonance: excitonic diffraction grating,” *Opt. Lett.* **41**, 104–106 (2016).
- ⁶⁸¹G. Grosso, H. Moon, B. Lienhard, S. Ali, D. K. Efetov, M. M. Furchi, P. Jarillo-Herrero, M. J. Ford, I. Aharonovich, and D. Englund, “Tunable and high-purity room temperature single-photon emission from atomic defects in hexagonal boron nitride,” *Nature Communications* **8** (2017), 10.1038/s41467-017-00810-2.
- ⁶⁸²J. Reithmaier, “Focused ion-beam implantation induced thermal quantum-well intermixing for monolithic optoelectronic device integration,” *IEEE Journal of Selected Topics in Quantum Electronics* **4**, 595–605 (1998).
- ⁶⁸³X. Jiang, W. Cai, W. Luo, Y. Xiang, N. Zhang, M. Ren, X. Zhang, and J. Xu, “Near-field imaging of graphene triangles patterned by helium ion lithography,” *Nanotechnology* **29**, 385205 (2018).
- ⁶⁸⁴H. Takashima, A. Fukuda, H. Maruya, T. Tashima, A. W. Schell, and S. Takeuchi, “Fabrication of a nanofiber Bragg cavity with high quality factor using a focused helium ion beam,” *Optics Express* **27**, 6792 (2019).
- ⁶⁸⁵W. R. McGehee, T. Michels, V. Aksyuk, and J. J. McClelland, “Two-dimensional imaging and modification of nanophotonic resonator modes using a focused ion beam,” *Optica* **4**, 1444 (2017).
- ⁶⁸⁶H. Lohmeyer, J. Kalden, K. Sebald, C. Kruse, D. Hommel, and J. Gutowski, “Fine tuning of quantum-dot pillar microcavities by focused ion beam milling,” *Applied Physics Letters* **92**, 011116 (2008).
- ⁶⁸⁷D. Chezganov, E. Vlasov, L. Gimadeeva, M. Neradovskiy, A. Akhmatkhanov, M. Chuvakova, D. Alikin, H. Tronche, F. Doutre, P. Baldi, and V. Shur, “Short-period domain patterning by ion beam irradiation in lithium niobate waveguides produced by soft proton exchange,” *Optics & Laser Technology* **158**, 108813 (2023).
- ⁶⁸⁸Z. Huang, W.-D. Li, C. Santori, V. M. Acosta, A. Faraon, T. Ishikawa, W. Wu, D. Winston, R. S. Williams, and R. G. Beausoleil, “Diamond nitrogen-vacancy centers created by scanning focused helium ion beam and annealing,” *Appl. Phys. Lett.* **103**, 081906 (2013).
- ⁶⁸⁹D. McCloskey, D. Fox, N. O’Hara, V. Usov, D. Scanlan, N. McEvoy, G. S. Duesberg, G. L. W. Cross, H. Z. Zhang, and J. F. Donegan, “Helium ion microscope generated nitrogen-vacancy centres in type Ib diamond,” *Appl. Phys. Lett.* **104**, 031109 (2014).
- ⁶⁹⁰Y. Song, Z. Xu, R. Li, H. Wang, Y. Fan, M. Rommel, J. Liu, G. V. Astakhov, G. Hlawacek, B. Li, J. Xu, and F. Fang, “Photoluminescence and raman spectroscopy study on color centers of helium Ion-Implanted 4H-SiC,” *Nanomanufacturing and Metrology* **3**, 205–217 (2020).
- ⁶⁹¹Z.-X. He, Q. Li, X.-L. Wen, J.-Y. Zhou, W.-X. Lin, Z.-H. Hao, J.-S. Xu, C.-F. Li, and G.-C. Guo, “Maskless generation of single silicon vacancy arrays in silicon carbide by a focused He⁺ ion beam,” *ACS Photonics* (2022), 10.1021/acsp Photonics.2c01209.
- ⁶⁹²J. Klein, A. Kuc, A. Nolinder, M. Altschner, J. Wierzbowski, F. Sigger, F. Kreupl, J. J. Finley, U. Wurstbauer, A. W. Holleitner, and M. Kaniber, “Robust valley polarization of helium ion modified atomically thin MoS₂,” *2D Mater.* **5**, 011007 (2017).
- ⁶⁹³J. Klein, M. Lorke, M. Florian, F. Sigger, L. Sigl, S. Rey, J. Wierzbowski, J. Cerne, K. Müller, E. Mitterreiter, P. Zimmermann, T. Taniguchi, K. Watanabe, U. Wurstbauer, M. Kaniber, M. Knap, R. Schmidt, J. J. Finley, and A. W. Holleitner, “Site-selectively generated photon emitters in monolayer MoS₂ via local helium ion irradiation,” *Nat. Commun.* **10**, 2755 (2019).
- ⁶⁹⁴N. Cassidy, P. Blenkinsopp, I. Brown, R. J. Curry, B. N. Murrin, R. Webb, and D. Cox, “Single ion implantation of bismuth,” *physica status solidi (a)* **218**, 2000237 (2020).
- ⁶⁹⁵S. P. Pavunny, A. L. Yeats, H. B. Banks, E. Bielejec, R. L. Myers-Ward, M. T. DeJarld, A. S. Bracker, D. K. Gaskill, and S. G. Carter, “Arrays of Si vacancies in 4H-SiC produced by focused Li ion beam implantation,” *Scientific Reports* **11** (2021),

- 10.1038/s41598-021-82832-x.
- ⁶⁹⁶S. Tamura, G. Koike, A. Komatsubara, T. Teraji, S. Onoda, L. P. McGuinness, L. Rogers, B. Naydenov, E. Wu, L. Yan, F. Jelezko, T. Ohshima, J. Isoya, T. Shinada, and T. Tani, "Array of bright silicon-vacancy centers in diamond fabricated by low-energy focused ion beam implantation," *Applied Physics Express* **7**, 115201 (2014).
- ⁶⁹⁷T. Schröder, M. E. Trusheim, M. Walsh, L. Li, J. Zheng, M. Schukraft, A. Sipahigil, R. E. Evans, D. D. Sukachev, C. T. Nguyen, J. L. Pacheco, R. M. Camacho, E. S. Bielejec, M. D. Lukin, and D. Englund, "Scalable focused ion beam creation of nearly lifetime-limited single quantum emitters in diamond nanostructures," *Nature Communications* **8** (2017), 10.1038/ncomms15376.
- ⁶⁹⁸M. Hollenbach, N. Klingner, N. S. Jagtap, L. Bischoff, C. Fowley, U. Kentsch, G. Hlawacek, A. Erbe, N. V. Abrosimov, M. Helm, Y. Berencén, and G. V. Astakhov, "Wafer-scale nanofabrication of telecom single-photon emitters in silicon," *Nature Communications* **13** (2022), 10.1038/s41467-022-35051-5, arXiv:2204.13173 [quant-ph].
- ⁶⁹⁹Y. Zhou, Z. Mu, G. Adamo, S. Bauerdick, A. Rudzinski, I. Aharonovich, and W. bo Gao, "Direct writing of single germanium vacancy center arrays in diamond," *New Journal of Physics* **20**, 125004 (2018).
- ⁷⁰⁰J. Ziegler, R. Klaiiss, A. Blaikie, D. Miller, V. R. Horowitz, and B. J. Alemán, "Deterministic quantum emitter formation in hexagonal boron nitride via controlled edge creation," *Nano Letters* **19**, 2121–2127 (2019).
- ⁷⁰¹R. Klaiiss, J. Ziegler, D. Miller, K. Zappitelli, K. Watanabe, T. Taniguchi, and B. Alemán, "Uncovering the morphological effects of high-energy ga^+ focused ion beam milling on hBN single-photon emitter fabrication," *The Journal of Chemical Physics* **157**, 074703 (2022).
- ⁷⁰²Q. Qian, L. Peng, N. Perea-Lopez, K. Fujisawa, K. Zhang, X. Zhang, T. H. Choudhury, J. M. Redwing, M. Terrones, X. Ma, and S. Huang, "Defect creation in WSe₂ with a microsecond photoluminescence lifetime by focused ion beam irradiation," *Nanoscale* **12**, 2047–2056 (2020).
- ⁷⁰³J. P. Thiruraman, P. M. Das, and M. Drndić, "Irradiation of transition metal dichalcogenides using a focused ion beam: Controlled single-atom defect creation," *Advanced Functional Materials* **29**, 1904668 (2019).
- ⁷⁰⁴J. L. Pacheco, M. Singh, D. L. Perry, J. R. Wendt, G. T. Eyck, R. P. Manginell, T. Pluyd, D. R. Luhman, M. P. Lilly, M. S. Carroll, and E. Bielejec, "Ion implantation for deterministic single atom devices," *Review of Scientific Instruments* **88**, 123301 (2017).
- ⁷⁰⁵J. E. Fröch, A. Bahm, M. Kianinia, Z. Mu, V. Bhatia, S. Kim, J. M. Cairney, W. Gao, C. Bradac, I. Aharonovich, and M. Toth, "Versatile direct-writing of dopants in a solid state host through recoil implantation," *Nature Communications* **11** (2020), 10.1038/s41467-020-18749-2.
- ⁷⁰⁶M. Kianinia, S. White, J. E. Fröch, C. Bradac, and I. Aharonovich, "Generation of spin defects in hexagonal boron nitride," *ACS Photonics* **7**, 2147–2152 (2020).
- ⁷⁰⁷E. Glushkov, M. Macha, E. Rãth, V. Navikas, N. Ronceray, C. Y. Cheon, A. Ahmed, A. Avsar, K. Watanabe, T. Taniguchi, I. Shorubalko, A. Kis, G. Fantner, and A. Radenovic, "Engineering optically active defects in hexagonal boron nitride using focused ion beam and water," *ACS Nano* **16**, 3695–3703 (2022).
- ⁷⁰⁸Y. V. Petrov, T. V. Sharov, A. P. Baraban, and O. F. Vyvenko, "Effect of helium ion beam treatment on the etching rate of silicon nitride," *Nucl. Instrum. Methods Phys. Res. B* **349**, 90–95 (2015).
- ⁷⁰⁹Y. V. Petrov, E. A. Grigoryev, and A. P. Baraban, "Helium focused ion beam irradiation with subsequent chemical etching for the fabrication of nanostructures," *Nanotechnology* **31**, 215301 (2020).
- ⁷¹⁰P. Maguire, J. Jadwiszczak, M. O'Brien, D. Keane, G. S. Duesberg, N. McEvoy, and H. Zhang, "Defect-moderated oxidative etching of MoS₂," *J. Appl. Phys.* **126**, 164301 (2019).
- ⁷¹¹E. Mitterreiter, Y. Liang, M. Golibrzuch, D. McLaughlin, C. Csoklich, J. D. Bartl, A. Holleitner, U. Wurstbauer, and A. S. Bandarenka, "In-situ visualization of hydrogen evolution sites on helium ion treated molybdenum dichalcogenides under reaction conditions," *npj 2D Materials and Applications* **3**, 25 (2019).
- ⁷¹²M. Heilmann, V. Deinhart, A. Tahraoui, K. Höflich, and J. M. J. Lopes, "Spatially controlled epitaxial growth of 2D heterostructures via defect engineering using a focused he ion beam," *npj 2D Materials and Applications* **5**, 1–7 (2021).
- ⁷¹³J. Lee, T. W. Saucer, A. J. Martin, D. Tien, J. M. Millunchick, and V. Sih, "Photoluminescence imaging of focused ion beam induced individual quantum dots," *Nano Letters* **11**, 1040–1043 (2011).
- ⁷¹⁴A. Portavoce, R. Hull, M. C. Reuter, and F. M. Ross, "Nanometer-scale control of single quantum dot nucleation through focused ion-beam implantation," *Physical Review B* **76**, 235301 (2007).
- ⁷¹⁵M. Gherasimova, R. Hull, M. C. Reuter, and F. M. Ross, "Pattern level assembly of ge quantum dots on si with focused ion beam templating," *Applied Physics Letters* **93**, 023106 (2008).
- ⁷¹⁶C. Akhmadaliev, B. Schmidt, and L. Bischoff, "Defect induced formation of CoSi₂ nanowires by focused ion beam synthesis," *Applied Physics Letters* **89**, 223129 (2006).
- ⁷¹⁷H. Li, L. Daukiya, S. Haldar, A. Lindblad, B. Sanyal, O. Eriksson, D. Aubel, S. Hajjar-Garreau, L. Simon, and K. Leifer, "Site-selective local fluorination of graphene induced by focused ion beam irradiation," *Sci. Rep.* **6**, 19719 (2016).
- ⁷¹⁸Y. Yamada, K. Takahashi, T. Ikuta, T. Nishiyama, Y. Takata, W. Ma, and A. Takahara, "Tuning surface wettability at the submicron-scale: Effect of focused ion beam irradiation on a self-assembled monolayer," *The Journal of Physical Chemistry C* **120**, 274–280 (2015).
- ⁷¹⁹Y. Zhao, D. Liu, J. Chen, L. Zhu, A. Belianinov, O. S. Ovchinnikova, R. R. Unocic, M. J. Burch, S. Kim, H. Hao, D. S. Pickard, B. Li, and J. T. L. Thong, "Engineering the thermal conductivity along an individual silicon nanowire by selective helium ion irradiation," *Nat. Commun.* **8**, 15919 (2017).
- ⁷²⁰H. S. Choe, R. Prabhakar, G. Wehmeyer, F. I. Allen, W. Lee, L. Jin, Y. Li, P. Yang, C.-W. Qiu, C. Dames, M. Scott, A. Minor, J.-H. Bahk, and J. Wu, "Ion write microthermotics: Programming thermal metamaterials at the microscale," *Nano Lett.* **19**, 3830–3837 (2019).
- ⁷²¹L. Jin, S. E. Zeltmann, H. S. Choe, H. Liu, F. I. Allen, A. M. Minor, and J. Wu, "Disorder recovers the Wiedemann-Franz law in the metallic phase of VO₂," *Phys. Rev. B Condens. Matter* **102**, 041120 (2020).
- ⁷²²H. S. Choe, J. Li, W. Zheng, J. Lee, J. Suh, F. I. Allen, H. Liu, H.-J. Choi, W. Walukiewicz, H. Zheng, and J. Wu, "Anomalous high electronic thermal conductivity and lorenz ratio in Bi₂Te₃ nanoribbons far from the bipolar condition," *Appl. Phys. Lett.* **114**, 152101 (2019).
- ⁷²³B. Liu and J. Fu, "Modulating surface stiffness of polydimethylsiloxane (PDMS) with kiloelectronvolt ion patterning," *Journal of Micromechanics and Microengineering* **25**, 065006 (2015).
- ⁷²⁴Y. Kim, A. Y. Abuelfilat, S. P. Hoo, A. Al-Abboodi, B. Liu, T. Ng, P. Chan, and J. Fu, "Tuning the surface properties of hydrogel at the nanoscale with focused ion irradiation," *Soft Matter* **10**, 8448–8456 (2014).
- ⁷²⁵Z.-J. Wang, F. I. Allen, Z.-W. Shan, and P. Hosemann, "Mechanical behavior of copper containing a gas-bubble superlattice," *Acta Mater.* **121**, 78–84 (2016).
- ⁷²⁶Y.-C. Wang, L. Tian, F. Liu, Y.-B. Qin, G. Zheng, J.-T. Wang, E. Ma, and Z.-W. Shan, "Helium ion microscope fabrication causing changes in the structure and mechanical behavior of silicon micropillars," *Small* **13** (2017), 10.1002/sml.201601753.
- ⁷²⁷M. Chen, J. P. Best, I. Shorubalko, J. Michler, R. Spolenak, and J. M. Wheeler, "Influence of helium ion irradiation on the structure and strength of diamond," *Carbon N. Y.* **158**, 337–

- 345 (2020).
- ⁷²⁸F. Bergner, G. Hlawacek, and C. Heintze, “Helium-ion microscopy, helium-ion irradiation and nanoindentation of eurofer 97 and ODS eurofer,” *J. Nucl. Mater.* **505**, 267–275 (2018).
- ⁷²⁹M. Balooch, F. I. Allen, M. P. Popovic, and P. Hosemann, “Mechanical and structural transformations of tungsten implanted with helium ions,” *J. Nucl. Mater.* **559**, 153436 (2022).
- ⁷³⁰M. Wurmschuber, M. Balooch, X. Huang, P. Hosemann, and D. Kiener, “Helium-induced swelling and mechanical property degradation in ultrafine-grained w and w-cu nanocomposites for fusion applications,” *Scripta Materialia* **213**, 114641 (2022).
- ⁷³¹J. Fassbender, D. Ravelosona, and Y. Samson, “Tailoring magnetism by light-ion irradiation,” *Journal of Physics D: Applied Physics* **37**, R179–R196 (2004).
- ⁷³²G. Pan, S. Takahashi, J. Walker, D. Mapps, K. Yamakawa, N. Honda, and K. Ouchi, “A new fabrication method for sub-micron trackwidth thin film heads,” *Journal of Magnetism and Magnetic Materials* **202**, 583–592 (1999).
- ⁷³³N. Nishimura, T. Hirai, A. Koganei, T. Ikeda, K. Okano, Y. Sekiguchi, and Y. Osada, “Magnetic tunnel junction device with perpendicular magnetization films for high-density magnetic random access memory,” *Journal of Applied Physics* **91**, 5246–5249 (2002).
- ⁷³⁴M. Albrecht, S. Ganesan, C. Rettner, A. Moser, M. Best, R. White, and B. Terris, “Patterned perpendicular and longitudinal media: a magnetic recording study,” *IEEE Transactions on Magnetics* **39**, 2323–2325 (2003).
- ⁷³⁵L. Serrano-Ramón, A. Fernández-Pacheco, M. R. Ibarra, D. Petit, R. P. Cowburn, T. Tyliczszak, and J. M. D. Teresa, “Modification of domain-wall propagation in co nanowires via Ga⁺ irradiation,” *The European Physical Journal B* **86**, 97 (2013).
- ⁷³⁶C. T. Nguyen, A. Balocchi, D. Lagarde, T. T. Zhang, H. Carrère, S. Mazzucato, P. Barate, E. Galopin, J. Gierak, E. Bourhis, J. C. Harmand, T. Amand, and X. Marie, “Fabrication of an InGaAs spin filter by implantation of paramagnetic centers,” *Applied Physics Letters* **103**, 052403 (2013).
- ⁷³⁷T. Devolder, C. Vieu, H. Bernas, J. Ferrié, C. Chappert, J. Gierak, J.-P. Jamet, T. Aign, P. Meyer, Y. Chen, F. Rousseaux, V. Mathet, H. Launois, and O. Kaitasov, “Ion beam-induced magnetic patterning at the sub-0.1 μm level,” *Comptes Rendus de l’Académie des Sciences - Series IIB - Mechanics-Physics-Astronomy* **327**, 915–923 (1999).
- ⁷³⁸P. Warin, R. Hyndman, J. Gierak, J. N. Chapman, J. Ferré, J. P. Jamet, V. Mathet, and C. Chappert, “Modification of co/pt multilayers by gallium irradiation—part 2: The effect of patterning using a highly focused ion beam,” *Journal of Applied Physics* **90**, 3850–3855 (2001).
- ⁷³⁹J. Gierak, D. Mailly, P. Hawkes, R. Jede, L. Bruchhaus, L. Bardotti, B. Prével, P. Mélinon, A. Perez, R. Hyndman, J.-P. Jamet, J. Ferré, A. Mougin, C. Chappert, V. Mathet, P. Warin, and J. Chapman, “Exploration of the ultimate patterning potential achievable with high resolution focused ion beams,” *Applied Physics A* **80**, 187–194 (2005).
- ⁷⁴⁰P. D. Townsend, “Optical effects of ion implantation,” *Reports on Progress in Physics* **50**, 501–558 (1987).
- ⁷⁴¹S. Lagomarsino, A. M. Flatae, H. Kambalathmana, F. Sledz, L. Hunold, N. Soltani, P. Reuschel, S. Sciortino, N. Gelli, M. Massi, C. Czelusniak, L. Giuntini, and M. Agio, “Creation of silicon-vacancy color centers in diamond by ion implantation,” *Frontiers in Physics* **8** (2021), 10.3389/fphy.2020.601362.
- ⁷⁴²J. Wang, X. Zhang, Y. Zhou, K. Li, Z. Wang, P. Peddibhotla, F. Liu, S. Bauerdick, A. Rudzinski, Z. Liu, and W. Gao, “Scalable fabrication of single silicon vacancy defect arrays in silicon carbide using focused ion beam,” *ACS Photonics* **4**, 1054–1059 (2017).
- ⁷⁴³J.-F. Wang, Q. Li, F.-F. Yan, H. Liu, G.-P. Guo, W.-P. Zhang, X. Zhou, L.-P. Guo, Z.-H. Lin, J.-M. Cui, X.-Y. Xu, J.-S. Xu, C.-F. Li, and G.-C. Guo, “On-demand generation of single silicon vacancy defects in silicon carbide,” *ACS Photonics* **6**, 1736–1743 (2019).
- ⁷⁴⁴P. Räcké, L. Pietzonka, J. Meijer, D. Spemann, and R. Wunderlich, “Vacancy diffusion and nitrogen-vacancy center formation near the diamond surface,” *Applied Physics Letters* **118**, 204003 (2021).
- ⁷⁴⁵M. Kianinia, Z.-Q. Xu, M. Toth, and I. Aharonovich, “Quantum emitters in 2d materials: Emitter engineering, photo-physics, and integration in photonic nanostructures,” *Applied Physics Reviews* **9**, 011306 (2022).
- ⁷⁴⁶L. Ma, Y. Tan, M. Ghorbani-Asl, R. Boettger, S. Kretschmer, S. Zhou, Z. Huang, A. V. Krashennnikov, and F. Chen, “Tailoring the optical properties of atomically-thin WS₂ via ion irradiation,” *Nanoscale* **9**, 11027–11034 (2017).
- ⁷⁴⁷S. Choi, T. T. Tran, C. Elbadawi, C. Lobo, X. Wang, S. Juodkazis, G. Seniutinas, M. Toth, and I. Aharonovich, “Engineering and Localization of Quantum Emitters in Large Hexagonal Boron Nitride Layers,” *ACS Applied Materials and Interfaces* **8**, 29642–29648 (2016).
- ⁷⁴⁸M. Fischer, J. M. Caridad, A. Sajid, S. Ghaderzadeh, M. Ghorbani-Asl, L. Gammelgaard, P. Bøggild, K. S. Thygesen, A. V. Krashennnikov, S. Xiao, M. Wubs, and N. Stenger, “Controlled generation of luminescent centers in hexagonal boron nitride by irradiation engineering,” *Science Advances* **7**, eabe7138 (2021).
- ⁷⁴⁹A. V. Krashennnikov, “Are two-dimensional materials radiation tolerant?” *Nanoscale Horizons* **5**, 1447–1452 (2020).
- ⁷⁵⁰C. L. Wu, H. T. Lin, H. A. Chen, S. Y. Lin, M. H. Shih, and C. W. Pao, “Defect formation and modulation during patterning supported graphene sheets using focused ion beams,” *Materials Today Communications* **17**, 60–68 (2018).
- ⁷⁵¹G. Nanda, G. Hlawacek, S. Goswami, K. Watanabe, T. Taniguchi, and P. F. Alkemade, “Electronic transport in helium-ion-beam etched encapsulated graphene nanoribbons,” *Carbon* **119**, 419–425 (2017).
- ⁷⁵²Z. Chen, L.-L. Niu, Z. Wang, L. Tian, L. Kecskes, K. Zhu, and Q. Wei, “A comparative study on the in situ helium irradiation behavior of tungsten: Coarse grain vs. nanocrystalline grain,” *Acta Mater.* **147**, 100–112 (2018).
- ⁷⁵³F. I. Allen, P. Hosemann, and M. Balooch, “Key mechanistic features of swelling and blistering of helium-ion-irradiated tungsten,” *Scr. Mater.* **178**, 256–260 (2020).
- ⁷⁵⁴L. Zhang, N. F. Heinig, S. Bazargan, M. Abd-Ellah, N. Moghimi, and K. T. Leung, “Direct-write three-dimensional nanofabrication of nanopillars and nanocones on si by nanotomefation using a helium ion microscope,” *Nanotechnology* **26**, 255303 (2015).
- ⁷⁵⁵C.-S. Kim, R. G. Hobbs, A. Agarwal, Y. Yang, V. R. Manfrinato, M. P. Short, J. Li, and K. K. Berggren, “Focused-helium-ion-beam blow forming of nanostructures: radiation damage and nanofabrication,” *Nanotechnology* **31**, 045302 (2020).
- ⁷⁵⁶X. Wen, R. Mao, and H. Hu, “3-d nanofabrication of silicon and nanostructure fine-tuning via helium ion implantation,” *Adv. Mater. Interfaces* , 2101643 (2022).
- ⁷⁵⁷K. Groot-Berning, G. Jacob, C. Osterkamp, F. Jelezko, and F. Schmidt-Kaler, “Fabrication of ¹⁵NV⁻ centers in diamond using a deterministic single ion implanter,” *New Journal of Physics* **23**, 063067 (2021).
- ⁷⁵⁸K. Groot-Berning, T. Kornher, G. Jacob, F. Stopp, S. T. Dawkins, R. Kolesov, J. Wrachtrup, K. Singer, and F. Schmidt-Kaler, “Deterministic single-ion implantation of rare-earth ions for nanometer-resolution color-center generation,” *Physical Review Letters* **123**, 106802 (2019).
- ⁷⁵⁹T. Schenkel, A. Persaud, S. J. Park, J. Meijer, J. R. Kingsley, J. W. McDonald, J. P. Holder, J. Bokor, and D. H. Schneider, “Single ion implantation for solid state quantum computer development,” *Journal of Vacuum Science & Technology B: Microelectronics and Nanometer Structures* **20**, 2819 (2002).
- ⁷⁶⁰I. W. Rangelow, J. Meijer, and T. Schenkel, “Device for accurately positioning individual particles on substrate surface, e.g.

- for quantum computer, has aperture at tip of end portion of cantilever beam,” patent DE10347969A1 (Universität Kassel, 34125 Kassel, DE; The Regents of the University of California, Berkeley, Calif., US, 2006).
- ⁷⁶¹J. Meijer, T. Vogel, B. Burchard, I. Rangelow, L. Bischoff, J. Wrachtrup, M. Domhan, F. Jelezko, W. Schnitzler, S. Schulz, K. Singer, and F. Schmidt-Kaler, “Concept of deterministic single ion doping with sub-nm spatial resolution,” *Applied Physics A* **83**, 321–327 (2006).
- ⁷⁶²J. Meijer, S. Pezzagna, T. Vogel, B. Burchard, H. Bukow, I. Rangelow, Y. Sarov, H. Wiggers, I. Plümel, F. Jelezko, J. Wrachtrup, F. Schmidt-Kaler, W. Schnitzler, and K. Singer, “Towards the implanting of ions and positioning of nanoparticles with nm spatial resolution,” *Applied Physics A* **91**, 567–571 (2008).
- ⁷⁶³B. N. Murdin, N. Cassidy, D. Cox, R. Webb, and R. J. Curry, “Error rates in deterministic ion implantation for qubit arrays,” *physica status solidi (b)* **258**, 2000615 (2021).
- ⁷⁶⁴V. Chandrasekaran, M. Titz, A. R. Flores, D. Campbell, J. Henshaw, A. C. Jones, E. S. Bielejec, and H. Htoon, “High-yield deterministic focused ion beam implantation of quantum defects enabled by in situ photoluminescence feedback,” *Advanced Science* **n/a**, 2300190 (2023), <https://onlinelibrary.wiley.com/doi/pdf/10.1002/advs.202300190>.
- ⁷⁶⁵M. Knoll and E. Ruska, “Das Elektronenmikroskop,” *Zeitschrift für Phys.* **78**, 318–339 (1932).
- ⁷⁶⁶F. Krause, “Das magnetische elektronenmikroskop und seine anwendung in der biologie,” *Die Naturwissenschaften* **25**, 817–825 (1937).
- ⁷⁶⁷E. Brüche and E. Haagen, “Ein neues, einfaches Übermikroskop und seine anwendung in der bakteriologie,” *Die Naturwissenschaften* **27**, 809–811 (1939).
- ⁷⁶⁸H. Ruska, B. v. Borries, and E. Ruska, “Die Bedeutung der Übermikroskopie für die Virusforschung,” *Archiv für die gesamte Virusforschung* **1**, 155–169 (1939).
- ⁷⁶⁹M. Ballerini, M. Milani, D. Batani, and F. Squadrini, “Focused ion beam techniques for the analysis of biological samples: A revolution in ultramicroscopy?” in *SPIE Proceedings*, edited by J.-A. Conchello, C. J. Cogswell, and T. Wilson (SPIE, 2001).
- ⁷⁷⁰J. Gierak, A. Septier, and C. Vieu, “Design and realization of a very high-resolution fib nanofabrication instrument,” *Nuclear Instruments and Methods in Physics Research Section A: Accelerators, Spectrometers, Detectors and Associated Equipment* **427**, 91–98 (1999).
- ⁷⁷¹B. Inkson, M. Mulvihill, and G. Möbus, “3d determination of grain shape in a FeAl-based nanocomposite by 3d FIB tomography,” *Scripta Materialia* **45**, 753–758 (2001).
- ⁷⁷²D. Pham, C. Xu, and J. Prince, “Current methods in medical image segmentation,” *Annu. Rev. Biomed. Eng.* **2**, 315–337 (2000).
- ⁷⁷³F. Lasagni, A. Lasagni, M. Engstler, H. Degischer, and F. Mücklich, “Nano-characterization of cast structures by FIB-tomography,” *Advanced Engineering Materials* **10**, 62–66 (2008).
- ⁷⁷⁴H. Ostadi, P. Rama, Y. Liu, R. Chen, X. Zhang, and K. Jiang, “3d reconstruction of a gas diffusion layer and a microporous layer,” *Journal of Membrane Science* **351**, 69–74 (2010).
- ⁷⁷⁵D. A. M. D. Winter, C. Schneijdenberg, M. Lebbink, B. Lich, A. J. Verkleij, M. R. Drury, and B. M. Humbel, “Tomography of insulating biological and geological materials using focused ion beam (FIB) sectioning and low-kV BSE imaging,” *Journal of Microscopy* **233**, 372–383 (2009).
- ⁷⁷⁶L. H. P. Hekking, M. N. Lebbink, D. A. M. D. E. Winter, C. T. W. M. Schneijdenberg, C. M. Brand, B. M. Humbel, A. J. Verkleij, and J. A. P. O. S. T., “Focused ion beam-scanning electron microscope: exploring large volumes of atherosclerotic tissue,” *Journal of Microscopy* **235**, 336–347 (2009).
- ⁷⁷⁷J. A. Heymann, M. Hayles, I. Gestmann, L. A. Giannuzzi, B. Lich, and S. Subramaniam, “Site-specific 3d imaging of cells and tissues with a dual beam microscope,” *Journal of Structural Biology* **155**, 63–73 (2006).
- ⁷⁷⁸M. Hayles, D. Stokes, D. Phifer, and K. Findlay, “A technique for improved focused ion beam milling of cryo-prepared life science specimens,” *Journal of Microscopy* **226**, 263–269 (2007), <https://onlinelibrary.wiley.com/doi/pdf/10.1111/j.1365-2818.2007.01775.x>.
- ⁷⁷⁹Y. Haridy, M. Osenberg, A. Hilger, I. Manke, D. Davesne, and F. Witzmann, “Bone metabolism and evolutionary origin of osteocytes: Novel application of fibsem tomography,” *Science Advances* **7**, eabb9113 (2021), <https://www.science.org/doi/pdf/10.1126/sciadv.abb9113>.
- ⁷⁸⁰M. S. Joens, C. Huynh, J. M. Kasuboski, D. C. Ferranti, Y. J. Sigal, F. Zeitvogel, M. Obst, C. J. Burkhardt, K. P. Curran, S. H. Chalasani, L. A. Stern, B. Goetze, and J. A. J. Fitzpatrick, “Helium Ion Microscopy (HIM) for the imaging of biological samples at sub-nanometer resolution,” *Scientific Reports* **3**, 3514 (2013).
- ⁷⁸¹C. G. Golding, L. L. Lamboo, D. R. Beniac, and T. F. Booth, “The scanning electron microscope in microbiology and diagnosis of infectious disease,” *Scientific Reports* **6** (2016), 10.1038/srep26516.
- ⁷⁸²M. Schmidt, J. M. Byrne, and I. J. Maasilta, “Bio-imaging with the helium-ion microscope: A review,” *Beilstein Journal of Nanotechnology* **12**, 1–23 (2021).
- ⁷⁸³A. Sharma, M. Schmidt, B. Kiesel, N. K. Mahato, L. Cralle, Y. Singh, H. H. Richnow, J. A. Gilbert, W. Arnold, and R. Lal, “Bacterial and archaeal viruses of himalayan hot springs at manikaran modulate host genomes,” *Frontiers in Microbiology* **9** (2018), 10.3389/fmicb.2018.03095.
- ⁷⁸⁴M. Leppänen, L.-R. Sundberg, E. Laanto, G. M. de Freitas Almeida, P. Papponen, and I. J. Maasilta, “Imaging bacterial colonies and phage-bacterium interaction at sub-nanometer resolution using helium-ion microscopy,” *Advanced Biosystems* **1**, 1700070 (2017).
- ⁷⁸⁵X. You, R. Kallies, I. Kühn, M. Schmidt, H. Harms, A. Chatzinotas, and L. Y. Wick, “Phage co-transport with hyphal-riding bacteria fuels bacterial invasion in a water-unsaturated microbial model system,” *The ISME Journal* (2021), 10.1038/s41396-021-01155-x.
- ⁷⁸⁶G. Vinner, Z. Rezaie-Yazdi, M. Leppanen, A. Stapley, M. Leaper, and D. Malik, “Microencapsulation of salmonella-specific bacteriophage felix o1 using spray-drying in a pH-responsive formulation and direct compression tableting of powders into a solid oral dosage form,” *Pharmaceuticals* **12**, 43 (2019).
- ⁷⁸⁷G. M. Almeida, M. Leppänen, I. J. Maasilta, and L.-R. Sundberg, “Bacteriophage imaging: past, present and future,” *Research in Microbiology* **169**, 488–494 (2018).
- ⁷⁸⁸N. Frese, P. Schmeurer, M. Wortmann, M. Schürmann, M. König, M. Westphal, F. Weber, H. Sudhoff, and A. Göhlhäuser, “Imaging of sars-cov-2 infected vero e6 cells by helium ion microscopy,” *Beilstein Journal of Nanotechnology* **12**, 172–179 (2021).
- ⁷⁸⁹D. F. Barreto-Vieira, M. A. N. da Silva, A. L. T. de Almeida, A. da Costa Rasinhas, M. E. Monteiro, M. D. Miranda, F. C. Motta, M. M. Siqueira, W. Girard-Dias, B. S. Archanjo, P. T. Bozza, T. M. L. Souza, S. S. G. Dias, V. C. Soares, and O. M. Barth, “SARS-CoV-2: Ultrastructural characterization of morphogenesis in an in vitro system,” *Viruses* **14**, 201 (2022).
- ⁷⁹⁰S.-C. Chen, N. Musat, O. J. Lechtenfeld, H. Paschke, M. Schmidt, N. Said, D. Popp, F. Calabrese, H. Stryhanyuk, U. Jaekel, Y.-G. Zhu, S. B. Joye, H.-H. Richnow, F. Widdel, and F. Musat, “Anaerobic oxidation of ethane by archaea from a marine hydrocarbon seep,” *Nature* **568**, 108–111 (2019).
- ⁷⁹¹N. Said, A. Chatzinotas, and M. Schmidt, “Have an ion on it: the life-cycle of bdellovibrio bacteriovorus viewed by helium-ion microscopy,” *Advanced Biosystems* , 1800250 (2018).
- ⁷⁹²M. K. LeTourneau, M. M. Marshall, L. S. Thomashow, and J. B. Harsh, “Impact of phenazine-1-carboxylic acid upon biofilm development in the rhizosphere of dryland and irrigated

- wheat," *Microscopy and Microanalysis* **21**, 711–712 (2015).
- ⁷⁹³A. Belianinov, M. C. Halsted, M. J. Burch, K. Songkil, and S. T. Retterer, "Biofilm structure of geobacter sulfurreducens by helium ion microscopy," *Microscopy and Microanalysis* **23**, 1152–1153 (2017).
- ⁷⁹⁴J. H. Moreno Osorio, P. Benettoni, M. Schmidt, H. Stryhanyuk, M. Schmitt-Jansen, G. Pinto, A. Pollio, L. Frunzo, P. N. L. Lens, H. H. Richnow, G. Esposito, and N. Musat, "Investigation of architecture development and phosphate distribution in chlorella biofilm by complementary microscopy techniques," *FEMS Microbiology Ecology* **95** (2019), 10.1093/femsec/fiz029.
- ⁷⁹⁵W. L. Rice, A. N. V. Hoek, T. G. Păunescu, C. Huynh, B. Goetze, B. Singh, L. Scipioni, L. A. Stern, and D. Brown, "High resolution helium ion scanning microscopy of the rat kidney," *PLoS ONE* **8**, e57051 (2013).
- ⁷⁹⁶X. Chen, C. N. B. Udlagama, C.-B. Chen, A. A. Bettiol, D. S. Pickard, T. Venkatesan, and F. Watt, "Whole-cell imaging at nanometer resolutions using fast and slow focused helium ions," *Biophysical Journal* **101**, 1788–1793 (2011).
- ⁷⁹⁷M. Schürmann, N. Shephard, N. Frese, K. Geishendorf, H. Sudhoff, A. Göhlhäuser, U. Rückert, C. Kaltschmidt, B. Kaltschmidt, and A. Thomas, "Technical feasibility study for production of tailored multielectrode arrays and patterning of arranged neuronal networks," *PLoS ONE* **13**, e0192647 (2018).
- ⁷⁹⁸M. Schürmann, N. Frese, A. Beyer, P. Heimann, D. Widera, V. Mönkemöller, T. Huser, B. Kaltschmidt, C. Kaltschmidt, and A. Göhlhäuser, "Helium ion microscopy visualizes lipid nanodomains in mammalian cells," *Small* **11**, 5781–5789 (2015).
- ⁷⁹⁹C. Sato, M. Sato, and S. Ogawa, "Imaging of immunogold labeling in cells and tissues by helium ion microscopy," *International Journal of Molecular Medicine* (2018), 10.3892/ijmm.2018.3604.
- ⁸⁰⁰H. Takei, K. Nagata, N. Frese, A. Göhlhäuser, and T. Okamoto, "Surface-enhanced raman spectroscopy for molecule characterization: HIM investigation into sources of SERS activity of silver-coated butterfly scales," *Nanomaterials* **11**, 1741 (2021).
- ⁸⁰¹C. D. Bandara, G. Ballerin, M. Leppänen, T. Tesfamichael, K. K. Ostrikov, and C. B. Whitchurch, "Resolving bio-nano interactions of e. coli bacteria-dragonfly wing interface with helium ion and 3d-structured illumination microscopy to understand bacterial death on nanotopography," *ACS Biomaterials Science & Engineering* **6**, 3925–3932 (2020).
- ⁸⁰²C. D. Bandara, M. Schmidt, Y. Davoudpour, H. Stryhanyuk, H. H. Richnow, and N. Musat, "Microbial identification, high-resolution microscopy and spectrometry of the rhizosphere in its native spatial context," *Frontiers in Plant Science* **12** (2021), 10.3389/fpls.2021.668929.
- ⁸⁰³W. Denk and H. Horstmann, "Serial block-face scanning electron microscopy to reconstruct three-dimensional tissue nanostructure," *PLoS Biology* **2**, null (2004).
- ⁸⁰⁴K. M. Harris, E. Perry, J. Bourne, M. Feinberg, L. Ostroff, and J. Hurlburt, "Uniform serial sectioning for transmission electron microscopy," *Journal of Neuroscience* **26**, 12101–12103 (2006), <https://www.jneurosci.org/content/26/47/12101.full.pdf>.
- ⁸⁰⁵K. Narayan and S. Subramaniam, "Focused ion beams in biology," *Nat. Methods* **12**, 1021–1031 (2015).
- ⁸⁰⁶G. Sergey, K. Denis, H. Ava, G. Gediminas, O. Viola, O. L. Kaluza, R. H. Law, M. O. Bryan, P. Roger, J. C. Whistock, and A. de Marco, "Oxygen plasma focused ion beam scanning electron microscopy for biological samples," (2018), [bioRxiv:457820](https://arxiv.org/abs/1804.05782).
- ⁸⁰⁷L. M. Hartnell, L. A. Earl, D. Bliss, A. Moran, and S. Subramaniam, "Imaging cellular architecture with 3D SEM," in *Encyclopedia of Cell Biology* (Elsevier, 2016) pp. 44–50.
- ⁸⁰⁸D. Drobne, M. Milani, A. Zrimec, V. Leser, and M. Berden Zrimec, "Electron and ion imaging of gland cells using the fib/sem system," *Journal of Microscopy* **219**, 29–35 (2005), <https://onlinelibrary.wiley.com/doi/pdf/10.1111/j.1365-2818.2005.01490.x>.
- ⁸⁰⁹V. Leser, D. Drobne, Z. Pipan, M. Milani, and F. Tatti, "Comparison of different preparation methods of biological samples for fib milling and sem investigation," *Journal of Microscopy* **233**, 309–319 (2009), <https://onlinelibrary.wiley.com/doi/pdf/10.1111/j.1365-2818.2009.03121.x>.
- ⁸¹⁰G. Knott, S. Rosset, and M. Cantoni, "Focussed ion beam milling and scanning electron microscopy of brain tissue," *J. Vis. Exp.* **53**, e2588 (2011).
- ⁸¹¹C. Kizilyaprak, A. Bittermann, J. Daraspe, and B. Humbel, "Fib-sem tomography in biology," in *Electron Microscopy: Methods and Protocols, Methods in Molecular Biology*, Vol. 1117, edited by J. Kuo (Springer Science+Business Media New York, 2014) Chap. 24.
- ⁸¹²C. Kobler, A. Saber, N. Jacobsen, H. Wallin, U. Vogel, K. Qvortrup, and K. Molhave, *Anal. Bioanal. Chem.*, 3863–3873 (2014).
- ⁸¹³D. Drobne, "3d imaging of cells and tissues by focused ion beam/scanning electron microscopy (fib/sem)," in *Nanoimaging: Methods and Protocols, Methods in Molecular Biology*, Vol. 950, edited by A. A. Sousa and M. J. Kruhlik (Springer Science+Business Media, 2013) Chap. 16.
- ⁸¹⁴G. Schmid, F. Zeitvogel, L. Hao, P. Ingino, M. Floetenmeyer, Y.-D. Stierhof, B. Schroepel, C. J. Burkhardt, A. Kappler, and M. Obst, "3-d analysis of bacterial cell-(iron)mineral aggregates formed during fe(ii) oxidation by the nitrate-reducing acidovorax sp. strain bofen1 using complementary microscopy tomography approaches," *Geobiology* **12**, 340–361 (2014), <https://onlinelibrary.wiley.com/doi/pdf/10.1111/gbi.12088>.
- ⁸¹⁵M. Marko, C. Hsieh, W. Moberlychan, C. Mannella, and J. Frank, "Focused ion beam milling of vitreous water: prospects for an alternative to cryoultramicrotomy of frozen-hydrated biological samples," *Journal of Microscopy* **222**, 42–47 (2006), <https://onlinelibrary.wiley.com/doi/pdf/10.1111/j.1365-2818.2006.01567.x>.
- ⁸¹⁶M. Hayles and D. De Winter, "An introduction to cryo-fib-sem cross-sectioning of frozen hydrated life science samples," *Journal of Microscopy* **281**, 138–156 (2021).
- ⁸¹⁷M. Lucas, M. Guentert, P. Gasser, F. Lucas, and R. Wepf, "Correlative 3d imaging: Clsm and fib-sem tomography using high-pressure frozen, freeze-substituted biological samples," in *Electron Microscopy: Methods and Protocols, Methods in Molecular Biology*, Vol. 1117, edited by J. Kuo (Springer Science+Business Media New York, 2014) Chap. 26.
- ⁸¹⁸S. Gorelick, G. Buckley, G. Gervinskis, T. K. Johnson, A. Handley, M. P. Caggiano, J. C. Whistock, R. Pocock, and A. de Marco, "PIE-scope, integrated cryo-correlative light and FIB/SEM microscopy," *eLife* **8** (2019), 10.7554/elife.45919.
- ⁸¹⁹J. Wang, S. Randolph, Q. Wu, A. Botman, J. Schardt, C. Bouchet-Marquis, X. Nan, C. Rue, and M. Straw, "Reactive oxygen fib spin milling enables correlative workflow for 3d super-resolution light microscopy and serial fib/sem of cultured cells," *Sci. Rep.* **11**, 13162 (2021).
- ⁸²⁰C. S. Xu, K. J. Hayworth, Z. Lu, P. Grob, A. M. Hassan, J. G. García-Cerdán, K. K. Niyogi, E. Nogales, R. J. Weinberg, and H. F. Hess, "Enhanced fib-sem systems for large-volume 3d imaging," *eLife* **6**, e25916 (2017).
- ⁸²¹D. M. Binkley, J. Deering, H. Yuan, A. Gourrier, and K. Grandfield, "Ellipsoidal mesoscale mineralization pattern in human cortical bone revealed in 3d by plasma focused ion beam serial sectioning," *Journal of Structural Biology* **212**, 107615 (2020).
- ⁸²²V. Baena, R. Conrad, P. Friday, E. Fitzgerald, T. Kim, J. Bernbaum, H. Berensmann, A. Harned, K. Nagashima, and K. Narayan, "Fib-sem as a volume electron microscopy approach to study cellular architectures in sars-cov-2 and other viral infections: A practical primer for a virologist," *Viruses* **13**

- (2021), [10.3390/v13040611](https://doi.org/10.3390/v13040611).
- ⁸²³M. Cortese, J.-Y. Lee, B. Cerikan, C. J. Neufeldt, V. M. Oorschot, S. Köhrer, J. Hennies, N. L. Schieber, P. Ronchi, G. Mizzon, I. Romero-Brey, R. Santarella-Mellwig, M. Schorb, M. Boermel, K. Mocaer, M. S. Beckwith, R. M. Templin, V. Gross, C. Pape, C. Tischer, J. Frankish, N. K. Horvat, V. Laketa, M. Stanifer, S. Boulant, A. Ruggieri, L. Chatel-Chaix, Y. Schwab, and R. Bartenschlager, “Integrative imaging reveals sars-cov-2-induced reshaping of subcellular morphologies,” *Cell Host & Microbe* **28**, 853–866.e5 (2020).
- ⁸²⁴J. Jansen, K. C. Reimer, J. S. Nagai, F. S. Varghese, G. J. Overheul, M. de Beer, R. Roverts, D. Daviran, L. A. Fermin, B. Willemsen, M. Beukenboom, S. Djudjaj, S. von Stillfried, L. E. van Eijk, M. Mastik, M. Bulthuis, W. den Dunnen, H. van Goor, J.-L. Hillebrands, S. H. Triana, T. Alexandrov, M.-C. Timm, B. T. van den Berge, M. van den Broek, Q. Nlandu, J. Heijnert, E. M. Bindels, R. M. Hoogenboezem, F. Mooren, C. Kuppe, P. Miesen, K. Grünberg, T. Ijzermans, E. J. Steenbergen, J. Czogalla, M. F. Schreuder, N. Somerdijk, A. Akiva, P. Boz, V. G. Puelles, J. Floege, T. B. Huber, H. Achdout, A. Aimon, E. Bar-David, H. Barr, A. Ben-Shmuel, J. Bennett, M. L. Boby, B. Borden, G. R. Bowman, J. Brun, S. BVNBS, M. Calmiano, A. Carbery, E. Cattermole, E. Chernychenko, J. D. Choder, A. Clyde, J. E. Cofland, G. Cohen, J. Cole, A. Contini, L. Cox, M. Cvitkovic, A. Dias, K. Donckers, D. L. Dotson, A. Douangamath, S. Duberstein, T. Dudgeon, L. Dunnett, P. K. Eastman, N. Erez, C. J. Eyermann, M. Fairhead, G. Fate, D. Fearon, O. Federov, M. Ferla, R. S. Fernandes, L. Ferrins, R. Foster, H. Foster, R. Gabizon, A. Garcia-Sastre, V. O. Gawriljuk, P. Gehrtz, C. Gileadi, C. Giroud, W. G. Glass, R. Glen, Itai glinert, A. S. Godoy, M. Gorichko, T. Gorrie-Stone, E. J. Griffen, S. H. Hart, J. Heer, M. Henry, M. Hill, S. Horrell, M. F. Hurley, T. Israely, A. Jajack, E. Jnoff, D. Jochmans, T. John, S. De Jonghe, A. L. Kantsadi, P. W. Kenny, J. Kiappes, L. Koekemoer, B. Kovar, T. Krojer, A. A. Lee, B. A. Lefker, H. Levy, N. London, P. Lukacik, H. B. Macdonald, B. Maclean, T. R. Malla, T. Matviuk, W. McCorkindale, B. L. McGovern, S. Melamed, O. Michurin, H. Mikolajek, B. F. Milne, A. Morris, G. M. Morris, M. J. Morwitzer, D. Moustakas, A. M. Nakamura, J. B. Neto, J. Neyts, L. Nguyen, G. D. Noske, V. Oleinikovas, G. Oliva, G. J. Overheul, D. Owen, V. Psenak, R. Pai, J. Pan, N. Paran, B. Perry, M. Pingle, J. Pinjari, B. Politi, A. Powell, R. Puni, V. L. Rangel, R. N. Reddi, S. P. Reid, E. Resnick, E. G. Ripka, M. C. Robinson, R. P. Robinson, J. Rodriguez-Guerra, R. Rosales, D. Rufa, C. Schofield, M. Shafeev, A. Shaikh, J. Shi, K. Shurrush, S. Sing, A. Sittner, R. Skyner, A. Smalley, M. D. Smilova, L. J. Solmesky, J. Spencer, C. Strain-Damarell, V. Swamy, H. Tamir, R. Tennant, W. Thompson, A. Thompson, W. Thompson, S. Tomasia, A. Tumber, I. Vakonakis, R. P. van Rij, L. van Geel, F. S. Varghese, M. Vaschetto, E. B. Vitner, V. Voelz, A. Volkamer, F. von Delft, A. von Delft, M. Walsh, W. Ward, C. Weatherall, S. Weiss, K. M. White, C. F. Wild, M. Wittmann, N. Wright, Y. Yahalom-Ronen, D. Zaidmann, H. Zidane, N. Zitzmann, R. P. van Rij, I. G. Costa, R. K. Schneider, B. Smeets, and R. Kramann, “Sars-cov-2 infects the human kidney and drives fibrosis in kidney organoids,” *Cell Stem Cell* **29**, 217–231.e8 (2022).
- ⁸²⁵D. Spohner, A. Steyer, L. Bertinetti, I. Orlov, L. Benoit, K. Pernet-Gallay, A. Schertel, and P. Schultz, “Cryo-fib-sem as a promising tool for localizing proteins in 3d,” *Journal of Structural Biology* **211**, 107528 (2020).
- ⁸²⁶H. Lim and D. Moon, “Microscopic and nanoscopic protein imaging by sims and helium ion microscopy,” *Biointerphases* **15**, 038501 (2020), <https://doi.org/10.1116/6.0000220>.
- ⁸²⁷H. F. Arlinghaus, “Possibilities and limitations of high-resolution mass spectrometry in life sciences,” *Applied Surface Science* **255**, 1058–1063 (2008), proceedings of the Sixteenth International Conference on Secondary Ion Mass Spectrometry, SIMS XVI.
- ⁸²⁸M. K. Passarelli, A. Pirkel, R. Moellers, D. Grinfeld, F. Kollmer, R. Havelund, C. F. Newman, P. S. Marshall, H. Arlinghaus, M. R. Alexander, A. West, S. Horning, E. Niehuis, A. Makarov, C. T. Dollery, and I. S. Gilmore, “The 3D OrbiSIMS—label-free metabolic imaging with subcellular lateral resolution and high mass-resolving power,” *Nature Methods* **14**, 1175–1183 (2017).
- ⁸²⁹I. S. Gilmore, S. Heiles, and C. L. Pieterse, “Metabolic imaging at the single-cell scale: Recent advances in mass spectrometry imaging,” *Annual Review of Analytical Chemistry* **12**, 201–224 (2019), pMID: 30848927, <https://doi.org/10.1146/annurev-anchem-061318-115516>.
- ⁸³⁰A. Merolli, L. Kasaei, S. Ramasamy, A. Kolloli, R. Kumar, S. S., and L. Feldman, *Scientific Reports* **12**, 3794 (2022).
- ⁸³¹C. Guillermier, D. Medina Cruz, J.-N. Audinot, and T. Wirtz, “Characterization of Biogenic Nanoparticles Via In-Situ Correlative Secondary Electron Helium Microscopy and Secondary Ion Mass Spectrometry,” *Microsc. Microanal.* **25**, 1062–1063 (2019).
- ⁸³²P. Benettoni, H. Stryhanyuk, S. Wagner, F. Kollmer, J. Moreno-Osorio, T. Schmidt, M. Reemtsma, and H.-H. Richnow, *J. Anal. At. Spectrom.*, 1098 (2019).
- ⁸³³J. Decelle, H. Stryhanyuk, B. Gallet, G. Veronesi, M. Schmidt, S. Balzano, S. Marro, C. Uwizeye, P.-H. Jouneau, J. Lupette, J. Jouhet, E. Maréchal, Y. Schwab, N. L. Schieber, R. Tucoulou, H. Richnow, G. Finazzi, and N. Musat, “Algal remodeling in a ubiquitous planktonic photosymbiosis,” *Current Biology* **29**, 968–978.e4 (2019).
- ⁸³⁴B. Forslund, K. G. Malmqvist, and J. Pallon, “Proton induced X-ray emission analysis of biological specimens—past and future.” *Scanning microscopy* **5**, 877–884 (1991).
- ⁸³⁵G. Basnakova, A. J. Spencer, E. Palsgard, G. W. Grime, and L. E. Macaskie, “Identification of the nickel uranyl phosphate deposits on *Citrobacter* sp. cells by electron microscopy with electron probe x-ray microanalysis and by proton-induced x-ray emission analysis,” *Environmental Science & Technology* **32**, 760–765 (1998), <https://doi.org/10.1021/es9705553>.
- ⁸³⁶N. Musat, R. Foster, T. Vagner, B. Adam, and M. M. M. Kuypers, “Detecting metabolic activities in single cells, with emphasis on nanoSIMS,” *FEMS Microbiology Reviews* **36**, 486–511 (2012), <https://academic.oup.com/femsre/article-pdf/36/2/486/18129385/36-2-486.pdf>.
- ⁸³⁷F. Calabrese, I. Voloshynovska, F. Musat, M. Thullner, M. Schlömann, H. H. Richnow, J. Lambrecht, S. Müller, L. Y. Wick, N. Musat, and H. Stryhanyuk, “Quantitation and comparison of phenotypic heterogeneity among single cells of monoclonal microbial populations,” *Frontiers in Microbiology* **10** (2019), [10.3389/fmicb.2019.02814](https://doi.org/10.3389/fmicb.2019.02814).
- ⁸³⁸T. Leefmann, C. Heim, A. Kryvenda, S. Siljeström, P. Sjövall, and V. Thiel, “Biomarker imaging of single diatom cells in a microbial mat using time-of-flight secondary ion mass spectrometry (ToF-SIMS),” *Organic Geochemistry* **57**, 23–33 (2013).
- ⁸³⁹M. A. Moreno, I. Mouton, N. Chevalier, J.-P. Barnes, F. Bassani, and B. Gautier, “Combined ToF-SIMS and AFM protocol for accurate 3d chemical analysis and data visualization,” *J. Vac. Sci. Technol. B* **36**, 03F122 (2018).
- ⁸⁴⁰J. M. Byrne, M. Schmidt, T. Gauger, C. Bryce, and A. Kappler, “Imaging organic–mineral aggregates formed by Fe(II)-oxidizing bacteria using helium ion microscopy,” *Environmental Science & Technology Letters* **5**, 209–213 (2018).
- ⁸⁴¹M. Tamisier, M. Schmidt, C. Vogt, S. Kümmel, H. Stryhanyuk, N. Musat, H.-H. Richnow, and F. Musat, “Iron corrosion by methanogenic archaea characterized by stable isotope effects and crust mineralogy,” *Environmental Microbiology* **24**, 583–595 (2022), <https://sfamjournals.onlinelibrary.wiley.com/doi/pdf/10.1111/1462-2920.15658>.
- ⁸⁴²K. Laufer, M. Nordhoff, M. Halama, R. E. Martinez, M. Obst, M. Nowak, H. Stryhanyuk, H. H. Richnow, and A. Kappler, “Microaerophilic Fe(II)-oxidizing zetapro-

- teobacteria isolated from low-fe marine coastal sediments: Physiology and composition of their twisted stalks,” *Applied and Environmental Microbiology* **83**, e03118–16 (2017), <https://journals.asm.org/doi/pdf/10.1128/AEM.03118-16>.
- ⁸⁴³J. R. Wilson, W. Kobsiriphat, R. Mendoza, H.-Y. Chen, J. M. Hiller, D. J. Miller, K. Thornton, P. W. Voorhees, S. B. Adler, and S. A. Barnett, “Three-dimensional reconstruction of a solid-oxide fuel-cell anode,” *Nature Materials* **5**, 541–544 (2006).
- ⁸⁴⁴S. Zils, M. Timpel, T. Arlt, A. Wolz, I. Manke, and C. Roth, “3d visualisation of PEMFC electrode structures using FIB nanotomography,” *Fuel Cells* **10**, 966–972 (2010).
- ⁸⁴⁵H. Schulenburg, B. Schwanitz, N. Linse, G. G. Scherer, A. Wokaun, J. Krbanjevic, R. Grothausmann, and I. Manke, “3d imaging of catalyst support corrosion in polymer electrolyte fuel cells,” *The Journal of Physical Chemistry C* **115**, 14236–14243 (2011).
- ⁸⁴⁶R. Moroni, M. Börner, L. Zielke, M. Schroeder, S. Nowak, M. Winter, I. Manke, R. Zengerle, and S. Thiele, “Multi-scale correlative tomography of a li-ion battery composite cathode,” *Scientific Reports* **6** (2016), 10.1038/srep30109.
- ⁸⁴⁷L. Zielke, T. Hutzenlaub, D. R. Wheeler, C.-W. Chao, I. Manke, A. Hilger, N. Paust, R. Zengerle, and S. Thiele, “Three-phase multiscale modeling of a LiCoO₂ cathode: Combining the advantages of FIB-SEM imaging and x-ray tomography,” *Advanced Energy Materials* **5**, 1401612 (2014).
- ⁸⁴⁸M. C. Paulisch, M. Gebhard, D. Franzen, A. Hilger, M. Osenberg, S. Marathe, C. Rau, B. Ellendorff, T. Turek, C. Roth, and I. Manke, “Operando synchrotron imaging of electrolyte distribution in silver-based gas diffusion electrodes during oxygen reduction reaction in highly alkaline media,” *ACS Applied Energy Materials* **4**, 7497–7503 (2021).
- ⁸⁴⁹M. Neumann, M. Osenberg, A. Hilger, D. Franzen, T. Turek, I. Manke, and V. Schmidt, “On a pluri-gaussian model for three-phase microstructures, with applications to 3d image data of gas-diffusion electrodes,” *Computational Materials Science* **156**, 325–331 (2019).
- ⁸⁵⁰S. Vierrath, L. Zielke, R. Moroni, A. Mondon, D. R. Wheeler, R. Zengerle, and S. Thiele, “Morphology of nanoporous carbon-binder domains in li-ion batteries—a FIB-SEM study,” *Electrochemistry Communications* **60**, 176–179 (2015).
- ⁸⁵¹A. Etienneble, A. Tranchot, T. Douillard, H. Idrissi, E. Maire, and L. Roué, “Evolution of the 3d microstructure of a si-based electrode for li-ion batteries investigated by FIB/SEM tomography,” *Journal of The Electrochemical Society* **163**, A1550–A1559 (2016).
- ⁸⁵²J. Billaud, F. Bouville, T. Magrini, C. Villevieille, and A. R. Studart, “Magnetically aligned graphite electrodes for high-rate performance li-ion batteries,” *Nature Energy* **1** (2016), 10.1038/nenergy.2016.97.
- ⁸⁵³Z. Liu, Y. chen K. Chen-Wiegart, J. Wang, S. A. Barnett, and K. T. Faber, “Three-phase 3d reconstruction of a LiCoO₂ cathode via FIB-SEM tomography,” *Microscopy and Microanalysis* **22**, 140–148 (2016).
- ⁸⁵⁴P. R. Shearing, N. P. Brandon, J. Gelb, R. Bradley, P. J. Withers, A. J. Marquis, S. Cooper, and S. J. Harris, “Multi length scale microstructural investigations of a commercially available li-ion battery electrode,” *Journal of The Electrochemical Society* **159**, A1023–A1027 (2012).
- ⁸⁵⁵Z. Liu, H. Wang, D. P. Singh, M. Wagemaker, K. T. Faber, and S. A. Barnett, “Three-phase 3d reconstruction of li-ion batteries electrodes via FIB-SEM tomography,” *ECS Meeting Abstracts MA2015-01*, 548–548 (2015).
- ⁸⁵⁶M. F. Lagadec, R. Zahn, and V. Wood, “Characterization and performance evaluation of lithium-ion battery separators,” *Nature Energy* **4**, 16–25 (2018).
- ⁸⁵⁷T. Shi, Y.-Q. Zhang, Q. Tu, Y. Wang, M. C. Scott, and G. Ceder, “Characterization of mechanical degradation in an all-solid-state battery cathode,” *Journal of Materials Chemistry A* **8**, 17399–17404 (2020).
- ⁸⁵⁸J. L. Houx, M. Osenberg, M. Neumann, J. R. Binder, V. Schmidt, I. Manke, T. Carraro, and D. Kramer, “Effect of tomography resolution on calculation of microstructural properties for lithium ion porous electrodes,” *ECS Transactions* **97**, 255–266 (2020).
- ⁸⁵⁹M. Kroll, S. L. Karstens, M. Cronau, A. Hölzel, S. Schlabach, N. Nobel, C. Redenbach, B. Roling, and U. Tallarek, “Three-phase reconstruction reveals how the microscopic structure of the carbon-binder domain affects ion transport in lithium-ion batteries,” *Batteries & Supercaps* **4**, 1363–1373 (2021).
- ⁸⁶⁰M. Ghadban, M. Sabharwal, C. Rea, X. Li, A. E. Goode, M. Smith, C. Murphy, and M. Secanell, “3d microscale modeling of NMC cathodes using multi-resolution FIB-SEM tomography,” *Journal of Power Sources* **562**, 232745 (2023).
- ⁸⁶¹A. G. Star and T. F. Fuller, “FIB-SEM tomography connects microstructure to corrosion-induced performance loss in PEMFC cathodes,” *Journal of The Electrochemical Society* **164**, F901–F907 (2017).
- ⁸⁶²N. Bevilacqua, T. Asset, M. Schmid, H. Markötter, I. Manke, P. Atanassov, and R. Zeis, “Impact of catalyst layer morphology on the operation of high temperature PEM fuel cells,” *Journal of Power Sources Advances* **7**, 100042 (2021).
- ⁸⁶³C. Netzeband, T. Arlt, K. Wippermann, W. Lehnert, and I. Manke, “Three-dimensional multiscale analysis of degradation of nano- and micro-structure in direct methanol fuel cell electrodes after methanol starvation,” *Journal of Power Sources* **327**, 481–487 (2016).
- ⁸⁶⁴K. Yakal-Kremski, G. A. Hughes, A. V. Call, and S. A. Barnett, “Effect of current switching on LSM-YSZ composite electrode durability,” *ECS Transactions* **41**, 129–136 (2012).
- ⁸⁶⁵B. J. Etzold, U. Krewer, S. Thiele, A. Dreizler, E. Klemm, and T. Turek, “Understanding the activity transport nexus in water and CO₂ electrolysis: State of the art, challenges and perspectives,” *Chemical Engineering Journal* **424**, 130501 (2021).
- ⁸⁶⁶Y. Wang, X. Lin, L. Zhang, G. Xiao, C. Guan, J. Yang, X. Lv, D. Liu, and J.-Q. Wang, “Three-dimensional microstructural characterization of solid oxide electrolysis cell with ce0.8gd0.2o2-infiltrated ni/YSZ electrode using focused ion beam-scanning electron microscopy,” *Journal of Solid State Electrochemistry* **25**, 1633–1644 (2021).
- ⁸⁶⁷F. Hegge, R. Moroni, P. Trinke, B. Bensmann, R. Hanke-Rauschenbach, S. Thiele, and S. Vierrath, “Three-dimensional microstructure analysis of a polymer electrolyte membrane water electrolyzer anode,” *Journal of Power Sources* **393**, 62–66 (2018).
- ⁸⁶⁸D. McLaughlin and S. Thiele, “FIB/SEM nanotomography of a CO₂ electrolyzer cathode catalyst layer,” *ECS Meeting Abstracts MA2020-01*, 2705–2705 (2020).
- ⁸⁶⁹M. Gebhard, T. Tichter, D. Franzen, M. C. Paulisch, K. Schutjajew, T. Turek, I. Manke, and C. Roth, “Improvement of oxygen-depolarized cathodes in highly alkaline media by electrospinning of poly(vinylidene fluoride) barrier layers,” *ChemElectroChem* **7**, 830–837 (2020).
- ⁸⁷⁰R. Grothausmann, S. Fiechter, R. Beare, G. Lehmann, H. Kropf, G. S. V. Kumar, I. Manke, and J. Banhart, “Automated quantitative 3d analysis of faceting of particles in tomographic datasets,” *Ultramicroscopy* **122**, 65–75 (2012).
- ⁸⁷¹D. Franzen, B. Ellendorff, M. C. Paulisch, A. Hilger, M. Osenberg, I. Manke, and T. Turek, “Influence of binder content in silver-based gas diffusion electrodes on pore system and electrochemical performance,” *Journal of Applied Electrochemistry* **49**, 705–713 (2019).
- ⁸⁷²D. McLaughlin, M. Bierling, R. Moroni, C. Vogl, G. Schmid, and S. Thiele, “Tomographic reconstruction and analysis of a silver CO₂ reduction cathode,” *Advanced Energy Materials* **10**, 2000488 (2020).
- ⁸⁷³K. Dong, Y. Xu, J. Tan, M. Osenberg, F. Sun, Z. Kochovski, D. T. Pham, S. Mei, A. Hilger, E. Ryan, Y. Lu, J. Banhart, and I. Manke, “Unravelling the mechanism of lithium nucleation and growth and the interaction with the solid electrolyte

- interface," *ACS Energy Letters* **6**, 1719–1728 (2021).
- ⁸⁷⁴Y. Xu, K. Dong, Y. Jie, P. Adelhelm, Y. Chen, L. Xu, P. Yu, J. Kim, Z. Kochovski, Z. Yu, W. Li, J. LeBeau, Y. Shao-Horn, R. Cao, S. Jiao, T. Cheng, I. Manke, and Y. Lu, "Promoting mechanistic understanding of lithium deposition and solid-electrolyte interphase (SEI) formation using advanced characterization and simulation methods: Recent progress, limitations, and future perspectives," *Advanced Energy Materials* **12**, 2200398 (2022).
- ⁸⁷⁵H. Zheng, J. Cui, and K. He, "A new cryo-FIB-TEM approach for damage-free characterization of garnet electrolytes in solid-state batteries," *Microscopy and Microanalysis* **26**, 2784–2785 (2020).
- ⁸⁷⁶J. Cui, H. Zheng, and K. He, "Air-protective cryo-FIB tomography of sensitive materials for energy applications," *Microscopy and Microanalysis* **26**, 1828–1829 (2020).
- ⁸⁷⁷S. Berg, D. Kutra, T. Kroeger, C. N. Straehle, B. X. Kausler, C. Haubold, M. Schiegg, J. Ales, T. Beier, M. Rudy, K. Eren, J. I. Cervantes, B. Xu, F. Beuttenmueller, A. Wolny, C. Zhang, U. Koethe, F. A. Hamprecht, and A. Kreshuk, "ilastik: interactive machine learning for (bio)image analysis," *Nature Methods* (2019), [10.1038/s41592-019-0582-9](https://doi.org/10.1038/s41592-019-0582-9).
- ⁸⁷⁸I. Arganda-Carreras, V. Kaynig, C. Rueden, K. W. Eliceiri, J. Schindelin, A. Cardona, and H. Sebastian Seung, "Trainable Weka Segmentation: a machine learning tool for microscopy pixel classification," *Bioinformatics* **33**, 2424–2426 (2017), https://academic.oup.com/bioinformatics/article-pdf/33/15/2424/25157857/btx180_supplementary_tws-manual.pdf.
- ⁸⁷⁹M. Ender, J. Joos, T. Carraro, and E. Ivers-Tiffée, "Three-dimensional reconstruction of a composite cathode for lithium-ion cells," *Electrochemistry Communications* **13**, 166–168 (2011).
- ⁸⁸⁰M. Salzer, A. Spettl, O. Stenzel, J.-H. Smätt, M. Lindén, I. Manke, and V. Schmidt, "A two-stage approach to the segmentation of FIB-SEM images of highly porous materials," *Materials Characterization* **69**, 115–126 (2012).
- ⁸⁸¹R. Moroni and S. Thiele, "FIB/SEM tomography segmentation by optical flow estimation," *Ultramicroscopy* **219**, 113090 (2020).
- ⁸⁸²M. Salzer, S. Thiele, R. Zengerle, and V. Schmidt, "On the importance of FIB-SEM specific segmentation algorithms for porous media," *Materials Characterization* **95**, 36–43 (2014).
- ⁸⁸³M. Salzer, T. Prill, A. Spettl, D. Jeulin, K. Schladitz, and V. Schmidt, "Quantitative comparison of segmentation algorithms for FIB-SEM images of porous media," *Journal of Microscopy* **257**, 23–30 (2014).
- ⁸⁸⁴O. Furat, M. Wang, M. Neumann, L. Petrich, M. Weber, C. E. Krill, and V. Schmidt, "Machine learning techniques for the segmentation of tomographic image data of functional materials," *Frontiers in Materials* **6** (2019), [10.3389/fmats.2019.00145](https://doi.org/10.3389/fmats.2019.00145).
- ⁸⁸⁵T. Arlt, M. Liebert, M. Paulisch, I. Lüdeking, C. Bergbreiter, L. Jörissen, and I. Manke, "Multi-scale analysis and phase segmentation of FIB and x-ray tomographic data of electrolyzer electrodes using machine learning algorithms," *ECS Transactions* **97**, 639–649 (2020).
- ⁸⁸⁶J. J. Bailey, A. Wade, A. M. Boyce, Y. S. Zhang, D. J. Brett, and P. R. Shearing, "Quantitative assessment of machine-learning segmentation of battery electrode materials for active material quantification," *Journal of Power Sources* **557**, 232503 (2023).
- ⁸⁸⁷M. Osenberg, A. Hilger, M. Neumann, A. Wagner, N. Bohn, J. R. Binder, V. Schmidt, J. Banhart, and I. Manke, "Classification of FIB/SEM-tomography images for highly porous multiphase materials using random forest classifiers," (2022), [arXiv:2207.14114 \[cond-mat.mtrl-sci\]](https://arxiv.org/abs/2207.14114).
- ⁸⁸⁸O. Ronneberger, P. Fischer, and T. Brox, "U-net: Convolutional networks for biomedical image segmentation," in *Medical Image Computing and Computer-Assisted Intervention—MICCAI 2015: 18th International Conference, Munich, Germany, October 5–9, 2015, Proceedings, Part III 18* (Springer, 2015) pp. 234–241.
- ⁸⁸⁹L. K. Scheffer, C. S. Xu, M. Januszewski, Z. Lu, S. ya Take-mura, K. J. Hayworth, G. B. Huang, K. Shinomiya, J. Maitlin-Shepard, S. Berg, J. Clements, P. M. Hubbard, W. T. Katz, L. Umayam, T. Zhao, D. Ackerman, T. Blakely, J. Bogovic, T. Dolafi, D. Kainmueller, T. Kawase, K. A. Khairy, L. Leavitt, P. H. Li, L. Lindsey, N. Neubarth, D. J. Olbris, H. Otsuna, E. T. Trautman, M. Ito, A. S. Bates, J. Goldammer, T. Wolff, R. Svirskas, P. Schlegel, E. Neace, C. J. Knecht, C. X. Alvarado, D. A. Bailey, S. Ballinger, J. A. Borycz, B. S. Canino, N. Cheatham, M. Cook, M. Dreher, O. Duclos, B. Eubanks, K. Fairbanks, S. Finley, N. Forknall, A. Francis, G. P. Hopkins, E. M. Joyce, S. Kim, N. A. Kirk, J. Kovalyak, S. A. Lauchie, A. Lohff, C. Maldonado, E. A. Manley, S. McLin, C. Mooney, M. Ndama, O. Ogundeyi, N. Okeoma, C. Ordish, N. Padilla, C. M. Patrick, T. Paterson, E. E. Phillips, E. M. Phillips, N. Rampally, C. Ribeiro, M. K. Robertson, J. T. Rymer, S. M. Ryan, M. Sammons, A. K. Scott, A. L. Scott, A. Shinomiya, C. Smith, K. Smith, N. L. Smith, M. A. Sobeski, A. Suleiman, J. Swift, S. Takemura, I. Talebi, D. Tarnogorska, E. Tenshaw, T. Tokhi, J. J. Walsh, T. Yang, J. A. Horne, F. Li, R. Parekh, P. K. Rivlin, V. Jayaraman, M. Costa, G. S. Jefferis, K. Ito, S. Saalfeld, R. George, I. A. Meinertzhagen, G. M. Rubin, H. F. Hess, V. Jain, and S. M. Plaza, "A connectome and analysis of the adult drosophila central brain," *eLife* **9** (2020), [10.7554/elife.57443](https://doi.org/10.7554/elife.57443).
- ⁸⁹⁰R. Court, M. Costa, C. Pilgrim, G. Millburn, A. Holmes, A. McLachlan, A. Larkin, N. Matentzoglou, H. Kir, H. Parkinson, N. H. Brown, C. J. O'Kane, J. D. Armstrong, G. S. X. E. Jefferis, and D. Osumi-Sutherland, "Virtual fly brain—an interactive atlas of the drosophila nervous system," *Frontiers in Physiology* **14** (2023), [10.3389/fphys.2023.1076533](https://doi.org/10.3389/fphys.2023.1076533).
- ⁸⁹¹L. K. Scheffer and I. A. Meinertzhagen, "The fly brain atlas," *Annual Review of Cell and Developmental Biology* **35**, 637–653 (2019).
- ⁸⁹²P. Agüi-Gonzalez, S. Jähne, and N. T. N. Phan, "SIMS imaging in neurobiology and cell biology," *Journal of Analytical Atomic Spectrometry* **34**, 1355–1368 (2019).
- ⁸⁹³D. S. McPhail, "Applications of secondary ion mass spectrometry (SIMS) in materials science," *Journal of Materials Science* **41**, 873–903 (2006).
- ⁸⁹⁴T. Wirtz, D. Dowsett, and P. Philipp, "SIMS on the Helium Ion Microscope: A Powerful Tool for High-Resolution High-Sensitivity Nano-Analytics," in²³, Chap. 13, pp. 297–323.
- ⁸⁹⁵A. Steele and B. Knuffman, "SIMS:ZERO," online (2023).
- ⁸⁹⁶F. A. Stevie, S. W. Downey, S. R. Brown, T. L. Shofner, M. A. Decker, T. Dingle, and L. Christman, "Nanoscale elemental imaging of semiconductor materials using focused ion beam secondary ion mass spectrometry," *Journal of Vacuum Science & Technology B: Microelectronics and Nanometer Structures* **17**, 2476 (1999).
- ⁸⁹⁷P. Gratia, G. Grancini, J.-N. Audinot, X. Jeanbourquin, E. Mosconi, I. Zimmermann, D. Dowsett, Y. Lee, M. Grätzel, F. D. Angelis, K. Sivula, T. Wirtz, and M. K. Nazeeruddin, "Intrinsic halide segregation at nanometer scale determines the high efficiency of mixed cation/mixed halide perovskite solar cells," *Journal of the American Chemical Society* **138**, 15821–15824 (2016).
- ⁸⁹⁸O. J. Usiobo, H. Kanda, P. Gratia, I. Zimmermann, T. Wirtz, M. K. Nazeeruddin, and J.-N. Audinot, "Nanoscale mass-spectrometry imaging of grain boundaries in perovskite semiconductors," *The Journal of Physical Chemistry C* **124**, 23230–23236 (2020).
- ⁸⁹⁹P. Gratia, I. Zimmermann, P. Schouwink, J.-H. Yum, J.-N. Audinot, K. Sivula, T. Wirtz, and M. K. Nazeeruddin, "The Many Faces of Mixed Ion Perovskites: Unraveling and Understanding the Crystallization Process," *ACS Energy Lett.* **2**, 2686–2693 (2017).

- ⁹⁰⁰C. Liu, Y. Yang, K. Rakstys, A. Mahata, M. Franckevicius, E. Mosconi, R. Skackauskaite, B. Ding, K. G. Brooks, O. J. Usiobo, J.-N. Audinot, H. Kanda, S. Driukas, G. Kavaliuskaite, V. Gulbinas, M. Dessimoz, V. Getautis, F. D. Angelis, Y. Ding, S. Dai, P. J. Dyson, and M. K. Nazeeruddin, "Tuning structural isomers of phenylenediammonium to afford efficient and stable perovskite solar cells and modules," *Nature Communications* **12** (2021), 10.1038/s41467-021-26754-2.
- ⁹⁰¹I. Zimmermann, P. Gratia, D. Martineau, G. Grancini, J.-N. Audinot, T. Wirtz, and M. K. Nazeeruddin, "Improved efficiency and reduced hysteresis in ultra-stable fully printable mesoscopic perovskite solar cells through incorporation of CuSCN into the perovskite layer," *Journal of Materials Chemistry A* **7**, 8073–8077 (2019).
- ⁹⁰²V. Sarbada, L. Yedra, A. Pshenova, A. Kercher, A. Marschilok, K. J. Takeuchi, E. Takeuchi, N. Dudney, T. Wirtz, S. Eswara, and R. Hull, "Correlative electron and ion beam analysis of the electrochemical performances of LiV3O8 cathode films as a function of microstructures," *Journal of Power Sources* **463**, 228177 (2020).
- ⁹⁰³L. Wheatcroft, N. Klingner, R. Heller, G. Hlawacek, D. Özkaya, J. Cookson, and B. J. Inkson, "Visualization and chemical characterization of the cathode electrolyte interphase using he-ion microscopy and in situ time-of-flight secondary ion mass spectrometry," *ACS Applied Energy Materials* **3**, 8822–8832 (2020).
- ⁹⁰⁴L. L. D. Taeye, M. J. Mees, and P. M. Vereecken, "Surpassing the 1 li/ti capacity limit in chlorine modified TiO₂-yCl₂y," *Energy Storage Materials* **36**, 279–290 (2021).
- ⁹⁰⁵J. Sastre, A. Priebe, M. Döbeli, J. Michler, A. N. Tiwari, and Y. E. Romanyuk, "Lithium garnet Li₇La₃Zr₂O₁₂ electrolyte for all-solid-state batteries: closing the gap between bulk and thin film Li-ion conductivities," *Advanced Materials Interfaces* **7**, 2000425 (2020).
- ⁹⁰⁶R. Dubey, J. Sastre, C. Cancellieri, F. Okur, A. Forster, L. Pompizii, A. Priebe, Y. E. Romanyuk, L. P. H. Jeurgens, M. V. Kovalenko, and K. V. Kravchyk, "Building a better Li-garnet solid electrolyte/metallic Li interface with antimony," *Advanced Energy Materials* **11**, 2102086 (2021).
- ⁹⁰⁷S. Nishinomiya, K. Toshin, R. Shishido, and S. Suzuki, "TOF-SIMS imaging of polyester/melamine resin with bismuth cluster ions," *Surface and Interface Analysis* **48**, 1114–1118 (2016).
- ⁹⁰⁸W. Gaderbauer, M. Arndt, T. Truglas, T. Steck, N. Klingner, D. Stifter, J. Faderl, and H. Groiss, "Effects of alloying elements on surface oxides of hot-dip galvanized press hardened steel," *Surface and Coatings Technology* **404**, 126466 (2020).
- ⁹⁰⁹A. Kosari, P. Visser, F. Tichelaar, S. Eswara, J.-N. Audinot, T. Wirtz, H. Zandbergen, H. Terryn, and J. Mol, "Cross-sectional characterization of the conversion layer formed on AA2024-t3 by a lithium-leaching coating," *Applied Surface Science* **512**, 145665 (2020).
- ⁹¹⁰K. Wiczerzak, A. Priebe, I. Utke, and J. Michler, "Practical aspects of focused ion beam time-of-flight secondary ion mass spectrometry analysis enhanced by fluorine gas coinjection," *Chemistry of Materials* **33**, 1581–1593 (2021).
- ⁹¹¹O. W. Kennedy, M. Zapf, J.-N. Audinot, S. Pal, S. Eswara, T. Wirtz, C. Ronning, and P. A. Warburton, "Photoluminescence of ZnO/ZnMgO heterostructure nanobelts grown by MBE," *Nanotechnology* **31**, 135604 (2020).
- ⁹¹²I. Fizeşan, S. Cambier, E. Moschini, A. Chary, I. Nelissen, J. Ziebel, J.-N. Audinot, T. Wirtz, M. Kruszewski, A. Pop, B. Kiss, T. Serchi, F. Loghin, and A. C. Gutleb, "In vitro exposure of a 3d-tetraculture representative for the alveolar barrier at the air-liquid interface to silver particles and nanowires," *Particle and Fibre Toxicology* **16** (2019), 10.1186/s12989-019-0297-1.
- ⁹¹³A. Priebe, J.-P. Barnes, T. E. J. Edwards, L. Pethö, I. Balogh, and J. Michler, "3D imaging of nanoparticles in an inorganic matrix using TOF-SIMS validated with STEM and EDX," *Analytical Chemistry* **91**, 11834–11839 (2019).
- ⁹¹⁴A. Priebe, J.-P. Barnes, T. E. J. Edwards, E. Huszár, L. Pethö, and J. Michler, "Elemental characterization of Al nanoparticles buried under a Cu thin film: TOF-SIMS vs STEM/EDX," *Analytical Chemistry* **92**, 12518–12527 (2020).
- ⁹¹⁵P. Lunca-Popa, J. Botsoa, M. Bahri, J. Crépellière, P. Desgardin, J.-N. Audinot, T. Wirtz, D. Arl, O. Ersen, M.-F. Barthe, and D. Lenoble, "Tunable interplay between atomistic defects morphology and electrical properties of transparent p-type highly conductive off-stoichiometric cu-cr-o delafossite thin films," *Scientific Reports* **10** (2020), 10.1038/s41598-020-58312-z.
- ⁹¹⁶T. N. Ooi, D. S. Mcphail, R. J. Chater, and B. A. Shollock, "Isotope exchange studies of oxidation mechanisms in nickel-base superalloys using FIB-SIMS techniques," *Surface and Coatings Technology* **201**, 3885–3888 (2006).
- ⁹¹⁷L. Sedláček, J. Kološová, J. Jiruše, and F. A. Stevie, "Insulator analysis using combined FIB-SEM instrument with TOF-SIMS," *Microscopy and Microanalysis* **20**, 306–307 (2014).
- ⁹¹⁸J. Lorinčík, I. Kašík, J. Vaniš, L. Sedláček, and J. Dluhoš, "Imaging of dopant distribution in optical fibers with an orthogonal TOF SIMS," *Surface and Interface Analysis* **46**, 238–240 (2014).
- ⁹¹⁹A. Priebe, L. Pethö, E. Huszar, T. Xie, I. Utke, and J. Michler, "High sensitivity of fluorine gas-assisted FIB-TOF-SIMS for chemical characterization of buried sublayers in thin films," *ACS Applied Materials & Interfaces* **13**, 15890–15900 (2021).
- ⁹²⁰F. C. Jundt, K. H. Purser, H. Kubo, and E. A. Schenk, "Proton-induced x-ray analysis of trace elements in tissue sections," *Journal of Histochemistry & Cytochemistry* **22**, 1–6 (1974).
- ⁹²¹R. Levi-Setti, Y. Wang, and G. Crow, "Scanning ion microscopy: Elemental maps at high lateral resolution," *Applied Surface Science* **26**, 249–264 (1986).
- ⁹²²R. Levi-Setti, "Structural and microanalytical imaging of biological materials by scanning microscopy with heavy-ion probes," Annual review of biophysics and biophysical chemistry **17**, 325–347 (1988).
- ⁹²³S. G. Boxer, M. L. Kraft, and P. K. Weber, "Advances in imaging secondary ion mass spectrometry for biological samples," *Annual Review of Biophysics* **38**, 53–74 (2009), PMID: 19086820.
- ⁹²⁴C. Szakal, K. Narayan, J. Fu, J. Lefman, and S. Subramaniam, "Compositional mapping of the surface and interior of mammalian cells at submicrometer resolution," *Analytical Chemistry* **83**, 1207–1213 (2011).
- ⁹²⁵P. Malmberg and H. Nygren, "Methods for the analysis of the composition of bone tissue, with a focus on imaging mass spectrometry (TOF-SIMS)," *PROTEOMICS* **8**, 3755–3762 (2008).
- ⁹²⁶J. Nuñez, R. Renslow, J. B. Cliff, and C. R. Anderton, "Nanosims for biological applications: Current practices and analyses," *Biointerphases* **13**, 03B301 (2018).
- ⁹²⁷K. Gillois, C. Stoffels, M. Leveque, I. Fourquaux, J. Blesson, V. Mils, S. Cambier, J. Vignard, H. Terrisse, G. Mirey, J.-N. Audinot, V. Theodorou, M.-H. Ropers, H. Robert, and M. Mercier-Bonin, "Repeated exposure of caco-2 versus caco-2/HT29-MTX intestinal cell models to (nano)silver in vitro: Comparison of two commercially available colloidal silver products," *Science of The Total Environment* **754**, 142324 (2021).
- ⁹²⁸A. D. Ost, T. Wu, C. Höschen, C. W. Mueller, T. Wirtz, and J.-N. Audinot, "4d surface reconstructions to study microscale structures and functions in soil biogeochemistry," *Environmental Science & Technology* **55**, 9384–9393 (2021).
- ⁹²⁹M. R. Ball, R. J. Taylor, J. F. Einsle, J.-N. Audinot, and R. J. Harrison, "Analytics on the FIB: ORION-SIMS and the discovery of a unique chondrite-like, precambrian impactor," *Microscopy and Microanalysis* **25**, 890–891 (2019).
- ⁹³⁰D. McPhail, "Some applications of SIMS in conservation science, archaeometry and cosmochemistry," *Applied Surface Science* **252**, 7107–7112 (2006).
- ⁹³¹K. Keune and J. J. Boon, "Imaging secondary ion mass spectrometry of a paint cross section taken from an early netherland-

- dish painting by roger van der weyden,” *Analytical Chemistry* **76**, 1374–1385 (2004).
- ⁹³²A. Adriaens and M. Dowsett, “Applications of SIMS to cultural heritage studies,” *Applied Surface Science* **252**, 7096–7101 (2006).
- ⁹³³Z. E. Voras, K. deGhetaldi, B. Baade, E. Gordon, G. Gates, and T. P. Beebe, “Comparison of oil and egg tempera paint systems using time-of-flight secondary ion mass spectrometry,” *Studies in Conservation* **61**, 222–235 (2016).
- ⁹³⁴P. Philipp, L. Rzeznik, and T. Wirtz, “Numerical investigation of depth profiling capabilities of helium and neon ions in ion microscopy,” *Beilstein Journal of Nanotechnology* **7**, 1749–1760 (2016).
- ⁹³⁵F. Kollmer, “Cluster primary ion bombardment of organic materials,” *Applied Surface Science* **231-232**, 153–158 (2004).
- ⁹³⁶H. M. Wu, L. A. Stern, J. H. Chen, M. Huth, C. H. Schwalb, M. Winhold, F. Porrati, C. M. Gonzalez, R. Timilsina, and P. D. Rack, “Synthesis of nanowires via helium and neon focused ion beam induced deposition with the gas field ion microscope,” *Nanotechnology* **24**, 175302 (2013).
- ⁹³⁷H. Wu, L. A. Stern, D. Xia, D. Ferranti, B. Thompson, K. L. Klein, C. M. Gonzalez, and P. D. Rack, “Focused helium ion beam deposited low resistivity cobalt metal lines with 10 nm resolution: implications for advanced circuit editing,” *Journal of Materials Science: Materials in Electronics* **25**, 587–595 (2014).
- ⁹³⁸J.-F. Lin, J. P. Bird, L. Rotkina, and P. A. Bennett, “Classical and quantum transport in focused-ion-beam-deposited pt nanointerconnects,” *Applied Physics Letters* **82**, 802–804 (2003).
- ⁹³⁹J.-F. Lin, J. P. Bird, and L. Rotkina, “Low-temperature decoherence in disordered pt nanowires,” *Physica E: Low-dimensional Systems and Nanostructures* **19**, 112–116 (2003).
- ⁹⁴⁰T. Tao, J. Ro, J. Melngailis, Z. Xue, and H. D. Kaesz, “Focused ion beam induced deposition of platinum,” *J. Vac. Sci. Technol. B: Microelectron. Process. Phenom.* **8**, 1826–1829 (1990).
- ⁹⁴¹A. Fernández-Pacheco, J. M. De Teresa, R. Córdoba, and M. R. Ibarra, “Metal-insulator transition in pt-c nanowires grown by focused-ion-beam-induced deposition,” *Physical Review B* **79**, 174204 (2009).
- ⁹⁴²J. M. De Teresa, R. Córdoba, A. Fernández-Pacheco, O. Montero, P. Strichovanec, and M. R. Ibarra, “Origin of the difference in the resistivity of as-grown focused-ion- and focused-electron-beam-induced pt nanodeposits,” *Journal of Nanomaterials* **2009**, 936863 (2009).
- ⁹⁴³P. G. Blauner, “Focused ion beam fabrication of submicron gold structures,” *J Vac Sci Technol B: Microelectron Nanometer Struct* **7**, 609 (1989).
- ⁹⁴⁴G. M. Shedd, H. Lezec, A. D. Dubner, and J. Melngailis, “Focused ion beam induced deposition of gold,” *Applied Physics Letters* **49**, 1584–1586 (1986).
- ⁹⁴⁵G. C. Gazzadi, J. J. Mulders, P. Trompenaars, A. Ghirri, A. Rota, M. Affronte, and S. Frabboni, “Characterization of a new cobalt precursor for focused beam deposition of magnetic nanostructures,” *Microelectronic Engineering* **88**, 1955–1958 (2011).
- ⁹⁴⁶A. D. Della Ratta, J. Melngailis, and V. C. Thompson, “Focused-ion-beam-induced deposition of copper,” *J. Vac. Sci. Technol. B* **11**, 2195–2199 (1993).
- ⁹⁴⁷J. Wang, M. Singh, M. Tian, N. Kumar, B. Liu, C. Shi, J. K. Jain, N. Samarth, T. E. Mallouk, and M. H. W. Chan, “Interplay between superconductivity and ferromagnetism in crystalline nanowires,” *Nature Physics* **6**, 389 EP – (2010), article.
- ⁹⁴⁸M. Kompaniits, O. V. Dobrovolskiy, C. Neetzel, E. Begun, F. Porrati, W. Ensinger, and M. Huth, “Proximity-induced superconductivity in crystalline cu and co nanowires and nanogranular co structures,” *J. Appl. Phys.* **116**, 073906 (2014).
- ⁹⁴⁹M. Kompaniits, O. V. Dobrovolskiy, C. Neetzel, F. Porrati, J. Brötz, W. Ensinger, and M. Huth, “Long-range superconducting proximity effect in polycrystalline Co nanowires,” *Appl. Phys. Lett.* **104**, 052603 (2014).
- ⁹⁵⁰O. V. Dobrovolskiy, V. M. Bevez, M. Y. Mikhailov, O. I. Yuzepovich, V. A. Shklovskij, R. V. Vovk, M. I. Tsindlekht, R. Sachser, and M. Huth, “Microwave emission from superconducting vortices in Mo/Si superlattices,” *Nat. Commun.* **9**, 4927 (2018).
- ⁹⁵¹H. Komano, Y. Ogawa, and T. Takigawa, “Silicon oxide film formation by focused ion beam (fib)-assisted deposition,” *Japanese Journal of Applied Physics* **28**, 2372–2375 (1989).
- ⁹⁵²R. J. Young and J. Puret, “Focused ion beam insulator deposition,” *Journal of Vacuum Science & Technology B: Microelectronics and Nanometer Structures* **13**, 2576 (1995).
- ⁹⁵³S. Lipp, “Tetramethoxysilane as a precursor for focused ion beam and electron beam assisted insulator (SiO_x) deposition,” *Journal of Vacuum Science & Technology B: Microelectronics and Nanometer Structures* **14**, 3920 (1996).
- ⁹⁵⁴K. Edinger, “Study of precursor gases for focused ion beam insulator deposition,” *Journal of Vacuum Science & Technology B: Microelectronics and Nanometer Structures* **16**, 3311 (1998).
- ⁹⁵⁵R. Córdoba, A. Ibarra, D. Maily, and J. M. De Teresa, “Vertical growth of superconducting crystalline hollow nanowires by he⁺ focused ion beam induced deposition,” *Nano Letters* **18**, 1379–1386 (2018).
- ⁹⁵⁶R. Córdoba, D. Maily, R. Rezaev, E. Smirnova, O. G. Schmidt, V. M. Fomin, U. Zeitler, I. Guillamon, h. Suderow, and J. M. De Teresa, “Three-dimensional superconducting nano-helices grown by he⁺-focused-ion-beam direct writing,” *Nano Letters* **19**, 8597–8604 (2019).
- ⁹⁵⁷R. Córdoba, A. Ibarra, D. Maily, I. Guillamón, H. Suderow, and J. M. De Teresa, “3d superconducting hollow nanowires with tailored diameters grown by focused he⁺ beam direct writing,” *Beilstein Journal of Nanotechnology* **11**, 1198–1206 (2020).
- ⁹⁵⁸P. Ortús, R. Córdoba, G. Hlawacek, and J. M. De Teresa, “Superconducting properties of in-plane w-c nanowires grown by he⁺ focused ion beam induced deposition,” *Nanotechnology* **32**, 085301 (2021).
- ⁹⁵⁹E. S. Sadki, S. Ooi, and K. Hirata, “Focused-ion-beam-induced deposition of superconducting nanowires,” *Applied Physics Letters* **85**, 6206–6208 (2004).
- ⁹⁶⁰E. S. Sadki, S. Ooi, and K. Hirata, “Focused ion beam induced deposition of superconducting thin films,” *Physica C-Superconductivity and Its Applications* **426**, 1547–1551 (2005).
- ⁹⁶¹D. Spoddig, K. Schindler, P. Rödiger, J. Barzola-Quiquia, K. Fritsch, H. Mulders, and P. Esquinazi, “Transport properties and growth parameters of pdc and wc nanowires prepared in a dual-beam microscope,” *Nanotechnology* **18**, 495202 (2007).
- ⁹⁶²I. J. Luxmoore, I. M. Ross, A. G. Cullis, P. W. Fry, J. Orr, P. D. Buckle, and J. H. Jefferson, “Low temperature electrical characterisation of tungsten nano-wires fabricated by electron and ion beam induced chemical vapour deposition,” *Thin Solid Films* **515**, 6791–6797 (2007).
- ⁹⁶³I. Guillamón, H. Suderow, S. Vieira, A. Fernández-Pacheco, J. Sesé, R. Córdoba, J. M. De Teresa, and M. R. Ibarra, “Nanoscale superconducting properties of amorphous w-based deposits grown with a focused-ion-beam,” *New Journal of Physics* **10**, 093005 (2008).
- ⁹⁶⁴W. Li, J. C. Fenton, Y. Wang, D. W. McComb, and P. A. Warburton, “Tunability of the superconductivity of tungsten films grown by focused-ion-beam direct writing,” *J. Appl. Phys.* **104**, 093913 (2008).
- ⁹⁶⁵Y. Sun, J. Wang, W. Zhao, M. Tian, M. Singh, and M. H. Chan, “Voltage-current properties of superconducting amorphous tungsten nanostrips,” *Scientific Reports* **3**, 1–7 (2013).
- ⁹⁶⁶R. Córdoba, T. I. Baturina, J. Sesé, A. Yu Mironov, J. M. De Teresa, M. R. Ibarra, D. A. Nasimov, A. K. Gutakovskii, V. A. Latyshev, I. Guillamón, H. Suderow, S. Vieira, M. R. Baklanov, J. J. Palacios, and V. M. Vinokur, “Magnetic field-induced dissipation-free state in superconducting nanostruc-

- tures," *Nature Communications* **4**, 1437 (2013).
- ⁹⁶⁷R. Córdoba Castillo, *Functional Nanostructures Fabricated by Focused Electron/Ion Beam Induced Deposition* (Springer International Publishing, 2014).
- ⁹⁶⁸R. Córdoba, P. Orús, S. Strohaber, T. E. Torres, and J. M. D. Teresa, "Ultra-fast direct growth of metallic micro- and nanostructures by focused ion beam irradiation," *Scientific Reports* **9**, 14076 (2019).
- ⁹⁶⁹P. Orús, V. M. Fomin, J. M. De Teresa, and R. Córdoba, "Critical current modulation induced by an electric field in superconducting tungsten-carbon nanowires," *Scientific Reports* **11**, 17698 (2021).
- ⁹⁷⁰F. Porrati, S. Barth, R. Sachser, V. O. Dobrovolskiy, A. Seybert, A. S. Frangakis, and M. Huth, "Crystalline niobium carbide superconducting nanowires prepared by focused ion beam direct writing," *ACS Nano* **13**, 6287–6296 (2019).
- ⁹⁷¹O. V. Dobrovolskiy, D. Y. Vodolazov, F. Porrati, R. Sachser, V. M. Bevez, M. Y. Mikhailov, A. V. Chumak, and M. Huth, "Ultra-fast vortex motion in a direct-write Nb-C superconductor," *Nat. Commun.* **11**, 3291 (2020).
- ⁹⁷²F. Porrati, F. Jungwirth, S. Barth, G. C. Gazzadi, S. Frabboni, O. V. Dobrovolskiy, and M. Huth, "Highly-packed proximity-coupled DC-Josephson junction arrays by a direct-write approach," *Adv. Func. Mater.* **n/a**, 2203889 (2022).
- ⁹⁷³E. J. Romans, E. J. Osley, L. Young, P. A. Warburton, and W. Li, "Three-dimensional nanoscale superconducting quantum interference device pickup loops," *Appl. Phys. Lett.* **97**, 222506 (2010).
- ⁹⁷⁴F. Sigloch, S. Sangiao, P. Orús, and J. M. de Teresa, "Direct-write of tungsten-carbide nanoSQUIDs based on focused ion beam induced deposition," *Nanoscale Advances* **4**, 4628–4634 (2022).
- ⁹⁷⁵A. Lapicki, E. Ahmad, and T. Suzuki, "Ion beam induced chemical vapor deposition (ibicvd) of cobalt particles," *Journal of Magnetism and Magnetic Materials* **240**, 47–49 (2002).
- ⁹⁷⁶Sanz-Martín, Magén, and Teresa, "High volume-per-dose and low resistivity of cobalt nanowires grown by Ga⁺ focused ion beam induced deposition," *Nanomaterials* **9**, 1715 (2019).
- ⁹⁷⁷C. Hyun, A. K. H. Lee, and A. de Lozanne, "Focused ion beam deposition of $\text{Co}_{71}\text{Cr}_{17}\text{Pt}_{12}$ and $\text{Ni}_{80}\text{Fe}_{20}$ on tips for magnetic force microscopy," *Nanotechnology* **17**, 921–925 (2006).
- ⁹⁷⁸S. Khizroev, J. A. Bain, and D. Litvinov, "Fabrication of nanomagnetic probes via focused ion beam etching and deposition," *Nanotechnology* **13**, 619–622 (2002).
- ⁹⁷⁹M. Gabureac, L. Bernau, I. Utke, and G. Boero, "Granular co-c nano-hall sensors by focused-beam-induced deposition," *Nanotechnology* **21**, 115503 (2010).
- ⁹⁸⁰L. Vogelaar, W. Nijdam, H. A. G. M. van Wolferen, R. M. de Ridder, F. B. Segerink, E. Flück, L. Kuipers, and N. F. van Hulst, "Large area photonic crystal slabs for visible light with waveguiding defect structures: Fabrication with focused ion beam assisted laser interference lithography," *Advanced Materials* **13**, 1551 (2001).
- ⁹⁸¹M. Esposito, V. Tasco, M. Cuscunà, F. Todisco, A. Benedetti, I. Tarantini, M. D. Giorgi, D. Sanvitto, and A. Passaseo, "Nanoscale 3d chiral plasmonic helices with circular dichroism at visible frequencies," *ACS Photonics* **2**, 105–114 (2014).
- ⁹⁸²M. Manoccio, M. Esposito, A. Passaseo, M. Cuscunà, and V. Tasco, "Focused ion beam processing for 3d chiral photonics nanostructures," *Micromachines* **12**, 6 (2020).
- ⁹⁸³M. Esposito, V. Tasco, F. Todisco, M. Cuscunà, A. Benedetti, D. Sanvitto, and A. Passaseo, "Triple-helical nanowires by tomographic rotatory growth for chiral photonics," *Nature Communications* **6**, 6484 (2015).
- ⁹⁸⁴M. Esposito, V. Tasco, F. Todisco, M. Cuscunà, A. Benedetti, M. Scuderi, G. Nicotra, and A. Passaseo, "Programmable extreme chirality in the visible by helix-shaped metamaterial platform," *Nano Letters* **16**, 5823–5828 (2016).
- ⁹⁸⁵M. Wang, R. Salut, H. Lu, M.-A. Suarez, N. Martin, and T. Grosjean, "Subwavelength polarization optics via individual and coupled helical traveling-wave nanoantennas," *Light: Science & Applications* **8**, 76 (2019).
- ⁹⁸⁶M. Wang, Z. Huang, R. Salut, M. A. Suarez, H. Lu, N. Martin, and T. Grosjean, "Plasmonic helical nanoantenna as a converter between longitudinal fields and circularly polarized waves," *Nano Letters* **21**, 3410–3417 (2021).
- ⁹⁸⁷M. Manoccio, M. Esposito, E. Primiceri, A. Leo, V. Tasco, M. Cuscunà, D. Zuev, Y. Sun, G. Maruccio, A. Romano, A. Quattrini, G. Gigli, and A. Passaseo, "Femtomolar biodection by a compact core-shell 3d chiral metamaterial," *Nano Letters* **21**, 6179–6187 (2021).
- ⁹⁸⁸G. Nanda, E. van Veldhoven, D. Maas, H. Sadeghian, and P. F. A. Alkemade, "Helium ion beam induced growth of hammerhead AFM probes," *J. Vac. Sci. Technol. B Microelectron. Nanometer Struct. Process. Meas. Phenom.* **33**, 06F503 (2015).
- ⁹⁸⁹J.-i. Fujita, S. Okada, R. Ueki, M. Ishida, T. Kaito, and S. Matsui, "Elastic double structure of amorphous carbon pillar grown by focused-ion-beam chemical vapor deposition," *Japanese Journal of Applied Physics* **46**, 6286–6289 (2007).
- ⁹⁹⁰K.-i. Nakamatsu, T. Ichihashi, K. Kanda, Y. Haruyama, T. Kaito, and S. Matsui, "Nanostructure analysis of nanosprings fabricated by focused-ion-beam chemical vapor deposition," *Japanese Journal of Applied Physics* **48**, 105001 (2009).
- ⁹⁹¹Y. Nakai, Y. Kang, M. Okada, Y. Haruyama, K. Kanda, T. Ichihashi, and S. Matsui, "Mechanical characteristics of nanosprings fabricated by focused-ion-beam chemical vapor deposition using ferrocene source gas," *Japanese Journal of Applied Physics* **49**, 06GH07 (2010).
- ⁹⁹²A. Reiser, L. Koch, K. A. Dunn, T. Matsuura, F. Iwata, O. Fogel, Z. Kotler, N. Zhou, K. Charipar, A. Piqué, P. Rohner, D. Poulikakos, S. Lee, S. K. Seol, I. Utke, C. Nisselroy, T. Zambelli, J. M. Wheeler, and R. Spolenak, "Metals by microscale additive manufacturing: Comparison of microstructure and mechanical properties," *Advanced Functional Materials* **30**, 1910491 (2020).
- ⁹⁹³R. Córdoba, M. Lorenzoni, J. Pablo-Navarro, C. Magén, F. Pérez-Murano, and J. M. De Teresa, "Suspended tungsten-based nanowires with enhanced mechanical properties grown by focused ion beam induced deposition," *Nanotechnology* **28**, 445301 (2017).
- ⁹⁹⁴S. Reyntjens and R. Puers, "Focused ion beam induced deposition: fabrication of three-dimensional microstructures and young's modulus of the deposited material," *Journal of Micromechanics and Microengineering* **10**, 181–188 (2000).
- ⁹⁹⁵J.-C. Yu, M. K. Abdel-Rahman, D. H. Fairbrother, and L. McElwee-White, "Charged particle-induced surface reactions of organometallic complexes as a guide to precursor design for electron- and ion-induced deposition of nanostructures," *ACS Applied Materials & Interfaces* **13**, 48333–48348 (2021).
- ⁹⁹⁶R. M. Thorman, S. J. Matsuda, L. McElwee-White, and D. H. Fairbrother, "Identifying and rationalizing the differing surface reactions of low-energy electrons and ions with an organometallic precursor," *The Journal of Physical Chemistry Letters* **11**, 2006–2013 (2020).
- ⁹⁹⁷W. G. Carden, H. Lu, J. A. Spencer, D. H. Fairbrother, and L. McElwee-White, "Mechanism-based design of precursors for focused electron beam-induced deposition," *MRS Communications* **8**, 343–357 (2018).
- ⁹⁹⁸S. Indrajith, P. Rousseau, B. A. Huber, C. Nicolafrancesco, A. Domaracka, K. Grygoryeva, P. Nag, B. Sedmidubská, J. Fedor, and J. Kočíšek, "Decomposition of iron pentacarbonyl induced by singly and multiply charged ions and implications for focused ion beam-induced deposition," *The Journal of Physical Chemistry C* **123**, 10639–10645 (2019).
- ⁹⁹⁹R. M. Thorman, P. A. Jensen, J.-C. Yu, S. J. Matsuda, L. McElwee-White, O. Ingólfsson, and D. H. Fairbrother, "Electron-induced reactions of $\text{Ru}(\text{CO})_4$: Gas phase, surface, and electron beam-induced deposition," *The Journal of Physical Chemistry C* **124**, 10593–10604 (2020).

- ¹⁰⁰⁰J. S. Ro, C. V. Thompson, and J. Melngailis, "Mechanism of ion beam induced deposition of gold," *Journal of Vacuum Science & Technology B: Microelectronics and Nanometer Structures* **12**, 73 (1994).
- ¹⁰⁰¹D. C. Joy, *Helium Ion Microscopy*, SpringerBriefs in Materials (Springer New York, New York, NY, 2013) p. 64.
- ¹⁰⁰²N. F. Mott and E. A. Davis, *Electronic processes in non-crystalline materials* (OUP Oxford, 2012).
- ¹⁰⁰³A. Lapicki and T. Suzuki, "Fabrication of magnetic dot arrays by ion beam induced chemical vapor deposition (ibicvd)," *IN-TERMAG Europe 2002 - IEEE International Magnetics Conference* **38**, 2589–2591 (2002).
- ¹⁰⁰⁴I. Utke, J. Michler, R. Winkler, and H. Plank, "Mechanical properties of 3d nanostructures obtained by focused electron/ion beam-induced deposition: A review," *Micromachines* **11**, 397 (2020).
- ¹⁰⁰⁵H. Plank, R. Winkler, C. H. Schwalb, J. Hütner, J. D. Fowlkes, P. D. Rack, I. Utke, and M. Huth, "Focused electron beam-based 3d nanoprinting for scanning probe microscopy: A review," *Micromachines* **11**, 48 (2019).
- ¹⁰⁰⁶M. Dukic, M. Winhold, C. H. Schwalb, J. D. Adams, V. Stavrov, M. Huth, and G. E. Fantner, "Direct-write nanoscale printing of nanogranular tunnelling strain sensors for sub-micrometre cantilevers," *Nature Communications* **7**, 12487 (2016).
- ¹⁰⁰⁷S. Matsui, "Focused-ion-beam deposition for 3-d nanostructure fabrication," *Nuclear Instruments and Methods in Physics Research, Section B: Beam Interactions with Materials and Atoms* **257**, 758–764 (2007).
- ¹⁰⁰⁸R. M. De Ridder, W. C. Hopman, and F. Ay, "Focused-ion-beam processing for photonics," *Proceedings of 2007 9th International Conference on Transparent Optical Networks, ICTON 2007* **2**, 212–215 (2007).
- ¹⁰⁰⁹P. Peinado, S. Sangiao, and J. M. De Teresa, "Focused electron and ion beam induced deposition on flexible and transparent polycarbonate substrates," *ACS Nano* **9**, 6139–6146 (2015).
- ¹⁰¹⁰M. Wang, R. Salut, M. A. Suarez, N. Martin, and T. Grosjean, "Chiroptical transmission through a plasmonic helical traveling-wave nanoantenna, towards on-tip chiroptical probes," *Optics Letters* **44**, 4861 (2019).
- ¹⁰¹¹J. S. Ro, V. C. Thompson, and J. Melngailis, "Microstructure of gold grown by ion-induced deposition," *Thin Solid Films* **258**, 333–335 (1995).
- ¹⁰¹²S. Matsui, "Focused-ion-beam chemical-vapor-deposition (FIB-CVD)," (Springer Netherlands, Dordrecht, 2012) pp. 866–876.
- ¹⁰¹³M. J. Perez-Roldan, J. J. L. Mulders, and P. H. F. Trompenaars, "Oxygen-assisted purification of platinum structures deposited by ion and electron beam induced processes," *Journal of Physics D: Applied Physics* **50**, 205307 (2017).
- ¹⁰¹⁴M. M. Shawrav, P. Taus, H. D. Wanzenboeck, M. Schinnerl, M. Stöger-Pollach, S. Schwarz, A. Steiger-Thirsfeld, and E. Bertagnolli, "Highly conductive and pure gold nanostructures grown by electron beam induced deposition," *Scientific Reports* **6**, 1–10 (2016).
- ¹⁰¹⁵A. Botman, J. J. L. Mulders, and C. W. Hagen, "Creating pure nanostructures from electron-beam-induced deposition using purification techniques: a technology perspective," *Nanotechnology* **20**, 372001 (2009).
- ¹⁰¹⁶K. Höflich, B. R. Yang, A. Berger, G. Leuchs, and S. Christiansen, "The direct writing of plasmonic gold nanostructures by electron-beam-induced deposition," *Advanced Materials* **23**, 2657–2661 (2011).
- ¹⁰¹⁷V. Cremers, R. L. Puurunen, and J. Dendooven, "Conformality in atomic layer deposition: Current status overview of analysis and modelling," *Applied Physics Reviews* **6**, 21302 (2019).
- ¹⁰¹⁸M. Cuscunà, M. Manocchio, M. Esposito, M. Scuderi, G. Nicotra, I. Tarantini, A. Melcarne, V. Tasco, M. Losurdo, and A. Passaseo, "Gallium chiral nanoshaping for circular polarization handling," *Materials Horizons* **8**, 187–196 (2021).
- ¹⁰¹⁹R. Kometani, S. Warisawa, and S. Ishihara, "Non-core-shell nanostructure deposition on focused-ion-beam chemical vapor deposition," *Japanese Journal of Applied Physics* **49**, 06GE03 (2010).
- ¹⁰²⁰M. Hentschel, J. Karst, and H. Giessen, "Tailored optical functionality by combining electron-beam and focused gold-ion beam lithography for solid and inverse coupled plasmonic nanostructures," *Advanced Optical Materials* **8**, 2000879 (2020).
- ¹⁰²¹J. M. De Teresa Noguerras, *Nanofabrication* (IOP Publishing Ltd, 2020).
- ¹⁰²²G. M. Atkinson, "30 nm resolution zero proximity lithography on high-z substrates," *Journal of Vacuum Science & Technology B: Microelectronics and Nanometer Structures* **10**, 3104 (1992).
- ¹⁰²³M. A. Hartney, "Surface imaging of focused ion-beam exposed resists," *Journal of Vacuum Science & Technology B: Microelectronics and Nanometer Structures* **9**, 3432 (1991).
- ¹⁰²⁴F. P. Stratton, "Microelectromechanical tunneling sensor fabrication and post-processing characterization using focused ion beams," *Journal of Vacuum Science & Technology B: Microelectronics and Nanometer Structures* **16**, 2449 (1998).
- ¹⁰²⁵N. R. Kiran, M. Chauhan, S. K. Sharma, S. Ghosh, and K. E. Gonsalves, "Resists for helium ion beam lithography: Recent advances," *ACS Applied Electronic Materials* **2**, 3805–3817 (2020).
- ¹⁰²⁶D. Winston, B. M. Cord, B. Ming, D. C. Bell, W. F. DiNatale, L. A. Stern, A. E. Vladar, M. T. Postek, M. K. Mondol, J. K. W. Yang, and K. K. Berggren, "Scanning-helium-ion-beam lithography with hydrogen silsesquioxane resist," *Journal of Vacuum Science & Technology B: Microelectronics and Nanometer Structures* **27**, 2702 (2009).
- ¹⁰²⁷V. Sidorkin, E. van Veldhoven, E. van der Drift, P. Alkemade, H. Salemink, and D. Maas, "Sub-10-nm nanolithography with a scanning helium beam," *J. Vac. Sci. Technol. B Microelectron. Nanometer Struct. Process. Meas. Phenom.* **27**, L18–L20 (2009).
- ¹⁰²⁸T.-J. Chang, T.-Y. Wang, C.-I. Wang, Z. da Huang, Y.-S. Jiang, C.-Y. Chou, W.-C. Kao, and M.-J. Chen, "Suppression of short channel effects in ferroelectric si junctionless transistors with a sub-10 nm gate length defined by helium ion beam lithography," *Journal of Materials Chemistry C* **9**, 8285–8293 (2021).
- ¹⁰²⁹W.-D. Li, W. Wu, and R. Stanley Williams, "Combined helium ion beam and nanoimprint lithography attains 4 nm half-pitch dense patterns," *J. Vac. Sci. Technol. B Microelectron. Nanometer Struct. Process. Meas. Phenom.* **30**, 06F304 (2012).
- ¹⁰³⁰J. Cai, Z. Zhu, P. F. A. Alkemade, E. van Veldhoven, Q. Wang, H. Ge, S. P. Rodrigues, W. Cai, and W.-D. Li, "3d volumetric energy deposition of focused helium ion beam lithography: Visualization, modeling, and applications in nanofabrication," *Advanced Materials Interfaces* **5**, 1800203 (2018).
- ¹⁰³¹R. Flatabø, A. Agarwal, R. Hobbs, M. M. Greve, B. Holst, and K. K. Berggren, "Exploring proximity effects and large depth of field in helium ion beam lithography: large-area dense patterns and tilted surface exposure," *Nanotechnology* **29**, 275310 (2018).
- ¹⁰³²D. Winston, V. R. Manfrinato, S. M. Nicaise, L. L. Cheong, H. Duan, D. Ferranti, J. Marshman, S. McVey, L. Stern, J. Notte, and K. K. Berggren, "Neon ion beam lithography (NIBL)," *Nano Letters* **11**, 4343–4347 (2011).
- ¹⁰³³X. Shi and S. A. Boden, "Scanning helium ion beam lithography," in *Materials and Processes for Next Generation Lithography*, edited by A. Robinson (Elsevier, 2016) pp. 563–594.
- ¹⁰³⁴A. Cattoni, D. Mailly, O. Dalstein, M. Faustini, G. Seniutinas, B. Rösner, and C. David, "Sub-10 nm electron and helium ion beam lithography using a recently developed alumina resist," *Microelectronic Engineering* **193**, 18–22 (2018).
- ¹⁰³⁵S. M. Lewis, M. S. Hunt, G. A. DeRose, H. R. Alty, J. Li, A. Wertheim, L. D. Rose, G. A. Timco, A. Scherer, S. G. Yeates, and R. E. P. Winpenny, "Plasma-etched pattern trans-

- fer of sub-10 nm structures using a metal-organic resist and helium ion beam lithography,” *Nano Letters* **19**, 6043–6048 (2019).
- ¹⁰³⁶R. Kumar, M. Chauhan, M. G. Moinuddin, S. K. Sharma, and K. E. Gonsalves, “Development of nickel-based negative tone metal oxide cluster resists for sub-10 nm electron beam and helium ion beam lithography,” *ACS Applied Materials & Interfaces* **12**, 19616–19624 (2020).
- ¹⁰³⁷S. Rashid, J. Walia, H. Northfield, C. Hahn, A. Olivieri, A. C. Lesina, F. Variola, A. Weck, L. Ramunno, and P. Berini, “Helium ion beam lithography and liftoff,” *Nano Futures* **5**, 025003 (2021).
- ¹⁰³⁸M. Yogesh, M. G. Moinuddin, M. Chauhan, S. K. Sharma, S. Ghosh, and K. E. Gonsalves, “Organiodine functionality bearing resists for electron-beam and helium ion beam lithography: Complex and sub-16 nm patterning,” *ACS Applied Electronic Materials* **3**, 1996–2004 (2021).
- ¹⁰³⁹L. Zhang, J. P. Thomas, X. Guan, N. F. Heinig, and K. T. Leung, “High-energy ion (He^+ , Si^{++} , Ga^+ , Au^{++}) interactions with PMMA in ion beam lithography,” *Nanotechnology* **31**, 325301 (2020).
- ¹⁰⁴⁰D. Xia, X. Zhu, F. Khanom, and D. Runt, “Neon and helium focused ion beam etching of resist patterns,” *Nanotechnology* **31**, 475301 (2020).
- ¹⁰⁴¹D. Maas, E. van Veldhoven, A. van Langen-Suurling, P. F. Alkemade, S. Wuister, R. Hoefnagels, C. Verspaget, J. Meessen, and T. Fliervoet, “Evaluation of EUV resist performance below 20nm CD using helium ion lithography,” in *SPIE Proceedings*, edited by O. R. Wood and E. M. Panning (SPIE, 2014).
- ¹⁰⁴²Y. Deng, X. Zhuang, W. Wang, R. Gu, D. He, L. Wang, and X. Cheng, “Direct visualization of beam-resist interaction volume for sub-nanometer helium ion beam-lithography,” *Nanotechnology* **32**, 415302 (2021).
- ¹⁰⁴³N. Kalhor and P. F. A. Alkemade, “Resist Assisted Patterning,” in ²³, Chap. 16, pp. 395–414.
- ¹⁰⁴⁴H. O. Funsten, J. W. Boring, R. E. Johnson, and W. L. Brown, “Low-temperature beam-induced deposition of thin tin films,” *Journal of Applied Physics* **71**, 1475–1484 (1992).
- ¹⁰⁴⁵P. Orús, F. Sigloch, S. Sangiao, and J. M. De Teresa, “Cryo-focused ion beam-induced deposition of tungsten-carbon nanostructures using a thermoelectric plate,” *Applied Sciences* **11**, 10123 (2021).
- ¹⁰⁴⁶E. Bilgiliyoy, R. M. Thorman, M. S. Barclay, H. Marbach, and D. H. Fairbrother, “Low energy electron- and ion-induced surface reactions of $\text{Fe}(\text{CO})_5$ thin films,” *The Journal of Physical Chemistry C* **125**, 17749–17760 (2021).
- ¹⁰⁴⁷M. E. Gross, W. L. Brown, L. R. Harriott, K. D. Cummings, J. Linnros, and H. Funsten, “Ion-beam direct-write mechanisms in palladium acetate films,” *Journal of Applied Physics* **66**, 1403–1410 (1989).
- ¹⁰⁴⁸P. Hoffmann, “Direct writing of iridium lines with a focused ion beam,” *Journal of Vacuum Science & Technology B: Microelectronics and Nanometer Structures* **9**, 3483 (1991).
- ¹⁰⁴⁹P. Hoffmann, G. B. Assayag, J. Gierak, J. Flicstein, M. Maar-Stumm, and H. van den Bergh, “Direct writing of gold nanostructures using a gold-cluster compound and a focused-ion beam,” *Journal of Applied Physics* **74**, 7588–7591 (1993).
- ¹⁰⁵⁰T. Bhuvana and G. U. Kulkarni, “Highly conducting patterned pd nanowires by direct-write electron beam lithography,” *ACS Nano* **2**, 457–462 (2008).
- ¹⁰⁵¹A. Salvador-Porroche, L. Herrer, S. Sangiao, J. M. de Teresa, and P. Cea, “Low-resistivity Pd nanopatterns created by a direct electron beam irradiation process free of post-treatment steps,” *Nanotechnology* **33**, 405302 (2022).
- ¹⁰⁵²A. Salvador-Porroche, L. Herrer, S. Sangiao, P. Philipp, P. Cea, and J. M. D. Teresa, “High-throughput direct writing of metallic micro- and nano-structures by focused ga^+ beam irradiation of palladium acetate films,” *ACS Applied Materials & Interfaces* **14**, 28211–28220 (2022).
- ¹⁰⁵³M. Kang, J. H. Wu, W. Ye, Y. Jiang, E. A. Robb, C. Chen, and R. S. Goldman, “Formation and evolution of ripples on ion-irradiated semiconductor surfaces,” *Appl. Phys. Lett.* **104**, 052103 (2014).
- ¹⁰⁵⁴F. M. Esmek, P. Bayat, F. Pérez-Willard, T. Volkenandt, R. H. Blick, and I. Fernandez-Cuesta, “Sculpturing wafer-scale nanofluidic devices for DNA single molecule analysis,” *Nanoscale* **11**, 13620–13631 (2019).
- ¹⁰⁵⁵D. Lebedev, G. Malyshev, I. Ryzhkov, A. Mozharov, K. Shugurov, V. Sharov, M. Panov, I. Tumkin, P. Afonicheva, A. Evstrapov, A. Bukatin, and I. Mukhin, “Focused ion beam milling based formation of nanochannels in silicon-glass microfluidic chips for the study of ion transport,” *Microfluid. Nanofluidics* **25**, 51 (2021).
- ¹⁰⁵⁶S. Waid, H. D. Wanzenboeck, M. Muehlberger, M. Gavagnin, and E. Bertagnolli, “Focused ion beam direct patterning of hardmask layers,” *J. Vac. Sci. Technol. B Microelectron. Nanometer Struct. Process. Meas. Phenom.* **32**, 041602 (2014).
- ¹⁰⁵⁷Z. Wang, Q. Wang, H. Li, J. Li, P. Xu, Q. Luo, A. Jin, H. Yang, and C. Gu, “The field emission properties of high aspect ratio diamond nanocone arrays fabricated by focused ion beam milling,” *Science and Technology of Advanced Materials* **6**, 799–803 (2005).
- ¹⁰⁵⁸G. Rius, J. Llobet, X. Borrísé, N. Mestres, A. Retolaza, S. Merino, and F. Perez-Murano, “Fabrication of complementary metal-oxide-semiconductor integrated nanomechanical devices by ion beam patterning,” *J. Vac. Sci. Technol. B Microelectron. Nanometer Struct. Process. Meas. Phenom.* **27**, 2691–2697 (2009).
- ¹⁰⁵⁹J. Llobet, G. Rius, A. Chuquitarqui, X. Borrísé, R. Koops, M. van Veghel, and F. Perez-Murano, “Arrays of suspended silicon nanowires defined by ion beam implantation: mechanical coupling and combination with CMOS technology,” *Nanotechnology* **29**, 155303 (2018).
- ¹⁰⁶⁰G. Rius, I. Martín, P. Godignon, A. Bachtold, J. Bausells, E. Lora-Tamayo, and F. Pérez-Murano, “Response of carbon nanotube transistors to electron beam exposure,” *Microelectronic Engineering* **84**, 1596–1600 (2007).
- ¹⁰⁶¹G. Rius, J. Llobet, M. Esplandiú, L. Solé, X. Borrísé, and F. Pérez-Murano, “Using electron and ion beams on carbon nanotube-based devices. effects and considerations for nanofabrication,” *Microelectronic Engineering* **86**, 892–894 (2009).
- ¹⁰⁶²S. Matsubara, H. Shichi, Y. Kawanami, and T. Hashizume, “Novel scanning ion microscope with H_3^+ gas field ionization source,” *Microscopy and Microanalysis* **22**, 614–615 (2016).
- ¹⁰⁶³M. Viteau, M. Reveillard, L. Kime, B. Rasser, P. Sudraud, Y. Bruneau, G. Khalili, P. Pillet, D. Comparat, I. Guerri, A. Fioretti, D. Ciampini, M. Allegrini, and F. Fuso, “Ion microscopy based on laser-cooled cesium atoms,” *Ultramicroscopy* **164**, 70–77 (2016), arXiv:1601.01446.
- ¹⁰⁶⁴M. Laurencich, L. Lapena, M. Lagaize, A. Houël, A. Delobbe, and E. Salançon, “Insulator on conductor ion source: first results and measurements,” in *FIT4NANO workshop*, edited by G. Hlawacek, G. Hobler, K. Höflich, T. Wirtz, and M. Marszalek (FIT4NANO, Krakow, 2022) p. 40.
- ¹⁰⁶⁵L. Bischoff and W. Pilz, “Flüssigmetall-Ionenquelle zur Erzeugung von Lithium-Ionenstrahlen,” patent DE102007027097B4 (Forschungszentrum Dresden - Rossendorf e.V., 01328 Dresden, DE, 2010).
- ¹⁰⁶⁶P. W. Hawkes and O. L. Krivanek, “Aberration correctors, monochromators, spectrometers,” in *Springer Handbook of Microscopy*, Springer Handbooks, edited by P. W. Hawkes and J. C. H. Spence (Springer International Publishing, Cham, 2019) Chap. 13, pp. 625–675.
- ¹⁰⁶⁷G. Hlawacek, I. Ahmad, M. A. Smithers, and E. S. Kooij, “To see or not to see: imaging surfactant coated nano-particles using HIM and SEM,” *Ultramicroscopy* **135**, 89–94 (2013).
- ¹⁰⁶⁸M. G. Stanford, B. B. Lewis, V. Iberi, J. D. Fowlkes, S. Tan, R. H. Livengood, and P. D. Rack, “In Situ Mitigation of Sub-surface and Peripheral Focused Ion Beam Damage via Simul-

- taneous Pulsed Laser Heating,” *Small* **12**, 1779–1787 (2016).
- ¹⁰⁶⁹L. Mele, S. Konings, P. Dona, F. Evertz, C. Mitterbauer, P. Faber, R. Schampers, and J. R. Jinschek, “A MEMS-based heating holder for the direct imaging of simultaneous in-situ heating and biasing experiments in scanning/transmission electron microscopes,” *Microscopy Research and Technique* **79**, 239–250 (2016).
- ¹⁰⁷⁰D. B. Boltje, J. P. Hoogenboom, A. J. Jakobi, G. J. Jensen, C. T. H. Jonker, M. J. Kaag, A. J. Koster, M. G. F. Last, C. de Agrela Pinto, J. M. Plitzko, S. Raunser, S. Tacke, Z. Wang, E. B. van der Wee, R. Wepf, and S. den Hoedt, “A cryogenic, coincident fluorescence, electron, and ion beam microscope,” *eLife* **11** (2022), 10.7554/elife.82891.
- ¹⁰⁷¹K. Sugioka and Y. Cheng, “Ultrafast lasers—reliable tools for advanced materials processing,” *Light: Science & Applications* **3**, e149–e149 (2014).
- ¹⁰⁷²G. Budnik, J. A. Scott, C. Jiao, M. Maazouz, G. Gledhill, L. Fu, H. H. Tan, and M. Toth, “Nanoscale 3d tomography by in-flight fluorescence spectroscopy of atoms sputtered by a focused ion beam,” *Nano Letters* **22**, 8287–8293 (2022).
- ¹⁰⁷³D. C. Joy, H. M. Meyer, M. Bolorizadeh, Y. Lin, and D. Newbury, “On the production of x-rays by low energy ion beams,” *Scanning* **29**, 1–4 (2007).
- ¹⁰⁷⁴B. Settles, “Active learning literature survey,” techreport (University of Wisconsin-Madison Department of Computer Sciences, 2009).
- ¹⁰⁷⁵HDF group, “Open source data management and storage suite,” online (2023), <https://www.hdfgroup.org/solutions/>.
- ¹⁰⁷⁶M. Könnecke, F. A. Akeroyd, H. J. Bernstein, A. S. Brewster, S. I. Campbell, B. Clausen, S. Cottrell, J. U. Hoffmann, P. R. Jemian, D. Männicke, R. Osborn, P. F. Peterson, T. Richter, J. Suzuki, B. Watts, E. Wintersberger, and J. Wuttke, “The NeXus data format,” *Journal of Applied Crystallography* **48**, 301–305 (2015), <https://www.nexusformat.org/>.
- ¹⁰⁷⁷W. Rasband, “ImageJ,” software (U.S. National Institutes of Health, Bethesda, Maryland, USA, 1997).
- ¹⁰⁷⁸C. Schneider, W. Rasband, and K. Eliceiri, “NIH Image to ImageJ: 25 years of image analysis,” *Nature Methods* **9**, 671–675 (2012).
- ¹⁰⁷⁹F. Pedregosa, G. Varoquaux, A. Gramfort, V. Michel, B. Thirion, O. Grisel, M. Blondel, P. Prettenhofer, R. Weiss, V. Dubourg, J. Vanderplas, A. Passos, D. Cournapeau, M. Brucher, M. Perrot, and Édouard Duchesnay, “Scikit-learn: Machine learning in python,” *Journal of Machine Learning Research* **12**, 2825–2830 (2011).
- ¹⁰⁸⁰M. Abadi, P. Barham, J. Chen, Z. Chen, A. Davis, J. Dean, M. Devin, S. Ghemawat, G. Irving, M. Isard, *et al.*, “Tensorflow: a system for large-scale machine learning,” in *OSDI’16: Proceedings of the 12th USENIX Conference on Operating Systems Design and Implementation* (USENIX Association, USA, 2016) pp. 265–283.
- ¹⁰⁸¹A. Paszke, S. Gross, F. Massa, A. Lerer, J. Bradbury, G. Chanan, T. Killeen, Z. Lin, N. Gimelshein, L. Antiga, *et al.*, “Pytorch: An imperative style, high-performance deep learning library,” *Advances in neural information processing systems* **32** (2019).
- ¹⁰⁸²Object Research Systems (ORS) Inc., “Dragonfly 2020.2,” online (2023), <http://www.theobjects.com/dragonfly>.
- ¹⁰⁸³S. M. Cea, S. Botelho, A. Chaudhry, P. Fleischmann, M. D. Giles, A. Grigoriev, A. Kaushik, P. H. Keys, H. W. Kennel, A. D. Lilak, R. Mehandru, M. Stettler, B. Voinov, N. Voynich, C. Weber, and N. Zhavoronok, “Process modeling for advanced device technologies,” *J Comput Electron* **13**, 18–32 (2013).
- ¹⁰⁸⁴J. K. Lorenz, E. Baer, A. Burenkov, A. Erdmann, P. Evanschitzky, and P. Pichler, “Challenges and opportunities for process modeling in the nanotechnology era,” *J Comput Electron* **13**, 3–17 (2013).
- ¹⁰⁸⁵F. Balestra, M. Graef, Y. Hayashi, N. Takaura, H. Ishiuchi, P. Gargini, and T. Conte, “International roadmap for devices and systems 2022: Executive Summary - IEEE IRDS™,” techreport (IEEE, 2022).
- ¹⁰⁸⁶P. S. Szabo, D. Weichselbaum, H. Biber, C. Cupak, A. Mutzke, R. A. Wilhelm, and F. Aumayr, “Graphical user interface for SDTrimSP to simulate sputtering, ion implantation and the dynamic effects of ion irradiation,” *Nuclear Instruments and Methods in Physics Research Section B: Beam Interactions with Materials and Atoms* **522**, 47–53 (2022).
- ¹⁰⁸⁷O. Buchnev, J. A. Grant-Jacob, R. W. Eason, N. I. Zheludev, B. Mills, and K. F. MacDonald, “Deep-Learning-Assisted Focused Ion Beam Nanofabrication,” *Nano Lett.* (2022), 10.1021/acs.nanolett.1c04604, publisher: American Chemical Society.
- ¹⁰⁸⁸M. Jain, S. Kretschmer, K. Höflich, J. M. J. Lopes, and A. V. Krashennnikov, “Atomistic Simulations of Defects Production under Ion Irradiation in Epitaxial Graphene on SiC,” *Physica Status Solidi (RRL) – Rapid Research Letters* **2200292**, 2200292 (2022).
- ¹⁰⁸⁹S. Refaely-Abramson, D. Y. Qiu, S. Louie, and J. B. Neaton, “Defect-Induced Modification of Low-Lying Excitons and Valley Selectivity in Monolayer Transition Metal Dichalcogenides,” *Physical Review Letters* **121**, 167402 (2018), 1804.05719.
- ¹⁰⁹⁰F. Bertoldo, S. Ali, S. Manti, and K. S. Thygesen, “Quantum point defects in 2D materials - the QPOD database,” *npj Computational Materials* **8**, 56 (2022), 2110.01961.
- ¹⁰⁹¹N. Mendelson, D. Chugh, J. R. Reimers, T. S. Cheng, A. Gottscholl, H. Long, C. J. Mellor, A. Zettl, V. Dyakonov, P. H. Beton, S. V. Novikov, C. Jagadish, H. H. Tan, M. J. Ford, M. Toth, C. Bradac, and I. Aharonovich, “Identifying carbon as the source of visible single-photon emission from hexagonal boron nitride,” *Nat. Mater.* **20**, 321–328 (2021).
- ¹⁰⁹²T. T. Tran, K. Bray, M. J. Ford, M. Toth, and I. Aharonovich, “Quantum emission from hexagonal boron nitride monolayers,” *Nat. Nanotechnol.* **11**, 37–41 (2016).
- ¹⁰⁹³Z. Shang, A. Hashemi, Y. Berencén, H.-P. Komsa, P. Erhart, S. Zhou, M. Helm, A. V. Krashennnikov, and G. V. Astakhov, “Local vibrational modes of Si vacancy spin qubits in SiC,” *Physical Review B* **101**, 144109 (2020), 2002.00067.